A System Concept Study and Experimental Evaluation of Miniaturized Electrodynamic Tethers to Enhance Picosatellite and Femtosatellite Capabilities

by

Iverson C. Bell

A dissertation submitted in partial fulfillment
of the requirements for the degree of
Doctor of Philosophy
(Electrical Engineering)
in the University of Michigan
2015

Doctoral Committee:

Professor Brian E. Gilchrist, Chair
Associate Professor John E. Foster
Professor Alec D. Gallimore
Professor Mark J. Kushner

To my family for their incredible support and motivation
Dr. Wyndolyn Bell, Dr. Iverson Bell, Jr., Cecelia Crutchfield,
Lauren Trabert, Eric Trabert, and Audrey Trabert

ACKNOWLEDGEMENTS

I would like to acknowledge and express my gratitude towards many people. Perhaps my biggest challenge is to list all of the people who have been supportive along the way. First and foremost, I would like to express my gratitude to my advisor, Professor Brian Gilchrist. This has been a prodigious experience, and I am grateful for his guidance and motivation.

I would also like to express my gratitude towards my committee members. Professor Alec Gallimore has offered me exceptional support and the use of his laboratory facilities, making my experimental research possible. I am eternally grateful to Professor John Foster, who offered his time to help me better understand hollow cathodes and Langmuir probe analysis. I would also like to express gratitude to Professor Mark Kusher for teaching me the fundamentals of plasma physics and exposing me to advanced fields of plasma physics through numerous Michigan Institute for Plasma Science and Engineering (MIPSE) seminars.

I would also like to thank colleagues in the Space Electrodynamics and Tether Systems (SETS) group as well as the Plasma and Electric Propulsion Laboratory (PEPL). I would like to extend a special thanks to Kimberly Trent for Cathode Test Facility (CTF) and hollow cathode training as well as for instituting a variety of much-needed facility upgrades. I would like to thank Scott Hall, Grant Miars, Omar Leon for assisting in editing sections of this thesis. I owe many thanks to my colleague Jesse McTernan for his keen technical insights. I also must thank Eric Viges at Electrodynamic Applications (EDA) for assembling the hollow cathode, sharing his vacuum facility, and offering so much help with mine.

I would also like to thank students I have worked with who have contributed substantially to my research, particularly Jamin Rager, Chen Lu, Abhishek Cauligi, and Bret Bronner.

I am grateful to all the students who have worked with me on the Miniature Tether Electrodynamics Experiment (MiTEE) mission. MiTEE is extremely challenging, and I owe the tremendous progress made in MiTEE to the high caliber of students we have currently working on the mission. It is essential, however, to thank the first project manager of MiTEE, Vritika Singh, and the first chief engineer, Kyle Hagen, who were the pioneers that helped launch MiTEE to its current status.

I am also grateful for the National Science Foundation, Air Force Office of Scientific Research, Michigan Space Grant Consortium, Rackham Graduate School, GEM, and MIPSE support. Their fellowships have enabled me to pursue this research, and for that I am grateful.

Many staff members have also played a vital role in my progress. I would like to thank Karla Johnson, Michelle Chapman, and Karen Liska.

I would also like to thank my family. I owe my preparation prior to the doctoral program and much of the progress I have made in the program to the unparalleled support provided by my mother, father, and sister over the years. I would also like to thank my friends and colleagues at the University of Michigan, Sasha Cai Lesher-Perez, Garen Vartanian, and Brandon Pitts, who have been a truly incredible bedrock of support. I would like to thank the Canterbury House family and Reid Hamilton for their support.

I would like to extend a special thank you to Lemar Thomas, Marquan Jackson, Lawrence Hood, John Sanders, Lewis Colson, Harold Curry, and Monroe Alford. These gentlemen provided an extended family and served as a source of inspiration.

Last but certainly not least, I would like to thank Zindzi Thompson. She has been supportive during the most strenuous and productive period of the doctoral process. I lack words to truly express my gratitude. She has contributed enormously to my focus and motivation and I am truly grateful for this.

TABLE OF CONTENTS

LIST OF FIGURES

LIST OF TABLES

ABSTRACT

A SYSTEM CONCEPT STUDY AND EXPERIMENTAL EVALUATION OF MINIATURIZED ELECTRODYNAMIC TETHERS TO ENHANCE PICOSATELLITE AND FEMTOSATELLITE CAPABILITIES

by

Iverson C. Bell

Chair: Brian E. Gilchrist

The work presented in this thesis evaluates the potential of electrodynamic tether (EDT) propulsion technology to provide picosatellites (100 g–1 kg) and femtosatellites (<100 g) with orbital maneuvering capability. The miniaturized EDT concept considered in this dissertation is a fundamentally novel paradigm because it is much shorter than a conventional EDT, with total length of about 10 meters, and it considers the use of a semi-rigid tether. A detailed trade study is presented that explores the feasibility of using EDTs for small satellite drag make-up and propulsion. The EDT anode's ability to draw current from the ionosphere and generate thrust with current through the tether is analyzed. This performance is traded against the power needed to overcome atmospheric drag forces. The trade study includes the development of a system concept and mission scenario. Three example small spacecraft were considered in this study: a 200-g planar picosat, a 150-g cubic picosat, and a 10-g "ChipSat." The results reveal that an insulated tether only a few meters long can provide these spacecraft with complete drag cancellation and the ability to change orbit. All of the spacecraft were able to generate a thrust force that exceeded drag at 500 km and 600 km, assuming a circular, equatorial orbit. Adequate thrust at higher altitudes is expected, but at lower altitudes, e.g. near

400 km, only the 200-g planar picosat appeared able to overcome drag. Further, the tether could also serve as a communication or scientific radio antenna.

EDT thrust estimates were made for a set of particular, but representative, cases and a few simplifying assumptions were made to facilitate estimating tether current. In all these cases, electrons were collected by the positively biased exposed conducting surfaces of a picosat or femtosat, presenting a variety of challenges for estimating current collection. The anode electron collection model was derived from an expression previously developed to interpret plasma parameters from the wide sweeping Langmuir probe instrument (WLP) on the International Space Station (ISS). In order to evaluate electron current collection, ground-based plasma experiments were conducted to capture key characteristics of the satellite-low-Earth-orbit (LEO) interaction. Tests were performed to investigate current collection in a flowing plasma and observe changes in collection due to (a) probe orientation relative to plasma flow and (b) magnetic field strength. Key parameters that impact electron collection, like the electrode shape, radius-to-Debye length ratio, r_p/λ_D, and the probe radius-to-electron thermal gyroradius ratio, were scaled to be representative of the orbital environment.

The laboratory data were analyzed to develop expressions for the current collection behavior of the 200-g planar picosat, the 150-g cubic picosat, and the 10-g ChipSat, The data indicated that the WLP-based collection model could be refined with small modification to the thrust estimates. Using the experimentally derived current collection model and a specific mission scenario, the peak estimated thrust for pairs of tethered 200-g planar picosats was 10% less than the thrust estimated by the WLP model, the peak estimated thrust for pairs of 150-g cubic picosat was 44% more than thrust estimated using the WLP model, and the peak estimated thrust for pairs of 10-g planar picosat was 35% more than the thrust estimated using the WLP model. It was also determined that the anode's current collection characteristic would be impacted by the orientation of the spacecraft relative to the magnetic field and the direction of motion depending on the shape of the anode. The refinements for thrust were relatively minor, suggesting that the miniaturized EDT concept may be capable of providing picosat and femtosat orbital maneuverability.

CHAPTER 1

Introduction and Background

1.1 Research Motivation and Problem Definition

The relatively new concept of “smartphone”-sized, sub-kilogram spacecraft is the next frontier in spacecraft miniaturization. Interest in very small spacecraft with their longest dimension in the tens of centimeters, and—more recently— down to a few centimeters, is motivated by the success of nanospacecraft (1–10 kg) and growing capabilities to integrate more functionality and sophistication into an even smaller volume. These spacecrafts are categorized as picosatellites (100 g–1 kg), femtosatellites (<100 g), or “picosats” and “femtosats” for short. Due to their small size and low mass, they can be much less expensive (on a per unit basis) to launch into orbit. It may also be possible to deploy them in large numbers to enable missions requiring distributed measurements in space and/or time (e.g., distributed aperture, simultaneous spatial sampling, or rapid re-sampling of a single location). However, without some degree of propulsion, these spacecraft would behave as an uncontrolled swarm rather than as a coordinated formation. Further, orbital lifetime is limited for low-mass spacecraft with high area-to-mass ratios. An appropriately miniaturized propulsion technology could increase orbital lifetime and unlock the potential for dynamically reconfigurable constellations and controlled de-orbiting for sub-kilogram spacecraft.

Short or miniaturized electrodynamic tethers (EDT) have the potential to provide propellantless propulsion (orbital maintenance, inclination change, boosting, and de-boosting), passive two-axis attitude stabilization, and enhanced communication capability to these uniquely small spacecraft. More generally, a miniaturized EDT has potential to exert controllable forces on objects in an ionosphere. This suggests that a miniaturized EDT may have other applications beyond propulsion of picosatellite and femtosatellites,

such as adjusting the orientation or "attitude" of larger spacecraft. The goal of this thesis is to investigate the feasibility of using miniaturized electrodynamic tethers for picosat or femtosat propulsion as well as to consider other capabilities the technology may provide.

1.1.1 Picosatellite and Femtosatellite Introduction

Picosats and femtosats are transformative emerging technologies inspired by the success of nanospacecraft and millimeter-scale wireless sensor network concepts (i.e., “SmartDust”) [1]. Advances in electronics miniaturization and reduced power consumption, as well as improvements in integrated circuit (IC) and microelectromechanical systems (MEMS) technology, are making possible the concept of very small spacecraft at the levels of fully monolithic semiconductor integrated circuits or hybrid integrated circuits. Effectively, this architecture can be thought of as a small “satellite-on-a-PCB” or “satellite-on-a-chip” [2]. In addition, many of the original concepts involved the “system-on-a-chip” model: a spacecraft on a chip that can take advantage of semiconductor batch production techniques to enable mass production of silicon satellites [3]–[5].

Picosats and femtosats are compared to other spacecraft in Table 1.1, which presents a range of mass classifications commonly used to categorize different types of artificial satellites [6]–[8]. Spacecraft with mass less than 500 kg are also categorized as small satellites or "smallsats" [7]. Thus, picosats and femtosats are currently the smallest small satellites.

Table 1.1: Artificial Satellite Mass Classifications [7], [8].

Classification		Mass Range
Large satellite		> 1000 kg
Medium size satellite		500 –1000 kg
Small satellite	Minisatellite	100 –500 kg
	Microsatellite	10–100 kg
	Nanosatellite	1–10 kg
	Picosatellite	0.1–1 kg
	Femtosatellite	< 0.1 kg

Modern smartphones serve as an everyday example of sophistication and capability at the high end of this extremely small, sub-kilogram scale. A typical smartphone has a mass of ~100 g and can fit in the palm of the hand [9], yet it contains many of the basic systems found in a simple spacecraft, like a computer, radio transmitter and receiver, battery, global positioning system (GPS) receiver, accelerometer, and 3-axis magnetometer. This suggests that matching or exceeding the capabilities of today's nanosat could be achievable near and below the 100-gram level (femtosats). In turn, it is possible to consider coordinated *fleets* of such sub-kilogram spacecraft, enabling a variety of transformative space missions. Figure 1.1 shows an illustration of a larger spacecraft releasing several picosats in orbit. This section will introduce the picosat and femtosat concepts by providing the historical context for their development and explore the key miniaturized technologies and advances that make them possible. Potential applications of these satellites are explained in a following section.

Figure 1.1: Visual illustration of small satellites being deployed from a larger satellite in Earth orbit. *The background image is a photograph of hurricane Isabel taken from the International Space Station (ISS)* [10]. *Photo courtesy of NASA.*

1.1.1.1 The Evolution of Picosatellites and Femtosatellites

The potential role of picosats and femtosats has evolved with advances in technology and our perception of their impact. At the beginning of the space flight era, spacecraft we now classify as "small satellites" were much less capable and some were simply precursors to larger, more capable spacecraft. Small satellites are defined as satellites with a mass of less than 500 kg. For example, the first two man-made satellites launched into orbit, Sputnik-1 in 1957 and Explorer-1 in 1958, were microsatellites (as defined in Table 1.1) while the next US spacecraft launched, Vanguard-1, was a 1.5 kg nanosatellite. The follow-up Sputnik, Explorer, and Vanguard satellites, however, were all heavier. The general trend at the time was to make satellites more capable, which meant size and mass increased to accommodate more functionality. Helvajian and Janson (2008) discuss the growth in average spacecraft mass during this period [11]. One explanation for this is that electronic and sensing technology was less capable early in the spaceflight era. The electronics were generally larger and required more energy than today's technology [7]. Larger spacecraft were needed to accomplish technologically sophisticated missions.

The few simple, sub-kilogram spacecraft that were launched were used for radar calibration, atmospheric density monitoring, and demonstrating technology in space. The first man-made sub-kilogram satellites launched into orbit, the Westford needles, were launched in 1963 as part of Project West Ford. The goal of the project was to facilitate over-the-horizon global radio communication. To do this, the project released 480 million 1.78 cm-long copper needles to create a distributed reflector for communications at approximately 8 GHz. The needles were in orbit in the 1500 km to 3600 km altitude range. Individually, each needle had a mass of only ~40 micrograms [12].

The individual Westford needles decayed within a few years. The relatively brief 5-year orbital lifetimes of the Westford needles has been attributed to the large area-to-mass ratio of the spacecraft, which made them sensitive to the effects solar radiation pressure as well as other orbital perturbations (discussed further in Chapter 2) [13].

However, many Westford needles formed clumps and some of these clumps currently remain in orbit, more than 50 years later, because they have *smaller* area-to-mass ratios [13], [14]. Project Westford represents the extreme end of spacecraft miniaturization and, in the context of this dissertation, provides motivation for small spacecraft maneuverability and controllability.

In 1963, the 700-gram US Air Force Environmental Research Satellite-5 (ERS-5) and ERS-6 picosats were launched into orbit. The next picosatellites, Calspheres 3,4, and 5, were launched in 1971 and used for atmospheric drag studies. An inflatable picosat was deployed later that year for radar calibration. Yet, because the average spacecraft mass was increasing, the next sub-kilogram satellites would not be launched for 14 years [11].

As time progressed through the 1960s and 1970s, spacecraft capabilities became more sophisticated, leading to advances in communication, remote sensing, exploration, and navigation. However, missions using large sophisticated spacecraft were more expensive. The factors that contributed to this are explained in Wertz, Everett, and Puschell (2011) [7]. One cost, the launch cost, was and still is high—current costs are on the order of $10,000 to $20,000 per kg—and although this represents only a portion of the overall cost of a space mission, it is a cost that increases with spacecraft mass [7]. As the cost of space missions increased, missions began to enter the "space spiral," where increasing cost caused longer schedules and less frequent missions that, in turn, prompted a demand for higher reliability. The demand for higher reliability (or lower risk) led to higher mission cost.

In general, the small spacecraft concept embraced today emerged as an alternative to large, expensive, and infrequently launched spacecraft. Perceptions about small spacecraft capabilities changed because of advances in miniaturized electronics and sensing technologies (discussed in the next sub-section) and a growing recognition of their mission-enabling potential. In the early 1980s, the Distributed Sensors Network (DSN) program at the Defense Advanced Research Projects Agency (DARPA) generated interest in the concept of spatially distributed, low-cost wireless sensor networks for terrestrial applications [15]. The distributed wireless sensor concept was later adopted by the space community. In 1988, the United Stated Strategic Defense Initiative

Organization and NASA's Jet Propulsion Laboratory (JPL) hosted the Microspacecraft for Space Science Workshop [16]. The workshop reached the following conclusions:

- nanosatellites were technically feasible
- these satellites could potentially enable missions requiring simultaneous multi-point measurements
- a key enabling feature would be the reduced spacecraft and launch costs associated with many small spacecraft as compared to using many large spacecraft for the same mission
- these small spacecraft would not necessarily be applicable to all types of space explorations and science

This workshop helped establish the value of small satellites as a platform for enabling new capabilities.

More recently, the vision of highly capable, extremely small spacecraft has begun to emerge as several sophisticated picosats have been developed and launched into orbit. In 2000, DARPA and the Aerospace Corporation launched a pair of smartphone-sized (2.5 cm × 7.6 cm × 10.2 cm) picosats with a mass of a few hundred grams in 2000. PicoSats 1 and 2 were identical 250-g satellites connected by a 30-m non-conducting tether [11]. Huang, Hansen, Janson, and Helvajia (2002) at the Aerospace Corporation designed and tested the structural members and key subsystems of a 100-g spacecraft called the Co-Orbital Satellite Assistant (COSA) [4]. A "satellite-on-a-PCB" design was developed by the University of Surrey to be an element in a space-based wireless sensor network. The standardized ~10 cm × 10 cm × 10 cm platform known as a "1U CubeSat" has also been used to develop larger picosats close to ~1 kg for meaningful missions [17], [18].

More recently, the PocketQube architecture is increasing in popularity, with a single PocketQube unit (called "1P") equal to $1/8^{th}$ of a standard 1U CubeSat in volume. TLogoQube, WREN, Eagle-1, and QubeScout-S1 are all PocketQube spacecraft examples [19], [20]. At the very small end of the scale, Atchinson and Peck (2009) of Cornell University designed a milligram level, 1 cm x 1 cm x 25 micron femtosatellite called "Sprite" [21]. A larger prototype of the Sprite femtosat underwent testing on the Materials International Space Station Pallet (MISSE-8) on the International Space Station

in 2011 and about 100 Sprite prototypes expected to be launched as part of the KickSat mission [22]. The N-prize competition also generated interest in femtosatellites. The N-prize was a competition to launch a femtosatellite between 9.99 and 19.99 grams into LEO and track it for at least 9 orbits. The competition motivated research for a femtosatellite proof-of-concept study [23], technology demonstrator [24], launcher [25], and payload management system [26]. In addition, research supporting sub-kilogram satellites has been done on orbital evolution [27], appropriate antennas [28], [29], and radiation hardening [30].

In 2014, AeroCube 6a and 6b set the standard, for the time, in sophisticated sensing capability at the sub-kilogram scale. Each AeroCube 6 spacecraft was a "0.5U" CubeSat size, where a "1U" CubeSat is approximately a 10-cm cube with a mass of about 1 kg. Each spacecraft included recently developed micro dosimeters for measuring radiation in LEO, an inter-satellite cross-link experiment, and attitude sensors [31]. Picosat and femtosat sizes and masses are compared in Table 1.2.

Table 1.2: Example picosats and femtosats size and mass.

Satellite	Size	Mass
AeroCube 6a,6b	10 cm×10 cm×5 cm	~500 g
PCBSat	10 cm×10 cm×2.5 cm	311 g
PICOSAT 1.0	10 cm×7.5 cm×2.5 cm	275 g
MCMSat [4]	10 cm×10 cm×1 cm	170 g
1Q PocketQube	5 cm×5 cm×5 cm	125 g
WikiSat V4.1	14.1 cm×3 cm×7 mm	19.7 g
SpaceChip	2 cm×2 cm×3 mm	~10 g
Sprite	1 cm×1 cm×25 μm	7.5mg

1.1.1.2 Miniaturized Technologies

Advances in technology miniaturization have helped make potential satellites at the sub-kilogram scale more capable. This section briefly lists advances in several key areas that enable spacecraft design at the picosat and femtosat scale. A list of several example technologies is provided in Table 1.3. A more thorough discussion is provided in Helvajian and Janson (2008) which also includes a discussion of novel miniaturized inertial measurement units (IMU) and magnetic field sensors [11].

1.1.1.2.1 Microelectronics

Spacecraft miniaturization has been made possible in part because of advances in low power microelectronics. Dr. Gordon Moore, co-founder of the Intel Corporation, observed that the number of electronic components in a dense integrated circuit doubled approximately every 18-24 months, and he expected the trend to continue [32]. This trend, popularly known as Moore's law, became a target for the semiconductor industry and has been repeated for more than 4 decades. As the minimum feature sizes (MFS) of transistors in integrated circuits (IC) decreased, the circuit density doubled. The reduction in feature size and advances in transistor technology have also produced faster and lower power transistors and more efficient microelectronics including microprocessors, microcontrollers, random access memory (RAM) chips, erasable programmable read only memory (EPROM).

1.1.1.2.2 Solar Cells

Advances in photovoltaic or solar cells efficiency enable small satellites to generate electrical power on the dayside of the orbit. The conversion efficiency of the solar energy incident on solar panels has increased significantly over time as solar cell technology has progressed. During the first two decades of the space age, solar cells for spacecraft were primarily single crystal silicon cells with low energy conversion efficiencies. Vanguard 1, launched in 1958, was the first spacecraft to use PV cells. Vanguard 1 carried a few small body-mounted silicon solar cells, delivering 50–100 mW with an energy conversion efficiency of about 7-8% [33]. Solar cell technology has advanced significantly in the intervening years. An incomplete list of common solar cell semiconducting materials includes silicon (Si), germanium (Ge), gallium arsenide (GaS), and gallium indium phosphide ($GaInP_2$). As of 2015, space-grade $GaInP_2$/GaAs/Ge solar cells with efficiencies around 28% can be purchased. This means that smaller cells and arrays can generate much more electrical energy for sensors and other systems.

1.1.1.2.3 Batteries

Advances in secondary or rechargeable battery technology provide small satellites the ability to operate on the night side of the orbit and store energy for operations that

require high peak power. A secondary or rechargeable battery converts electrical energy into chemical energy when charging and chemical energy into electrical energy when discharging. A spacecraft using solar cells recharges in sunlight and discharges during eclipse. Nickel Cadium (NiCd) secondary batteries were first launched into space on Explorer 6 in 1959 and were in common use for decades because of their long cycle life [34]. Later, NiCd batteries were replaced by nickel-metal hydride batteries for small spacecraft and NiH batteries for large spacecraft. More recently, lithium-ion batteries have been used in space missions. This is in part because their energy storage density is more than twice that of NiCd batteries. Space-qualified lithium ion batteries can be purchased for CubeSats with energy storage densities of about 150 Whr/kg in comparison to about 23-30 Whr/kg for NiCd electrical energy and similar values for NiH and nickel metal hydride batteries [7]. As a result, small satellites can store energy in a much smaller volume than before.

1.1.1.2.4 Sensors

A variety of small sensors have also been proposed for small spacecraft missions. Some examples are given here. Dimensions of example sensors are provided Table 1.3. The Miniaturized ElectroStatic Analyzer (MESA) is capable of providing *in situ* electron and ion density and temperature measurements, potentially enabling detection of ionospheric depletions or "plasma bubbles" [35]. Particles in the 0–20 eV range can be detected. The use of MESA would require attitude control because the instrument needs to be oriented in the ram direction to measure ions. MESA has flown on the MISSE-6, MISSE-7, and FalconSat 5 missions [36]. At a smaller scale, the Flat Plasma Spectrometer (FlaPS) is capable of analyzing the energy and angular distributions of ions and electrons in the 10 eV–50 keV range. The instrument is described as a single "pixel" that could be combined with other FlaPS pixels. FlaPS was launched on the FalconSat 3 mission [37]. The Gas Chromatography Chip is an example of a MEMS-based "micro gas chromatograph" (μGC) designed for terrestrial applications [38]. However, a similarly sized μGC could be considered for *in situ* studies of the upper atmosphere.

It has also been suggested that coordinated, controllable groups of sub-kilogram satellites could perform remote sensing missions. Small, low power, CMOS-fabricated

image sensors (like those used in smartphones) have been demonstrated in space and can be useful for visible Earth imaging, sun sensing, and attitude determination [39].

Table 1.3: Example technologies appropriate for small satellites

Component	Approximate size
Miniaturized ElectroStatic Analyzer (MESA) [35]	10 cm×10 cm×3 cm
Gas Chromatography Chip [38]	10 cm×10 cm×3 mm
MEMS Flat Plasma Spectrometer (FlaPS) [37]	~1 cm^3 (per pixel)
Visible imaging sensor [40]	2.5 mm×2.5 mm×2.9 mm

1.1.2 Potential Picosatellite and Femtosatellite Applications

Single picosats and femtosats have the potential to enable a variety of unique missions. Uses of individual sub-kilogram spacecraft include:

- Deployable satellites capable of inspecting larger satellites, assisting in the calibration of onboard equipment [4], or enhancing exploration of other bodies, similar to the Philae probe deployed from the Rosetta spacecraft to land on and inspect
- An educational platform, where the relatively low development and launch cost of the spacecraft allow educational institutions to exploit spacecraft mission opportunities to provide hands-on learning opportunities for space system design and engineering principles
- A technology demonstration platform for testing small components in the space environment

Picospacecraft have been applied to each of these areas. IKAROS, the first solar-sail mission flown in interplanetary space, deployed a pair of 500-g inspector picospacecraft to monitor solar sail deployment [41]. The PocketQube picosatellites mentioned in Section 1.1.1.1 were designed by university students. Finally, there have been numerous picosatellite technology demonstration missions since the start of the space age.

Although it is expected that picosat and femtosat capabilities will improve over time, in general, it is not expected that individual pico- or femtosats will replace larger, more capable satellites for identical missions; instead, it has been proposed that the new mission paradigms using pico- and femtosatellites will be based on "doing less with more." By this, it is meant that more numbers of smaller, simpler, and specialized satellites can *synergistically* perform portions of a larger spacecraft mission at lower cost or a range of unique mission scenarios not otherwise possible [42]. Coordinated *fleets* of these satellites, for example, could provide the ability to perform simultaneous, multi-point remote or *in situ* sensing and rapid re-measurement of a single location. Applications of distributed picosats and femto spacecraft include:

- global observation and monitoring to enhance disaster awareness, preparedness, and response (i.e., earthquake, forest fire, tsunamis)
- simultaneous, multi-point *in situ* sensing of large-scale phenomena in space (i.e., ionospheric depletion regions, magnetotail behavior, or upper atmosphere monitoring)
- synthesizing very large sparse virtual apertures for high-resolution remote sensing
- fractionated spacecraft architecture, where subsystem components are divided between different components

None of the missions requiring fleets of picosats or femtosats has been attempted although enabling technologies are being investigated.

The Cyclone Global Navigation Satellite System (CYGNSS) serves as a good example of the potential of coordinated small satellite constellations. The CYGNSS constellation is composed of 8 microsatellites. Each spacecraft uses reflected Global Positioning System (GPS) signals to measure ocean surface wind speed [43]. These measurements can be utilized to improve tropical cyclone intensity forecasts. Conventional space-based tropical cyclone measurements are made from larger, monolithic spacecraft in polar orbit in LEO [44]. Polar orbits provide global coverage but spacecraft in these orbits are able to make infrequent tropical cyclones measurements. In contrast, the CYGNSS constellation has a much higher spatial resolution and re-

sampling rate than the traditional monolithic spacecraft [43]. The CYGNSS constellation is also considered a cost-effective approach to achieving this capability [44].

1.1.3 The Need for Picosatellite and Femtosatellites Propulsion

Technology that would enable pico- or femtosat maneuverability (e.g., propulsion) could significantly impact the range of potential applications for their uses. Flat picosats and femtosats have an inherently high area-to-mass ratio [21]. These satellites have taken this shape because their PCBs and silicon-based wafers are thin, flat squares. Although this can be exploited to take advantage of interesting dynamics, this also means that the naturally occurring environmental perturbations in orbit, such as atmospheric drag and solar radiation pressure, have an especially strong influence on the dynamics of satellites at this size and mass scale [21]. The result is that their orbital lifetimes in low Earth orbit (LEO) can be very short. A more complete discussion of orbital perturbations is provided in the following chapter, but here we simply discuss the impact atmospheric drag has on reducing the orbital lifetimes of small spacecraft.

Estimates of the orbital lifetimes are shown in Table 1.4. The lifetimes were estimated using analysis from Space Mission Analysis and Design (SMAD) [7]. Three representative small satellites were used in the analysis. Each was assumed to be in a circular, 0° inclination (equatorial) orbit at 400-km, 500-km and 600-km altitude, and an average neutral atmospheric density was assumed at each altitude. Section 2.1.2 in Chapter 2 provides additional detail on this calculation. Table 1.4 illustrates that orbital lifetimes in LEO can be extremely short, ranging from a few months to just a few hours depending on altitude and solar condition [45]. A "low drag" orientation is one where the minimum cross-sectional area is facing the direction of motion and a "high drag" orientation is one where the maximum cross-sectional area is facing the direction of motion. It can be seen that high drag orientations generally produce shorter orbital lifetimes. However, for both orientations, the spacecraft orbits decay in a relatively short time.

Table 1.4: Orbital lifetime estimates for different picosats and femtosats.

Parameters	1-kg CubeSat	200-g Picosat		8-g Femtosat	
Dimensions	10×10×10 cm	10×10×2 cm		3.8×3.8×0.1 cm	
Configuration	1 face in ram direction	Low drag	High drag	Low drag	High drag
Ram area	100 cm^2	20 cm^2	100 cm^2	0.4 cm^2	14.4 cm^2
Alt = 300 km	Weeks	Weeks	Days	Month	Hours
Alt = 400 km	Months	Months	Weeks	Months	Days
Alt = 500 km	≥1 Year	≥1 Year	Months	Years	Weeks

Some form of propulsion would be necessary to increase mission lifetime of individual spacecraft and maintain or reconfigure a spacecraft formation. While a spacecraft using a chemical or electric propulsion system with proper attitude pointing can overcome the continuous force of atmospheric drag, the mass and volume of propellant required will increase with the spacecraft's intended lifetime. However, a propulsion technology that does not require fuel or propellant could be used to maintain orbit over the spacecraft's operational lifetime as well as allow formations of picosats and femtosats to be dynamically maneuvered and reconfigured many times. Maneuverability would also be essential for collision avoidance.

Although propulsion capability would be significantly enabling for spacecraft at this scale, adequate communication, attitude control, payload volume, radiation protection, thermal management, and energy storage and generation also present significant challenges for picosats and femtosats.

1.1.4 Picosatellites and Femtosatellite Propulsion Options

As described earlier, sub-kilogram spacecraft are expected to have an inherently high area-to-mass ratio, which results in an undesirably brief orbital lifetime in LEO due to atmospheric drag. Propulsion is therefore needed to increase mission lifetime. Missions using large "fleets" of spacecraft would also require coordination and maneuverability, again suggesting the need for propulsion. Wright and Ferrer (2015) provided an excellent summary of propulsion technologies that have been appropriately

scaled for small spacecraft [46]. This section provides an incomplete listing of propulsion technologies for small spacecraft.

Helvajian and Janson (1999) summarize early developments of microthrusters, which are miniaturized actuators equipped with small scale micomachined nozzles and propellant reservoirs [11]. One microthruster propellant concept is the MEMS solid propellant array that utilizes small, solid propellant packages that are combusted. A MEMS solid propellant microthruster array chip, for example, can lie flat, be integrated into the ChipSat structure, and provide thrust for each unit of propellant. A survey of MEMS-based microthrusters can be found in Rossi (2002) [47].

Microfabricated electrospray thrusters are also being investigated seriously. These propulsion devises generate thrust from ions that are generated from an ionic liquid. Although present electrospray thruster designs require very high voltages (on the order of 1 kilovolt) to extract and accelerate the liquid propellant, a miniaturized power processing unit (PPU) prototype capable of providing the necessary voltage has recently been designed [48].

The proposed Sprite spacecraft, a milligram-level, millimeter-scale architecture, is capable propellantless maneuvering using the solar radiation pressure force [49]. Lücking, Colombo, and McInnes (2012) explore the use of an electrochromic coating on an ultra-small spacecraft to facilitate solar sailing [50]. The electrochromic coating changes reflectivity when current is passed through the material. Peck, Streetman, Saaj, and Lappas (2007) have also explored the potential to propellantlessly alter the orbit of a charged spacecraft as it travels through a planetary magnetic field by exploiting the Lorentz force [51].

The objective of this dissertation is to investigate the potential of short, semi-rigid electrodynamic tethers (EDT) to provide propellantless propulsion for picosatellites and femtosatelltes. Early studies showed that a short (few meters long), semi-rigid EDT has the potential to provide propellantless propulsion for satellites at this scale.

1.1.5 Electrodynamic Tethers for Picosatellites and Femtosatellites

An EDT miniaturized for picosats and femtosats is a short, conducting wire with insulation connecting a pair of nearly identical picosats or femtosats. The system concept is shown in Figure 1.2. Both of the satellites are equipped with solar panels, a battery, a power supply, a cold cathode electron emitter, and are capable of collecting electrons on the surface. By changing the tether's current direction, the direction of the resulting propulsion force can be reversed.

EDTs show potential to provide propellantless propulsion for picosats and femtosats. EDTs can also be used for harvesting electrical energy from the orbit, allowing for propellantless, self-powered deorbiting. Furthermore, this same tether could serve as an enhanced communication or scientific radio antenna aperture. The miniature EDT concept considered in this dissertation is a fundamentally novel paradigm because it is semi-rigid and much shorter than traditional EDTs, with a total length on the order of 10 meters.

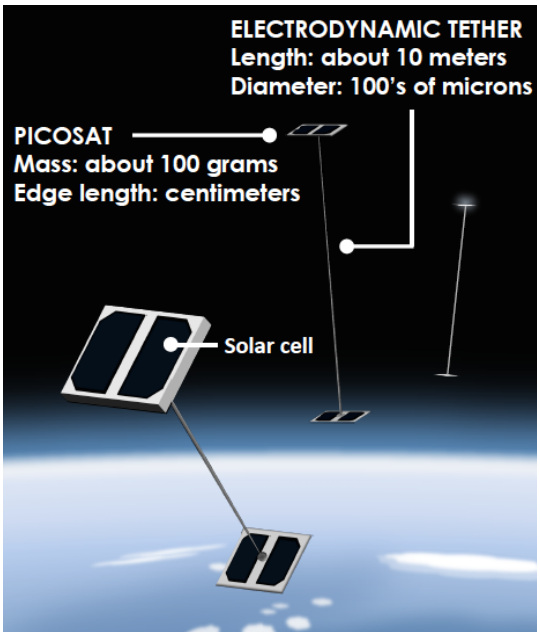

Figure 1.2: Concept of miniaturized electrodynamic tether (EDT) connecting pairs of picosats and orbiting as a maneuverable coordinated fleet.

1.2 Summary of Research Contributions

The scientific contributions provided by this dissertation include:

- a detailed tradeoff study evaluating the feasibility of miniature electrodynamic tethers to provide propulsion capability to an emerging class of small satellites
- a simulated mission scenario in orbit validating the feasibility of miniaturized tethers for picosatellite and femtosatellite propulsion
- experimental data and analysis that refines current collection estimates to tethered pico- and femtosats and, more broadly, to spherical, cylindrical, cubic, and planar electrodes in a directional, weakly-magnetized plasma
- evaluation of tether performance in a range of altitudes, inclinations, and solar conditions

1.3 Dissertation Overview

The five chapters of the dissertation are organized as follows:

- Chapter 1 introduces the picosatellite and femtosatellite concepts.
- Chapter 2 provides background on the EDT concept and describes the key elements of an EDT.
- Chapter 3 develops a trade study on the feasibility of using miniaturized EDTs for picosatellite and femtosatellite propulsion. Other benefits of the tether are considered.
- Chapter 4 presents models used to estimate electron current collection by EDTs. These models are compared to results from ground-based plasma experiments that capture key characteristics of the low Earth orbit (LEO) plasma–tether system interaction, such as the current collector's geometry, the ratio of the Debye length to the collector's characteristic dimensions, and the ratio of the electron gyroradius to the collector's characteristic dimension. This chapter describes the characterization of the laboratory plasma, compares the environment with LEO, and presents the current–

voltage (*I*–*V*) characteristics of planar, cylindrical, and cubic test articles in the plasma, each test article approximating a small spacecraft in LEO.

- Chapter 5 describes the impact of the experimental results on the system concept trade study. An electron current collection model is developed to estimate current collection in the orbital environment. Revised current collection estimates are developed from laboratory data and system performance is evaluated.
- Chapter 6 discusses the conclusions of the dissertation and future work.

CHAPTER 2

Electrodynamic Tether Fundamentals

An electrodynamic tether (EDT) is a long conducting structure that can be used for propulsion as well as power generation, attitude control, communication, and formation flight. This chapter provides background on EDT propulsion and describes several applications of EDTs.

2.1 Fundamentals of Spacecraft Propulsion

This section defines basic terms that are central to EDT attitude dynamics and propulsion. The first sub-section provides an overview of basic orbital mechanics. The orbital geometry, energy, and velocity are defined for a spacecraft. The orbital mechanics sub-section is followed by a description of the role of propulsion systems in modifying spacecraft orbits, with an emphasis on propulsion in the low Earth orbit (LEO) environment.

2.1.1 Orbital Mechanics Fundamentals

Orbital mechanics provides the tools to analyze the motion of spacecraft around the Earth. Newton's law of universal gravitation states that two objects attract each other with a gravitational force given by [52]

$$\mathbf{F}_g = -\frac{GMm}{r^2}\frac{\mathbf{r}}{r}, \qquad \text{(Eq. 2.1)}$$

where M is the mass of the reference body or primary, m is the mass of the second body or secondary, G is the gravitational constant ($G = 6.67384\times10^{-11}$ N·m^2 ·kg^{-2}), $\mathbf{r}$ is the position vector of the secondary relative to the primary, and r is the distance between the two objects. The sign of Equation 2.1 can be explained by the convention used for the vector $\mathbf{r}$: $\mathbf{r}$ is defined to be positive pointing outwards from the primary and the

gravitational pull on the secondary is directed towards the primary, or in the negative **r** direction. In our case, the primary is the planet Earth and the secondary is a spacecraft, so the constant $\mu=MG$=398,600 km^3 s^{-2} can be substituted into Equation 2.1. The gravitational force on the secondary can then be expressed as

$$\mathbf{F}_{\mathrm{g}} = -\frac{\mu m}{r_{\mathrm{sc}}^2}\frac{\mathbf{r}_{\mathrm{sc}}}{r_{\mathrm{sc}}}, \qquad \text{(Eq. 2.2)}$$

where $\mathbf{r}_{\mathrm{sc}}$ is the position of the spacecraft and r_{sc} is the distance between the spacecraft center of gravity and the center of the Earth. A spacecraft's altitude can be computed by subtracting the radius of the Earth from r. The mean Earth radius, 6,371 km, is often used.

According to Newton's second law, the force of gravity on the spacecraft is

$$\mathbf{F}_{\mathrm{g}} = m\mathbf{a}_{\mathrm{g}}, \qquad \text{(Eq. 2.3)}$$

where $\mathbf{a_g}$ is the gravitational acceleration vector, or $\ddot{\mathbf{r}}$ in polar coordinates. Assuming that gravity is the only force acting on the spacecraft, Newton's second law and Newton's law of universal gravitation can be combined to give the two-body equation of motion for the position of a spacecraft affected by gravity, which is

$$\ddot{\mathbf{r}}_{\mathbf{sc}} + \frac{\mu}{r_{\mathrm{sc}}^3}\mathbf{r}_{\mathbf{sc}} = 0. \qquad \text{(Eq. 2.4)}$$

The solution to the two-body equation of motion is the polar equation of a conic section, suggesting that a spacecraft in a gravitational field will follow a hyperbolic, parabolic, or elliptical path. (A radial path is also possible if there is no velocity component perpendicular to **r**.) An illustration of an elliptical orbit is shown in Figures 2.1 and 2.2. The primary focus of the conic section will be located at the center of the primary, or, in this case, the center of the Earth. Implicit in Equation 2.4 are the assumptions that gravity is the only force acting on the spacecraft, Earth is spherically symmetric, the spacecraft's mass is much less than the mass of the Earth, and the spacecraft and Earth are the only two bodies in the system.

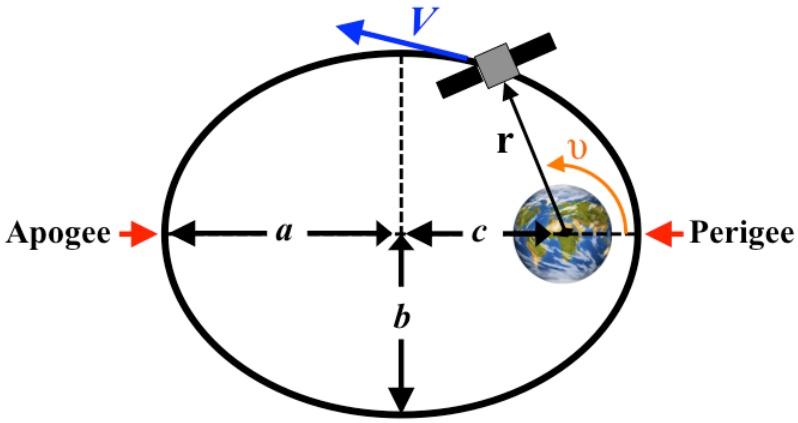

Figure 2.1: Illustration of a spacecraft in Earth orbit. The spacecraft is shown in grey. The semi-major axis, *a*; the semi-minor axis, *b*; the spacecraft position, r; the primary focus-to-center distance, *c*; and the true anomaly, υ, are indicated.

Energy and momentum are conserved in the orbit. The potential energy of a spacecraft in a gravity force field is

$$E_P = -\frac{m\mu}{r_{sc}}. \quad \text{(Eq. 2.5)}$$

The potential energy increases (i.e., E_P becomes less negative) as r_{sc} increases. The kinetic energy of the spacecraft is given by

$$E_K = \frac{1}{2}mV_{sc}^2, \quad \text{(Eq. 2.6)}$$

where V_{sc} is the spacecraft's velocity. Although the kinetic and potential energy may vary over the orbit, the sum, or the total mechanical energy, is constant. The total mechanical energy per unit mass, or the specific mechanical energy, is

$$\varepsilon_{sm} = \frac{V_{sc}^2}{2} - \frac{\mu}{r_{sc}} = -\frac{\mu}{2a}, \quad \text{(Eq. 2.7)}$$

where *a* is the semi-major axis of the conic section. Here, specific mechanical energy is referred to simply as "orbital energy." The orbital energy of a spacecraft following an elliptical path is negative. As the semi-major axis increases, the orbital energy also increases. At zero orbital energy, the spacecraft escapes gravitational attraction and follows a parabolic path. A spacecraft with even greater energy follows a hyperbolic path.

The term “orbit” in this thesis generally refers to the closed elliptical path traversed by a spacecraft.

The expression for specific mechanical energy also gives the orbital velocity of a spacecraft,

$$V_{\mathrm{sc}} = \sqrt{\frac{\mu(2a - r_{\mathrm{sc}})}{a r_{\mathrm{sc}}}}. \qquad \text{(Eq. 2.8)}$$

Equation 2.8 reveals that the fastest velocity occurs at the point of closest approach, perigee, and the slowest velocity occurs at the farthest point on the ellipse, apogee. In the case of a circular orbit, the velocity of a spacecraft will be

$$V_{\mathrm{sc,cir}} = \sqrt{\frac{\mu}{r_{\mathrm{sc}}}}. \qquad \text{(Eq. 2.9)}$$

Equation 2.9 reveals that the orbital velocity in a circular orbit decreases with altitude. As a result, the kinetic energy of the orbit also decreases with altitude.

Angular momentum is also conserved. The specific angular momentum is the angular momentum divided by mass and is expressed as

$$\mathbf{h} = \mathbf{r_{sc}} \times \mathbf{V_{sc}}. \qquad \text{(Eq. 2.10)}$$

A spacecraft with position $\mathbf{r_{sc}}$ and velocity $\mathbf{V_{sc}}$ will travel on an orbital plane that is fixed in inertial space.

A spacecraft’s orbit can be described in a geocentric-equatorial coordinate system, which is shown in Figure 2.2. The reference plane is the Earth’s equatorial plane, the origin is located at the center of the Earth, the *x*-axis lies in the equatorial plane and points towards the vernal equinox (♈, the position of the Sun on the first day of spring), the *z*-axis points to the North Pole, and the *y*-axis completes the orthogonal set. The six classical orbital elements are provided for completeness, although only three are used in this thesis [7], [52]:

- The semi-major axis, *a*, is half the distance across the longest axis, the major axis. As mentioned, *a* can be used to determine altitude.
- The eccentricity, *e*, is the shape of the elliptical orbit, measured as the ratio of the distance between the foci, 2*c*, and the major axis, 2*a*. The eccentricity vector, **e**, points from the center of the Earth to perigee.

- The orbital inclination, i_{inc}, or simply "inclination" is the tilt between the orbital plane and the equatorial plane. The inclination can be measured between **h** and the *z*-axis. Orbits in the equatorial plane are known as equatorial orbits and orbits perpendicular to the equatorial plane are known as polar orbits. A prograde orbit has $0° \leq i_{inc} < 90°$ and a retrograde orbit has $90° < i_{inc} \leq 80°$.
- The right ascension of the ascending node, Ω, describes the orbital plane's orientation with respect to the *x*-axis. The line of nodes marks the intersection of the orbital plane with the equatorial plane. The ascending node is the point where the spacecraft crosses the equatorial plane from the Southern Hemisphere. The right ascension of the ascending node is the angle along the equatorial plane between the *x*-axis and the ascending node. This element gives the "swivel" of the orbit. The ascending node vector **n** goes from the center of the Earth to the ascending node.
- The argument of perigee, ω, is the angle between the ascending node and perigee, measured in the direction of spacecraft motion.
- True anomaly, υ, is the polar angle along the orbital path measured from perigee to the spacecraft's position vector $\mathbf{r}_{sc}$. True anomaly varies with

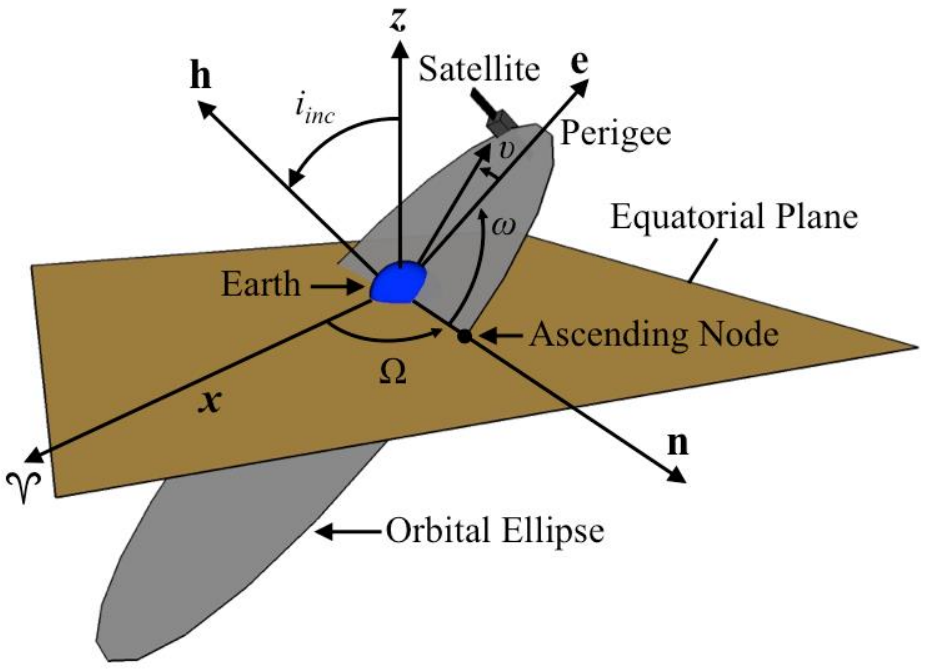

Figure 2.2: Classical elements of an elliptical orbit.

time and is needed to determine the position of the spacecraft.

Inclination, altitude, and eccentricity are used often in this thesis to describe an orbits.

2.1.2 Orbit Perturbations

Orbit perturbations are defined as forces that cause an orbit to depart from a reference orbit, which here is the idealized two-body or "Keplerian" orbit described in the previous section [53]. Atmospheric drag, solar radiation pressure, Earth's non-spherical shape, and gravity from other bodies like the Sun and the Moon can perturb Earth orbits.

The atmospheric drag force is the dominant perturbation below ~600 km [7]. Drag removes energy from the orbit as friction. As the orbital energy is reduced, the semi-major axis becomes smaller, causing the spacecraft to fly closer to the Earth through an even denser region of the atmosphere with higher drag. When the altitude is sufficiently low, the spacecraft re-enters the atmosphere and orbital motion ceases.

The magnitude of the drag force is

$$F_{\text{drag}} = \frac{1}{2}\rho C_D A V_{\text{scd}}^2 \,, \qquad \text{(Eq. 2.11)}$$

where A is the spacecraft cross-sectional area, C_D is the drag coefficient, V_{scd} is the spacecraft's velocity with respect to the atmosphere, and ρ is the atmospheric density. The drag force vector points in the anti-velocity direction. The change in the spacecraft's semi-major axis due to atmospheric drag effects per orbit is given by [7]

$$\Delta a_{\text{rev}} = 2\pi \left(\frac{C_d A}{m}\right) \rho a^2 \qquad \text{(Eq. 2.12)}$$

for a circular orbit. It can be seen that the loss of altitude scales with a spacecraft's cross sectional area-to-mass ratio. The orbital lifetime of a spacecraft can be estimated as [7]

$$\text{Lifetime} \approx \frac{H}{\Delta a_{\text{rev}}} \,, \qquad \text{(Eq. 2.13)}$$

where H is the atmospheric density scale height. H is defined as the distance where the atmospheric density drops by e^{-1}. A spacecraft deorbits essentially immediately if perigee is lowered to ~75 km or less because of atmospheric drag, although this altitude is by no means a "hard limit" for deorbiting a spacecraft [7].. The orbital lifetime expression reveals that lifetime is proportional to the inverse of the area-to-mass ratio, or [7]

$$\beta_{\text{sc}} = {}^{m}/_{C_D A}\,, \qquad \text{(Eq. 2.14)}$$

the ballistic coefficient. Generally speaking, spacecraft with small β_{sc} have shorter orbital lifetimes than spacecraft with large β_{sc} when drag is the dominant perturbation. The solar radiation pressure force exceeds drag as the dominant perturbation above ~ 800 km [7].

The Earth's non-spherical mass distribution can also perturb orbits. The Earth has a bulge and is about 22 km wider at the equator than at the poles. Although this does not affect orbital energy, it causes the orbital plane to *precess* like a wobbling spinning top, moving the right ascension of the ascending node and the argument of perigee within the orbital plane. The greatest effect is at low altitudes and low inclinations because these orbits are closest to the Earth's equatorial bulge.

Other forces can perturb orbital motion. Gravitational forces from the Sun and the Moon can cause variation in the orbital elements. Relativistic effects can also impact orbital motion, but these effects are not dominant for spacecraft in LEO [52].

2.1.3 Orbit Maneuvering and Maintenance

Propulsion technology gives spacecraft the ability to maintain or change orbital elements. Maintaining altitude ("orbital maintenance"), boosting, de-boosting, and changing inclination are examples of propulsion maneuvers. To maintain altitude in a region where atmospheric drag is significant, a propulsion device, or thruster, generates force in the direction of motion that is equal to the drag force. If thrust exceeds drag and the thruster produces a *net* force in the direction of motion, the maneuver increases the orbital energy and the spacecraft boosts to a higher orbit. Thrusting in the direction opposite spacecraft motion removes energy from the orbit and de-boosts the spacecraft. To change the orbital plane, an out-of-plane thrust maneuver is performed.

The change in orbital energy over an altitude change can be characterized by the difference in velocity between the initial and final orbits, or

$$\Delta \text{V} = \left| V_{\text{sc,final}} - V_{\text{sc,initial}} \right|, \qquad \text{(Eq. 2.15)}$$

where $V_{\text{sc,initial}}$ is the initial velocity and $V_{\text{sc,final}}$ is the final velocity. More generally, ΔV is a measure of the total impulse (i.e., thrust integrated over time) to perform a maneuver, which includes the impulse of maintaining altitude. For a circular orbit, the ΔV required

to make up for atmospheric drag is approximately $\Delta a_{rev}(\frac{1}{2}V_{sc}a^{-1})$, or Equation 2.12 multiplied by $\frac{1}{2}V_{sc}a^{-1}$ [7]. As a result, the ΔV required for drag make-up scales with β_{sc}^{-1}.

Several estimated ΔV values are shown in Table 2.1. The solar minimum and maximum columns represent periods of low and high solar activity, respectively, in the Sun's ~11-year solar cycle. In LEO, solar maximum is associated with elevated drag and solar minimum is associated with reduced drag. Solar activity is explained further in Chapter 3. The values in Table 2.1 are from Table I-1of Wertz, Everett, and Puschell (2011) [7]. The assumptions are as follows:

- The ΔV required for 1 km altitude change assumes a Hohmann transfer, which is the most efficient form of orbital transfer. A discussion of different orbital transfer types is beyond the scope of this dissertation, but can be read in Sellers (2000) [52].
- The ΔV required to deorbit is the ΔV required to change an initially circular orbit at the stated altitude to an elliptical orbit with an unchanged apogee and a 50 km perigee.
- The ΔV required to maintain altitude in solar minimum and maximum assume a spacecraft with a ballistic coefficient of 50 kg m^{-2}.
- The atmospheric conditions assumed for solar minimum and maximum are provided in Wertz, Everett, and Puschell (2011) [7].

It can be seen in Table 2.1 that the ΔV for orbital maintenance scales with the lifetime of the mission and grows substantially at lower altitude.

Table 2.1: ΔV Required for Orbital Maintenance and Maneuvers [7]

Altitude	ΔV to Maintain Altitude in Solar Min (m s^{-1} yr^{-1})	ΔV to Maintain Altitude in Solar Max (m s^{-1} yr^{-1})	ΔV for a 1 km Altitude Change (m s^{-1})	ΔV to Deorbit (m s^{-1})
300 km	202	827	0.58	74
400 km	19.2	156	0.57	102.3
500 km	2.56	37.2	0.55	129.8

One method of generating thrust and ΔV is to eject propellant mass. The thrust force produced by ejecting propellant is

$$\mathbf{T} = \dot{m}\mathbf{u_e}, \qquad \text{(Eq. 2.16)}$$

where $\dot{m}$ is the rate of change of mass by exhaust of propellant and $\mathbf{u_e}$ is the effective exhaust velocity relative to the body. The accelerated spacecraft mass decreases *exponentially* with the ratio of ΔV to exhaust speed, or [54]

$$\frac{m_f}{m_i} = e^{\frac{\Delta V}{u_e}}, \quad \text{(Eq. 2.17)}$$

where m_i is the initial mass with propellant and m_f is the mass of the spacecraft without the exhausted propellant. In other words, the propellant mass (and volume) increases with ΔV. Because ΔV needed for orbital maintenance scales with mission lifetime, the propellant required for orbital maintenance also increases with mission lifetime. Boosting and de-boosting maneuvers only add to the total propellant needed.

This motivated the development of propulsion systems capable of achieving high exhaust velocities. The specific impulse of a propulsion system [54],

$$I_{sp} = \frac{u_e}{g_0}, \quad \text{(Eq. 2.18)}$$

where g_0 is the sea level gravitational acceleration, or 9.80665 m s^{-2}, is often used. The specific impulse is the total impulse normalized by the weight of the propellant used over the burn, and is a measure of how efficiently thrust is produced. Electric propulsion systems like Hall effect thrusters and ion thrusters, for example, achieve extremely high specific impulse (1000s of seconds) as compared to conventional chemical rockets (100s of seconds) [7].

Another approach is to use propulsion technology that can generate ΔV without ejecting propellant. Propellantless propulsion can enable missions with large ΔV budgets without a large propellant mass or volume. Non-conducting and conducting space tethers are capable of providing propellantless (or, in some cases, *nearly* propellantless) orbit maneuvering and offer a variety of other features that can be mission enabling.

2.2 Space Tether Background

2.2.1 Space Tether Description

A space tether is a long, thin structure connected to a spacecraft. Space tethers that have flown have been very long, ranging from 100s of meters to 10s of kilometers

long. Space tethers can perform a variety of functions on orbit. This section explains these capabilities and discusses possible space tether applications.

2.2.2 Gravity-gradient Stabilization

Tethers, both conducting and non-conducting, can provide tethered spacecraft with vertical stabilization through the gravity-gradient force and torque. Figure 2.3 shows the stabilizing force on tethered spacecraft. To simplify the explanation, the spacecraft are represented by masses M_L and M_U, connected by a massless tether, and in a Keplerian circular orbit.

Before the spacecraft are separated, the pair can be treated as a single spacecraft in orbit. From Equation 2.9, the distance between the center of the Earth and the center of gravity of the spacecraft, r_{cg}, gives us the spacecraft's orbital velocity. The magnitude of this velocity is

$$V_{\mathrm{cg}} = \sqrt{\frac{\mu}{r_{\mathrm{cg}}}}. \qquad \text{(Eq. 2.19)}$$

The orbital velocity can also be represented as an angular velocity,

$$\omega_{\mathrm{cg}} = \frac{V_{\mathrm{cg}}}{r_{\mathrm{cg}}} = \sqrt{\mu / r_{\mathrm{cg}}^3}, \qquad \text{(Eq. 2.20)}$$

where the orbital period is $\omega_{\mathrm{cg}}^{-1}$.

In the reference frame of the spacecraft, it experiences a gravitational and centrifugal force that are equal and balanced at the center of gravity. The centrifugal force is given by [55]

$$\mathbf{F_c} = m\omega^2\mathbf{r}, \qquad \text{(Eq. 2.21)}$$

where $\omega = V/r$. The gravitational force is given by Equation 2.2.

After the tethered spacecraft are separated vertically, the upper spacecraft moves away from the Earth and the lower spacecraft moves towards the Earth, but the center of gravity remains unchanged. There are no external forces on the tethered pair to add or remove orbital energy, so the radius of the center of gravity r_{cg} has to remain fixed. As a result, the velocity of the center of gravity V_{cg} and angular velocity ω_{cg} are also unchanged.

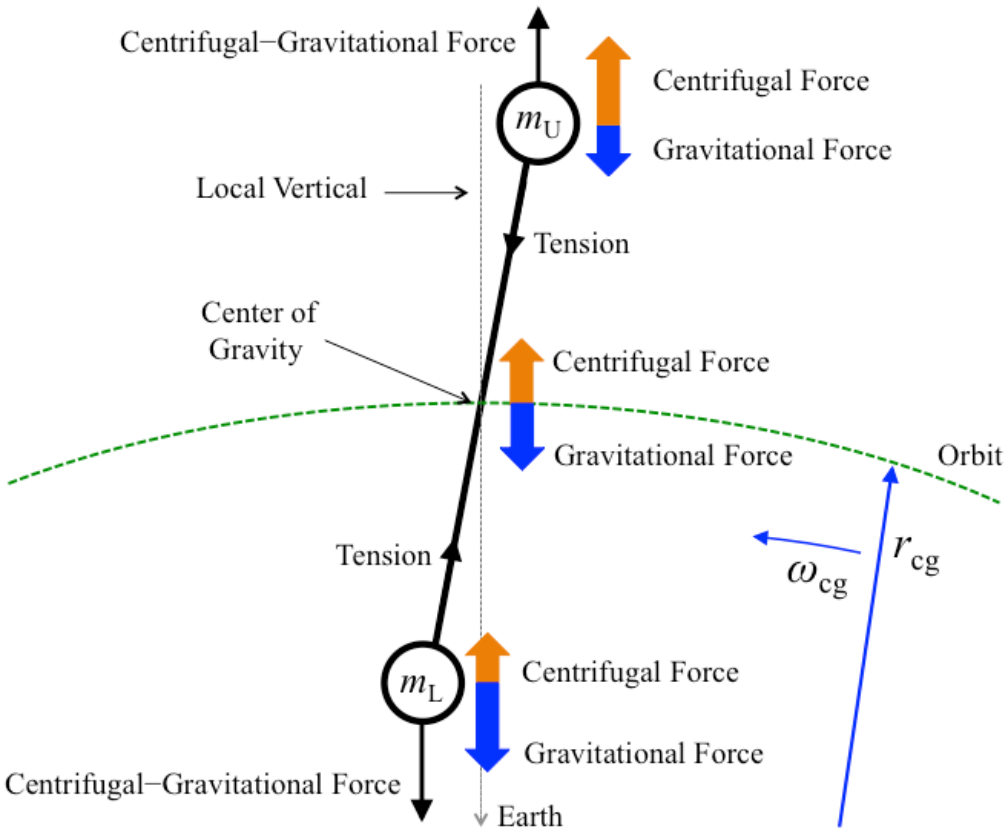

Figure 2.3: Illustration of tethered spacecraft showing forces on each end.

Although the gravity and the centrifugal forces are balanced at the center of gravity, the forces are not balanced above and below this point. The gravitational field strength decreases by r^2, so the spacecraft closest to Earth will experience a larger gravitation force than the upper spacecraft. Also, in the inertial reference frame, the tethered system rotates around the Earth once per orbit at angular velocity ω_{cg}. In the reference frame of the tether, a centrifugal force that scales with r (Eq. 2.18) acts on the tethered system. The vertically diminishing gravity force and increasing centrifugal force mean that the upper spacecraft experiences a larger centrifugal force than gravity force and the lower spacecraft experiences a larger gravity force than centrifugal force. The resulting net upward force on the upper mass and downward force on the lower mass produces tension in the tether.

If the two spacecraft were instead flying untethered in their respective orbits, the lower mass, M_L, would move at a higher orbital velocity than the upper mass, M_U. Over time the two spacecraft would drift apart. However, when a tether connects the two bodies, they are forced to orbit at the same angular velocity, ω_{cg}. If this were not true, the tether would have to stretch indefinitely to accommodate the growing distance between the spacecraft. The angular velocity ω_{cg} lies between what each of the spacecraft's velocities would be if they were orbiting independently. Effectively, the upper spacecraft is pulling back the lower spacecraft and the lower spacecraft is dragging the upper spacecraft.

For the mass above the center of gravity (m_U), the net force is the difference between the centrifugal and gravitational forces, or [55]

$$F_{\mathrm{gg}} = m_U \omega_{cg}^2 \left(r_{\mathrm{cg}} + L_U\right) - \frac{\mu m_U}{\left(r_{\mathrm{cg}} + L_U\right)^2}, \qquad \text{(Eq. 2.22)}$$

where L_U is the distance between the center of mass and the upper spacecraft. Assuming that r is small compared to L_U, the magnitude of the gravity-gradient force can be approximated as [55]

$$F_{\mathrm{gg}} \approx 3 L_U m_U \omega_{cg}^2. \qquad \text{(Eq. 2.23)}$$

The net force on the upper spacecraft is directed upwards. The spacecraft below the center of gravity experiences an equal force in the downward or nadir direction. Acceleration due to the gravity-gradient force is about 4×10^{-7} g m^{-1} in LEO, where 1 g is the acceleration due to gravity on the equator at mean sea level on the surface of the Earth. The gravity-gradient force can be significant for long tethers connecting massive spacecraft. The tension force in the 19.7-km Tethered Spacecraft Systems Reflight (TSS-1R) tether reached about 65 N or 15 pounds [55].

Displacing the system from the local vertical produces a restoring force on each spacecraft that generates a restoring torque on the entire system. The torque is [7]

$$\mathrm{T_g} = \frac{3\mu}{r_{\mathrm{cg}}^3} \mathrm{u_n} \times (\mathrm{I_{sc}} \cdot \mathrm{u_n}), \qquad \text{(Eq. 2.24)}$$

where $\mathbf{u_n}$ is the unit vector pointing towards the center of the Earth, or nadir, and $\mathbf{I_{sc}}$ is the spacecraft mass moment of inertia. The tether will move about the local vertical with an

in-plane and out-of-plane pendulum-like motion known as liberation at 1.73 and 2 times the orbital frequency, respectively [55].

2.2.3 Momentum Exchange

A pair of tethered spacecraft flying in orbits that are vertically separated will transfer or exchange angular momentum. If a tether did not connect the two spacecraft in Figure 2.3, the upper spacecraft would orbit at a slower velocity than the lower spacecraft. However, when a tether connects the spacecraft pair, the kinetic energy from the lower spacecraft is transferred to the upper spacecraft, speeding it up so it orbits at the angular velocity of the center of gravity. Angular momentum scales with velocity, so the lower spacecraft actually transfers angular momentum to the upper spacecraft through the tether. Momentum is transferred through the horizontal component of tether tension.

If the tether connection to one of the spacecraft is broken, the spacecraft pair will travel freely in their orbits. The upper spacecraft, having a high kinetic energy for its orbit, will be boosted into a higher elliptical orbit. The lower spacecraft, having too little kinetic energy for its orbit, will be de-boosted to a lower orbit. The tether release point becomes apogee for the lower spacecraft and perigee for the upper spacecraft. This process has been compared to the Olympic hammer throw [56]. In the hammer throw, an athlete spins and releases a weight at the end of a wire and, in reaction to this, takes a step back. The lower spacecraft could be seen as "throwing" the upper spacecraft into a higher orbit or vice versa. The momentum exchange process has been demonstrated successfully on the Small Expendable Deployer System (SEDS-1) and YES-2 missions [56].

The description above is of "hanging," "static," or "stationary" momentum exchange tethers. The rule of thumb for stationary tethers is that the payload will be released into an orbit with a change in altitude of *approximately* 7 times the distance between the hanging payload and the center of gravity. If the payload is released from the top, the apogee will be increased by about 7 times this distance. Larger orbital changes can be accomplished if the payload is given additional velocity by rotating the tether. This could involve taking advantage of naturally occurring tether librations or by spinning the tether system [7], [55].

2.2.4 Space Tether Applications

2.2.4.1 Spatially-separated Platforms

A natural application of space tethers is to exploit the gravity gradient force to maintain a vertical spatial separation between spacecraft. A constellation of gravity-gradient stabilized tethered spacecraft stays in a near-vertical orientation with roughly fixed interspacecraft spacing, which provides the capability to make simultaneous, multi-point in situ and remote sensing vertical measurements on orbit. Potential applications for a tethered constellation include interferometry, synthetic aperture radar, and in situ measurement of vertical plasma features in the ionosphere [55].

Space tethers can also provide access to regions that are generally inaccessible to spacecraft for extended periods. Currently, spacecraft orbit above 200 km because the atmospheric density below this altitude is high and mission lifetimes are short. For example, the orbital lifetime for a 200 kg m^{-2} (high ballistic coefficient) spacecraft at a 150-km altitude in low drag conditions (i.e., solar minimum) is only about 14 hours [7]. The ΔV to maintain orbit in these conditions is about 8,000 m s^{-1} yr^{-1}, which is extremely high, so orbital maintenance is not currently attempted at this altitude. In situ measurements have been made at altitudes below 200 km by sub-orbital sounding rockets, but each set of sounding rocket measurements is taken over a short time period only a few minutes long. Alternatively, a large space platform at a higher orbit and a lower drag environment could deploy a tethered instrument downwards. Although the lower altitude has higher drag, this would enable long-term measurements in the upper atmosphere and even at different altitudes provided the instrument is capable of collecting data during descent [55].

2.2.4.2 Momentum Exchange

Momentum-exchange tethers can be used to place spacecraft into higher or lower orbit. This principle could also be used to “harvest the momentum” of discarded mass in orbit. Spacecraft launches typically involve multi-stage rockets. After the fuel supply of the final rocket is exhausted, the spent rocket could be deployed from the spacecraft by a tether and the spacecraft could potentially use the momentum of the tethered to boost

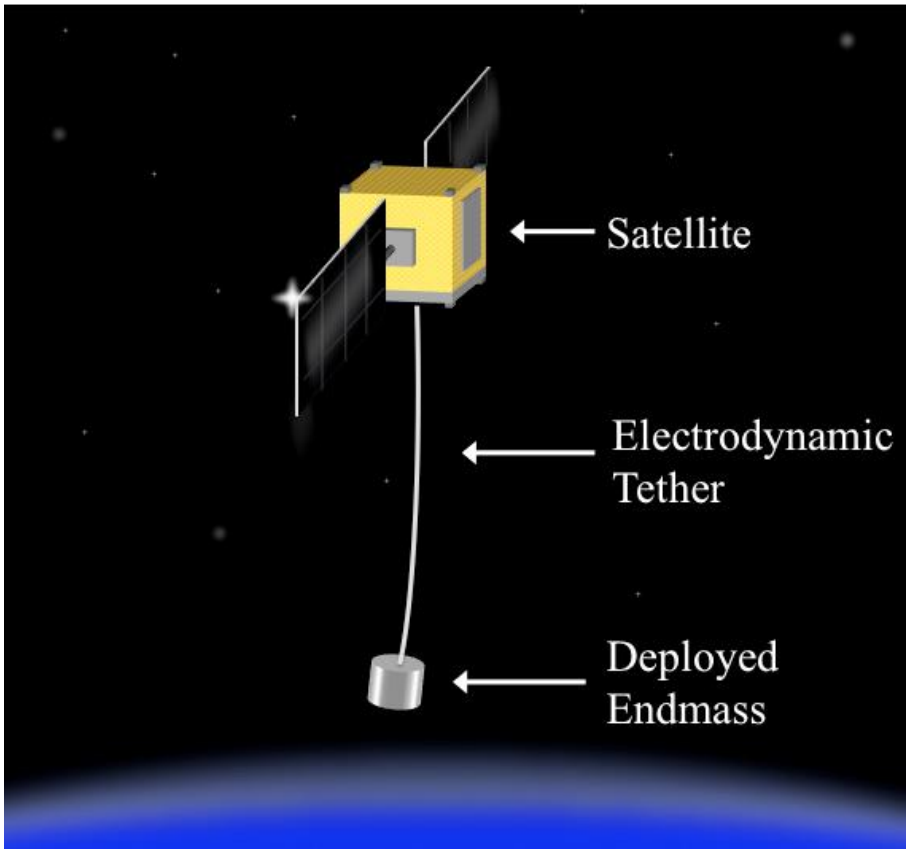

Figure 2.4: Illustration of an electrodynamic tether and deployed endmass.

itself to a higher altitude. Additionally, concepts have been proposed using multiple, rotating momentum-exchange tethers at different altitudes as a method to boost small spacecraft from LEO into a geosynchronous transfer orbit (GTO), lunar orbit, and even interplanetary trajectory [56]

2.3 Electrodynamic Tether Background

2.3.1 Electrodynamic Tether Description

An electrodynamic tether or EDT is a space tether capable of conducting electric current. Figure 2.4 shows an illustration of an EDT system. As the EDT travels across geomagnetic field lines, a motional electromotive force (emf) is induced along its length. If the tether is able to electrically connect to the surrounding ionospheric plasma at each end, the tether will conduct current. Figure 2.5 shows an illustration of an EDT

exchanging charge with the ambient plasma. The current in the tether interacts with the ambient magnetic field to produce a propulsive force,

$$\mathbf{F_{Tether}} = \int_0^L \boldsymbol{I}_{\mathbf{tether}} \cdot d\mathbf{L} \times \mathbf{B}, \qquad \text{(Eq. 2.25)}$$

where I_{tether} is the tether current in segment d**L**, L is the total tether length, and **B** is the magnetic field flux density vector. In LEO, the thrust generated by the emf opposes motion and de-boosts the spacecraft over time. A power supply onboard the spacecraft with a voltage exceeding the emf can reverse the current and generate a boosting force. The out-of-plane component of thrust can also be used to produce inclination change. Therefore, by managing the flow of electrical current conducted by the tether and where thrust is applied along the orbit, EDTs can produce thrust to boost, de-boost, or change inclination.

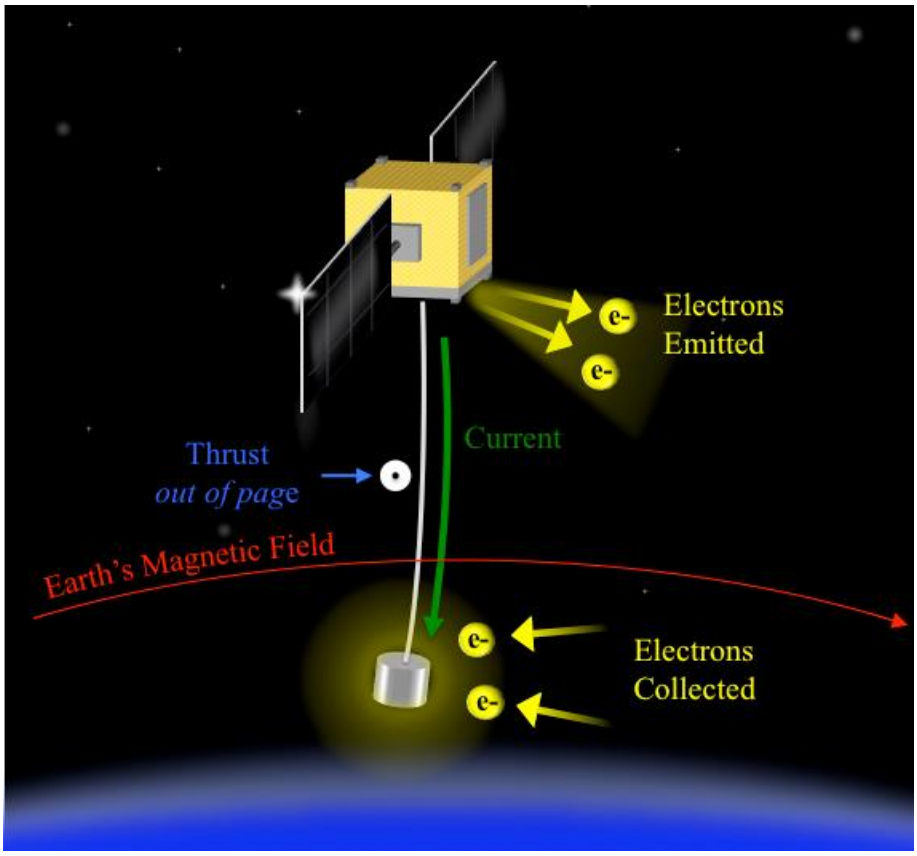

Figure 2.5: Illustration of electrodynamic tether exchanging current with the ionosphere at each end.

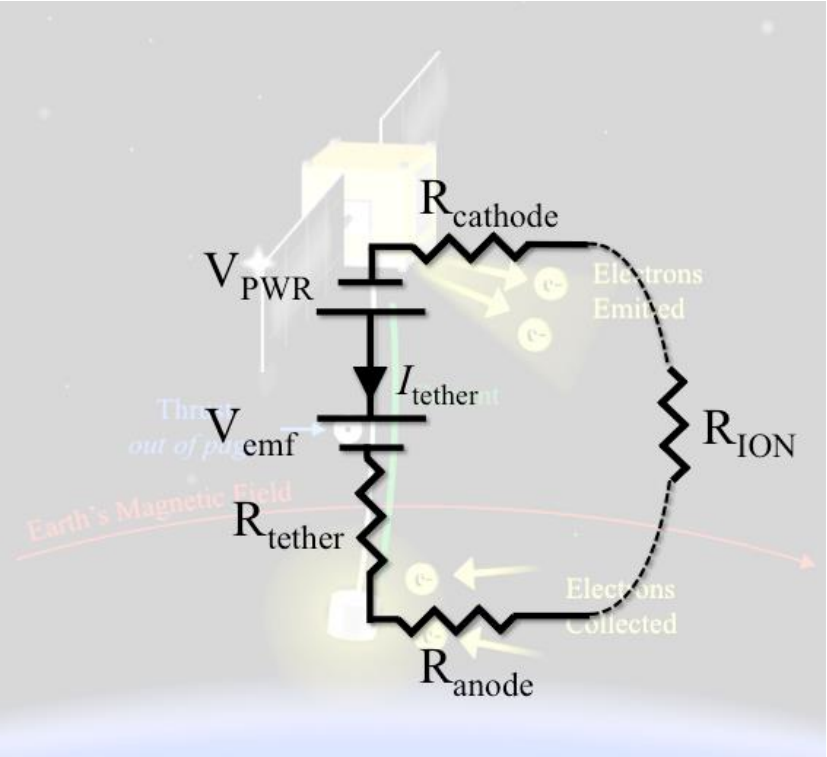

Figure 2.6: Circuit model of electrodynamic tether DC circuit.

2.3.2 Electrodynamic Tether DC Circuit Model

This section will describe the following elements that are part of the EDT current loop: the tether, motional emf, anode plasma contactor, cathode plasma contactor, and the ambient ionosphere. The current in the tether satisfies Kirchoff's voltage law,

$$0 = I_{\text{tether}}R_{\text{tether}} + \text{V}_{\text{emf}} + \text{V}_{\text{cathode}} + \text{V}_{\text{anode}} + \text{V}_{\text{ION}} + \text{V}_{\text{PWR}}, \qquad \text{(Eq. 2.26)}$$

where R_{tether} is the resistance of the tether, V_{emf} is the motional emf, V_{ION} is the voltage drop across the ionosphere, V_{PWR} is the voltage of a power supply, and $\text{V}_{\text{cathode}}$ and V_{anode} are the voltage drops of the cathode and anode plasma contactors, respectively. The cathode voltage drop can be represented by $I_{\text{tether}}R_{\text{cathode}}$ and the anode voltage drops can be represented by and $I_{\text{tether}}R_{\text{anode}}$. The resistances R_{cathode} and R_{anode} are non-linear impedances of the cathode and anode. Figure 2.6 shows a simplified circuit model representing the dc EDT circuit.

2.3.2.1 Electrodynamic Tether

An EDT is a long conductor. A fully insulated EDT can be represented as a resistive element. Uninsulated or bare tethers connect to the ambient plasma and collect current along their length, functioning as anodes or cathodes. Bare tethers are be discussed in the anode and cathode sub-sections.

The DC resistance of an insulated EDT can be modeled as

$$R_{tether} = \frac{\rho_c L}{A_c}, \quad \text{(Eq. 2.27)}$$

where ρ_c is the DC resistivity and A_c is the cross section of the conductor. Resistance per unit length for conventional long EDTs can be on the order of 10–100 $\Omega\,\mathrm{m}^{-1}$. For example, the 19.7-km TSS-1R tether had a resistance of 1650–1750 Ω [57].

A conductor's resistance approximately scales with its temperature, so a rise in the tether's temperature can increase resistive losses further. Joule heating ($I_{\mathrm{tether}}{}^2 r_{\mathrm{tether}}$) can cause the tether temperature to increase. Joule heating can be controlled by selecting low resistivity conductors or increasing tether diameter. Solar energy (direct and albedo) can also contribute to tether heating. The atmosphere in orbit does not convectively cool exposed spacecraft surfaces, so the thermal energy of long tethers is primarily lost as emitted radiation. Metals tend to have low emissivity and, as a consequence, are often not efficient at radiating thermal energy. Some bare metals can reach high temperatures on orbit in sunlight, with common metals like aluminum and gold capable of reaching equilibrium temperatures in the range of 150–400ºC [7]. This may have the effect of periodically increasing losses in the tether. However, thin surface coatings with an appropriate emissivity and absorptivity can reduce the extent of solar heating .

2.3.2.2 Motional Electromotive Force

The motion of an EDT around a planetary body with a magnetic field induces the motional electromotive force. As an EDT crosses magnetic field lines, the Lorentz force acts on the individual charged particles in the tether. The Lorentz force is [58]

$$\mathbf{F_{Lorentz}} = q(\mathbf{E} + \mathbf{V_{sc}} \times \mathbf{B}), \quad \text{(Eq. 2.28)}$$

where q is the particle charge, $\mathbf{V_{sc}}\times\mathbf{B}$ is the motional emf, and $\mathbf{E}$ is the ambient electric field. The magnitude of the ambient electric field $\mathbf{E}$ in the equatorial and mid-latitude region of the ionosphere is on the order of ~0–3 mV·m^{-1} [59]–[61], which is less than 3% of the induced motional emf for a vertically aligned tether, so the ambient field will be ignored. The expression can be rewritten as [58]

$$\mathbf{F_{Lorentz}} = q\mathbf{E_{tot}}, \quad \text{(Eq. 2.29)}$$

where [58]

$$\mathbf{E_{tot}} = \mathbf{E} + \mathbf{V_{sc}} \times \mathbf{B}. \quad \text{(Eq. 2.30)}$$

The potential across the tether can be represented as [58]

$$V_{emf} = -\int_0^{\boldsymbol{L}} \mathbf{E_{tot}} \cdot d\mathbf{L} \approx -\int_0^{\boldsymbol{L}} \mathbf{V_{sc}}(\boldsymbol{l}) \times \mathbf{B}(\boldsymbol{l}) \cdot d\mathbf{L}, \quad \text{(Eq. 2.31)}$$

where V_{emf} is negative because it accelerates electrons.

For a vertical EDT in a prograde LEO orbit, V_{emf} will bias the upper portion of the tether positive with respect to the lowest portion. Cutting through magnetic field lines at orbital velocities of about 7500 km·s^{-1}, which is typical for LEO, the magnitude of the motional electric field will be ~0.1–0.3 V·m^{-1}. The induced potential can be large for a long tether. The TSS-1R mission measured a V_{emf} of about 3.5 kV across a 19.7 km-long EDT [55]. It should be noted that V_{emf} will vary over time because of tether librations and variation in the angle between the magnetic field vector and the velocity vector.

2.3.2.3 Cathode

The cathode provides an electrical connection between the EDT and the ambient plasma by attracting positively charged ions or emitting electrons into the ionosphere. This section gives an overview of several approaches to ion collection and electron emission.

Ionospheric ions can be collected by an exposed conducting surface on a spacecraft. An unbiased electrode inserted into a plasma will initially collect thermal ion and electron flux on its surface. Electrons have a higher mobility than ions, so the electrode's surface rapidly accumulates negative charge and reaches a potential below the plasma potential of the quasi-neutral bulk plasma. The potential of the floating electrode

(or "floating potential") retards the flow of plasma electrons and ensures that the electron and ion fluxes are equal. In orbit, this balance can be shifted somewhat based on electron emission due to solar ultraviolet (UV) flux on the spacecraft surfaces [62]. An electrode biased below the floating potential will collect net ion current from the surrounding plasma.

Electrons and ions in the bulk plasma respond to the negative disturbance and re-distribute themselves to screen out the electric field. The characteristic length for electric field screening (exponentially decaying) is the Debye length, expressed as [63]

$$\lambda_D = \sqrt{\frac{\varepsilon_0 k T_e}{q^2 n_e}}, \quad \text{(Eq. 2.32)}$$

where ε_0 is the permittivity of free space. The disturbed region known as the sheath extends several Debye lengths or more, depending on the electrode potential with respect to the plasma. The effective sheath size is such that the thermal current collected at the sheath edge is equal to the tether current. Therefore, the sheath essentially extends the effective area for particle collection beyond the surface of the electrode. Although the potential difference is mostly screened out in the sheath, a fraction of the total voltage falls in a second, extended region that connects the sheath to the plasma known as the pre-sheath [64].

The random ion current entering the sheath in LEO is low due. Estimates for ion current are given below. The ion and electron temperatures in LEO are approximately equal, so the ion current collected by the sheath edge can be expressed as [63]

$$I_{\mathrm{IS}} = A_{\mathrm{probe}} n_i q \sqrt{\frac{k T_i}{2\pi m_i}}, \quad \text{(Eq. 2.33)}$$

where A_{probe} is the surface area of the electrode in contact with the plasma, n_i is ion density, T_i is the electron temperature, k is the Boltzmann constant, and m_i is the ion mass. Assuming a relatively high ion density in LEO of 1×10^{12} m^{-3}, an ion temperature of ~0.1 eV, and atomic oxygen ions, the ion saturation current density is only on the order of 5 μA m^{-2} [62]. The tether current needed for picosat and femtosat drag make-up in LEO is estimated in Chapter 3 to be in the range of 10–10,000 μA. And for most proposed applications, conventional kilometer-long EDT systems require even more

current, on the order of 0.1−10 A [65], [66]. As a result, the area required for ion collection can be large, requiring either a large cathode surface and/or a large negative voltage at the cathode to expand the sheath. Long, bare section of EDT have been proposed to provide the need collection surface area [67].

Electrons can also be emitted into the ionosphere without the requirement for extremely large cathode surface area. One approach to electron emission is to use a thermionic or hot cathode. Electrons at the surface of a heated material can acquire sufficient kinetic energy to overcome the electrostatic forces holding them to the material's surface. The energy needed for an electron to escape from the surface into the vacuum outside of a material is known as the work function, Φ_w. The thermionic emission current density from a material into a vacuum is given by the Richardson-Dushman equation,

$$J_{\mathrm{RD}} = A_{\mathrm{th}} T^2 \exp\left(-q\phi_w / kT\right), \qquad \text{(Eq. 2.34)}$$

where T is the filament temperature and A_{th} is the Richardson-Dushman constant of the emitting material. The Richardson-Dushman equation shows that the thermionic emission current increases with temperature. The emission current is also higher for materials with lower work functions. Refractory metals like tungsten have high melting points, allowing them to be used as emitters. However, they have high work functions of 4–5 eV [68], so they require high temperature for emission, exceeding 2000°C for ~0.1 A cm^{-2} [69]. Materials with lower work functions in the 1–4 eV range, like thoriated tungsten, lanthanum hexaboride (LaB_6), and barium oxide (BaO), enable lower temperature emission [69]. The development of materials with even lower work functions is ongoing [70].

As electrons are emitted, a space charge cloud can grow around the emitter. Space charge presents an electrostatic barrier that reflects emitted electrons. For efficient emission, cathodes often use electrodes to establish an electric field that accelerates electrons away from the cathode. If the electrode fails to accelerate the entire space charge cloud, space charge effects will persist [71].

A strong electric field at the surface of the cathode can also produce electron emission. Field emission cathodes use an intense electric field to deform the potential

barrier holding electrons to the cathode. The deformation of the barrier increases the probability that electrons can escape, allowing some electrons to quantum mechanically tunnel out of the emitting material despite not having the energy to escape thermally. The emission current is given by the Fowler-Nordheim expression, which can be expressed in terms of the voltage as

$$I_{\mathrm{FN}} = a_{\mathrm{FN}} V_{\mathrm{gate}}^2 \exp\left(-b_{\mathrm{FN}} / V_{\mathrm{gate}}\right), \quad \text{(Eq. 2.35)}$$

where V_{gate} is the potential applied to the cathode and a_{FN} and b_{FN} are the Fowler–Nordheim current and voltage coefficients, respectively. Normally, field emission cathodes use strong electric fields on the order of 10^5–10^8 V cm^{-1} [72], [73]. Localized intense electric fields can be generated, for example, by geometrical field enhancement at the tips of Spindt cathode cones [74] and carbon nanotubes [75], reducing the applied voltage needed for emission. The so-called "triple-point" between metal, dielectric, and vacuum can also experience high electric fields that can be exploited for electron emission. Current densities exceeding 10^7 A cm^{-2} have been reported [76], but current densities at this level are typically achieved for extremely small emitter areas (i.e., a single geometrically-enhanced emitter a few micrometers across or an array occupying a small area), and the emission current is small. No data has been reported for field emitter cathodes operating in the LEO environment. The electron emission characteristic may be degraded by surface contamination and erosion from the ambient plasma, and mitigating or resolving these problems is an area of ongoing investigation [72].

Electron photoemission is another approach to emitting electrons into the ionosphere. Photons can energize electrons, allowing some to be emitted from the material via the photoelectric effect. The UV radiation from the sun can naturally generate a photoelectric current which depends on the solar flux, solar incidence angle, and material. Commonly used structural materials like stainless steal can emit 10s of μA m^{-2} [62]. UV light emitting diodes (LED) have been proposed as a technology that would enable photoelectron emission from low work function materials on the day and night side of an orbit [77]. Photoemission, field emission, and thermionic emission can be combined to enhance emission current. However, the work function at the surface is

important for all of these techniques, so contamination on the material's surface can significantly degrade emission levels.

A hollow cathode plasma contactor (HCPC) can also be used to generate a conductive connection to the ambient ionosphere. Generally, a HCPC is a hollow tube that has an orifice plate on one end and a cylindrical insert next to the orifice plate. The insert emits electrons and is typically made from a low-work-function material, such as BaO or LaB_6 [69]. The HCPC tube is wrapped in a heater that raises the temperature of the insert, causing the insert to emit thermionically and ionize gas flowing in the HCPC. The plasma plume expands out of the orifice and connects with the lower density ionosphere. The cathode plume and the ionospheric plasma meet at a region known as the double layer or double sheath and it represents a transition between the plume and the ionosphere. Electrons are accelerated across the double layer into the ionospheric plasma [55], [69], [71]. The plasma ions generated by the hollow cathode neutralize the space charge, so the cathode can generate high emission current densities, typically much higher than thermionic and FEA cathodes [69].

2.3.2.4 Anode

The anode provides an electrical connection between the EDT and the ambient plasma by emitting ions and collecting electron current from the ionosphere. A HCPC (operating in a different mode) and a positively biased electrode are both examples of anodes.

The HCPC mentioned in the previous section is capable of conducting current in both directions. The Plasma Motor Generator (PMG) mission demonstrated the capability of a HCPC to provide an EDT with electron emission and collection capability on orbit [55]. In the electron collecting mode or "ignited mode," the HCPC attracts electrons from the ambient ionosphere, ionizing gas from the cathode. Current understanding of the HCPC electron collection process in LEO is not sufficient to precisely estimate the collection current on orbit [71]. There are two theoretical models that have been proposed to estimate current collection. The model proposed by Katz et al. (1995) assumes the hollow cathode plume expands approximately spherically to a radius where the plume plasma frequency and the electron cyclotron frequency are equal [78]. Electrons arriving

at this boundary can be scattered across magnetic field lines and accelerated to the HCPC. The second model, proposed by Gerver et al. (1990), assumes that the plume expands approximately cylindrically and along magnetic field lines [79]. Electrons are collected across magnetic field lines by collisions and accelerated by the double sheath at the ends of the cylinder. The Situational Awareness Sensor Suite for the International Space Station (SASSI) has been proposed to investigate the complex HCPC plume interaction with the LEO environment and the ISS [80].

Alternatively, a conductor exposed to the plasma that is biased above the floating potential can collect electron current. The current collected by the anode varies depending on its potential with respect to the ionosphere, the characteristics of the ionosphere, the spacecraft size, and the specific orbital parameters (e.g., velocity). Spherical anodes have been operated in orbit and the theory is important in this thesis, so collection to spherical anodes will be explored here.

If the electrode is biased at the plasma potential, V_s, a random thermal electron current reaches the electrode given by

$$I_{\text{thermal}} = A_{\text{probe}} n_e q \sqrt{\frac{kT_e}{2\pi m_e}}, \quad \text{(Eq. 2.36)}$$

where n_e is electron density, T_e is the electron temperature, and m_e is the electron mass. The electrode would collect a net current composed of ion and electron thermal current, but the ion thermal current would be much smaller so we assume this is the total current collected.

When the electrode bias is higher than the plasma potential, it enters the electron saturation region and the effective collection area increases. The exact collection current depends on collector geometry and ambient plasma conditions like plasma density, temperature, flow velocity as well as magnetic field strength. If the sheath is very large with respect to the electrode in a collisionless, non-drifiting, unmagnetized plasma, orbital-motion-limited (OML) theory can be used to predict the collection current to simple electrode geometries (spheres, infinite cylinders, and infinite plates). If $V_{\text{anode}} > V_p$ (e.g., collection in the electron saturation regime) and $\lambda_D > r_p$, the current is given by [81]

$$I_{\text{OML}} = I_{\text{thermal}} \left(1 + \frac{q(V_{anode} - V_p)}{kT_e}\right)^{\beta}, \quad \text{(Eq. 2.37)}$$

where β = 1 for a sphere, β = 0.5 for an infinitely long cylinder, and β = 0 for an infinite plate. The increase in current with applied voltage in Equation 2.37 corresponds to expansion of the sheath with voltage. If $\lambda_D << r_p$, the sheath is extremely thin and the resulting collection current is simply the thermal current incident at the spacecraft's surface [82].

The magnetic field in LEO is sufficiently large that it impacts current collection. Ignoring collisions and electric fields, electrons in LEO travel in a helical trajectory along magnetic field lines with a gyroradius (or Larmor radius) given by

$$r_L = \frac{m_e v_\perp}{qB}, \quad \text{(Eq. 2.38)}$$

where $v_\perp$ is the electron velocity perpendicular to the magnetic field. If the electrode is large with respect to the gyroradius, the collection current at the sheath edge is limited to electrons traveling along intersecting magnetic flux tubes. Parker–Murphy provides the theoretical model for electron collection by a large ($r_L << r_p$), positively biased sphere in a non-drifting, collisionless, magnetized plasma, given by [83]

$$I_{\mathrm{PM}} = \frac{I_{\mathrm{thermal}}}{2}\left(1 + \left(\frac{q(V_{\mathrm{anode}} - V_p)}{\varphi_0}\right)^{\frac{1}{2}}\right), \quad \text{(Eq. 2.39)}$$

where the intermediate potential φ_0 is given by

$$\varphi_0 = \frac{m_e \omega_{\mathrm{ce}}^2 r_p^2}{8q}, \quad \text{(Eq. 2.40)}$$

where the electron gyrofrequency, ω_{ce}, is equal to qB/m_e. The electron thermal current is divided by 2 because the collection area is $2\pi r_p^2$, or the 2-dimensional projection of the sphere perpendicular to the magnetic field.

The Parker–Murphy model was modified based on mission data from the Tether Spacecraft Systems Reflight (TSS-1R), which was theorized to be affected by the plasma speeds experienced in orbit. In LEO, a spacecraft can travel at orbital speed that is greater than the ion thermal speed and less than the electron thermal speed, a condition known as "mesothermal." The Parker–Murphy model modified to account for mesothermal speed can be expressed as [84]

$$I_{\mathrm{TSS-1R}} = \alpha \frac{I_{\mathrm{thermal}}}{2}\left(1 + \left(\frac{q(V_{anode} - V_p)}{\varphi_0}\right)^{\beta}\right), \qquad \text{(Eq. 2.41)}$$

where, based on the TSS-1R mission results, average values for β and α can be estimated as: $\beta \approx 0.5$ and $\alpha \approx 2.5$. Parker-Murphy was generally validated by suborbital orbital missions (e.g., SPEAR-1 and CHARGE-2B) where the relative velocity of the plasma with respect to the spacecraft is not as high as it is in LEO where TSS-1R was in orbit [85]. Mesothermal plasma speed causes significant sheath asymmetry and possibly instability (e.g., turbulent electron scattering) that affects current collection [86]–[88]. It was also shown in [89] for conducting cylinders and tapes that high-speed plasma flow produces current collection enhancement.

The small cross-sectional dimension of positively biased bare tethers makes it a more effective collector of electrons on a per-unit-area basis than a large sphere at equal bias voltage. This is because the small cross sectional diameter allows current collection to take place in the orbit motional regime for a cylinder, which gives higher current density than a large sphere collecting magnetically limited current [67].

2.3.2.5 Ionospheric Plasma

The ionospheric plasma completes the circuit of an EDT system. However, the exact mechanism for electrical current closure for a tether system in the ionosphere is not completely understood. Present understanding is that EDT electrical current closure is an AC process. It is briefly described in the following paragraph.

As the EDT system moves through the ionosphere, the anode and cathode exchange charge with the ionospheric plasma. The plasma disturbances caused by the anode and cathode predominantly travel along magnetic field lines like parallel transmission lines. These transmission lines are momentarily excited when the tether ends electrically contact them. This has been described as "plucking" the magnetic field transmission lines. Final circuit closure occurs at lower altitudes of the ionosphere where collisions with neutrals allow electrons to cross magnetic field lines. However, tether current is DC because the geomagnetic field is a continuous medium. Experimental data suggest that current closure is an AC process. Ground-based radar observations during the PMG experiment detected traveling ionospheric disturbances propagating along

geomagnetic field lines that were attributed to PMG's EDT [90]. The impedance of the plasma has been estimated to be ~1–10s of ohms, assuming the current loop is closed along magnetic flux tubes intersecting each end of the tether system [55].

2.3.3 Electrodynamic Tether Applications

2.3.3.1 Electric Field Measurements

Electric fields play an important role in global plasma dynamic and energetic processes. A high-impedance EDT can act as a double probe capable of precisely measuring the vertical component of the ionospheric electric field over a wide range of distances. In this configuration, there is no DC tether current, both plasma contactors are floating, and the total potential across the tether can be measured with a voltmeter. The total potential is made up of the motional emf, the ambient electric field, and natural and man-made electromagnetic radiation. The sheath voltage drops on each end and the difference in work functions of each plasma contactor must also be taken into account to reduce uncertainty. The average ambient field can be derived from the total potential in the tether if the largest voltage, the motional emf, is determined from the tether orientation and dynamics and the magnetic field flux density vector. TSS-1R used this technique to make measurements of the average ambient electric fields in the low latitude F-region of the ionosphere that were consistent with spacecraft and ground-based measurements in similar conditions [60].

2.3.3.2 Power Generation

The EDT provides a means of converting the energy of the orbit into electrical energy. The voltage drop over a long EDT may be 100s of volts to kilovolts. If electrical contact is made with the ionospheric plasma at each end and the motional emf exceeds the other voltage drops in the circuit, the emf can drive current through the tether and electrical loads. Recent computational simulations found that a 10-km-long EDT with a HCPC on each end was able to deliver ~1 kW average power to a load in the range of 400 km to 600 km altitude [58]. However, the electrical power is harvested at the expense

of orbital energy, as the direction of the current flowing along the tether de-orbits the tether system when it is generating power.

Tether systems offer the capability to generate electrical power over an entire orbit. In contrast, solar arrays require direct sunlight and only generate power on the dayside of an orbit. The EDT power that is generated, however, can fluctuate substantially. As the Earth's magnetic field rotates with respect to the orbital plane, the magnetic field vector changes and the coupling between the tether and the planetary magnetic field varies. Additionally, the plasma density varies over the orbit and this changes the voltage drops in the plasma contactor sheaths as the contactor voltage adjusts to collect the same current [58]. On the night side, power is reduced since the electron density is lower.

2.3.3.3 Propulsion

EDTs can provide propellantless orbital maneuvering. The naturally occurring emf produces a Lorentz force that removes orbital energy from the tether system. This can be exploited to enable passive de-boosting of spacecraft. The Terminator Tape™ is a 250-m-long tape EDT developed by Tethers Unlimited, Inc. to passively de-orbit microspacecraft. The EDT can also be used for orbital maintenance or boosting. There is also an out of plane component of the tether that can produce an inclination change. The ability to generate a propulsion force on a tether has been demonstrated by several missions, including TSS-1 and PMG (described later).

2.3.3.4 Radiation Belt Remediation

The EDT is also capable of remediating the radiation belts. The Earth's magnetic field traps high-energy particles of natural and man-made origin in a region known as the Van Allen Radiation Belts. The long, bare high voltage generates a sheath that acts as a scattering structure for high-energy electrons, reducing the pitch angle between the velocity vector and the magnetic field vector and causing some of them to fall into the atmosphere, where they collide with neutrals in the upper atmosphere and are removed from the radiation belts [91].

Plasma waves generated by EDTs can also be used for radiation belt remediation. By connecting and temporarily driving electrical current in physically separate regions of the magnetized ionospheric plasma, EDTs can generate very low-frequency (VLF) disturbances which can propagate in the ionosphere. VLF waves are thought to interact through a gryo-resonance with high-energy electrons trapped in the Earth's radiation belts, causing them to scatter into the loss cone [92].

2.3.3.5 Electrodynamic Tether as an Antenna

When the EDT current is modulated or pulsated, the EDT can function as an antenna. Small electrical elements can be placed along the tether to adjust the EDTs resonant frequency. The antenna may be useful for communicating to ground, communicating to other spacecraft, launching plasma waves, or making remote measurements.

2.4 Tether Design Considerations

2.4.1 Materials for Tethers

Tether can be composed of a variety of materials, including metals, polymers, and insulating films. An incomplete list of tether design considerations and materials is provided below. Space tethers often use relatively low density and high specific strength materials with sufficient flexibility to allow long-term compact storage. In addition, EDTs often have a metallic conductor that has high conductivity and insulation with a high dielectric strength. Absorptivity and emissivity are also important properties because they impact the tether's equilibrium temperature in sunlight. In general, materials that are rapidly damaged by atomic oxygen (AO) and UV radiation are avoided [55].

A few examples of materials that have considered for space tethers are Dyneema®, Zylon®, Kevlar®, Spectra®, Dacron®, and Teflon® as well as aluminum and copper metal. Dyneema®, Kevlar®, Spectra®, Dacron®, and Zylon® are all high-strength fibers, which allows relatively thin and light-weight tethers with diameters of ~1 millimeter to withstand the forces experienced on orbit. Aluminum and copper, on the other hand, can be used to make conducting tethers. Aluminum has a lower density than copper, so an

aluminum EDT would weigh less than an equivalent copper EDT. In contrast, copper has a higher conductivity than aluminum, so a copper EDT would experience less resistive loss than an equivalent aluminum EDT. High-dielectric-strength materials that have relatively low atomic oxygen reactivity like Teflon® can be used to insulate the EDT. In addition, some high strength insulating yarns like Kevlar™ can be coated in conductors (metalized) and some high strength yards incorporate conductive wires. Some more recent EDT design concepts incorporate low work function coatings on the conducting tether to enable electron emission along the length of the tether [93].

2.4.2 Reducing the Probability of Failure due to Space Debris Collisions

Collision with space debris poses a risk to space tethers. Natural space debris includes micrometeoroids and artificial debris includes human-generated objects like spent rocket stages and paint chips. By 2009, the United States Space Command (USSPACECOM) tracked over 15,000 objects larger than ~10 cm in LEO through the Space Surveillance Network. Using ground-based sensors and inspections of returned spacecraft surfaces NASA statistically determined the population of objects 1 cm or greater to exceed 300,000. This debris cloud is a hazard to spacecraft because of its kinetic energy. The average relative velocity between the debris and spacecraft is about 9–10 km s^{-1}, but peak velocities can exceed 14 km s^{-1} [7]. For comparison, a 100-milligram debris fragment traveling at 10 km s^{-1} has the same kinetic energy as a bowling ball moving at 37 m s^{-1} (80 miles per hour). The current "rule of thumb" is that a collision with debris only ⅓ the tether diameter can sever the tether or, in the case of a glancing blow, cause severe damage to the tether and insulation [55]. The probability of a collision scales with cross-sectional area. Although tethers are thin, they can have large collision cross sections because of their long lengths. The hazard has motivated the development of space tethers with a high probability to survive collisions. One approach is to make the diameter larger and another is to construct the tether with a web of interconnected, redundant load bearing strands. The first strategy was implemented in the Tether Physics and Survivability Experiment (TiPS). The 4-kilometer TiPS tether

survived for over 10 years [93]. TiPS was deployed in a 552 km altitude orbit in 63.44° inclination.

2.5 Historical Context: Relevant Space Tether Concepts and Missions

In the following section, milestones and select sub-orbital and orbital flights are described, showing the evolution of the tether concept. A comprehensive history of electrodynamic tethers can be found in Chen et al. (2013) [94].

2.5.1 Early Ideas

The genesis of the space tether concept can be traced to the pioneer of rocket science, Konstantin Tsiolkovsky. In 1895, Tsiolkovsky published in *Dreams of Earth and Sky* his vision of a tower touching the ground and stretching into space past geostationary orbit, with a counterweight located at the top. He called this a "beanstalk," and this was the origin of the space elevator. The center of mass of the space elevator would be at geostationary orbit, allowing it to orbit at the rotation speed of the Earth, and the cable could be held in tension by the centrifugal force because of the counterweight extending beyond GSO. Space elevators have been proposed as a disruptive technology that could allow payloads to be transported into and returned from space without the need for a traditional launch vehicle or propellant. The concept was explored later in the 1960s and 1970s by Yuri Artsutanov; Isaacs et al., who renamed it "sky hook"; and Jerome Pearson [56], [95]. Space elevator feasibility studies continue.

In 1974, Colombo provided the idea for a skyhook suspended from the space shuttle orbiter, noting the potential for gravity gradiometric measurements and upper atmosphere experiments at low altitudes (100–200 km) [96]. This tether was much shorter than the previously proposed space elevator and did not reach the surface of the Earth. The NASA atmospheric, magnetosphesic and plasmas in space (AMPS) Science Definition Study recognized the scientific value of long conducting wires deployed from the orbiter [92]. It was suggested that a gravity-gradient stabilized body deployed from the orbiter and connected to it with a long wire would induce emf along the wire. (It should be noted that an emf is also induced on the conducting bodies of spacecraft in

orbit, and this effect and its potential applications had been discussed much earlier by Drell et al. [97]) The range of phenomena could be studied from the Orbiter, including magnetohydrodynamic waves in space, magnetic field aligned current, and VLF radio waves [98].

2.5.2 Gemini Missions

The first space mission to utilize a long tether, Gemini XI, was launched by NASA in 1966 [56]. One of the mission's objectives was to demonstrate passive attitude stabilization of the two spacecraft connected by a tether and create artificial gravity by spinning the tethered spacecraft pair. The manned Gemini spacecraft docked with the Agena Target Vehicle (ATV) and astronauts on Gemini manually attached a 50 m tether to ATV. The attitude dynamics of the system were not well understood, and initially there were difficulties achieving attitude stabilization. However, stabilization and ~1 milligee (1/1000 of Earth gravity) of artificial gravity was achieved by spinning the tethered system at 0.15 rpm. Learning from the Gemini XI mission, the crew of Gemini XII achieved a degree of gravity-gradient stabilization of the tether about the local vertical [56].

2.5.3 CHARGE 2

The next space tethers would be flown onboard sub-orbital sounding rockets launched in the 1980s. The first of these was the tethered payload experiment (TPE), the first project to test electrically conducting tethers in space. A "mother" payload on the rocket injected an electron beam into the surrounding ionosphere. Key objectives were to measure characteristics of the plasma perturbed by the electron beam and the rise in electric potential of the mother with respect to a tethered "daughter" payload that was deployed from it [99]. Battery malfunctions prevented the electron gun from operating in the first two TPE missions, but the third experiment, named the cooperative high altitude rocket gun experiment (CHARGE-1), worked briefly and electric current was measured in the tether. Two more CHARGE missions were flown. It was noted that a cold gas injection system onboard the mother payload generated a plasma cloud that helped neutralize the rocket during electron beam injection and increased the current flowing in

the tether. Also, the current was modulated and the tether was operated as a radio antenna [99].

2.5.4 TSS and TSS-1R

The next orbital flight for electrodynamic tethers would be the tethered spacecraft system (TSS-1) mission aboard the Space Shuttle orbiter Atlantis on flight STS-46 in 1992. The goal of TSS-1 was to show the feasibility of deploying and controlling a tethered system in orbit and to demonstrate the potential of using a tethered system as a platform to conduct unique science experiments. A conducting, 1.6 m-diameter spherical spacecraft was deployed upwards and became positively biased relative to the Orbiter due to the naturally occurring V_{emf} along the tether length. The current loop was closed on conducting surfaces of the orbiter (primarily through the space shuttle main engine nozzles) and using electron guns on the space shuttle [87].

There was a jam in the deployment mechanism that stopped the tether at 268 m of the total 20 km, but for the first time in an orbital flight measurements were made of the electric potential drop across a conducting tether, orbiter charging, and tether current-voltage characterization. The mission also verified that the tether was gravity gradient stabilized at only 268 m total length. The tether was reeled back in after 30 hours and the mission was reflown in 1996 as TSS-1R on Space Shuttle orbiter Atlantis on flight STS-75.

Similar to the initial TSS-1 mission, the key objective of TSS-1R was to deploy a tethered 1.6 m-diameter spherical spacecraft upward from the Orbiter and study tether dynamics and explore space plasma-electrodynamic processes, specifically those processes involve in the generation of ionospheric currents. The EDT deployed ~19.7 m of the total 20.7 km, generating a motional emf of ~3.5 kV. A break in the tether insulation near the Orbiter caused gas trapped in the tether to leak and ultimately become ionized, and sustain an arc to the surrounding plasma, severing the tether in the process [100]. Modern tether designs use different assembly practices to prevent this failure. Interestingly, the current was sustained about 90 s after the tether broke and the copper strands at the failure point collected more current than the larger, ion-collecting surface of

the Orbiter. However, prior to the break, there were more than 5 hours of useful calibration and science operations data that was collected during tether deployment.

One key finding was that the tether currents were 2–3 times higher than previously predicted by models assuming stationary or relatively slow velocity plasma in the presence of a strong magnetic field. In addition, energetic electrons not naturally found in the ionosphere environment with energies as high as 10 keV were collected by the spherical spacecraft. The induced potential between both points of plasma contact at each end of the deployed tether was measured, demonstrating the capability to measure vertical electric fields in LEO [56], [57].

2.5.5 PMG

The plasma motor generator (PMG) experiment was launched in 1993. A spent Delta rocket upper stage was connected to a second payload by a 500-m conducting tether. PMG was equipped with a hollow cathode plasma contactor on both sides of the tether that gave it the ability to emit ionized gas and exchange charge with ionosphere at each end. PMG demonstrated the ability to use the naturally occurring EMF potential difference to conduct current in tether, showing capability of generating electrical power or functioning as an orbital "generator." PMG also demonstrated the ability to reverse the direction of current and operate the tether as an orbit boosting motor. Tether currents in the hundreds of milliamperes were measured [55], [90].

2.5.6 PicoSat Missions

As mentioned in the previous chapter, the PicoSat mission was launched in 2000 to perform tests on MEMS RF switches and demonstrate small spacecraft in formation flying and interspacecraft communication. The pair of ~250 g spacecraft, each roughly the size of a deck of cards, were connected by a ~30 m tether. The tether ensured that the interspacecraft communication link would not exceed a specified distance. There were concerns about tracking the small spacecraft from ground, so the tether had small gold strands imbedded in it increase the radar cross section of the tethered picospacecraft. PicoSat 1 and 2 were the first tethered picospacecraft operated in space. Another tethered pair was launched a year later [11].

CHAPTER 3

Miniaturized Electrodynamic Tether System Concept Study

This chapter evaluates the capability of miniaturized electrodynamic tethers (EDTs) to provide orbital maneuverability for picosats and femtosats. The miniaturized EDT considered here is a short (several meters), conducting tether connecting a pair of nearly identical picosats or femtosats that work together as a unit. Figure 3.1 shows an illustration of the basic concept. Each spacecraft has solar panels, energy storage capability, a power supply, a cold cathode electron emitter, and is capable of collecting electrons on its surface. With this configuration, the tether current can be reversed to change the direction of the force. In this chapter, key components of the system concept are described and the ability of the EDT system to draw electrical current from the ionosphere and generate thrust is evaluated. Mission scenarios were also developed to further assess orbital maneuvering capability.

3.1 Picosatellite and Femtosatellite Characteristics

The first step in the trade study was to establish the size, shape, and mass of adequately representative spacecraft to be utilized. Size, shape, and mass are important because they help determine the atmospheric drag force on the spacecraft and orbital lifetime, which, in turn, establishes the required thrust for drag make-up using the miniaturized tether (including the tether's own drag) as well as the ability to change orbital parameters. In addition, the gravity-gradient force, which causes tension in a tethered system and a restoring torque along the local vertical, is proportional to the mass of the spacecraft. Finally, the size and shape of a spacecraft affect the electrical power that can be generated by surface mounted solar cells and used for propulsion.

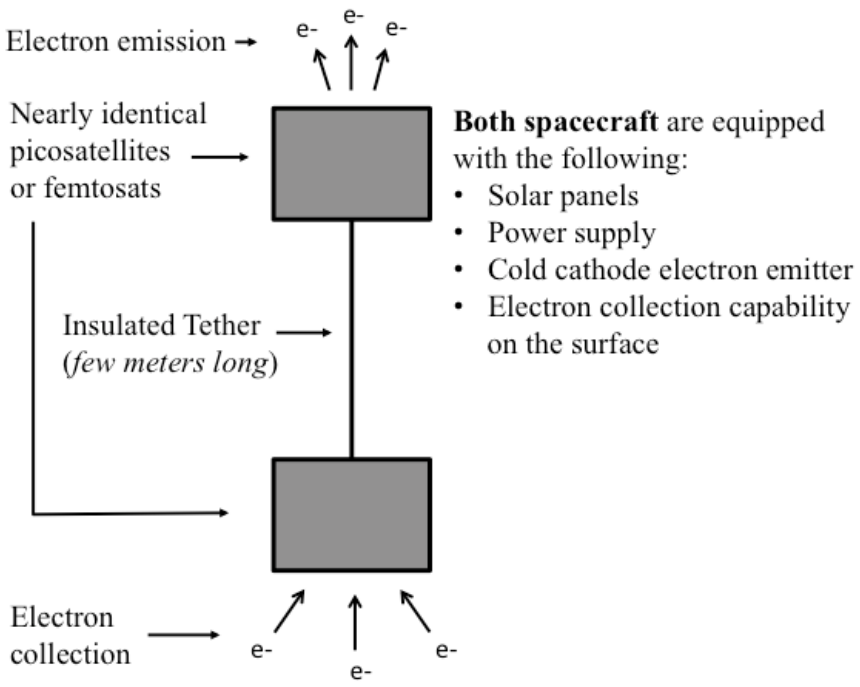

Figure 3.1: Simplified schematics of the basic miniaturized electrodynamic tether system concept.

The dimensions of the representative spacecraft selected for this study are provided in Table 3.1. Simple illustrations are shown in Figure 3.2. A range of existing and proposed picosat and femtosat designs influenced these dimensions. The largest spacecraft considered, a 200-g planar picosat, is approximately the same size as PCBSat, a picosatellite concept developed by the University of Surrey to be an element in a space-based wireless sensor network [6]. This shape would offer large faces for mounting solar cells and low drag if attitude could be maintained. Passive attitude maintenance can be accomplished, for example, by designing the spacecraft so the center of mass is offset from the center of pressure along the velocity vector [49], [101]. The 150-g cubic picosat takes its dimensions from the PocketQube architecture. The cubic shape offers more component height and could be designed by stacking PCBs vertically. The smaller 10-g ChipSat was inspired by the Sprite femtosat [22]. It is also assumed that the 10-g ChipSat is oriented so the minimum cross-sectional area is perpendicular to the spacecraft's velocity. Although the spacecraft concepts in Table 3.1 are intended to be representative of different picosat and femtosat concepts, spacecraft near and below 100 g are a relatively new and evolving architecture and may assume a variety of shapes and sizes over time.

Table 3.1: Mass and Dimensions of Spacecraft Considered in the Trade Study

Description	Dimensions (cm)	Drag Area (cm^2)
200-g planar picosat	10 × 10 × 2	20
150-g cubic picosat	5 × 5 × 5	25
10-g ChipSat	2.5 × 2.5 × 0.5	1.25

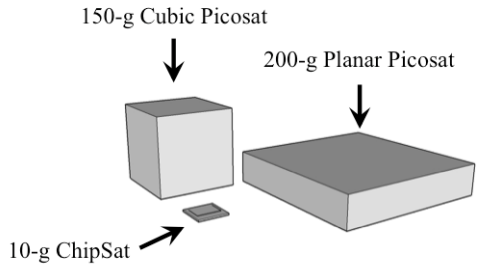

Figure 3.2: Simple illustration depicting the picosats and femtosat considered in this system concept. The spacecraft are represented by gray blocks. The black patches represent square and rectangular solar cells. The 150-g picosat is shown to the left, the 200-g planar picosat is shown to the right and the 10-g ChipSat is shown in between.

3.2 The Orbital Environment

The conditions of the orbital environment heavily influence EDT performance. Here, we will use Earth conditions as the basis of this study, but other planets with a magnetoplasma such as Jupiter are also possible candidates for the work reported here. The density of the Earth's upper atmosphere decreases roughly exponentially with altitude, and as a result, the atmospheric drag decreases with altitude. The dominant neutral species for a range of altitudes is atomic oxygen. Figure 3.3a provides a profile showing the variation in neutral mass density with altitude. Figure 3.3a presents the volumetric mass density (g cm^{-3}) in LEO rather than the number density (cm^{-3}) because atmospheric drag is typically calculated using volumetric mass density (see Equation 2.11 in section 2.1.2 in Chapter 2).

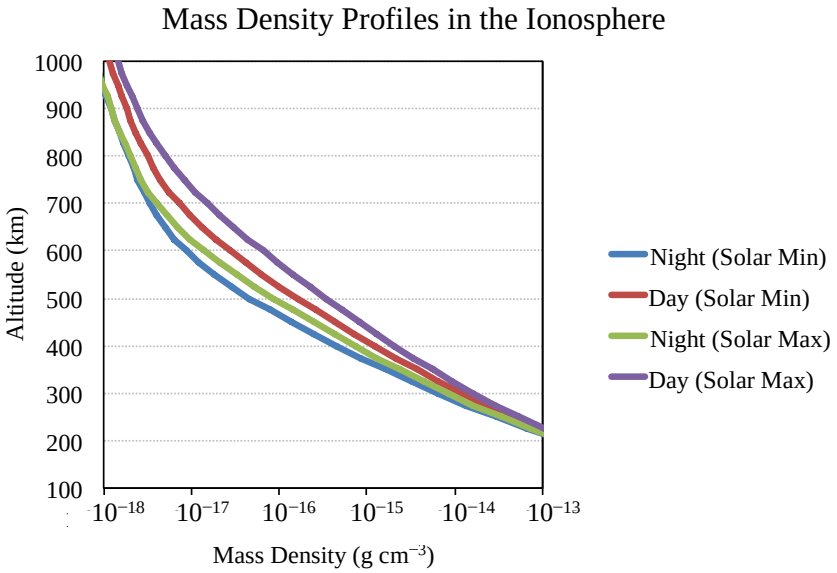

(a)

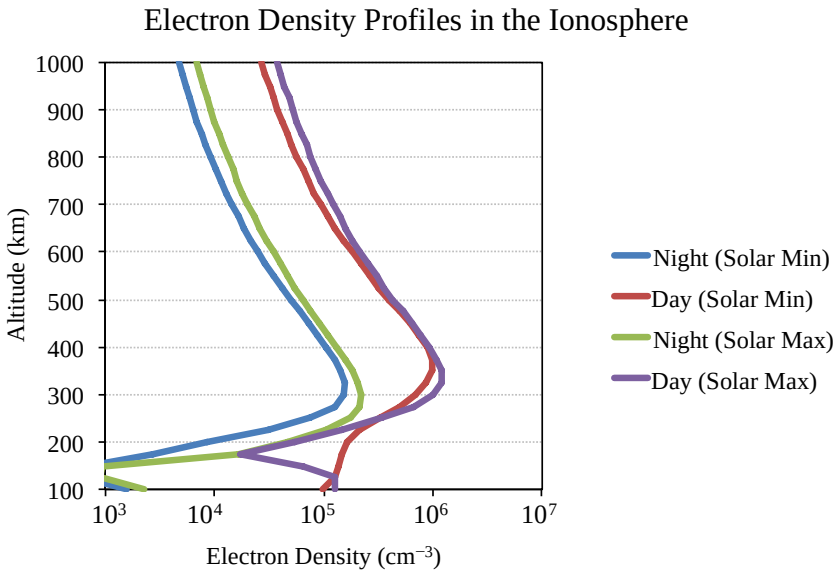

(b)

Figure 3.3: Typical Neutral Mass Density and Electron Density Profiles in the Earth's ionosphere. The neutral density profiles were produced using the MSIS-E-90 atmosphere model and the electron densities were produced using IRI 2012 ionosphere model. January 1, 2009 was the date used for the low solar activity, or solar min, and July 1, 2011 was the date used high solar activity, or solar max. The local time for daytime profiles was 2:00 p.m. and the local time for the nighttime profiles was 2:00 a.m. All values are in the equatorial plane at 0°N 0°E.

Ultraviolet, extreme ultraviolet (EUV), X-ray, and corpuscular radiation from the Sun heat, ionize, and excite the neutral constituents in the upper atmosphere, generating the ionospheric plasma. The ion composition in low Earth orbit (LEO) follows the neutral atmosphere composition, and the most abundant ion species in the peak density regions is O^+ [62]. Figure 3.2b shows typical electron density profiles in the ionosphere. The peak electron density, and thus EDT thrust capability, occurs in the F region of the ionosphere between 300 and 500 km altitudes, so the orbital environment considered in this study was within this region. The atmospheric density above the F region decreases with altitude more rapidly than the plasma density, so EDT drag make-up and propulsion at 600 km was also considered in this study. Although temperature is not shown in Figures 3.2b, electron and ion temperatures are generally a few tenths of an electron volt (~0.1 eV) in LEO.

The neutral and plasma density vary with local time, latitude, altitude, and solar and geomagnetic activity. The plasma density is highest about 2 hours after local noon [62]. Peak electron and ion densities are around 10^6 cm^{-3} and can drop by an order of magnitude on the night side of the F region. The solar radiation flux also varies over the course of the Sun's ~11 year cycle. Higher solar activity raises the solar radiation flux, particularly the EUV flux, which raises the temperature of the upper atmosphere and causes it to expand outwards. It also increases the average plasma density in LEO. Differences in atmospheric and plasma density between solar maximum and minimum can be 2 orders of magnitude [7]. Corpuscular precipitation at high latitudes also transfers energy to the ionosphere. High-energy charged particles from the solar wind interact with the geomagnetic field and some of them penetrate into the ionosphere near the Earth's poles.

The magnetic field in LEO can be approximated as a dipole tilted 11° from the axis and offset towards the Atlantic Ocean [61]. More precise models, like the International Geomagnetic Reference Field (IGRF) models, can be used to calculate the magnetic field elements around the Earth more accurately [102]. Because vertically oriented EDTs produce peak in-plane thrust near the equatorial plane, the focus here is on low inclinations orbits. Near the equatorial plane in LEO, the magnetic field, the neutral atmosphere, and the ionosphere approximately co-rotate with the Earth [61], [103]. The

speed of rotation, $v_{co\text{-}rotate}$, can be crudely approximated at latitudes close to the Equatorial plane in LEO as the rotational speed of the surface of the Earth at the Equator, where $v_{co\text{-}rotate} \approx 0.4$ km s^{-1} [104]. Although all the analysis in this chapter is carried out assuming the tether is in the equatorial plane, the analysis is extended to a wider range of inclinations in Chapter 5.

Atmosphere and ionosphere assumptions in this study are summarized in Table 3.2. The electron densities used in this study was determined by averaging the electron density around an equatorial orbit at 400 km, 500 km, and 600 km altitudes. The ionospheric conditions were obtained using the International Reference Ionosphere-2007 (IRI-2007) model during July 1, 2011, which was during the solar high period of solar cycle 23 [105], [106]. The neutral density was similarly taken from the Mass-Spectrometer-Incoherent-Scatter (MSIS-E-90) model [107]. The drag force scales with the neutral density and the thrust scales with electron density, so the elevated neutral-to-electron-density ratio during high solar activity actually represents the worst-case scenario for thrusting. Other solar conditions and altitudes are also considered in Chapter 5.

Table 3.2: Ionosphere and Neutral Atmosphere Conditions Used in this Study.

Value	400-km Altitude	500-km Altitude	600-km Altitude
Electron Temperature (eV)	0.11 eV	0.14 eV	0.15
Neutral Density (g cm^{-3})	5×10^{-15}	9×10^{-16}	2×10^{-16}
Electron Density (cm^{-3})	1×10^{6}	7×10^{5}	3×10^{5}
Magnetic Field (G)	~0.35		
Circular Orbital Velocity (km s^{-1})	7.7	7.6	7.6
Atmosphere, Ionosphere, Magnetic Field Eastward Rotation Speed (km s^{-1})	~0.4		
Dominant Ion Species	O^{+}		

3.3 Miniaturized Electrodynamic Tether Characteristics

The miniaturized EDT considered in this study is a short, insulated, conducting tether with a circular cross-section that connects a pair of identical picosats or femtosats. The relatively short EDT considered here for these very small spacecraft is also assumed

to be a “semi-rigid” structure. This is in contrast to much longer flexible tether systems with much larger end-bodies, where the gravity-gradient would provide the tension necessary for deployment and stability in the presence of lateral forces (e.g., drag and solar radiation pressure). For example, in the TSS missions, the Space Shuttle orbiter, which had a mass of about 100,000 kg, deployed a 521 kg, 1.6-m diameter sphere as the second end-body. In this case, the gravity gradient torque oriented the tether along the local vertical and the force pulled the long, flexible structure approximately straight. Vertical orientation is important because a tether that is straight and aligned along the local vertical in a low inclination orbit in LEO can generate peak in-plane thrust.

As will be discussed, drag and thrust forces along the length of a tether can cause tether bowing [55], [108], allowing us to treat the tether as a very thin beam undergoing elastic deformation [109]. Bowing can be less significant for long tethers when the gravity-gradient tension force is large [110]. In the case of a short EDT connecting less massive spacecraft, however, the gravity gradient force is smaller (gravity-gradient force is described in section 2.2.2 of Chapter 2). We assume here that if the gravity-gradient tension force is small, a tether with a sufficient level of *flexural rigidity* or *bending stiffness* may be important for the tether to resist large deflection and hold its shape once deployed on orbit. Calculation for gravity-gradient are presented later in the chapter and compared to other forces, but here we assume for the moment that some degree of flexural rigidity is needed to reduce bowing. In addition, the tether should be flexible enough to be spooled or coiled for storage (with diameters similar to spacecraft dimensions) until the tether is deployed on orbit. In this thesis, a "semi-rigid" tether is one that satisfies both of these conditions, or has bending stiffness (again, assuming gravity-gradient is not dominant at these length scales) as well as flexibility for long-term storage. The semi-rigidity analysis presented here informs the types of tether materials as well as range of tether diameters that are considered in the system concept trade study. This section provides additional detail on tether semi-rigidity and describes the materials considered for the tether.

3.3.1 Tether Semi-rigidity

Here, a first-order analysis is presented to begin to characterize the tether structure mechanically. The purpose of this thesis is not to conduct an exhaustive or even complete analysis on tether mechanical properties. Instead, the goal here is to guide the selection of representative tether materials and determine approximate minimum and maximum tether radii to be considered in the trade study. It has been suggested that a tether with some degree of flexural rigidity can be treated as a beam [110], so that is the analysis applied here. Although this is an instructive first step in characterizing the tether, it should be clear to the reader that the need for EDT rigidity is reduced in the presence of a strong gravity-gradient force.

In order to store the tether in a coiled shape prior to tether deployment without risking permanent deformation, it is necessary to calculate the minimum radius of curvature that the tether can experience without exceeding the material's yield stress. The yield stress, σ_y, is the maximum stress that a material can sustain before it begins to permanently deform, or deform plastically. The normal stress, σ, on an object in tension is equal to the tension divided by the object's cross-sectional area, or

$$\sigma = \frac{P}{A_{\text{obj}}}, \tag{Eq. 3.1}$$

where P is tension and A_{obj} is the cross-sectional area of the object. The normal strain, ε, is defined as the change in length of an object under tension divided by the object's original length. According to Hooke's law, the normal stress and normal strain of an object under tension (or compression) are directly proportional, which can be expressed as [111]

$$\sigma = E\epsilon, \tag{Eq. 3.2}$$

where the Young's modulus, E, represents a material's resistance to elastic deformation. A shear force, in contrast, acts perpendicular to the axis of the object (i.e., transverse to the axis of extension) and would produce shear strain [111].

Treating the wire as a thin beam and assuming that the wire, in a storage condition, experiences uniform bending, the shear stress is negligible and the only stresses that will be significant to the coiled tether are normal stresses [111], [112]. The

radius of curvature, R_{curv}, of a beam under pure bending is related to Young's modulus and normal stress by the bending formula

$$\frac{E}{R_{\text{curve}}} = \frac{\sigma_{\max}}{r_{\text{wire}}}, \quad \text{(Eq. 3.3)}$$

where σ_{max}, is the maximum normal stress and r_{wire} is wire radius. Selection of σ_{max} as yield stress σ_y or the stress that produces permanent, plastic deformation in a material, produces the expression for the minimum radius of curvature,

$$R_{\text{curve}-\min} = \frac{E}{\sigma_y} r_{\text{wire}}, \quad \text{(Eq. 3.4)}$$

which is the minimum radius of curvature that can be applied to the wire before plastic deformation occurs. The conclusion here is that a tether material with a relatively high yield stress is desired so minimum radius of curvature will be small.

The expression for minimum radius of curvature also suggests an upper bound for the tether radii that can be considered. Simply re-arranging Equation 3.4 gives

$$r_{\text{wire}-\max} = \frac{\sigma_y}{E} R_{\text{curve}}, \quad \text{(Eq. 3.5)}$$

where $r_{wire\text{-}max}$ is the maximum wire radius that can be used without the wire undergoing plastic deformation. To be clear, r_{wire} represents the radius of the wire and R_{curve} represents the bending radius of the wire. If the tether is stored inside or between the picosats or femtosats, R_{curve} is limited by the size of the spacecraft, providing an upper bound for the tether radius that can be used. If the tether radius exceeds $r_{wire\text{-}max}$, residual stress is induced in the wire, and this can cause an initially straight wire to acquire residual curvature and a helical shape after deployment [110].

In practice, $r_{wire\text{-}max}$ will be even smaller than the radius predicted by Equation 3.5. Yield stress often refers to a stress where the material has undergone a small deformation beyond the elastic limit, typically 0.1−0.2% strain, so the stress in the material should be maintained below the yield strength. In addition, a process known as creep or cold flow can induce deformation when stress is applied to an object over long time periods. Using a thinner tether or a larger bending radius (if possible) would reduce the applied stress in the tether.

It is likely that the tether will have a much higher area-to-mass ratio than the satellites on each end, so it will experience a stronger acceleration due to drag. The drag force can cause tether bowing, and the effect can be more pronounced in the absence of a dominant gravity-gradient tension force [108]. It should be noted that here it is assumed that the drag force is equal on both spacecraft, though the bowing effect can worsen result is that the tether may bend or bow in orbit. Sufficient bowing reduces the vertical length of the tether, which in turn can reduce thrust. To investigate tether bowing due to drag, the EDT system was transformed into an equivalent static system by adding inertial forces [113]. In the transformed "static" system, the sum of the forces and torques acting on the system is zero. This technique allows EDT deflection to be solved like the deflection along a simply supported beam. The details of the derivation may be found in Bell et al. (2011) [114]. The variation in drag force along the structure causes a maximum deflection at the center calculated by

$$y_{\max} = \frac{10L^3}{384EI_{\text{area}}}\left(\frac{F_{\text{EDTdrag}}m_{\text{sc}} - F_{\text{scdrag}}m_{\text{EDT}}}{2m_{\text{sc}} + m_{\text{EDT}}}\right), \quad \text{(Eq. 3.6)}$$

where m_{sc} is the spacecraft mass, m_{EDT} is the tether mass, $F_{EDTdrag}$ is the drag on the tether, and F_{scdrag} is the drag on the spacecraft. It should be noted that this derivation assumes that mass and the drag force are the same for both tethered spacecraft. The deflection y_{max} gives the maximum bowing distance, which is the distance the center of the tether moves relative to the tethered spacecraft. The maximum deflection scales with drag, so deflection is expected to be larger at lower altitudes where the drag forces are higher. The radius that limits the maximum tether deflection to y_{max} is

$$r_{\text{semi-rigid}} = \left(\frac{40L^3}{384\pi E y_{\max}}\left(\frac{F_{\text{EDTdrag}}m_{\text{sc}} - F_{\text{scdrag}}m_{\text{EDT}}}{2m_{\text{sc}} + m_{\text{EDT}}}\right)\right)^{1/4}. \quad \text{(Eq. 3.7)}$$

Generally, $r_{semi\text{-}rigid}$ increases with tether length to prevent large deflections. However, when the tether is sufficiently long, the gravity-gradient force may be able provide the tension to reduce bowing even for a flexible tether. Thus, EDTs with smaller radii and/or composed of lower Young's modulus materials can be considered when the gravity-gradient force dominates over other forces. The gravity-gradient force is calculated later in the chapter and compared against other forces.

3.3.2 Tether Materials

In this section we discuss materials that are simply representative of possible materials that could be used to make miniaturized EDTs. Characteristics for materials considered in this study for the tether are summarized in Table 3.2. The central conductor is Monel® K-500 (referred to here as "Monel"). Monel® is a high-strength nickel-copper alloy that has a high Young's modulus and yield strength. The high yield stress allows the tether to be bent at relatively small radii of curvature. The maximum tether radius that can be bent to a specified radius of curvature without plastically deforming is presented in Figure 3.4a. If the tether is stored inside or sandwiched between the spacecraft, the radius of curvature would likely be less than half of the spacecraft width otherwise a tether in a circular coil could not fit inside or between the spacecraft. This suggests a maximum tether radius that can be considered for each spacecraft. In addition, the high Young's modulus of the material allows the tether to be made relatively thin without experiencing significant bowing in orbit. This can be seen in Equation 3.7, where the tether radius needed to reduce bowing scales as $L^{3/4}$. The minimum radii that would make a Monel tether a relatively "semi-rigid" structure in a 400 km circular orbit are shown in Figure 3.4b. The radii range from 10s of micrometers to a few hundred micrometers, increasing with tether length. If the tether is sufficiently long and the gravity-gradient force is dominant over other forces in orbit, however, the tether will be held in tension and smaller radii could be considered. Monel also has good high-temperature performance- the Young's modulus does not reduce by more than 1% from 0–300°C. Although the author was not able to locate the Young's modulus of Monel at lower temperatures, the Young's modulus of metals generally increases at lower temperatures [115]. Alloys like Inconel exhibit similar properties and could also be considered.

The outer insulator is Dupont™ Teflon® PFA (referred to here as "Teflon"). Teflon has a high dielectric strength and UV radiation resistance and relatively low reactivity with atomic oxygen [118]. The high dielectric strength allows a very thin layer of Teflon to be used, but mechanical robustness may require thicker layers. It is assumed here that the insulation is 12.5 μm (0.5 mil) thick. This is many times the minimum thickness needed to prevent electrical breakdown. Teflon typically has low friction, but it can be treated to make it adhere more easily.

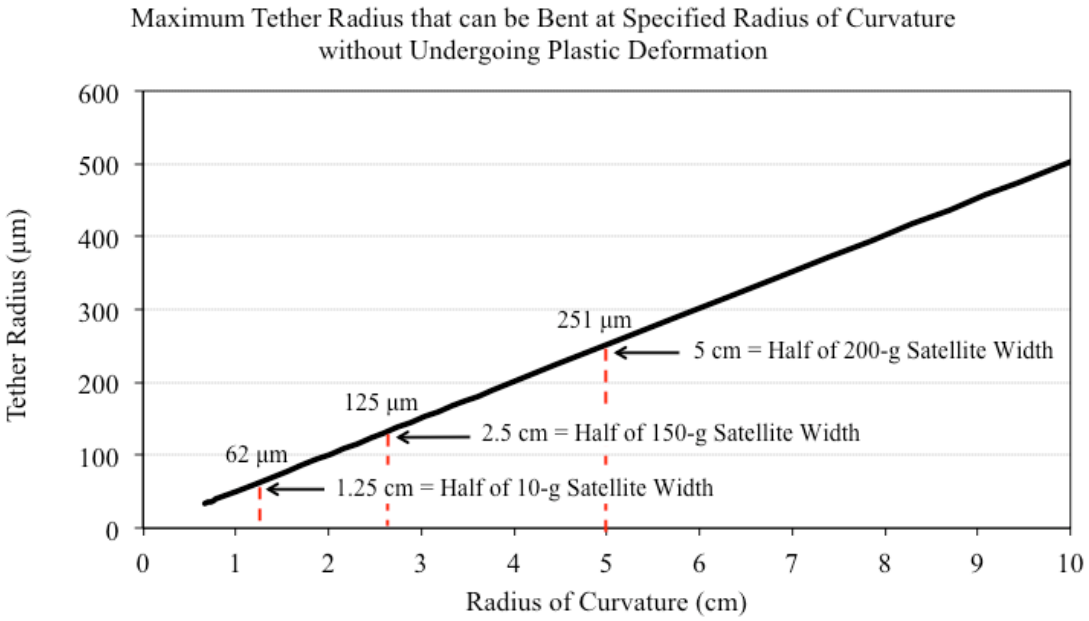

(a)

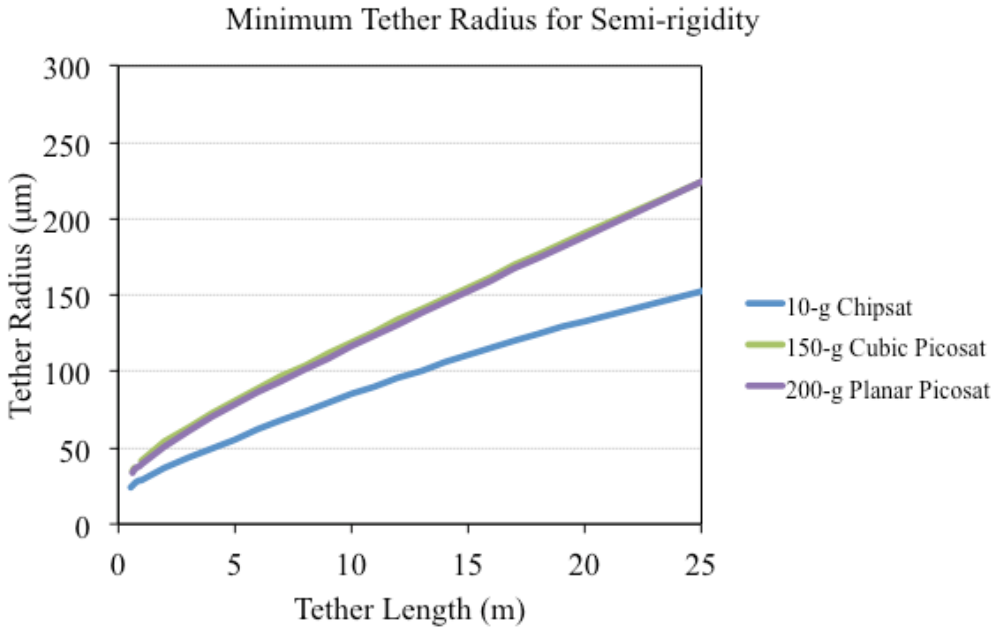

(b)

Figure 3.4: (a) Maximum tether radii that can be used without causing plastic deformation and (b) minimum radii for tether semi-rigidity. The minimum radii of the 150-g cubic picosat and the 200-g planar picosat are approximately identical.

Table 3.3: Properties of Tether Materials.

Monel K-500 [116]	
Electrical resistivity (21°C)	6.15×10^{-7} Ω m
Mass density	8.44 g cm^{-3}
Elastic Modulus, Tension (21°C)	179 GPa
Yield Strength, spring temper cold-drawn wire	896−1241 MPa (900 MPa assumed)
Teflon PFA film [117]	
Dielectric Strength	260 V μm^{-1}
Mass density	2.15 g cm^{-3}
Elastic Modulus, Tension (21°C)	0.48 GPa
Yield Strength (21°C)	12 MPa

3.4 Miniaturized Electrodynamic Tether DC Circuit Model

The miniaturized EDT can be modeled by electrical circuit elements representing the tether, anode, cathode, ionospheric plasma, motional emf, and the floating potential. An illustration of the dc tether circuit is shown in Figures 3.5 and 3.6. In the boosting and de-boosting modes, the upper and lower spacecraft switch between electron collection and emission to reverse the direction of current and thrust. The anode is biased above the plasma potential to collect sufficient current for propulsion. The spacecraft operating the cathode is assumed to be at the floating potential of the spacecraft without electron emission. A negative voltage (with respect to spacecraft electrical common or "ground") is applied to the cathode to produce electron emission. The motional emf and the current through resistance of the tether also produce a voltage across the tether. The circuit is a closed current loop, so the sum of the voltages is zero (Kirchoff voltage law). A circuit equation consisting of the voltage drops can be written as

$$V_{\text{anode}} + V_{\text{cathode}} = V_{\text{float}} + V_{\text{gate}} + V_{\text{emf}} + I_{\text{tether}}R_{\text{tether}} + \Phi_{anode} + V_{\text{ION}}, \quad \text{(Eq. 3.8)}$$

where V_{anode} is the anode power supply voltage, V_{cathode} is the cathode power supply voltage, V_{float} is the floating potential of the electron emitting spacecraft (the spacecraft opposite the anode), V_{gate} is the base-gate voltage for a electron field emitter cathode, V_{emf} is the motional emf across the tether, $I_{\text{tether}}R_{\text{tether}}$ is the voltage drop across the tether due

to the tether's ohmic resistance, Φ_p is the anode sheath potential, and V_{ion} is the voltage drop in the ionosphere. This section explains how the circuit elements in the miniaturized tether circuit are modeled.

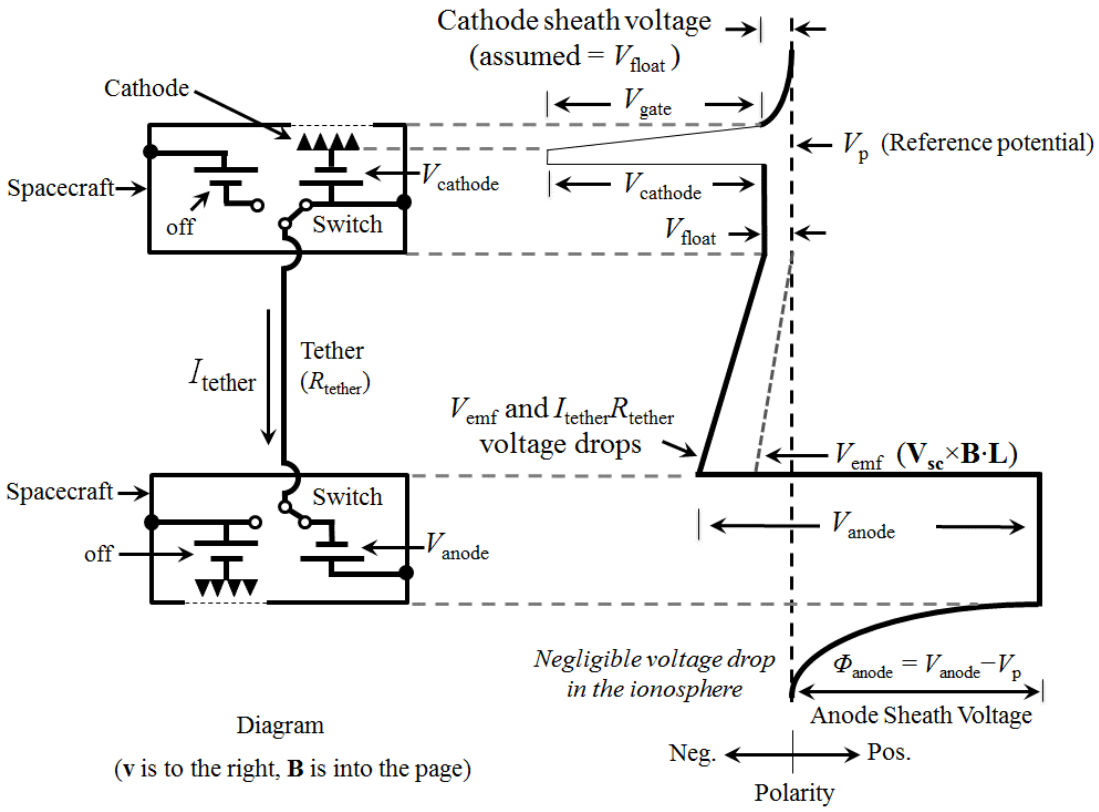

Figure 3.5: Tether circuit and potential diagram for a boosting configuration for a system capable of both boost and deboost. It should be noted that the power supply configuration could be changed to reduce the overall number of power supplies needed.

3.4.1 Tether

The tether is simply modeled as a resistive element, using the room temperature resistivity of Monel® to calculate resistance. The tether resistance induced voltage drop is assumed small relative to the other impedances in the circuit, but it can be reduced even further by coating the tether core with a thin, highly conductive material like gold or

silver. The power dissipated in the tether is not a dominant factor because this loss term scales with resistance and the square of current, both of which are small values.

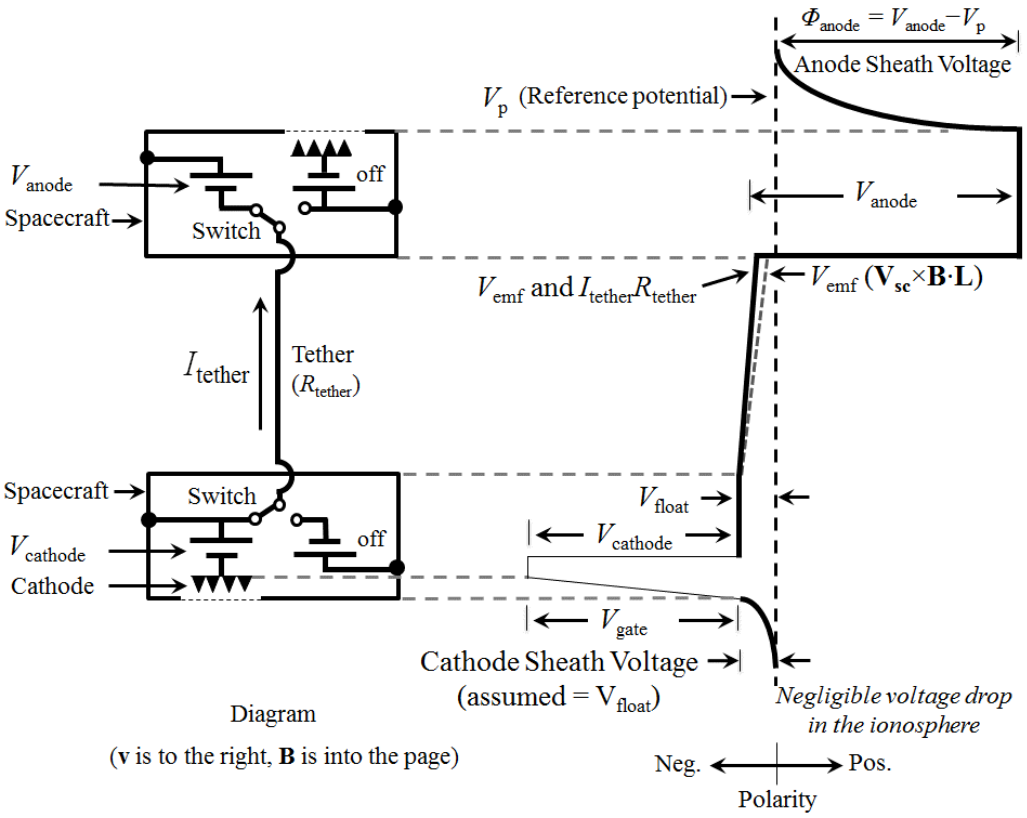

Figure 3.6: Tether circuit and potential diagram in for a de-boosting configuration. It should be noted that the power supply configuration could be changed to reduce the overall number of power supplies needed.

3.4.2 Motional Electromotive Force

The emf across the tether can be calculated as $\mathbf{V}_{sc}\times\mathbf{B}\cdot\mathbf{L}$. The geomagnetic field rotates with the Earth, so the velocity used to calculate motional emf should be in the reference frame of the Earth's rotation. As mentioned earlier in the chapter, the Earth rotates eastward at the equator at velocity $V_{\text{co-rotate}} \approx 0.4$ km s^{-1} [104], [119]. The emf can then be estimated as,

$$V_{\text{emf}} \approx (V_{sc} - V_{\text{co-rotate}})B, \qquad \text{(Eq. 3.9)}$$

which is approximated at low inclinations for vertically-aligned tethers in LEO. This is a special case for the largest motional emf for a given tether length and magnetic field. The resulting emf is on the order of ~1V for a short tether, so the power supply voltage required to exceed the emf and boost a miniaturized tether is low.

3.4.3 Cathode

Electron emission can be achieved through the use of a field emitter array (FEA) cathode mounted on the surface of one of the tethered satellites [120]. For a typical FEA cathode, electrons are emitted from the "base," where there is a 2-D array of carbon nanotubes or micrometer-scale cones. A positively biased grid, or "gate," near the base establishes an electric field (at the level of single $V \cdot nm^{-1}$) that induces quantum mechanical tunneling of electrons out of the emitter tips and into the ambient plasma. The emission current is controlled by adjusting the base-gate voltage, which adjusts the electric field strength at the emitter tips. An illustration of the field emitter circuit is shown in Figure 3.7. The benefits of the field emitter array include its flat-panel scalability, meaning that it has a low profile and can fit very well into different faces of a small satellite. FEAs are extremely sensitive to surface contamination, so robustness of FEAs in the space environment is currently being explored [121], [122]. Thermionic emitters could also be used, but they were not considered here because they require additional electrical power to heat the emitting filament. A hollow cathode plasma contactor was not used because it uses gas and is not propellantless as a result.

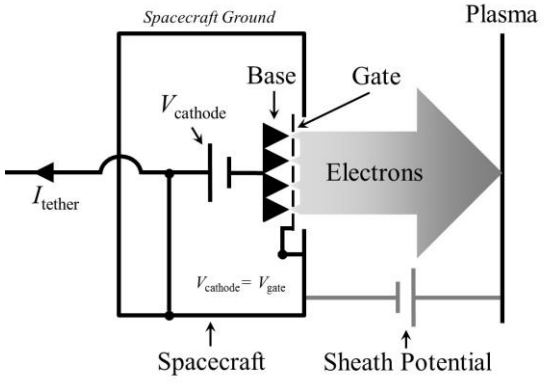

Figure 3.7: Illustration of field emitter array cathode in a grounded-gate configuration.

The FEA here is modeled after a Spindt-style 2.5×2.5 mm array characterized in Whaley and Bellew (2009) [123]. The expression for FEA current emission was provided in Chapter 2 and is provided again here as

$$I_{\mathrm{FN}} = a_{\mathrm{FN}} V_{\mathrm{gate}}^2 \exp\left(-b_{\mathrm{FN}} / V_{\mathrm{gate}}\right), \qquad \text{(Eq. 3.10)}$$

where V_{gate} is the potential applied to the cathode and a_{FN} and b_{FN} are the Fowler–Nordheim current and voltage coefficients, respectively. The Fowler-Nordheim voltage and current coefficients were 0.03 A V^{-2} and 487 V, respectively, and were determined in laboratory conditions [123]. The emission current-voltage characteristic is shown in Figure 3.8. The "turn-on" voltage, or the voltage where the cathode produced 1 μA, is 30 V. At 75 V, the cathode emission current density was of ~15 A cm^{-2}. The leakage current to the gate was reported to be low, so it is assumed be negligible here.

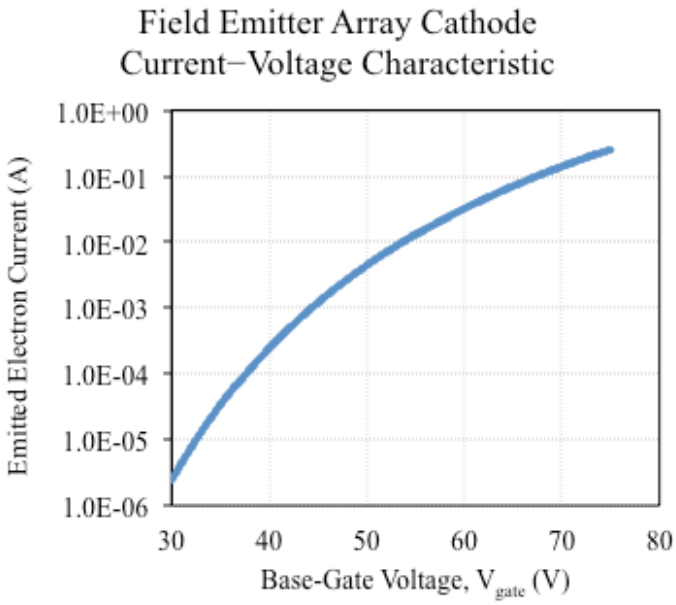

Figure 3.8: Field Emitter array current−voltage characteristic calculated using the cathode performance parameters from Whaley et al. (2009) [123].

In this study, the gate is connected to spacecraft ground and the cathode power supply negatively biases the emitting base with respect to the gate. It is assumed that the spacecraft outer conducting surface (spacecraft ground) floats a few kT_e/q below the

plasma potential. Here, the spacecraft is assumed to float at approximately −0.5 V relative to the plasma potential [124], which is also the cathode sheath voltage.

Generally, it is important to maintain the spacecraft relatively close to the plasma potential to maintain emission efficiency [120]. If the spacecraft floating potential drops well below the plasma potential, the sheath expands and the electron current crossing the sheath can become space-charge limited. If the spacecraft potential rises above the plasma potential, the sheath retards emitted electrons. The electron current is returned to the spacecraft if the spacecraft potential rises above the emission energy of the electrons and crates a space charge limited condition. An alternative multi-acceleration grid configuration was studied to enhance emission efficiency further [125], but the configuration here was selected because of its relative simplicity.

3.4.4 Anode

Electrons are collected on the opposite tethered spacecraft by positively biased conducting surfaces (relative to plasma potential) that are exposed to the plasma environment. Since it was assumed that much of the spacecraft surfaces would be covered with solar cells, a transparent conductor (like indium tin oxide, or ITO) could be used to coat the solar cells [126]. The impact of ITO on solar collection is discussed in section 3.5.2. It is expected that these current-collecting picosats and femtosats will have non-standard geometry for practical reasons and have characteristic dimensions of the same order as the Debye length and the electron gyroradius, so predicting collection current is challenging (relative to approximations appropriate for dimensions small or large with respect to Debye length). This section identifies the challenges associated with estimating current collection and the simplifying assumptions used to estimate current.

One of the assumptions of the Parker–Murphy model (and its TSS-1R modified version) is that the gyroradius is small relative to the collector size [57], [83]. In the region of LEO considered in this trade study, the average gyroradius for thermal electrons is approximately 3 cm. The TSS-1R anode had a radius of 80 cm. The satellite considered in this trade study has an equivalent radius of 5 cm (and more generally we consider pico- and femtosats that are even smaller). Thus, the TSS-1R modified Parker–Murphy model is not directly applicable. In addition, the possible cuboid shape of the picosat and

femtosat complicates predicting current (as compared to, for example, spherical or long cylinders). Many of the proposed picosat and femtosat designs are planar and rectangular because components are mounted on printed circuit boards (PCBs) and/or semiconductor wafers, giving the spacecraft body the same planar/rectangular shape. The Parker–Murphy and TSS-1R modified Parker–Murphy models are only defined for conducting spheres while OML theory is defined for spheres, infinitely long cylinders, and infinite plates. Experiments have been conducted to better understand the current collection behavior of picosat-shaped and spherical electrodes in a flowing plasma, but the electrode sizes relative to the Debye length were large compared to our electrodes [126].

Simplifying assumptions were made here to facilitate estimating the anode current with an attempt to be conservative in the assumptions. For a conductor in an unmagnetized, non-drifting plasma, the sheath surrounding the conductor will expand with increasing bias voltage. If the sheath is very large with respect to the conductor, it may conceal the fine details of the anode's shape [127]. It was therefore assumed that at potentials that are high enough, the cuboid-shaped satellite would collect current *approximately* like a sphere with a diameter equal to the spacecraft's longest edge. The equivalent radius of the 200-g planar picosat, for example, would be 5 cm.

In order to evaluate this assumption, sheath thickness was estimated. In order to make a rough estimate of the sheath, it was reasoned that the current collected by a positively biased conductor must equal the net current passing through the outer edge of the sheath boundary. For this application, it was also safe to assume that the potential difference between the conducting body and the undisturbed ambient plasma would be much larger than the ambient electron temperature, T_e, across the sheath (the pre-sheath potential is ignored here). It was also assumed that the entire spacecraft's surface would be conducting and capable of collecting electron current. Expressions are given in Chapter 2 for the electron thermal current at the sheath edge and the electron current collected by a spherical probe in an isotropic, non-drifting, non-magnetic plasma in the thick sheath regime. Since the electron thermal current at the sheath edge is equal to the current collected by the probe (using the same assumptions mentioned), we reason here that a crude approximation of the sheath radius can be obtained by solving for the sheath

radius when the thermal current at the sheath edge and the collected current are equal [128]. The sheath radius is given by [128]

$$r_s = r_p\sqrt{1+\frac{q\Phi_{\text{anode}}}{kT_e}}, \qquad \text{(Eq. 3.11)}$$

where Φ_{anode} is the potential difference between the anode and the plasma. Bettinger and Walker (1965) developed another estimate for sheath thickness for conducting spherical Langmuir probes in stationary, non-magnetized, isotropic Maxwellian plasmas [129]. The estimated sheath radius is [129]

$$r_{\text{BW}} = 0.83 r_p^{1/3}\lambda_D^{2/3}\sqrt{\frac{q\Phi_{\text{anode}}}{kT_e}}. \qquad \text{(Eq. 3.12)}$$

The sheath thickness estimated in Equation 3.12 by Bettinger and Walker (1965) is generally much smaller than the sheath radius estimated in Equation 3.11 and is dependent on the probe bias voltage as well as the Debye length. The estimated sheath thicknesses using Equations 3.11 and 3.12 for a positively biased 5-cm sphere are compared in Figure 3.9. The large estimated sheath radius relative to the probe size, regardless of models in [16] or [17], helps justify using the spherical collector approximation. However, the thick sheath estimate is more appropriate when plasma densities are low because λ_D is larger. T_e = 0.1 eV and n_e =10^4–10^6 cm^{-3}

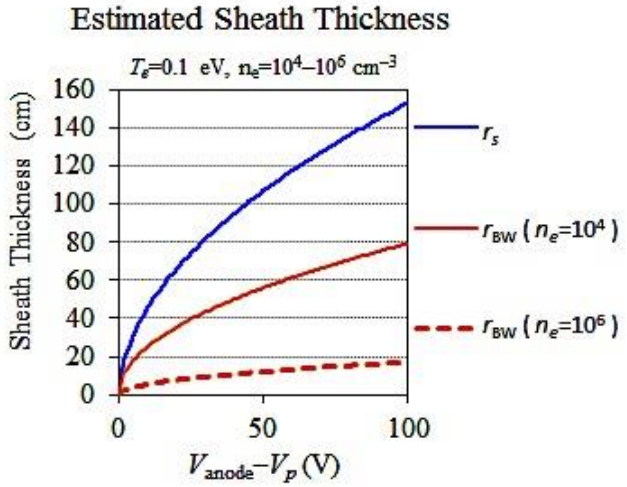

Figure 3.9: Estimated sheath thickness for a 5-cm spherical electrode. The maximum and minimum values were calculated assuming T_e= 0.1 eV an n_e =10^4–10^6 cm^{-3}. The curve labeled r_s is the sheath size calculated from Equation 3.11 [128]. The curves labeled r_{BW} are the sheath sizes calculated using Equation 3.12. [129].

After assuming a spherical collector, an expression was selected that was developed to interpret plasma parameters from the Floating Potential Measurement Unit (FPMU) on the International Space Station (ISS). The FPMU employed the wide sweeping Langmuir probe instrument (WLP), a sphere of 5 cm radius, to do current–voltage (*I*–*V*) sweeps in LEO from –20 V up to +80 V (with respect to the local structure potential of the ISS. The expression [130]

$$I_{\mathrm{WLP}} = \frac{I_{\mathrm{thermal}}}{2}\left(1 + \frac{q\Phi_p}{kT_e}\right)^{\beta} \qquad \text{(Eq. 3.13)}$$

was then fit to current–voltage data in the electron saturation region with different values of the dimensionless parameter β. The values of β were reported to vary between 0.5 and 1, although no explanation was provided for the variation [130]. In the 2-hour window provided, the value of β was ~0.65 when the electron density was similar to the densities assumed in this study at 400 km and 500 km, so β = 0.65 is assumed in this model. The current−voltage characteristic is shown in Figure 3.10. Current scales with plasma density, so the current collected at a fixed voltage varies with altitude and around the orbit.

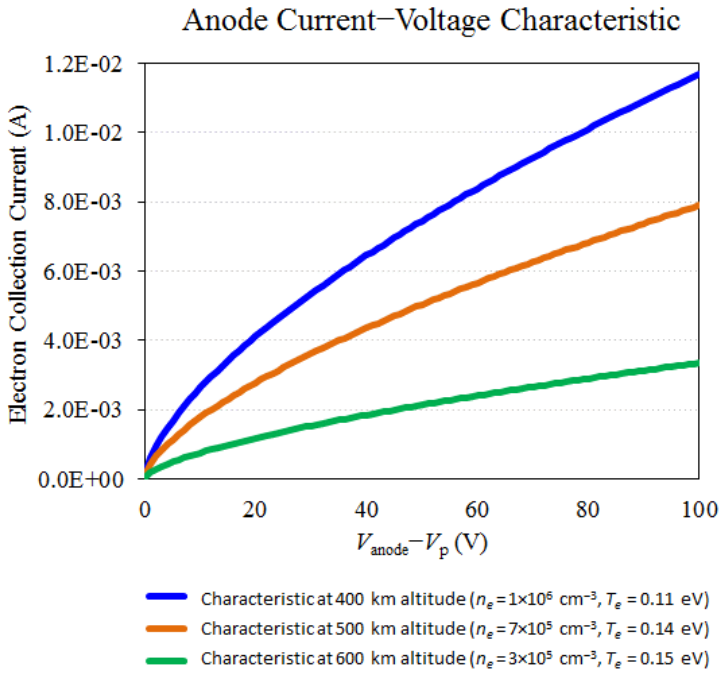

Figure 3.10: Current–voltage characteristic for a 5-cm radius spherical electrode at 400 km, 500 km, and 600 km altitudes [130].

3.4.5 Ionospheric Plasma

The voltage drop in the ionospheric plasma is assumed to negligible. Impedance estimates in LEO range from a few ohms to 10s of ohms [90], [131], [132]. The impedance is very small relative to the anode and cathode impedances, so it is not included in this circuit model.

3.5 Picosatellite and Femtosatellite Propulsion Power

Although EDT propulsion can be propellantless, on-board electrical power is required to generate thrust. The power generated on-board a picosat or femtosat is limited, so it is important to determine if the spacecraft can generate the power necessary for drag make-up. In this section of the chapter, the ability to generate electrical power is estimated and compared, later, to the power required to generate a force for drag make-up at 400 km, 500 km, and 600 km altitudes.

3.5.1 Estimated Propulsion Power Generation Capability

In this section, the power available for propulsion is estimated. A variety of assumptions are made to estimate propulsion power. Those assumptions are provided in the following paragraphs, with the appropriate justification.

It is assumed that solar cells lining the outer surface of the spacecraft are used to generate electrical power. To boost throughout the entire orbit, a spacecraft needs to generate enough power on the dayside to meet all the power demands during the day (P_d) and eclipse (P_e). It is also important to account for the efficiency of distribution and storage during daylight (X_d) and eclipse (X_e). The power the solar arrays must provide during sunlight is [7]

$$P_{\text{sa}} = \frac{\frac{P_e T_{\text{ecl}}}{X_e} + \frac{P_d T_d}{X_d}}{T_d}, \qquad \text{(Eq. 3.14)}$$

where T_d and T_{ecl} are the length of the orbit in sunlight and eclipse, respectively. Assuming that the power needed during day and night are approximately equal, an orbital

average power, P_{av}, can be used instead, where $P_{av} = P_d = P_e$. The resulting expression for the power the solar array must provide during sunlight becomes

$$P_{sa} = \left(\frac{1}{X_e}\left(\frac{T_{ecl}}{T_d}\right) + \frac{1}{X_d}\right) P_{av}. \quad \text{(Eq. 3.15)}$$

To determine the time in eclipse, T_{ecl}, the orbital period, P_{orb}, can be calculated as developed in the following several equations [7]. The orbital period is

$$P_{orb} = 2\pi\sqrt{\frac{a^3}{\mu}}. \quad \text{(Eq. 3.16)}$$

which is obtained by dividing 2π by the orbital frequency, ω_{cg}. For a circular orbit, the semi-major axis, a, is the sum of the radius of Earth, R_E, and the altitude, H_{alt}. The angular radius of the spherical Earth as seen from the spacecraft is [7]

$$\rho_{sc} = \sin^{-1}\left(\frac{R_E}{R_E + H_{alt}}\right). \quad \text{(Eq. 3.17)}$$

The time in eclipse can then be calculated as [7]

$$T_{ecl} = P_{orb}\left(\frac{\rho_{sc}}{180^\circ}\right). \quad \text{(Eq. 3.18)}$$

The eclipse time for a spacecraft in a circular orbit 300–600 km is about 36 minutes and the orbital period ranges from about 92 minutes to 97 minutes, depending on altitude. The time in sunlight is the difference between the orbital period and the time in eclipse.

The term X_e represents the efficiency of the power distribution through batteries to individual loads and X_d represents the efficiency directly to the loads. Assuming solar panel peak power tracking (PPT) power regulation, typical values of the energy conversion efficiency are X_e = 0.60 and X_d = 0.80. A PPT was assumed because it extracts the maximum power from a solar cell array. PPTs are active devices and they currently use around 4–7% of the total power [7].

The anode and cathode may require bias voltages on the order of 10s of volts to a few hundred volts to emit and collect sufficient current for drag make-up and somewhat more for orbital maneuvering, so a separate dc-dc converter will likely be needed to step-up the solar array output or battery voltage for the cathode and anode. The efficiency of this conversion, η_{up}, for the anode and cathode was assumed to be 90% [7]. Also, to estimate the peak thrusting capability of the ED tether, it was assumed that the power

available for propulsion, P_{prop}, was 70% of the total orbital average power generated by the spacecraft. This percentage was estimated using results from Ekpo and George (2013), which concluded that ~30% of picosat and femtosat power may be required for other spacecraft subsystems, including the communication and command and data handling subsystems [133]. Using the propulsion power expression developed in this section, the power generated for propulsion can be estimated assuming a higher or lower fraction of power generated for propulsion. The power generated by the solar cells can now be expressed as

$$P_{\text{sa}} = \left(\frac{1}{X_e}\left(\frac{T_{\text{ecl}}}{T_d}\right) + \frac{1}{X_d}\right)\frac{1}{\eta_{\text{up}}\eta_{\text{prop}}}P_{\text{prop}}, \quad \text{(Eq. 3.19)}$$

where η_{prop} is the fraction of on-board power generated for propulsion (recall that here, η_{prop} = 0.7). Equation 3.18 shows the power spacecraft must deliver during sunlight, P_{sa}, to meet the propulsion power requirement during the orbit, P_{prop}.

To determine the relationship between the solar cell delivered power and area, the solar cell efficiency must be considered. The energy conversion efficiency, η_{conv}, is the power output divided by the power input. Here, triple junction GaAs solar cells were considered because they can have a high conversion efficiency of ~30%. The average power per unit area on the surface of a solar cell perpendicular to the Sun's rays, Φ_{sun}, is about 136.8 mW cm^{-2}, so an ideal solar cell with η_{conv} = 0.3 would produce about 41 mW cm^{-2}. However, factors like heating of the solar cells and reduction in collection area due to interconnect cabling and mounting can reduce the power production capability of a solar cell. Combined, these loses make up the inherent degradation of the solar cell, I_{d}, which is above and beyond η_{conv}. A conservative I_{d} of 0.6 was assumed here. It has also been assumed that the spacecraft surfaces were coated in an ITO coating to increase the current collection area. Although ITO is transparent at optical frequencies, a small portion of the incident solar energy is reflected and absorbed by the ITO. Measurements of light transmitted through glass found that ITO reduces transmission efficiency by a few percent, so the efficiency of the solar cell coating, η_{ITO}, can be assumed to be 0.95 [134].

At the beginning of life, the array's power output per area is

$$P_{\text{BOL}} = \phi_{\text{sun}}\eta_{\text{conv}}\eta_{\text{ITO}}I_d\cos(\theta_{\text{sun}}), \quad \text{(Eq. 3.20)}$$

where the incidence angle of the sun, θ_{sun}, is measured between the vector normal to the surface of the array and the Sun line [7]. Over the mission, however, the solar cell performance degrades and the power per unit area decreases. Radiation and thermal cycling in and out of eclipse, for example, can contribute to the gradual degradation in performance of solar cells. This effect, known as life degradation, or L_d, can be calculated as [7]

$$L_d = (1 - D)^{L_i}. \quad \text{(Eq. 3.21)}$$

where L_i is the spacecraft's lifetime in years and D is the degradation per year. Degradation per year for the triple junction solar arrays assumed here is ~0.5% per year [7]. Generally, such a small lifetime degradation can be ignored, but it will be included in the calculation here for an estimated 10 year lifetime to ensure that the power generation estimates are not too high. The array's power conversion per unit area at the end of life is

$$P_{\text{EOL}} = P_{\text{BOL}} L_d. \quad \text{(Eq. 3.22)}$$

The solar array area is given by

$$A_{\text{sa}} = \frac{P_{\text{sa}}}{P_{\text{EOL}}}. \quad \text{(Eq. 3.23)}$$

The solar power that can be generated for propulsion, P_{prop}, can then be expressed in terms of the solar array area as

$$P_{\text{prop}} = \Phi_{\text{sun}} A_{\text{sa}} \eta_{\text{eff}} \left(\frac{1}{X_e} \left(\frac{T_{\text{ecl}}}{T_d} \right) + \frac{1}{X_d} \right)^{-1}, \quad \text{(Eq. 3.24)}$$

where $\eta_{\text{eff}} = \eta_{\text{conv}} \eta_{\text{up}} \eta_{\text{prop}} \eta_{\text{ITO}} I_{\text{d}} \cos(\theta_{\text{sun}}) (1-D)^L$. This expression is the identical for the sunlight reflected from Earth except only the Earth-facing solar cell area can be considered and the reflected power per area, Φ_{albedo}, is about 30% of direct sunlight [7]. The small energy contribution from Earth infrared radiation was neglected.

It was assumed that all 6 sides of the 200-g planar satellite and the 150-g cubic satellite had body-mounted solar cells, 2 of which face the sun at any given time. For the 200-g satellite, the sun-facing area was a 10 × 10 cm face and one of the 2×10 cm faces. The 10-g ChipSat is much thinner, so it was assumed that it only had body-mounted solar cells on its 2 largest faces and one faces the sun at a time. The portion of the total surface area that could be covered in solar cells was estimated using currently available 2 × 2 cm

and 1.55 × 3.18 cm solar cells. Allowing for spacing between cells, it was estimated that the large 10×10 cm face on the 200-g planar picosat could be covered by 9 of the 2×2 cm solar cells and the 2×10 cm edges could be covered by 2 of the 1.55×3.18 solar cells. It was assumed that all 6 sides of the 150-g cubic picosat could be covered by four 2 × 2 cm solar cells. The small ChipSat would likely require a unique solar cell geometry, but it was assumed that a little less than 50% of the top and bottom faces could be used for solar collection. No pointing was assumed, so the average solar angle θ_{sun} for body-mounted solar cells was estimated to be ~45°. It was also assumed that the nadir-facing side could generate power from Earth albedo and the albedo angle was estimated as ~0°. A summary of assumptions is provided in Table 3.4.

Using Equation 3.19, it was estimated that a pair of 200-g planar picosats, 150-g cubic picosats, and the 10-g ChipSat could generate about 530 mW, 330 mW, and 30 mW for propulsion, respectively. Individually, the propulsion power for each of these satellites would be about half of this. The anode and cathode voltages are not identical, but they are similar. It will be necessary in a more sophisticated model to account for the power lost anode and cathode separately. These power generation estimates are consistent (on an order-of-magnitude basis) with the power generation estimates of other picosat and femtosat concepts [42], [49], [133], [135]. As a validation exercise, the analysis presented here was used to calculate the electrical power generated by $50Sat, which is similar in size to the 150-g cubic picosat and the 200-g planar picosat. The peak electrical power of the $50Sat was about 312 mW [136] (to the author's knowledge, no other power values were reported for this spacecraft or any other of a similar size). Using $50Sat's orbital parameters and solar cell area and efficiency, the analysis developed here calculated a peak power generation that was only about 50 mW below the reported peak power. This result suggests that the power generation estimates presented here are reasonable and possibly even conservative.

Table 3.4: Power Generation Estimate Assumptions.

Average solar constant, Φ_{sun}		136.8 mW cm^{-2}
Average Earth albedo, Φ_{albedo}		41.0 mW cm^{-2}
Solar cell energy conversion efficiency (triple junction GaAs), η_{conv}		30%
Efficiency due to ITO coating on solar cells, η_{ITO}		0.95
Total inherent degradation, I_d		0.6
Performance degradation per year, D		0.5%
Life degradation, L_d		0.95
Average solar angle		45°
Average albedo angle		0°
Fraction of the orbit spent in eclipse, T_{ecl}		0.4
Fraction of the orbit spent in sunlight, T_d		0.6
Efficiency of electrical power distribution from solar array through battery to spacecraft loads, (distribution efficiency during eclipse) X_e		0.6
Efficiency of electrical power distribution from solar array *directly to* spacecraft loads (distribution efficiency on the dayside), X_d		0.8
Fraction of total generated power available for propulsion, η_{prop}		0.7
Efficiency of additional voltage boost converter for the anode and cathode, η_{up}		0.9
Solar cell area facing the Sun, solar cell area facing Earth	200-g planar sat	46 cm^2 (sun), 36 cm^2 (albedo)
	150-g cubic sat	32 cm^2 (sun), 16 cm^2 (albedo)
	10-g ChipSat	2.5 cm^2 (sun), 2.5 cm^2 (albedo)
Propulsion power generated by the pair of spacecraft, P_{prop}	200-g planar sat	530 mW
	150-g cubic sat	320 mW
	10-g ChipSat	30 mW

3.5.2 Estimated Power Needed for Drag Make-up

The electrical power required to drive current through the tether is the sum of the power dissipated in the tether ($I_{tether}^2 R_{tether}$), the power required to overcome emf ($I_{tether} V_{emf}$), and the power required by the anode ($I_{tether} V_{anode}$) and the cathode ($I_{tether} V_{gate}$). There is also a small potential difference across the sheath traversed by electrons emitted from the cathode, and here this is equal to the spacecraft floating potential, V_{float}. The impedance of the plasma is relatively small, so it is ignored. All together, the total power for EDT boosting is

$$P_{\text{prop}} = I_{\text{tether}}\left(V_{\text{float}} + V_{\text{gate}} + V_{\text{emf}} + I_{\text{tether}}R_{\text{tether}} + \Phi_{\text{anode}}\right). \quad \text{(Eq. 3.25)}$$

The power dissipated by the anode and cathode make up a majority of the electrical demand for the miniature tether application. The ohmic loss in the tether is not dominant because it scales with resistance and the square of current, both of which are relatively small. The emf is also small because the tethers are relatively short.

To estimate the minimum current needed for drag make-up, the assumed ED thrust is set equal to the drag force, giving an estimate for the tether current needed for drag make-up (assuming a vertical tether, perpendicular magnetic field , and thrust that is entirely in-plane),

$$I_{\text{tether}} = \frac{{}^{1}/_{2}\rho C_d A v_{\text{drag}}}{LB}, \quad \text{(Eq. 3.26)}$$

where L is tether length, B is magnetic field strength, and v_{drag} is the relative velocity between the spacecraft and the atmosphere. The tether current needed for drag make-up is dependent on neutral density, so if neutral density increases due to a change in ambient conditions, the drag make-up current must increase as well.

The power required for drag make-up was compared against the power generated for ED tether thrust to assess the feasibility of drag make-up. Figures 11a–c compare the estimated power demand to the estimated power generated for propulsion for the three representative spacecraft sizes. At each altitude considered, there is a tether length that minimizes the required drag make-up power. Very short ED tethers require relatively large current to overcome the atmospheric drag force on the ultra-small satellites. On the other hand, tether rigidity decreases with length, so a very long tether may have a larger radius to prevent severe bending or bowing. The current is minimized when these two effects are balanced.

It should be made clear that this assumes that the gravity gradient tension force is relatively small. In the case of significant gravity gradient tension, it is possible to use a much thinner tether, producing a linear increase in atmospheric drag with length. The increase in drag due to a thinner tether would be less significant, and in this case it is feasible that the required drag make-up power would be even less than estimated here.

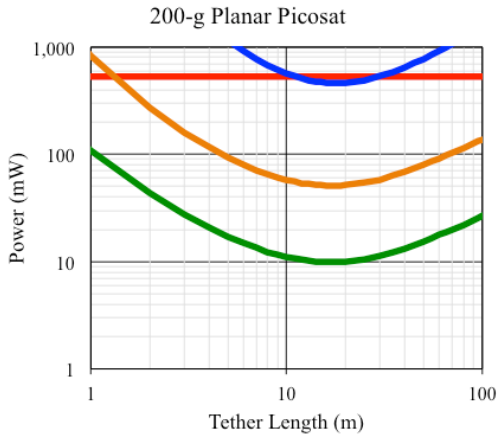

(a)

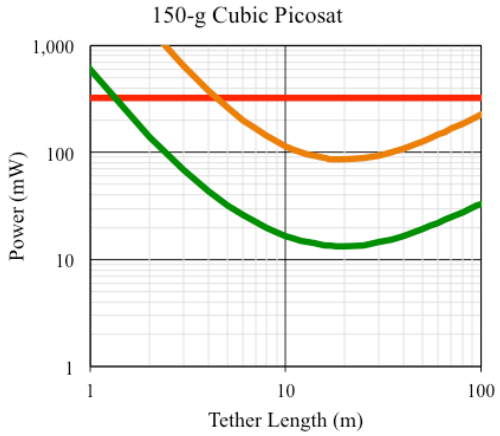

(b)

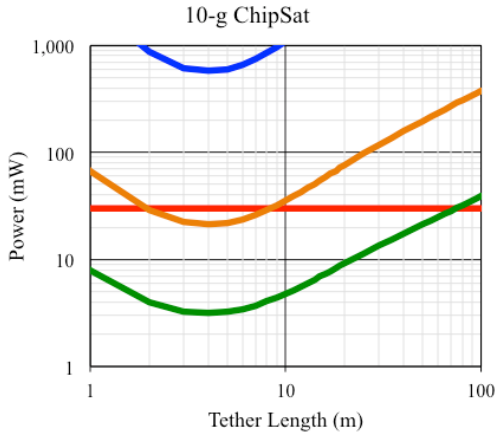

(c)

Figure 3.11: Estimated power needed for drag make-up at 400 km (blue), 500 km (orange), and 600 km (greem), and power available for propulsion (red).

When the spacecraft generate more power for propulsion than is needed for drag make-up, boosting may be possible. All of the spacecraft show potential to generate sufficient power for drag make-up at 500 km and 600 km altitudes, but the 200-g planar picosat is the only spacecraft in this study capable of generating power for drag make-up at 400 km.

It should also be made clear that these results do not necessarily suggest that a larger spacecraft size will be more or less capable of overcoming atmospheric drag. The dominant factors considered here are the ballistic coefficient and the surface area for electrical power generation. In the minimum cross-sectional drag area orientation, the 200-g planar picosat and the 10-g planar ChipSats have the lowest drag profiles. It was assumed here that the 200-g planar picosat, however, has more surface area devoted to electrical power generation. This combination of large surface area for propulsion power generation and a low drag profile are the reasons the 200-g planar picosat is able to generate a drag make-up force as low as 400 km. This conclusion is based on the electrical power generation estimates developed in the previous section, the assumptions for various impedances in the tether circuit, and the drag assumptions, including the assumption that the tether radius should increase with tether length to ensure the tether behaves as a "semi-rigid" structure on orbit. If a spacecraft is able to generate more power for propulsion than estimated, if the impedances in the tether circuit are less than estimated, or a thinner radius tether can be used, each of the spacecraft are more capable of generating a drag make-up force than is estimated here.

3.5.3 Using the Tether for Power Generation

An electrodynamic tether can also generate power for small spacecraft. Bilén *et al.* (2010) explores the potential for a 10 × 10 × 30 cm nanosatellite, or “3U CubeSat”, with a starting altitude of 500 km (circular) and a 28° inclination [137]. Simulations done by Bilén *et al.* (2010) showed that a 1300 m aluminum tether stored in a single 10 × 10 × 10 cm unit (or “1 U”) of the nanosatellite is capable of producing around 44 W peak power and 42 W average power over a 10 minute period.

At the spacecraft and tether scale considered here, however, the tethers are much shorter and the motional emf is much smaller. The motional emf is also only ~1 V for a

tether that is a few meters long. Power generation is also significantly limited by the ability of plasma contactors to facilitate current flow between the spacecraft and the surrounding plasma environment. Relatively small satellites are further limited by mass and volume constraints. Therefore, effective power generation for picosats and femtosats requires advances in plasma contactor technology that produces compact and efficient contactors.

3.6 Miniaturized Electrodynamic Tether Forces

3.6.1 Thrust Compared to Other Forces

The atmospheric drag force and the gravity-gradient force are the dominant forces that impact the dynamics of spacecraft in LEO with longest dimensions on the order of a few meters [21]. In the context of this study, the longest dimensions considered here correspond to the length of the tether, which is estimated to be a few meters long, suggesting that atmospheric drag and gravity-gradient forces will be the dominant forces on the tethered spacecraft. Figures 3.12a–c show the thrust, atmospheric drag, and gravity-gradient force estimates for each spacecraft. The solar radiation pressure force at these altitudes is below other forces by roughly an order of magnitude, so it is not shown. In previous studies, it was determined that the solar pressure radiation force is on the order of 10^{-9} N for a femtosat similarly sized to the 10-g ChipSat and 10^{-8} N for picosats similarly sized to the 200-g planar picosat and the 150-g cubic picosat [138]. All three spacecraft show potential to generate a drag make-up force at 500 km and 600 km altitudes. Only the 200-g planar satellite appears able to produce thrust of the same order as drag at 400 km. Tether lengths were selected for each spacecraft to maximize the thrust-to-drag ratio. This motivated the choice of an 11-m long tether for the 200-g planar picosat, a 12-m tether for 150-g cubic picosat, and a 4-m tether for 10-g ChipSat. The tether lengths, radii, and currents are shown in Table 3.5. If drag make-up does not appear feasible because of the satellite's power generation limitations, the maximum available thrust power and the corresponding maximum achievable current and thrust are listed in italics in Table 3.5.

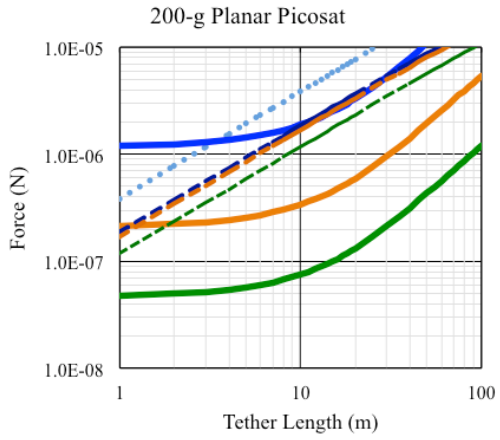

(a)

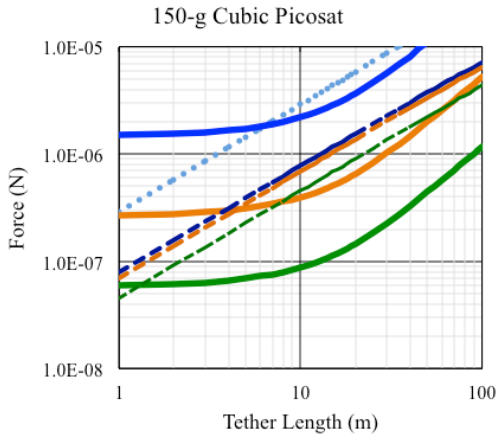

(b)

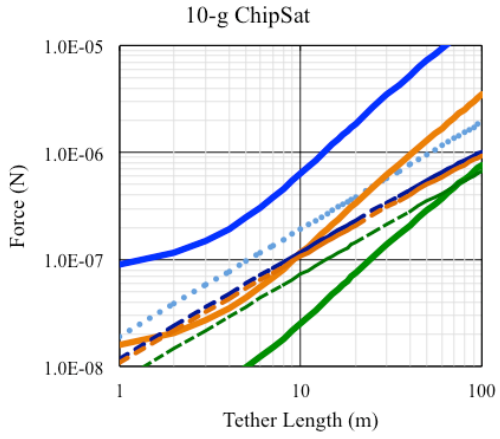

(c)

Figure 3.12: Estimated thrust force (dashed lines) and drag force (solid lines) at 400 km (blue), 500 km (orange), and 600 km (green) altitudes. The gravity-gradient forces is shown as light blue dotted lines.

The gravity-gradient force is included because a strong gravity-gradient force suggests a restoring torque that may provide attitude stability. The gravity-gradient force decreases with increasing altitude, but the variation from 400 km to 600 km is very small so only one gravity-gradient curve is shown for each spacecraft. The larger spacecraft (150 g and 250 g) generate a gravity-gradient force exceeding other forces at 400 km, 500 km, and 600 km. This suggests that the gravity-gradient force may help ensure a degree of stability for these spacecraft. For the 10-g ChipSat, the gravity-gradient force only appears to be dominant at 500 km and 600 km. It should be noted that there are other potential effects that have been investigated for longer tethers, including instabilities pumped by the variation of thrusting around the orbit, and these should be investigated at the smaller scale as well [139]. The dynamics of deployment are also important, but they lie beyond the scope of this dissertation. In fact, as understand of the deployment process evolves, they may be additional requirements imposed on the tensile strength of the tether material.

Table 3.5: System Concept Summary.

Parameter		200-g planar picosat	150-g cubic picosat	10-g ChipSat
Tether length		11 m	12 m	4 m
Tether radius		130 µm	140 µm	51 µm
Tether mass		4.1 g	5.3 g	190 mg
Available propulsion power		530 mW	320 mW	30 mW
Estimated Peak Tether Current	400 km	6.2 mA	*2.6 mA*	*395 µA*
	500 km	5.6 mA	2.3 mA	360 µA
	600 km	3.9 mA	1.5 mA	243 µA
Estimated Peak Thrust Force	400 km	2.0 µN	*0.9 µN*	*47 nN*
	500 km	1.9 µN	0.8 µN	43 nN
	600 km	1.3 µN	0.5 µN	29 nN
Gravity-gradient force		4.2 µN	3.5 µN	77 nN

It will be important to study the relative strength of the drag and gravity gradient torques in order to understand the resulting tether attitude. If the center of mass and the center of pressure are vertically displaced, the aerodynamic drag torque will rotate the

system. If the gravity-gradient torque is strong enough, however, it will counteract this rotation and restore the tether to an equilibrium along the local vertical. It may be possible for the 10-g ChipSat to use multiple tethers on several axes if attitude stability is not feasible [140], [141].

3.6.2 Thrust Efficiency

The instantaneous power expended generating EDT thrust is

$$P_{\text{Thrust}} = \boldsymbol{F}_{\mathbf{thrust}} \cdot \boldsymbol{V}_{\mathbf{sc}}, \quad \text{(Eq. 3.27)}$$

or, expanding the expression for the Lorentz force, is

$$P_{\text{Thrust}} = (I_{\text{tether}}\mathbf{L} \times \mathbf{B}) \cdot \boldsymbol{V}_{\mathbf{sc}}. \quad \text{(Eq. 3.28)}$$

The magnitude of the EDT thrust power can also be expressed in terms of the electromotive force as [142]

$$|P_{\text{Thrust}}| = V_{\text{emf}} I_{\text{tether}}, \quad \text{(Eq. 3.29)}$$

For an EDT operating in de-boost mode in LEO, the electromotive force helps drive current in the tether, converting orbital energy into electrical energy. In boost mode, however, the EDT system has to use external energy, i.e., the solar energy converted to electrical energy and current flow, to increase the orbital energy of the satellite over time. For either deboost or boost mode, the overall EDT power losses include power used to collect and emit current in the ionosphere and power dissipated in ohmic loss in the tether.

The EDT thrust efficiency was calculated for an equatorial orbit by taking the ratio of the thrust power and the total dissipated power, or P_{total}. Recall, the study has assumed an equatorial orbit to maximize peak in-plane thrust. The thrust efficiency can be expressed as

$$\text{Thrust Efficiency} = \frac{P_{\text{thrust}}}{P_{\text{total}}}, \quad \text{(Eq. 3.30)}$$

Figures 3.13a−c show the thrust power efficiency for a tether in boost mode, assuming the EDT system uses the total available propulsion power for maximum thrust at the equator. The thrust efficiency increases with the tether length because the electromotive force increases with length.

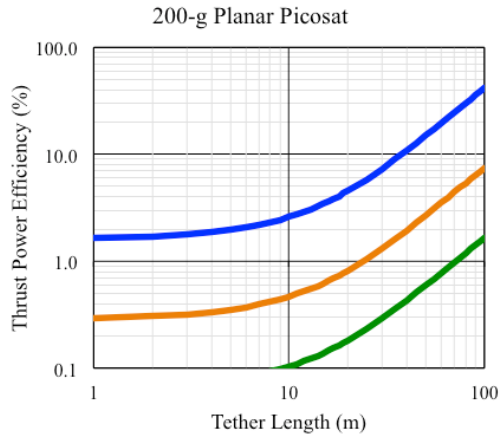

(a)

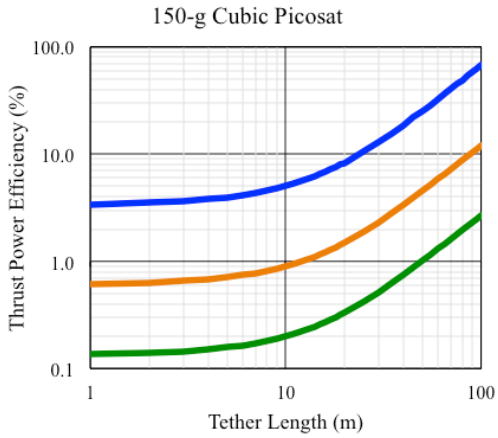

(b)

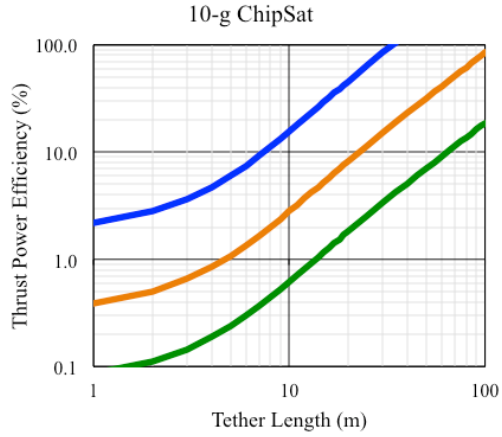

(c)

Figure 3.13: Percentage of available power used for thrust at 400 km (blue), 500 km (orange), and 600 km (green) altitudes, assuming the total power available is used to achieve maximum thrust.

For tether lengths below 100 meters, a majority of the available power is dissipated in collecting current from the ionosphere and only a small percentage increases the energy of the orbit over time. The thrust efficiency is higher at 400 km than 600 km because the electron density is higher at 400 km, producing higher tether currents for the same propulsion power. The EDT system described here might be considered inefficient. However, the solar power available can provides what is needed and the EDT is propellantless, so it is believed that the EDT can still provide a viable approach for propulsion.

Also, although thrust efficiency is calculated here for an equatorial orbit, it should be noted that as the inclination approaches a 90° or polar inclination, there are periods during the orbit that the thrust force is directed out of plane. In that case, in-plane and out-of-plane thrust efficiency should be calculated separately. Here, it was assumed thrust is directed entirely in plane, primarily producing force for drag make-up, boosting, de-boosting and not inclination change.

The low efficiency reported here is in contrast to larger, more traditional EDT systems, which utilize much longer tethers and larger end-bodies. Larger end-bodies have more current collection area and can also make use of hollow cathodes for more efficient current collection, so a smaller fraction of the total power is dissipated to collect the required current. Longer tethers generate a higher electromotive force. By utilizing longer tethers and larger end-bodies, the larger EDT systems are generally more efficient. The efficiencies of each miniaturized tether scaled appropriately for picosat and femtosat propulsion is summarized in Table 3.6. It can be seen that the efficiencies are less than 10% for each of the miniaturized Efficiencies around 80% have been calculated for tether that are 10s of kilometers long [142].

Further, the study presented here has attempted to be conservative. The anode model in particular was accompanied by a variety of conservative assumptions for current collection. It may also be necessary to revise the anode collection model. The collection theory does not calculate the exact current collected by the anode, so it may be necessary to analyze and experimentally verify assumptions made to see if the current collection estimates here are too conservative. An anode that requires less voltage to collect the same current would be more efficient and could consequently raise the efficiency of the

propulsion system. Laboratory experiments are presented in the following chapter that aim to understand and characterize the anode electron collection model.

Table 3.6: Efficiency of the miniaturized EDTs considered in this study for picosat and femtosat propulsion. The efficiency is calculated for equatorial orbit at 400 km, 500 km and 600 km altitude.

Altitude	200-g planar picosats with 11-m tether	150-g cubic picosat with 12-m tether	10-g ChipSat with 4-m tether
400 km altitude	2.7%	5.6%	4.7%
500 km altitude	0.5%	1%	0.8%
600 km altitude	0.1%	0.2%	0.2%

3.7 Miniaturized Electrodynamic Tether Orbital Maneuvering Simulations

The TEthered Mission Planning and Evaluation Software Tool (TeMPEST) allows the EDT system to be simulated in orbit. TeMPEST incorporates geomagnetic field models, ionospheric and atmospheric conditions, plasma contactor modeling, and precise orbital calculations to predict propulsion performance [137]. The version of TeMPEST used here to simulate tether propulsion modeled the neutral density environment using Mass-Spectrometer-Incoherent-Scatter (MSIS-E-90) model, modeled the plasma parameters using the International Reference Ionosphere-2007 (IRI-2007) model, and modeled the magnetic field environment using the International Geomagnetic Reference Field (IGRF 11) [102], [105], [107].

The simulations were initiated on January 1, 2000, which was during solar maximum, so the heightened neutral-to-electron-density ratio presented a worst-case scenario for thrusting. The simulations were also performed in 0° inclination orbits that were initially circular. The TeMPEST simulations did not incorporate tether librations, so the tether was assumed to be straight and vertically oriented throughout the orbit. Although these affects are not studied in this dissertation, it is important to incorporate attitude dynamics in future tether system simulations because the dynamics affects the $I_{\text{tether}}\mathbf{L}\times\mathbf{B}$ force that is produced.

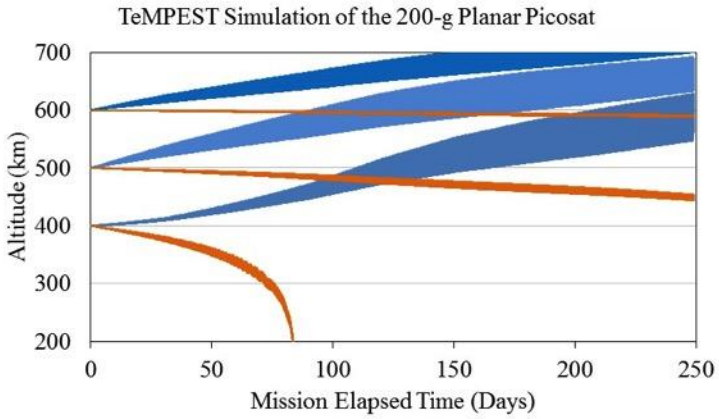

(a)

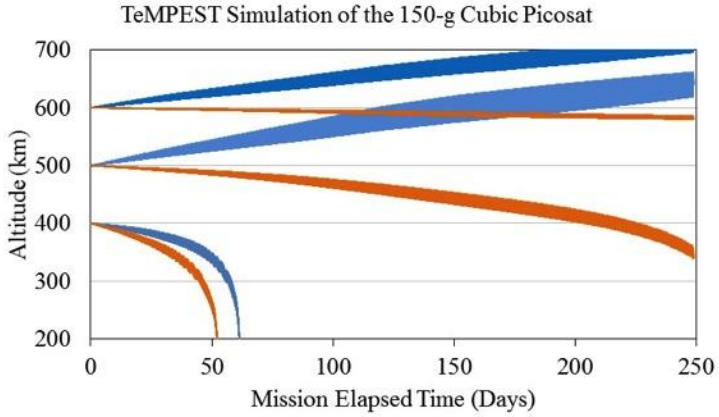

(b)

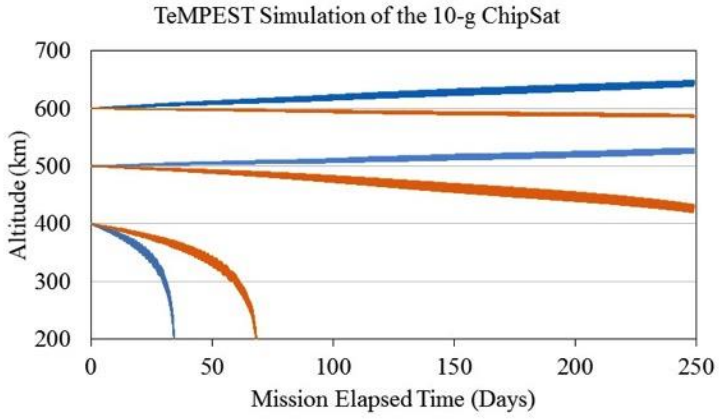

(c)

Figure 3.14: Simulation of altitude change for a single spacecraft (orange) starting at 400 km, 500 km, and 600 km compared with dual tethered spacecraft with an EDT providing a boosting force (blue). The simulation was performed using TeMPEST and the propulsion power values listed in Table 3.5

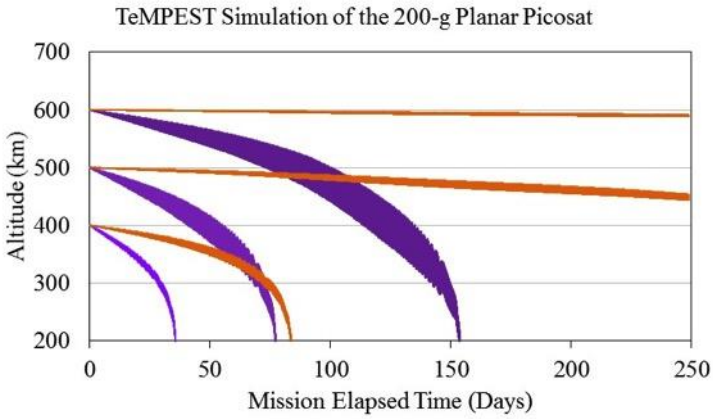

(a)

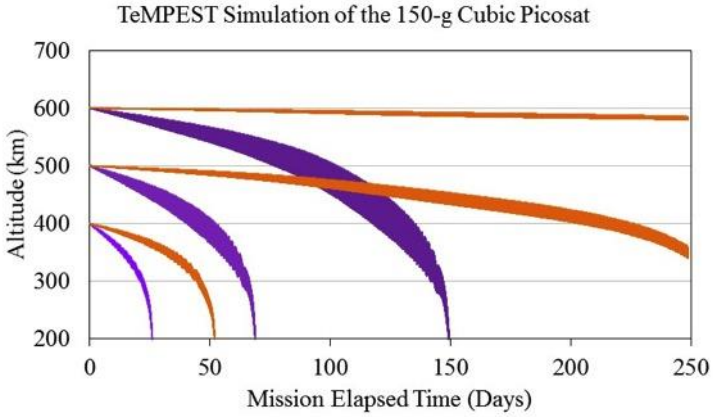

(b)

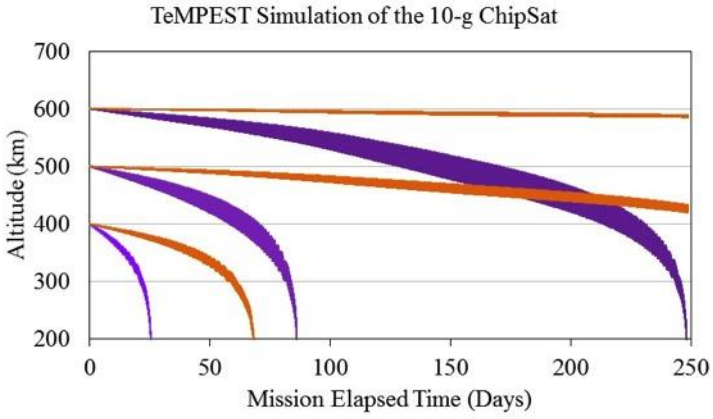

(c)

Figure 3.15: Simulation of a single spacecraft (orange) starting at 400 km, 500 km, 600 km compared with dual spacecraft with an EDT providing a de-boosting force (purple). The simulation was performed using TeMPEST and the propulsion power values listed in Table 3.5

TeMPEST was used to generate Figures 3.14a–c and 3.15a–c. The tether dimensions were the same as those provided in Table 3.5. Figure 3.14a–c shows the change in altitude in orange for individual spacecraft without propulsion at 400-km, 500-km, and 600-km starting altitudes. In the same set of figures, the change in altitude is shown in blue for an EDT providing an orbit-raising propulsion force to a tethered pair of spacecraft. Figures 3.15a–c shows the change in altitude for an EDT providing a de-boosting force.

Rapid drag de-boost can be seen without an ED tether at 400-km and 500-km starting altitudes. The atmosphere is much more tenuous at 600 km, so orbital decay occurs much more slowly. Drag make-up and boost capability at 500 km and 600 km is shown for all of the picosats and femtosats using a low-power, miniaturized EDT. The 200-g planar picosat also shows potential to boost at 400 km. Separately, in the following figure, Figure 3.15a–c, the change in altitude for tethered spacecraft using a miniaturized EDT to provide a *de-boosting force* is shown. A miniaturized EDT providing a de-boosting force shortened the orbital lifetime to less than one year. The lifetimes are only about one to two months long at lower starting altitudes.

Capability to boost and de-boost could significantly enhance maneuverability. For example, a miniaturized EDT could potentially raise the altitude of a spacecraft, maintain the higher altitude, and de-orbit the spacecraft at the end of the mission or, alternatively, maintain a lower altitude to accomplish a different set of mission objectives.

Although the altitude curves in Figures 3.14a–c and Figure 3.15a–c appear to widen, this only represents increasing eccentricity of the satellite over time. The effect is particularly pronounced for EDTs that are continuously boosting (which was the case here). The thrust force increases in regions of the ionosphere where the electron density is higher, and the uneven thrust in each orbit results in an increasing orbital eccentricity. However, EDT boosting can be planned so the satellite orbit eccentricity degradation is minimized [55].

3.8 Miniaturized Tether as an Antenna

Picosat and femtosats have inherently small antenna apertures and low transmission power, but a conducting coating (e.g., gold, copper, silver, etc.) of adequate

thickness compared to the skin depth on the semi-rigid tether core would provide the potential for a high performing, long, directional "traveling wave" antenna. The conducting layer would only need to be a few skin depths in thickness (on the order of micrometers, depending on frequency) to radiate the electromagnetic signal with low resistive loss.

The radiation pattern of the ultra-small satellite ED tether was modeled at 430 MHz using ANSYS® HFSS™ simulation software as shown in Figure 3.16 [66]. The antenna can be modeled as a long traveling wave antenna. For a picosat or femtosat that has a small body dimension relative to wavelength, it was necessary to attach a small quarter wave grounded stub to the spacecraft with the transmitter. It was also found that at the CubeSat scale, a 1U conducting satellite frame (10 cm × 10 cm × 10 cm) could be used in lieu of the additional short stub as it is approximately at a resonant quarter wavelength. The *z*-axis in Fig. 13.15 points in the nadir direction.

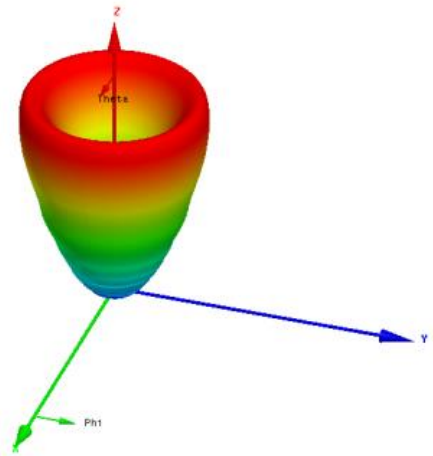

Figure 3.16: The 3D radiation pattern for a 10-meter-long tether radiating at 430 MHz [66].

CHAPTER 4

Experimental Validation of the Electron Current Collection Model

This chapter presents measurements and analysis of electron current collection in a laboratory plasma environment that captures key characteristics of the low Earth orbit (LEO)-tether system interaction. The laboratory plasma is characterized and compared to LEO and current−voltage ($I-V$) characteristics of planar and cubic probes approximating small spacecraft in LEO are presented. The following chapter presents a set of revised electron current collection models based on the experimental measurements presented here.

4.1 Review of Simplifying Assumptions Made to Facilitate Estimating Current Collection

In the analysis presented in the previous chapter, electrodynamic tether thrust estimates were based on a set of simplifying assumptions made to facilitate estimating tether current. Those assumptions are briefly reviewed here.

In our system concept, electrons were collected by the positively biased exposed conducting surfaces of a picosat or femtosat. It was assumed that the entire surface was conducting and that insulating surfaces would be coated with an appropriate conductor. Solar cells, for example could be coated in indium tin oxide (ITO) to increase overall current collection area [134], [143], [144].

It was also assumed that the spacecraft's conducting surfaces would be biased well above the plasma potential to attract the electron current needed for propulsion. Thus, the focus of this chapter and the following chapter is the electron collection current

above the plasma potential or the electron saturation current (described in Chapter 2, section 2.3.2.4).

At a large voltage relative to the plasma potential, it was assumed that the non-neutral sheath region between the immersed object's surface and the ambient plasma would expand outwards, increasing the effective collection area, concealing the fine details of the anode's geometry, and allowing us to approximate the spacecraft as spherical in shape. Estimates for the sheath size are provided in Chapter 3 (Figure 3.9, section 3.4.4), but in general the sheath was estimated to extend well beyond the collector's surface in LEO. Current collection was then estimated by assuming that the anode collects current like a sphere with an equivalent diameter equal to the satellite's longest edge.

After assuming the collector could be approximated as a sphere, an expression was utilized that was developed to interpret current collection and plasma parameters from the wide sweeping Langmuir probe instrument (WLP) on the International Space Station (ISS). The WLP is a 5-cm-radius sphere in the LEO ionospheric environment that is roughly the size of the spacecraft considered in this study. The expression [145]

$$I_{\text{anode}} = \frac{I_{\text{thermal}}}{2}\left(1 + \frac{q(V_{\text{anode}} - \Phi_p)}{kT_e}\right)^{\beta} \quad \text{(Eq. 4.1)}$$

was fit to the electron saturation region of the Langmuir probe *I*–*V* sweeps of the WLP instrument. The term Φ_p is the plasma potential and V_{anode}–Φ_p is the sheath potential. The electron thermal current,

$$I_{\text{thermal}} = A_{\text{probe}} n_e q \sqrt{\frac{kT_e}{2\pi m_e}}, \quad \text{(Eq. 4.2)}$$

is the random thermal current collected at the edge of the sheath and A_{probe} is the surface area of the spherical WLP instrument (i.e., $4\pi r_p$). The parameter β was observed to vary between 0.5 and 1, which is shown in Figure 9 of Barjatya et al. (2009) [145]. An explanation for the variation in β was not provided. For our model, we chose $\beta = 0.65$ because this was the apparent value of β when the measured electron density was in the range of electron densities considered in this study.

It should also be noted that Equation 4.1 has a coefficient of ½, written as $\frac{1}{2}I_{thermal}$. It was mentioned in Barjatya et al. (2009) that the *surface area* term, A_{probe}, was multiplied by ½ to ensure that the estimates for electron and ion density agreed when interpreting the WLP *I–V* sweeps [145]. Indeed, after the ½ coefficient was included, the electron and ion density measurements were in agreement by ±10% percent and agreed closely with measurements from other instruments on board the ISS [145]. However, a complete explanation for the ½ coefficient was not provided [146]. Interestingly, in the Parker-Murphy model for large spherical electrodes, the area is also multiplied by a ½ term [83], although in that context it represents the cross-sectional area normal to the magnetic field lines, or $2\pi r_p^2$.

In the following sections, we describe a set of ground-based laboratory experiments in which key characteristics of the orbital environment were simulated in order to refine previous current estimates. The *I–V* characteristics obtained in the experiments described in this chapter are compared to *I–V* characteristics calculated using Equation 4.1 with $\beta = 0.65$. This expression is referred to here as the WLP model.

4.2 Experimental Investigation of Electron Collection to Picosatellite- and Femtosatellite-shaped Probes in a Flowing Plasma

In order to evaluate electron current collection, ground-based plasma experiments were conducted to capture key characteristics of the satellite-LEO interaction. Three test campaigns were performed to investigate current collection in a flowing plasma and observe changes in collection due to (a) probe orientation relative to plasma flow and (b) magnetic field strength. The first experiment was the baseline experiment designed to study current collection in a flowing plasma. In the second experiment, the probes were re-oriented relative to the plasma flow to observe the impact of changing the cross-sectional area facing into the flow. In the third experiment, the impact of scaling the magnetic field to simulate the LEO environment was assessed. These experiments are referred to throughout the chapter as Test Campaign 1, Test Campaign 2, and Test Campaign 3.

This section begins by describing the parameters that the experiments aimed to capture. This is followed by a description of the experimental setup. The section closes with a description of the plasma environment and a presentation of the *I*−*V* characteristics.

4.2.1 Identifying Key Elements of the LEO Plasma Environment

The objective of these experimental tests was to evaluate current collection in an environment that captured key characteristics of the LEO environment. In this section, these characteristics are described. For the sake of the reader, relevant information, assumptions, and quantitative relationships dispersed in Chapters 2 and 3 are consolidated and summarized again here.

4.2.1.1 Collector Shape and Appropriately Scaled Size

One consideration for these tests was to properly scale the size of the experimental collecting probes relative to the Debye length since ground experiments would need to be different, for practical reasons, than the Earth's ionosphere. The ratio of the probe size, denoted by the equivalent probe radius, r_p, to the Debye length plays an important role in current collection behavior. In a collisionless, non-drifiting, unmagnetized plasma where $r_p/\lambda_D \leq 1$, orbital-motion-limited (OML) theory can be used to predict the collection current to simple electrode geometries (spheres, infinite cylinders, and infinite plates) [147]. (Although OML theory can be used for infinite plates, the parameter r_p/λ_D in their case is either infinite or not defined.) If $V_{\text{anode}} > V_p$ (e.g., collection in the electron saturation regime), the current is given by [81]

$$I_{\text{OML}} = I_{\text{thermal}} \left(1 + \frac{q(V_{\text{anode}} - V_p)}{kT_e}\right)^{\beta}, \qquad \text{(Eq. 4.3)}$$

where $\beta = 1$ for a sphere, $\beta = 0.5$ for an infinite cylinder, and $\beta = 0$ for an infinite plate. The increase in current with applied voltage represents an increase in the sheath size. If $r_p/\lambda_D >> 1$, the sheath is extremely thin and the resulting collection current is simply the thermal current incident at the satellite's surface, corresponding to $\beta = 0$ in Equation 4.2

[82]. Thus, the ratio r_p/λ_D is an important factor for current collection. One goal of the experiment is to produce a ratio of r_p/λ_D in the laboratory environment that lies within a range of r_p/λ_D expected for our application in the LEO environment.

In the orbital environment considered earlier in this study (i.e., 400-km, 500-km, and 600-km altitude orbits at low latitudes), λ_D can range from a few millimeters to roughly a centimeter [148]. The plasma parameters assumed in the orbital environment for this study are provided in Table 3.2. The equivalent radii of the current-collecting spacecraft are about the same size as the Debye length, on the order of a few centimeters. As a result, $r_p/\lambda_D \approx 1{-}10$ in LEO. This suggests that current collection considered here takes place in a regime that lies between the thin ($r_p/\lambda_D >> 1$) and thick ($r_p/\lambda_D \leq 1$) sheath regimes. The parameter r_p/λ_D is calculated in the ionospheric and laboratory environments later in this section and presented in Table 4.4.

While a spherical collector model was assumed for early system analysis, this assumption needs to be validated or refined based on expected collector geometry. Many previously proposed picosat and femtosat designs were "box-shaped" because components were mounted on printed circuit boards (PCBs) and/or semiconductor wafers, giving the spacecraft body a planar/rectangular shape [2], [20], [22], [23]. Section 2.3.2.4 of Chapter 2 presented the Parker–Murphy and TSS-1R modified Parker–Murphy models as expressions that can be used to estimate electron current collection in LEO. However, the Parker–Murphy and TSS-1R modified Parker–Murphy models are only defined for large conducting spheres [57]. Similarly, OML theory (Equation 4.3) is only defined for spheres, infinitely long cylinders, and infinite plates [149]. Laboratory experiments have been conducted to better understand the current collection behavior of picosat-shaped and spherical electrodes in a flowing plasma, but the electrode sizes relative to the Debye length were large compared to the electrodes considered in this study [126]. Thus, in the experiments presented here, the objective was to represent the non-standard geometry of the collecting bodies and the size of the collector with respect to the Debye length. This also motivated the use of "box-shaped" probes in the laboratory experiments.

4.2.1.2 Magnetic Field Effects

The impact of the Earth's magnetic field was also considered and appropriate scaling to provide a probe radius-to-electron gyroradius ratio, or r_p/r_L, that would be representative of LEO was assessed. The electron gyroradius-to-probe radius ratio is an important parameter for evaluating the effect of the magnetic field on current collection [149]. In response to the Lorentz force ($\mathbf{F}_L = q\mathbf{v}\times\mathbf{B}$), charged particles travel around magnetic field lines with a gyroradius $r_L = mv_\perp/qB$, where $v_\perp$ is the component of electron velocity perpendicular to field lines. Magnetic field effects are often neglected when r_L is very large relative to the probe radius but are considered an important factor affecting current collection when r_L is small relative to the probe radius [149]. In general, strong magnetic fields ($r_p/r_L >> 1$) have been observed to reduce electron collection current [150]. In LEO, the electron gyroradius is on the order of a few centimeters [62], which is roughly the same scale as the picosats and femtosats considered in this study, so our goal was to generate a magnetic field where $r_p/r_L \sim 1$ and investigate the impact on electron collection. Thermal ion gyroradii are on the order of 1−10 m in LEO while the thermal electron gyroradii are on the order of 1−10 cm [148]. The ion gyroradii in LEO are many times larger than the picosats and femtosats [62], so we assume ions are not magnetized.

The ratio of the electron gyrofrequency to the collision frequency can also be used to assess the effect of magnetic field on current collection. Electrons in the presence of a magnetic field gyrate around field lines, traveling on magnetic flux tubes, and are collected when intersecting flux tubes reach the probe [151]. According to classical theory, collisions provide a mechanism for electron cross-field transport. Classical electron diffusion across magnetic field lines is [152]

$$D_{e\perp} = \frac{D_{e\parallel}}{1+\left(\omega_{ce}/\nu_e\right)^2}, \qquad \text{(Eq. 4.4)}$$

where $D_{e\parallel}$ is the diffusion coefficient parallel to magnetic field lines, ω_{ce} is the electron gyrofrequency $\omega_{ce}=qB/m_e$, and ν_e is the electron collision frequency. However, as will be seen later in the chapter, the parameter ω_{ce}/ν_e could not be scaled fully to represent the LEO environment. The effect of this is assessed later in the chapter.

4.2.1.3 Plasma Flow

It was also important in the experimental tests to generate high-speed plasma flow to approximately account for the effects of plasma flow on electron current collection in LEO. An orbiting spacecraft in LEO travels through the ionospheric plasma at about 7.5 km s^{-1}, which exceeds the ion thermal velocity but is less than the electron thermal velocity, or is "mesothermal" [153]. Mesothermal speed causes significant sheath asymmetry; a region of compression develops on the side of the spacecraft facing into the plasma flow and a rarefied wake region forms immediately behind the spacecraft [148]. The relative motion of a current collecting body with respect to the plasma can enhance electron current collection.

Enhancement in electron collection current was explored by Weber et al. (1979) for high-speed, unmagnetized plasmas [154]. It was suggested that when a planar probe perpendicular to a flowing plasma was biased above the plasma potential to the directed kinetic energy of the ions (i.e., the beam energy), ions were reflected. The reflected ions would form a positive space charge region in front of the positively biased probe, producing an expansion of the sheath around the probe, increasing the effective collection area, and enhancing the electron collection current [155], [156]. However, Weber et al. (1979) did not determine the magnitude of the electron collection enhancement [154]. It was also observed in Choinière et al. (2005) for conducting cylinders and tapes that high-speed plasma flow produced electron current collection enhancement above the directed energy of the ions [89].

Current collection enhancement has also been observed in mesothermal, magnetized plasmas. Recall that the Parker−Murphy model describes current collection in a collisionless, non-drifting, magnetized plasma (also, $r_p/r_L >> 1$). The electron collection current estimated by the Parker−Murphy model scales with the square root of the bias voltage. In the TSS-1 and TSS-1R missions the spherical electrodes were traveling at mesothermal speed and significant current enhancement beyond the Parker−Murphy model was observed. Electron saturation current 4−6 times the Parker−Murphy current was measured in the TSS-1 mission [157]. In the TSS-1R mission, electron saturation current 2−3 times the Parker−Murphy current was measured. The enhancement appeared when the anode was biased above the ram kinetic energy of

the O^+ ions and were accompanied by the onset of instabilities (e.g., turbulent electron scattering) that affected and enhanced current collection [86]–[88]. Interestingly, the electron saturation current in the TSS-1 and TSS-1R missions both scaled with the square root of voltage like the Parker−Murphy model, so electron saturation current could be approximated by the Parker−Murphy model expression multiplied by ~4−6 in the case of TSS-1 and ~2−3 in the case of TSS-1R.

Several theories have been developed to explain this behavior, but there is currently no agreement on the physical mechanism causing electron current enhancement in a mesothermal, magnetized plasma. Furthermore, although Weber et al. (1979) provided an explanation for electron current enhancement in high-speed plasma, there is currently no analytical model that allows for the magnitude of the enhancement to be calculated. Additional information on the various theories and models exploring this topic is provided in Laframboise (1997), Cooke and Katz (1998), and Singh and Leung (1998) [88], [158], [159].

4.2.2 Experimental Setup and Plasma Source Characteristics

4.2.2.1 Vacuum Chamber

The experiments were performed in the cathode test facility (CTF) at University of Michigan's Plasmadynamics and Electric Propulsion Laboratory (PEPL). The CTF is a cylindrical, aluminum tank that is approximately 60 cm in diameter and 2.4 m in axial length. A CVI Torr Master® Cryopump was used to reach a base pressure in the range of about 2.5 µTorr. The pump speed for xenon was approximately 1,500 l s^{-1} [160]. The pressure was measured about 1.4 m from the cryopump with a Varian 564 Bayard-Alpert type ionization gauge mounted on the top of the chamber and at the position inside the chamber where the probe measurements were taken. Figure 4.1 shows a schematic illustration of CTF with the test equipment.

4.2.2.2 Plasma Source

A lanthanum hexaboride (LaB_6) hollow cathode, assembled by ElectroDynamics Applications, Inc., was used to generate a laboratory plasma environment that would simulate the relative velocity between the ionospheric plasma and orbiting spacecraft. The hollow cathode is shown in Figure 4.2. Cathodes operated in conditions similar to those presented here have been observed to generate a high-speed flowing plasma [160], [161]. The cathode here was different, however, because the keeper electrode was connected to ground and the cathode tube was biased negative with respect to the keeper. The cathode was located at the chamber centerline about ~150 cm from the cryopump, with the plasma plume directed toward the cryopump. Measurements were taken 20 cm downstream from the cathode and 2 cm below the cathode axis.

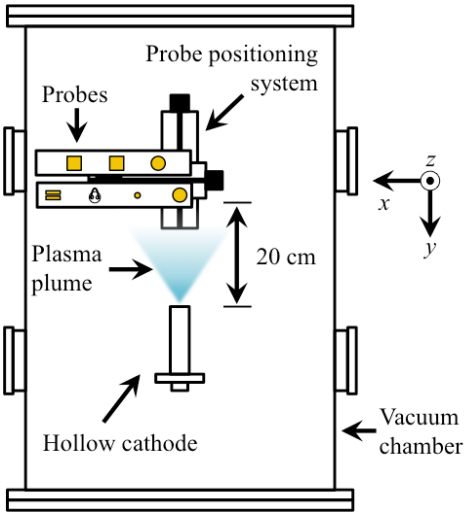

Figure 4.1: Setup of the vacuum chamber for current−voltage characterization experiments. The illustration provides a "top down" view of the setup in the vacuum chamber. The locations of the experimental probes, the hollow cathode plasma source, and the probe positioning system are shown. The probe positioning system moved the probes so all probe measurements were taken at the same location 20 cm downstream from the hollow cathode.

Xenon was used as the source gas for the hollow cathode because it is chemically inert and has a relatively low first ionization energy (~12.1 eV) [162]. The cathode was operated with a 3 standard cubic cm^3/min (sccm) flow rate to maintain a low chamber pressure, which was desirable to appropriately simulate the LEO environment (described in sections 4.2.3.2 and 4.2.3.3). It should be noted that O^+ is the dominant ion species in the altitude range considered in this study, so the ion species in the laboratory

experiments was much more massive than in LEO. This can cause additional sheath asymmetry as the elongated rarefied wake region elongates with ion mass [62]. The dominant impact is to reduce ion collection on the wake side of the probes [62]. Although there were attempts to run the experiment using xenon, argon, and krypton (argon and krypton are closer in mass to oxygen), only xenon provided the capability to generate a stable, quiescent plasma at flow rates below 5 sccm for the hollow cathode used here.

Figure 4.3 shows an illustration of the hollow cathode electrical schematic. Prior to initiating the plasma discharge, the LaB_6 insert was heated by applying ~200 W to the heater coil. Next, the cathode flow rate was increased to 10 sccm of xenon. To initiate the discharge, a −30-V bias was applied to the cathode tube with respect to the cathode assembly's graphite keeper. As mentioned earlier, the keeper was connected to the facility ground and the cathode was biased negative with respect to the keeper. After the keeper power supply detected current and a faint plasma plume glow was visible outside the cathode orifice, the keeper voltage was adjusted to raise the discharge current. The values for keeper current and voltage are Table 4.1. The cathode flow rate was then reduced to 3 sccm.

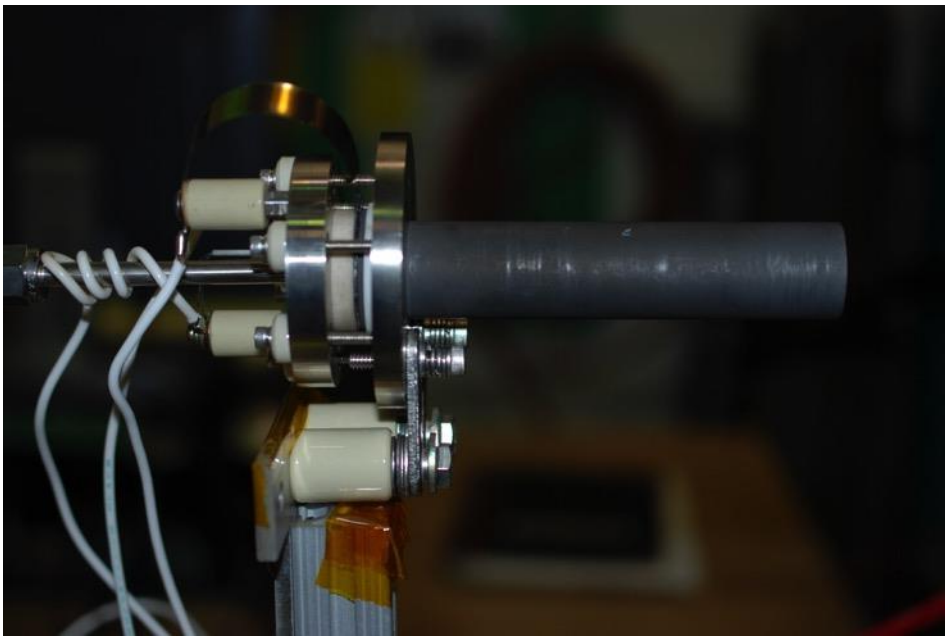

Figure 4.2: Hollow cathode assembly. The dark grey cylindrical graphite keeper shaft shown is about ~10 cm in length.

The hollow cathode that was used was originally sized for a minimum flow rate of 5 sccm [163]. In order to sustain the cathode discharge with lower flow rates, it was necessary to continuously supply power to the keeper and the heater. The operating conditions for each test are listed in Table 4.1. The cathode voltage (relative to the keeper) decreased slowly by about 2−3 V during each test campaign, changing at a rate of 0.3 V per hour, so only the average cathode-to-keeper voltage is provided in Table 4.1. There is some variation in operating conditions between test campaigns, particularly the keeper current. This may be attributed to aging or "wear and tear" of the cathode over time.

Table 4.1: Hollow cathode operating parameters for Test Campaign 1, 2, and 3.

Parameter	**Test Campaign 1**	**Test Campaign 2**	**Test Campaign 3**
Flowrate (sccm)	3	3	3
Pressure (Torr)	1.8×10^{-4}	1.9×10^{-4}	1.9×10^{-4}
Average Cathode-to- Keeper Voltage (V)	−30	−25	−24
Keeper Current (A)	1.8	2.8	2.5
Heater Current (A)	6	6	6

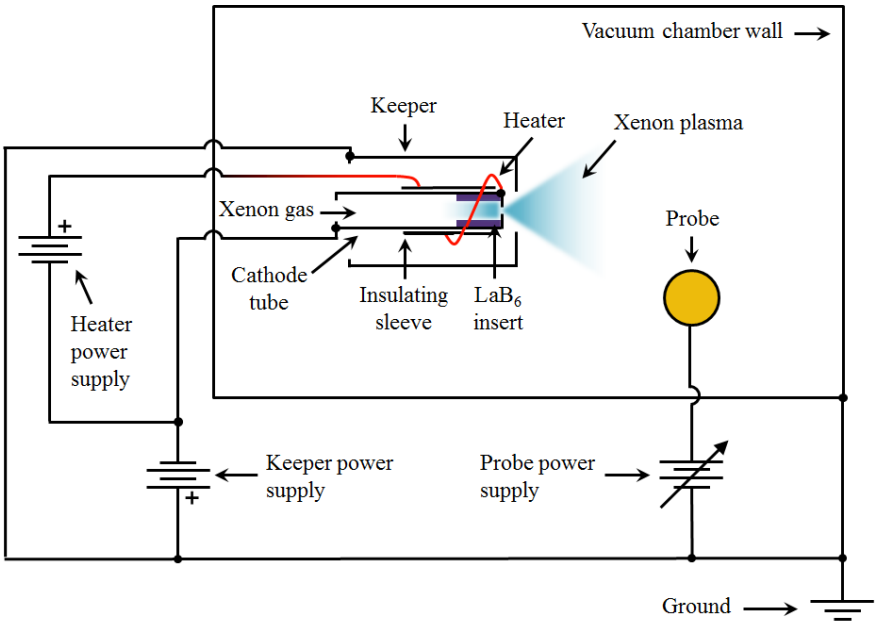

Figure 4.3: Hollow cathode assembly and probe electrical connections.

4.2.2.3 Plasma Diagnostic and Test Probes

Here, the probes used in the experiment are described as well as the apparatus used to hold and position them. Figure 4.4 shows the probes arranged for Test Campaign 1, Figure 4.6 shows the probes arranged for Test Campaign 2, and Figure 4.10 shows the probe arranged for Test Campaign 3. Figure 4.5 shows the probes setup in the vacuum chamber for Test Campaign 1, which is the same setup used in the other test campaigns. The heavy insulation used in the experiments is addressed later in this chapter.

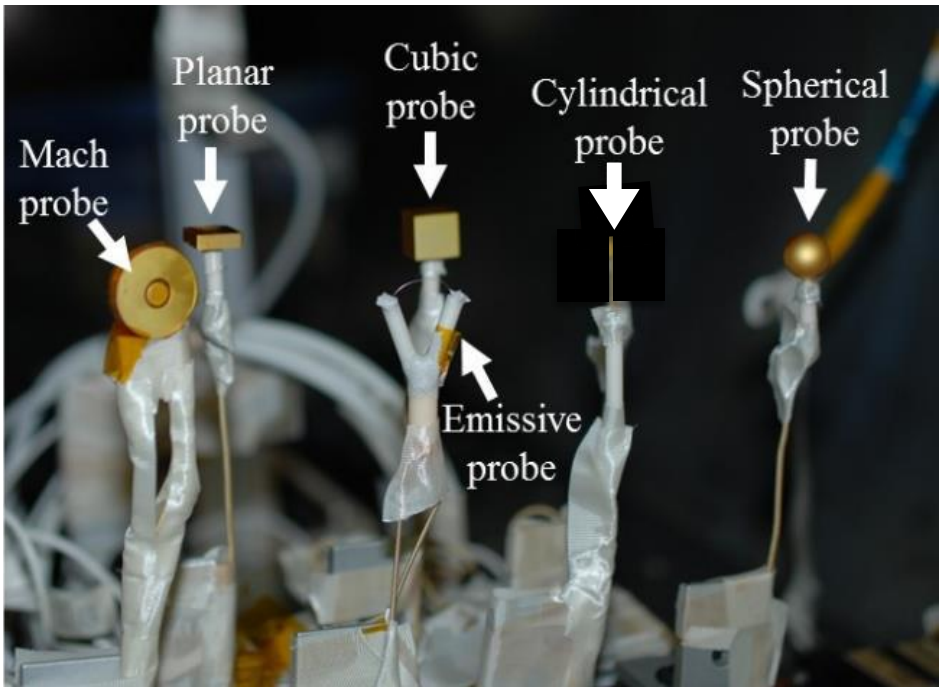

Figure 4.4: Picture of the probes mounted in the chamber. From left to right, the Mach probe, the planar probe, the emissive probe, the cubic probe, the cylindrical probe, and the spherical probe are shown.

The probes were positioned in two rows: four probes were located in the row closest to the cathode and three were located in the row farthest from the cathode. The probes in each row were separated by 5 cm, the rows were separated by 5 cm, and the probes in the row farthest from the cathode were positioned halfway between the probes in the front row so that no probe was behind another with respect to the cathode. The probes were mounted on a pair of linear motion stages, referred to in Figure 4.1 as the "probe positioning system." The motion stages allowed each probe's I−V characteristics

to be taken in the same position downstream from the hollow cathode. The *x*-axis motion stage moved the probes in each row directly downstream from the hollow cathode and the *y*-axis motion stage varied the distance between the probes and the cathode. In short, all measurements in all experimental tests were taken at the same location downstream from the hollow cathode.

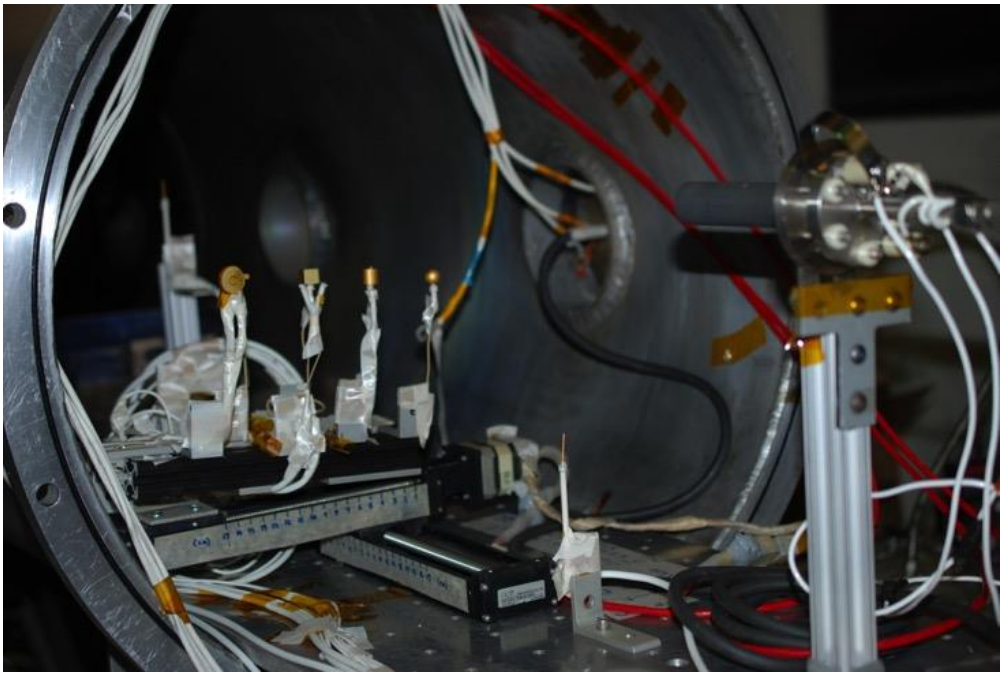

Figure 4.5: Picture of probes mounted on the linear motion stages and the hollow cathode. The setup shown here is from Test Campaign 1.

The probes used to make plasma diagnostic measurements included a 0.95-cm radius planar Mach probe, a 1.1-cm diameter spherical Langmuir probe, a 1-mm radius cylindrical Langmuir probe, and an emissive probe. In addition, a 1.1-cm ×1.1-cm × 0.3-cm planar probe and a 1.1-cm^3 cubic probe were included in the experiment to represent the 200-g planar picosat and the 150-g cubic picosat considered in this study. In Test Campaign 1 and 3, the planar probe was oriented edge-on with a cross sectional area of 1.1 cm × 0.3 cm facing the hollow cathode. In Test Campaign 2, the planar probe was re-oriented so the larger cross sectional area of 1.1 cm × 1.1 cm was facing the hollow cathode. A 1.1-cm diameter cylindrical probe can also be seen in Figure 4.4 behind the thinner and longer 1-mm-radius cylindrical Langmuir probe, but the 1.1-cm diameter

cylindrical probe was not representative of a femtosat or picosat considered here, so the *I–V* characteristics are not discussed.

In the modeling of current-collection performance mentioned in an earlier section, it was assumed that at potentials much larger than the plasma potential the cubic and planar satellites would both collect current like a sphere with an equivalent diameter equal to the satellite's longest edge. To assess this assumption experimentally, the diameter of the spherical probe was chosen to be equal to the edge length of the planar and cubic probes. The dimensions of the cubic and planar probes were also selected to be approximately representative of a current collecting cubic and planar picosat or femtosat in the ionosphere after scaling with respect to λ_D.

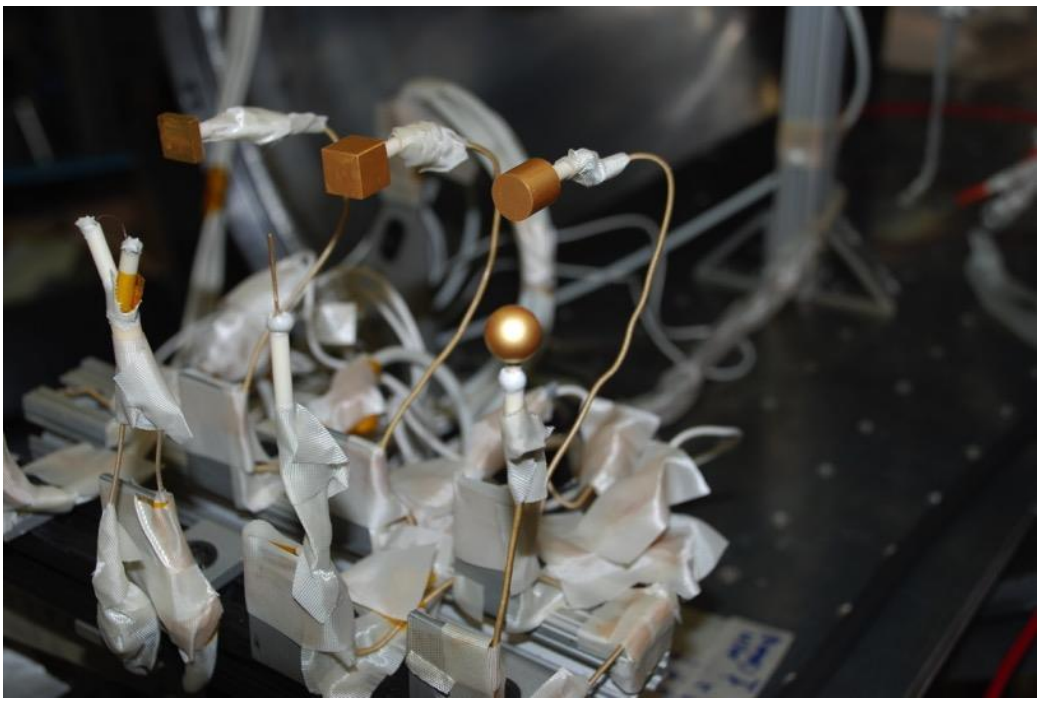

Figure 4.6: Picture of probes in Test Campaign 2 with orientation rotated with respect to plasma flow.

The Mach probe was used to provide a rough estimate of the ion drift velocity [150]. The probe was composed of two single-sided planar Langmuir probes mounted back-to-back, separated by Kapton tape. Each side had a 0.16-cm radius center collector and a ~6 mm-wide guard ring. The collector-to-guard spacing was ~1 mm. A bias was applied to the guard and the center collector, but only the current from the center collector was measured. The probe was oriented so one side was facing the hollow

cathode. *I–V* sweeps of each side were done separately and the non-collecting side was grounded as done in Oksuz and Hershkowitz (2004) [164].

The emissive probe was used to measure the plasma potential. The probe was a 127 μm (5 mil) diameter, 1.5-cm long throated tungsten filament. Emissive probe measurement can be disturbed by the sheath that forms around the filament supports [165], so a "Y" shape was used to ensure that the hottest segment of wire, generally assumed to be the center of the exposed filament, would be separated from the supports by many λ_D.

With an exception of the emissive probe, each of the probes were composed of type 316 stainless steel and plated in 5 μm of gold. The probes were coated in gold because gold is a good conductor, is inert, and exhibits low variations in work function or "work function patchiness." As described by Brace (1998), variations in work function can occur in certain polycrystalline conductors and can also be caused by surface contamination [166]. The "patchiness" means that some sections or "patches" of the probe have a different potential than other sections during an *I−V* sweep [167]. For example, section of the probe may be biased to the plasma potential while others may be biased to a potential in the electron retardation regime. Non-uniform probe surface potential can produce incorrect electron temperature measurements by "smearing" the electron retardation region of the *I–V* characteristic [166]. Gold generally exhibits low work function patchiness [168], so work function patchiness due to the probe's material is not considered a primary source of error in these laboratory experiments.

The impact of the heavy insulation (shown in Figure 4.4) on current collection is evaluated in section 4.2.3.4. In general, it is thought to have a small effect on the plasma parameter measurements and an even smaller effect on the electron saturation current. The largest amount of insulation is used near the Mach probe, which has a ~6 mm guard ring separating the center conductor from the insulation, so this probe is likely the least impacted by the insulation.

4.2.2.4 Current–Voltage Measurement System

The *I–V* sweeps for each of the probes were conducted by a Keithley 2400 SourceMeter. The SourceMeter was controlled via GPIB by a computer running a virtual

instrument under LabVIEW. The computer commanded the Keithley 2400 to perform a linear staircase *I–V* sweep from about –70 V to 50 V with a 0.1 V resolution. The maximum voltage in the *I–V* sweep was limited to about 50 V to prevent the probe current from affecting the hollow cathode. All probes were biased with respect to the vacuum chamber.

During each voltage step, current measurements were averaged by the SourceMeter over 13 milliseconds. This decreased reading noise and set the instrument's display resolution to 4 digits, which is on the order of 10^{-6} A when measuring maximum current of ~10^{-2} A [169]. To further reduce noise in the plasma diagnostic measurements, 3 or more *I–V* sweeps were averaged. *I–V* sweeps from the spherical and cylindrical Langmuir probes were also obtained before and after the planar, cubic, Mach, and emissive probes to determine the plasma parameters and observe changes in the plasma environment over time.

The emissive probe also had a power supply to heat the filament. The emissive probe filament current was provided by a set of D batteries and controlled by a pair of variable resistors. An illustration of the emissive probe schematic is shown in Figure 4.7.

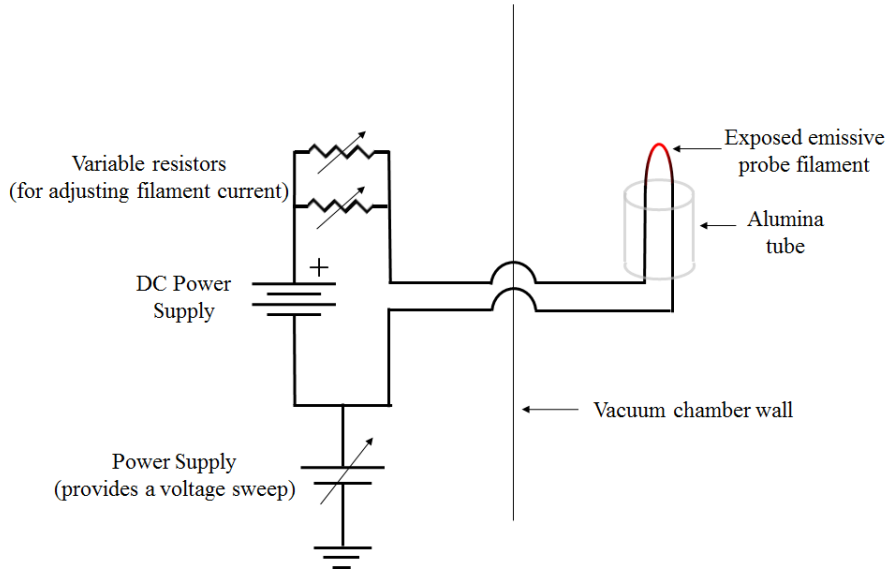

Figure 4.7: Simplified illustration of the emissive probe schematic.

Contamination on the surface of a probe can also impact the accuracy of Langmuir probe measurements by increasing the resistance of portions or the entire probe.

Contamination usually appears as hysteresis in linear up and down *I–V* sweeps [150], [166]. To detect this, up and down *I–V* sweeps were compared throughout the experiment, and, when hysteresis was visible, the probes were biased to 50 V or more to heat them with electron saturation current [170]. The procedure was repeated until hysteresis was no longer apparent, after which measurements were made. Hysteresis was generally not observed for some time following cleaning.

Possible sources of contamination include the adhesive from the fiberglass tape used to insulate the electrical lead wires of the diagnostic probes, residual gases in the vacuum chamber, and adsorbed xenon ions. The sources of contamination were not studied for this dissertation, but Wehner and Medicus (1952), Winkler et al. (2000), and Stamate and Ohe (2002) provide additional information on contamination sources and the impact on plasma measurements [167], [171], [172].

4.2.2.5 Helmholtz Coil

A Helmholtz coils inside the vacuum chamber was used to adjust the magnitude of the field where the probe *I–V* sweeps were obtained in Test Campaign 3. Figure 4.8 shows an illustration of the Helmholtz coil in the test setup. A simple illustration of a Helmholtz coil is shown in Figure 4.9. A Helmholtz coil is composed of a pair of electrical windings or solenoids that produce a fairly uniform magnetic field in the mid-plane between them [173]. Adjusting the coil current can control the strength of the magnetic field. At the center between the coils, the magnetic field generated by coils of radius r_H separated by distance r_H is [174]

$$B_z = \left(\frac{4}{5}\right)^{3/2} \frac{\mu_0 n I_H}{r_H}, \qquad \text{(Eq. 4.5)}$$

where n is the number of turns in each coil, I is the current carried by the coils, μ_0 is the permeability of free space (assuming the medium between the coils is free space), and B_z is directed axially with respect to the coils.

The magnetic field was measured inside the chamber at the probe location by a Lakeshore Magnetometer. Using the convention shown in Figure 4.1, where the *x*-axis is directed to the left of the chamber, the *y*-axis is directed towards the hollow cathode, and the *z*-axis is directed vertically upwards, the magnetic field, B, was $-0.07\,\hat{x} - 0.13\hat{y}$

$-0.39\hat{z}$ G. The Helmholtz coil was placed to produce a vertical magnetic field capable of significantly reducing the largest component of the ambient field, the vertical component, so the effect of reducing the field could be assessed during the experiment. The Helmholtz coil used in Test Campaign 3 is shown in Figure 4.10. Magnetic field measurements were obtained at the location the probe current measurements were taken. The magnitude of the vertical field is provided in Table 4.2. The magnetic field was observed to vary only slightly, by about 10%, over several centimeters horizontally in the midplane and was similarly uniform about a centimeter vertically up and down from the midplane. The *x* and *y* components of the magnetic field were essentially unchanged as the Helmholtz coil current increased.

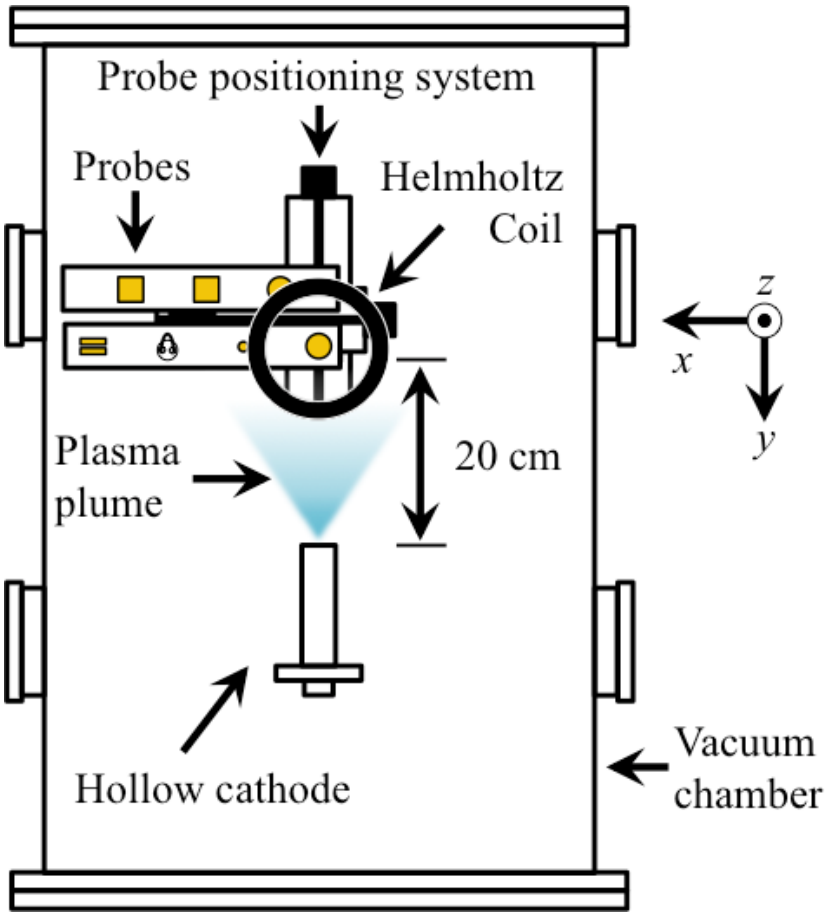

Figure 4.8: Illustration of the experimental setup in Test 3. The position of the Helmholtz coil shown was fixed in test 3 and the probes were moved by the linear motion stages to the same position inside the coil downstream form the cathode.

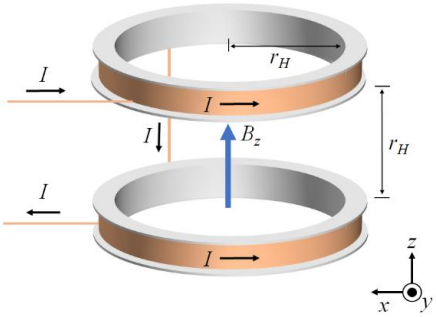

Figure 4.9: Simplified illustration of a Helmholtz coil. Current driven through the upper and lower solenoids to produce a nearly uniform magnetic field in the center of the mid-plane between the coils.

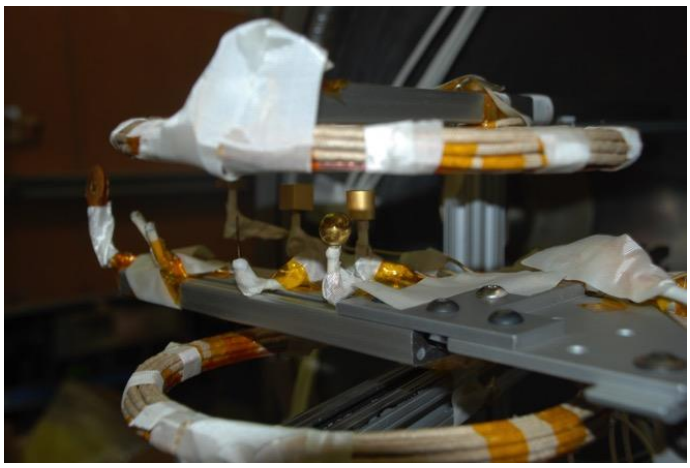

Figure 4.10: Picture of the probes in the Helmholtz coil in Test 3. The coil radius was 7.6 cm.

Table 4.2: Helmholtz coil current and magnetic field measurements at location of probe measurements.

Helmholtz Coil Current (A)	Vertical Component of Magnetic Field, B_z, Measured at the Center of the Midplane Between Coils (G)
0 A	-0.4 G
0.4 A	0.02 G
1.2 A	1 G
2.05 A	2 G
2.80 A	3 G
3.59 A	4 G
4.42 A	5 G
5.27 A	6 G

4.2.3 Analyzing the Plasma Environment

4.2.3.1 Plasma Parameter Measurements and Analysis

Here, the procedures used to determine the plasma parameters for each test campaign are described. The plasma parameters were obtained from the spherical and cylindrical Langmuir probe current voltage sweeps. Figure 4.11 shows example sweeps. The current measured by the probe is the sum of the electron and ion currents. The convention here is that "positive" current represents a net collection of electrons and "negative" current represents net collection of ions. In the case of the emissive probe, the electron emission also generates negative current. Linear up and down sweeps, shown in Figure 4.11a, reveal a lack of hysteresis in the probe current-voltage (*I*–*V*) characteristic. This suggests that the probes were clean [170].

To obtain the plasma potential, the electron temperature, and the electron density, the contributions from ions was subtracted from the *I*–*V* sweep [175]. A sharp "knee" in the *I*–*V* curve that is indicative of the plasma potential was not easily identifiable from the *I*–*V* curve. However, the plasma potential could be identified from the inflection point as a peak in the first derivative of the *I*–*V* curve [150]. This is shown in Fig. 4.11b. Using this method, the average plasma potentials were determined to be −24.5 V, −21.5 V, and −23 V for Test Campaigns 1, 2, and 3, respectively. The spherical and cylindrical Langmuir probes plasma potential measurements typically agreed by ~0.2 V. A second, smaller peak in the first derivative of the *I*–*V* curve is also apparent in Figure 4.11 near −25 V and is discussed in the following section.

It is not clear why the plasma potentials were below ground potential. The plasma potential could be the result of the somewhat uncommon electrical scheme used here, where the keeper was grounded, the cathode was biased between −25 V and −30 V relative to ground, and no positively biased external anode was used. Future work will include a more detailed investigation studying the plasma potential in the cathode plume.

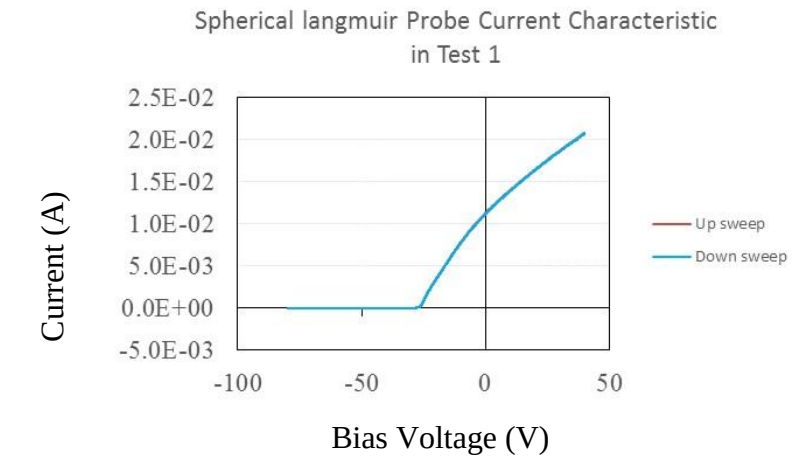

(a)

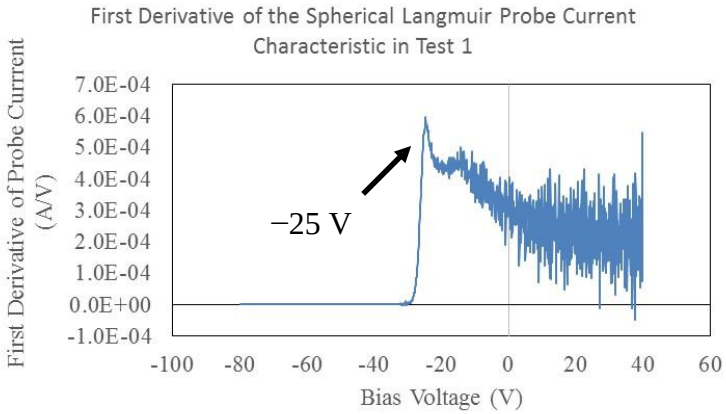

Figure 4.11: Spherical probe *I*−*V* characteristic and the first derivative of the characteristic from Test 1. An up and down sweep are shown in (a), illustrating a lack of hysteresis. The first derivative of a spherical probe *I*−*V* characteristic is shown in (b). The plasma potential was determined at the inflection point, which is indicated as −25 V.

An emissive probe was also used to check the plasma potential measurement. The *I*–*V* curves for the emissive probe were obtained for varying levels of filament current. As the filament current increased, the probe became hotter and the emission level increased, modifying the *I*–*V* characteristic, which is shown in Figure 4.12. An approximate value of plasma potential can be deduced by the separation point of the *I*–*V* curves [176]. An alternative technique determines the plasma potential from the floating potential of a hot emitting probe. These two technique identified plasma potential within 0.3−0.5 V of the inflection point of the cylindrical and spherical probe *I*–*V* curves.

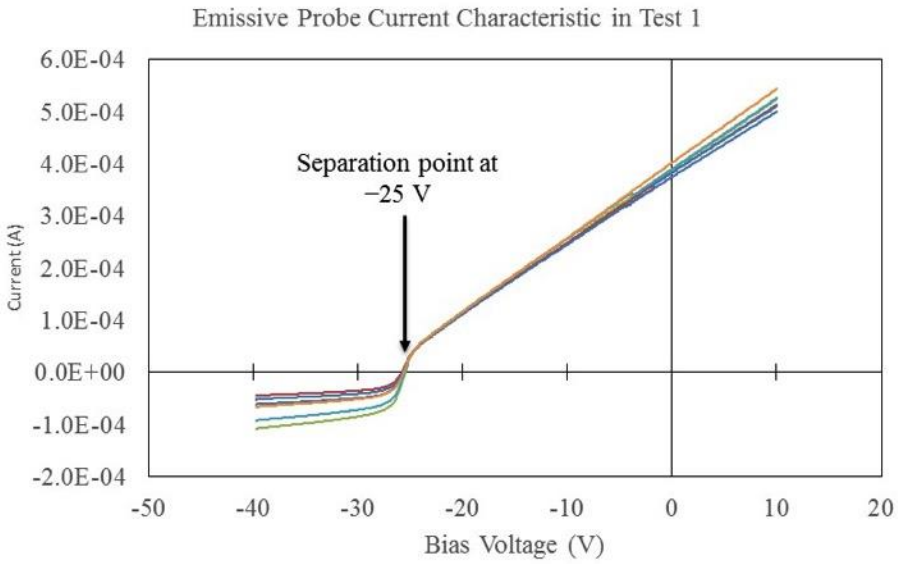

Figure 4.12: Example emissive probe current characteristics at varying filament current levels.

The electron density and temperature were then determined from the electron energy distribution function (EEDF) of the spherical probe's *I–V* characteristic. It was shown by Druyvesteyn that the second derivative of the electron current is proportional to the energy distribution [150]. The Druyvesteyn formula is given by [177], [178]

$$F(\epsilon) = \frac{2m_e}{q^2 A_{\text{probe}}} \sqrt{\frac{2q(V_p - V)}{m_e}} \left(\frac{d^2 I}{dV^2}\right), \quad \text{(Eq. 4.6)}$$

where ϵ is the electron energy. An EEDF is shown in Figure 4.13. The electron density can be obtained by integrating the EEDF, or [178]

$$n_e = \int_0^\infty F(\epsilon)\, d\epsilon. \quad \text{(Eq. 4.7)}$$

The effective electron temperature is defined by the mean electron energy, or [178]

$$T_e = \frac{2}{3}\langle\epsilon\rangle = \frac{2}{3n_e}\int_0^\infty \epsilon F(\epsilon)\, d\epsilon. \quad \text{(Eq. 4.8)}$$

The EEDF was then compared to a Maxwell-Boltzmann distribution and a Druyvestyn distribution using the derived values of electron temperature. A normalized, isotropic Maxwellian EEDF is expressed as [179]

$$F_M(\epsilon) = \frac{2}{(kT_e)^{3/2}}\sqrt{\frac{\epsilon}{\pi}}\exp\left(-\frac{\epsilon}{kT_e}\right), \quad \text{(Eq. 4.9)}$$

and a normalized Druyvesteyn distribution is expressed as [179]

$$F_D(\epsilon) = \frac{0.5648 n_e}{(kT_e)^{3/2}}\sqrt{\epsilon}\exp\left(-0.243\left(\frac{\epsilon}{kT_e}\right)^2\right), \quad \text{(Eq. 4.10)}$$

The difference between the distributions is apparent in Figure 4.13. The Druyvesteyn distribution was determined to be a reasonable fit to the measured EEDF. A Druyvesteyn distribution have been observed previously in the plume of hollow cathodes operating under similar cathode operating conditions (i.e., low current and low flow rate) [180].

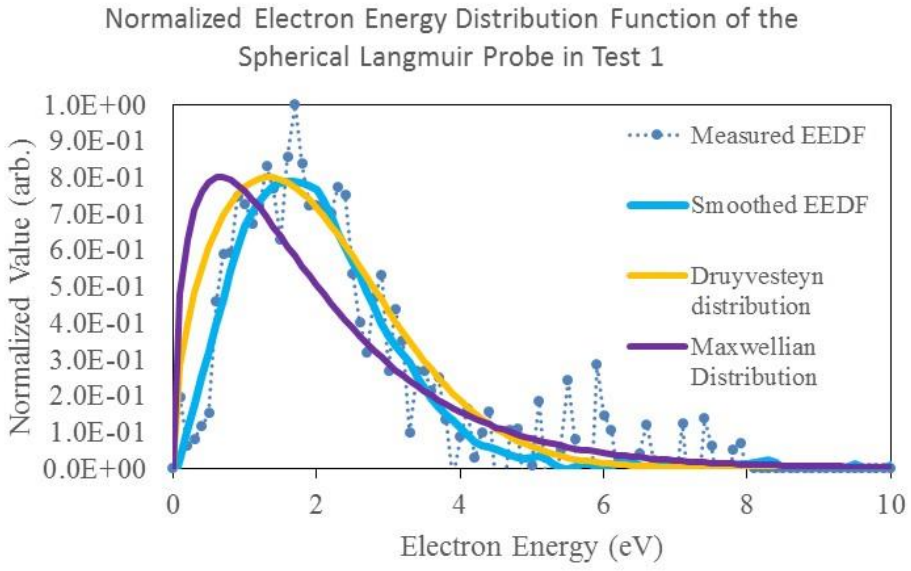

Figure 4.13: Measured electron energy distribution function (EEDF) compared to calculated Druyvesteyn and Maxwellian distributions. The measured EEDF was smoothed by a moving average filter. The EEDF is smoothed here for presentation purposes, but smoothing was generally unnecessary and produced a negligible change in the calculated electron density or temperature.

The electron density and temperature are shown for each test Campaign in Table 4.4. Plume measurements from a low-current hollow cathode in [181] operating with a configuration similar to our tests reported similar electron temperatures near and below 1 eV.

4.2.3.2 Plasma Flow Conditions

In this section, the plasma flow in the experiment is evaluated. It was necessary to generate high-speed plasma in order to simulate motion in LEO. Plasma flow and effects on current collection are described in section 4.2.1.3. Three measurements are analyzed here to confirm the presence of plasma flow and *approximately* estimate plasma drift energy:

1. An analysis of the ion saturation current characteristic of the cylindrical probe.
2. A comparison of the ion saturation current collected by the upstream side of the Mach probe to the ion saturation current collected by the downstream side of the Mach probe.
3. An analysis of the electron saturation current characteristic of the upstream side of the Mach probe.

These measurements and the corresponding analysis are described in this section. The flow velocity measurements are followed by a discussion on the charge exchange ion population, which represent a degradation of the plasma flow and generation of an additional thermalized, non-drifting plasma.

First, the ion saturation current characteristic of the 0.5-mm radius cylindrical probe was used to give an approximate estimate for flow velocity. The ion saturation current is the current measured below the electron retardation regime. The ion current to a thin, OML cylinder (i.e., $r_p/\lambda_D \leq 1$) in a collisionless, unmagnetized plasma flowing with energy U_{ev} is given in Appendix F of Choiniere (2004) [182]

$$I_i = A_{\text{probe}}\sqrt{2}\frac{e^{1.5}}{\pi\sqrt{m_i}}n_i\sqrt{\frac{1}{2}T_i + U_{\text{ev}} + V_p - V}, \qquad \text{(Eq. 4.11)}$$

where I_i is the ion saturation current, T_i is the ion temperature, V_p is the plasma potential, and V is the potential of the probe. The directed ion energy is

$$U_{\text{ev}} = \frac{1}{2}\frac{m_i {U_{\text{ion}}}^2}{q}, \qquad \text{(Eq. 4.12)}$$

where U_{ion} is the velocity of the ions. Assuming the ion temperature is small relative to U_{ev}, a line fit to I_i^2–V curve can then be used to estimate the plasma density and the beam

energy. Figure 4.14 shows an example of the square of the ion saturation current and a first degree polynomial fit to the characteristic. The square of the ion saturation current was fit in MATLAB® using the method of least-squares. Table 4.3 lists the estimated ion drift velocities derived from this measurement.

The ion saturation characteristic is relatively noisy, so it is not expected that the ion drift energy derived from this measurement is precise. The coefficient of determination, or R^2, is an indication of how well the measured data fit the data. R^2 values close to 1 generally indicate a good fit. $R^2 = 0.74$ in Test Campaign 1, $R^2 = 0.72$ in Test Campaign 2, and $R^2 = 0.64$ in Test Campaign 3, suggesting that the fit was not very good. In addition, Equation 4.11 assumes that the entire population of ions is drifting, which is not the case here due to charge exchange (discussed later).

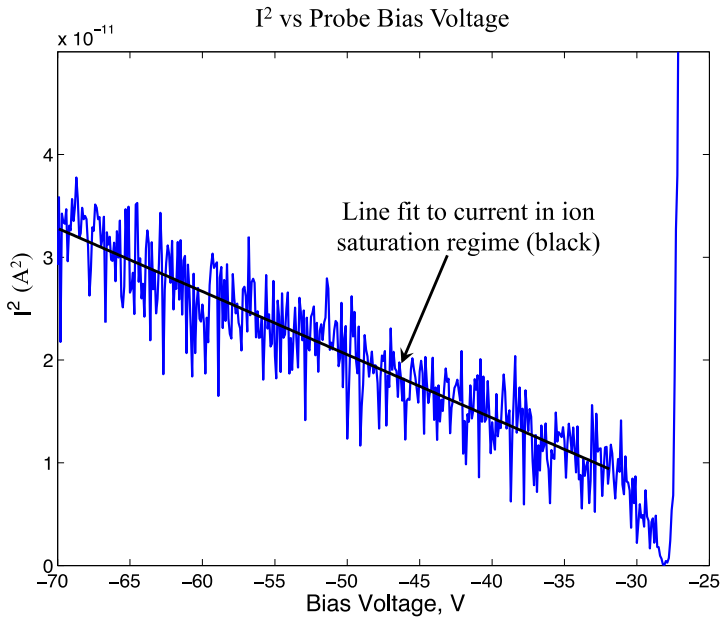

Figure 4.14: First degree polynomial fit to the square of the cylindrical probe's ion saturation current. This method can be used to estimate ion drift energy. The line was fit using least-squares fitting in MATLAB. The coefficient of determination, or R^2, was 0.74.

Next, the Mach probe was used to help determine the ion flow velocity normal to the probe face. In a high-speed flowing plasma, a rarefied wake region forms on the downstream side of an object. The ion saturation current on the downstream side decreases as well. The upstream-to-downstream ion saturation current ratio can be related to the Mach number, where the Mach number is the ratio of plasma velocity to the ion

sound speed. The measured ratios of upstream to downstream current are listed in Table 4.3.

The Mach number, M_∞, can be calculated with the expression [183]

$$M_\infty = \frac{1}{K} \ln \frac{I_u}{I_d}, \quad \text{(Eq. 4.13)}$$

where I_u is the ion saturation current collected on the upstream face of the Mach probe, I_d is the ion saturation current collected on the downstream face of the Mach probe, and K is the calibration factor. The drift velocity, or v_d, can be calculated using the relationship [183]

$$M_\infty = \frac{v_d}{\sqrt{kT_e/m_i}}, \quad \text{(Eq. 4.14)}$$

where $(kT_e/m_i)^{1/2}$ is the ion acoustic velocity. Although Equation 4.13 and Equation 4.14 have been applied successfully to calculate the ion flow velocity in magnetized plasmas where the ion gyroradius is small compared to the probe dimensions, it is much more difficult to calculate velocity using Equations 4.13 and 4.14 in a plasma where the ion gyroradius is larger than the probe dimensions [183]. In plasmas where the ions are not magnetized, there is little agreement on the Mach probe calibration factor K [183]. It is influenced by a variety of parameters, including the ion temperature, which was not measured in this experiment. Hutchinson (2002), Oksuz and Hershkowitza (2004), and Ko and Hershkowitz (2006) describe the challenges of using Equations 4.13 and 4.14 to make accurate velocity measurements when the ion gyroradius is larger than the probe dimensions [164], [184], [185]. So rather than using the ratio of upstream-to-downstream current to calculate the Mach number, instead this ratio is presented here simply to suggest the presence of directional plasma flow on the upstream face of the Mach probe.

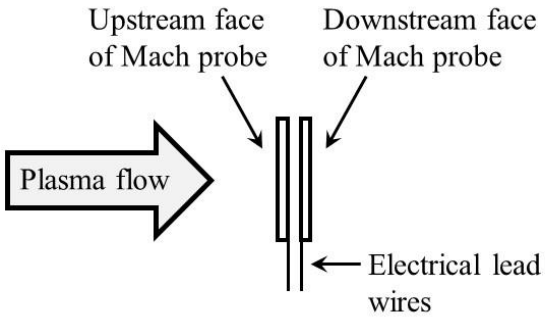

(a)

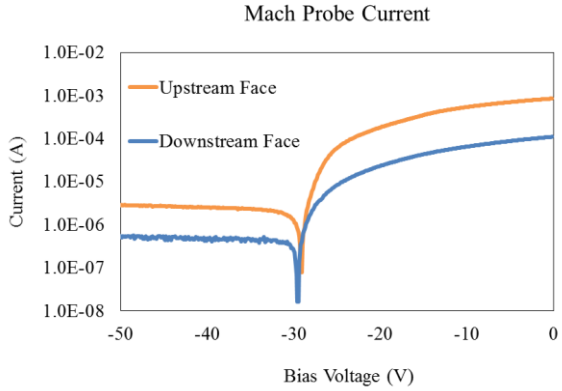

(b)

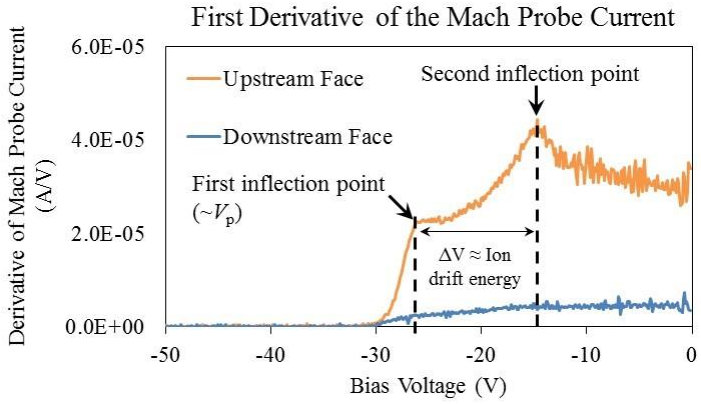

(c)

Figure 4.15: (a) Simple Mach probe illustration. (b) The semilog *I*−*V* characteristics of the upstream and downstream sides of the Mach probe. (c) The first derivative of the *I*−*V* characteristics of the upstream and downstream sides of the Mach probe. The Mach probe displays a small second inflection point above the plasma potential. The potential difference between the first and second inflection points indicates the ion drift energy.

In addition, the electron saturation characteristic of the upstream face of the Mach probe can also be used to give an approximate value for ion drift energy. The upstream side revealed an interesting feature that is shown in Figure 4.15c. The first derivative of the upstream side shows two distinct peaks while the downstream side has a much shallower slope that lacks the second peak. A similar “two-peaked” first derivative was observed in the *I−V* characteristics of the other probes during the three test campaigns. This additional inflection point or "knee" above the plasma potential is a feature commonly associated with directed ion motion [155], [156]. For a planar probe facing an ion beam, the first peak indicates a potential slightly positive with respect to the plasma potential [164] and the second peak is associated with the potential where the streaming ions are reflected from the probe. The streaming and reflected ions form a space charge region in front of the probe and this produces an expansion of the sheath region around the probe, increasing the effective collection area and increasing the current [155]. Thus, the electron saturation current on the upstream face can be used to provide a measure of the ion beam energy. Weber et al. (1979) and Skøelv et al. (1984) have suggested using this feature to determine plasma flow velocity [154], [155]. The second peak in the first derivative of the *I−V* characteristics was typically observed about ~10 V above the plasma potential. This might suggest an ion beam with energy of ~10 eV, but an independent ion energy measurement would be needed to confirm this.

The rough estimates of ion drift from the upstream side of the Mach probe are provided in Table 4.3. Due to the noise in the electron saturation current, inflection points were difficult to identify and appeared as a broad "hump" in the first derivative that was spread out over several volts. As a result, this measurement was only accurate to a few eV of the actual value beam energy. In future experiments, it will be important to measure the ion drift energy using more precise techniques, like using retarding potential analyzer (RPA) or laser induced florescence (LIF).

It should be noted that the plasma drift energy observed here is consistent with plasma drift energy measured by Williams et al (1998) using LIF in the plasma plume of a hollow cathode under similar operating conditions [160]. More recently, high-speed ions flowing axially away from a hollow cathode have also been measured by Farnell et al. (2011) and Foster and Patterson (2005) [186], [187]. An explanation of the

mechanism responsible for the high-speed plasma flow is beyond the scope of this dissertation.

It is also of interest that the downstream side of the Mach probe displayed no second inflection point indicative of plasma flow. This suggests that there was plasma flowing toward the upstream face and the downstream face of the Mach probe measured a more thermalized, non-drifting population of plasma.

Table 4.3: Estimated ion drift energy from the cylindrical probe ion saturation current measurement and the Mach probe as well as the ratio of upstream ion saturation current to downstream ion saturation current.

Test Campaign Set	J_u/J_d	**Ion drift energy estimate from upstream face of the Mach Probe (eV)**	**Ion drift energy estimate from the Cylindrical Probe (eV)**
Test Campaign 1	4.7	11	7
Test Campaign 2	4.8	10	8
Test Campaign 3	1.9	11	13

Charge exchange (CEX) collisions influence our ability to generate a high-speed plasma downstream from a plasma source. A CEX event is a collision between a fast ion and a slow moving neutral that produces a fast neutral and a slow ion [162]. As more ions undergo CEX collisions, the plasma becomes less representative of the LEO environment [188]. Operating the cathode at low flow rates reduces the amount of background gas in the vacuum chamber and reduces CEX ion production [189].

On average, a xenon ion will experience a $Xe^{+}-Xe$ CEX collision after traveling one mean free path [190],

$$\lambda_{\mathrm{MFP}} = \frac{1}{n_g \sigma_{\mathrm{Xe}}}, \qquad \text{(Eq. 4.15)}$$

where n_g is the gas density and σ_{Xe} is the CEX collision cross section of xenon. The Xe^{+} CEX collision cross section is dependent on energy. It would be necessary to measure the ion energy distribution in this experimental setup to calculate the cross section more accurately. This measurement will be considered for future experiments. Using the Mach probe and cylindrical probe results, for this analysis it was estimated that the plasma ion drift energy was on the order of ~10 eV, Calculating the cross sections in this range, it was then estimated that the cross section was 82×10^{-16} cm^{-2} [162], [191].

The percentage of the directional plasma beam that has not experienced a CEX collision (the "beam survival percentage") can be estimated by applying Beer's law [192],

$$T = e^{-x/\lambda_{\mathrm{MFP}}}, \quad \text{(Eq. 4.16)}$$

where x is the distance from the plasma source. The neutral density was measured inside the vacuum chamber 2 cm from the cathode orifice to the probe location in 1 cm increments. To make an approximate estimate for the percentage of plume ions that undergo collisions, the beam survival was calculated at the probe location. The result is that ~15% of ions originating 2 cm downstream from the cathode continue to the probe without a charge exchange collision.

The estimated beam survival is low. Using this analysis, ~85% of the ions have experienced a charge exchange collision 20 cm from the hollow cathode (this is the distance where all probe measurements were obtained). More importantly, this suggests that a majority of the ions were thermalized and non-drifting. The impact of the low ion beam survival on current characteristics was explored in Choinière et al. (2005), where the "knee" above the plasma potential decreased as the ion beam survival reduced. As mentioned earlier in this section, this "knee" is associated with an increase in electron collection current. Thus, low beam survival results in less electron collection current enhancement [89].

To summarize, it has been estimated that the majority of the ions were non-drifting while a smaller portion made up a high-speed, drifting population. This tells us that the experimental test campaigns did not fully capture mesothermal conditions representative of LEO. Operating the experiment in a vacuum facility with a higher xenon pumping speed could potentially achieve this.

4.2.3.3 Comparison of the LEO Plasma Environment with the Laboratory Environment

The laboratory environment is compared with the LEO environment in Table 4.4. The LEO orbital environmental parameters were determined from Hastings and Garret (1996) [62]. The laboratory plasma had several key elements of the LEO environment. The Debye length was about 0.5−1 mm for both test campaigns, so the spherical, cubic, and planar probes, each ~1 cm across, had characteristic dimensions of about $10-20\lambda_D$. The probe dimensions, scaled by the Debye length, were approximately representative of

anode dimensions in LEO. Normalized by the electron temperature, the maximum probe bias in Test Campaign 1, Test Campaign 2, and Test Campaign 3 was $46kT_e/q$, $100kT_e/q$, and $140kT_e/q$ respectively. The maximum voltage of 0 V in Test Campaign 1 and Test Campaign 2 would be roughly 5 V, 10 V, and 14 V respectively, in LEO, assuming kT_e/q is around 0.1 eV.

Test Campaign 3 also captures the magnetization parameter r_p/r_L in some conditions in LEO at the maximum magnetic field value of 6 G. The parameter ω_{ce}/ν_e, however, was not fully representative of LEO. Assuming a magnetic field strength in LEO of ~0.35 G [71], $\omega_{ce} \approx 1$ MHz. Collisions between like particles produce little diffusion [152], so the electron collision frequency can be calculated as the sum of the electron-ion collision frequency and the electron neutral collision frequency, or [190]

$$\nu_e = \nu_{ei} + \nu_{en}, \tag{Eq. 4.17}$$

where ν_{ei} is the electron-ion collision frequency and ν_{en} is the electron-neutral collision frequency. The electron-ion collision frequency is given by [193]

$$\nu_{ei} = 2.9 \times 10^{-12} \frac{n_e \ln\Lambda}{(kT_e/q)^{3/2}}, \tag{Eq. 4.18}$$

where $\ln\Lambda$ is the coulomb logarithm, and $\ln\Lambda \approx 10$. Equation 4.16 gives the electron-ion collision frequency in Hz. Assuming that $n_e = 10^4$–10^6 cm^{-3} and $T_e = 0.1$ eV in LEO [62], the electron-ion collision frequency ranges from about 5−1200 Hz.

The electron-neutral collision frequency can be calculated as

$$\nu_{en} = \sigma_{en} n v_{the}, \tag{Eq. 4.19}$$

where σ_{en} is the effective electron neutral scattering cross section, n is the neutral density, and, v_{th} is the electron thermal velocity, $v_{th} = (8kT_e/\pi m_e)^{1/2}$. Equations 4.18 and 4.19 give the collision frequency in Hz. The effective electron-neutral scattering cross section in LEO is on the order of 5×10^{-23} cm^2 [62]. Electron-neutral collisions are far less frequent in the altitude range of LEO considered here, however, and ν_{ei} dominates. Using the Mass Spectrometer Incoherent Scatter Radar (MSIS-E-90) to calculate the orbital average neutral density in the environmental conditions considered in this trade study (i.e., solar maximum, 400−600 km altitude, equatorial orbit), the neutral density is estimated to be on the order of 10^5–10^8 cm^{-3}, although it may be lower in solar minimum conditions in

this altitude range [107]. The resulting electron-neutral collision frequency is on the order of 0.01−10 Hz. This collision frequency is consistent with calculations in Kelley (2009) [61]. In other words, in the LEO environment it can be assumed that $\nu_e \approx \nu_{ei}$. As a result, in LEO $\omega_{ce}/\nu_e = 8\times10^2–1.7\times10^5$ Hz and $(\omega_{ce}/\nu_e)^2 >> 1$.

In the laboratory environment, the electron-neutral scatting cross section for xenon was estimated from [190]

$$\sigma_{en} = 6.6 \times 10^{-19} \left(\frac{\frac{kT_e}{4q} - 0.1}{1+\left(\frac{kT_e}{4q}\right)^{1.6}} \right). \quad \text{(Eq. 4.20)}$$

The neutral density was determined from pressure measurements made where the probes were positioned downstream from the hollow cathode. The collision frequency was calculated using Equation 4.17. To be clear, in the laboratory environment the electron-neutral collision frequency is not much smaller than the electron-ion collision frequency. Recall that in LEO $\nu_{ei} >> \nu_{en}$, so $\nu_e \approx \nu_{ei}$. In the laboratory environment, the electron-neutral frequency is estimated to be ~1−100 times higher than the electron-ion collision frequency. The collision frequencies are provided more explicitly in Table 5.2 in section 5.2.1 of Chapter 5. For the maximum magnetic field generated in the test campaigns, $\omega_{ce} \approx 20$ MHz.

The parameter ω_{ce}/ν_e in the experimental test campaigns was much less than ω_{ce}/ν_e in the LEO environment, specifically because the electron collision frequency in the experiment was much higher than in LEO. The higher collision frequency in the laboratory test campaigns had the potential to produce a higher rate of cross-field diffusion, possibly enabling higher current collection as a result. Test Campaign 3, however, did generate ω_{ce}/ν_e only a few times smaller than in LEO. As a result of this and other scaling parameters, Test Campaign 3 appears to be most representative of the LEO environment.

In future experiments, it will be important to reduce the background neutral density to lower the electron collision frequency. Operating the experiment in a vacuum facility with a higher xenon pumping speed could potentially achieve this. As mentioned in the previous section, a lower background pressure would also reduce charge exchange

collision effects, which would make the plasma more of a directed beam and reduce the thermal, non-drifting population.

A summary of the comparison between the laboratory plasma and the LEO environment is provided here:

- The parameter r_p/λ_D is representative of the LEO environment in all of the experimental test campaigns. The probes are also shaped appropriately to represent "box-like" picosats and femtosats.
- The parameter r_p/r_L is representative of the LEO environment in Test Campaign 3.
- The parameter ω_{ce}/ν_e and the large estimated charge exchange ion population are not fully representative of the LEO environment. This effect is due to the high neutral background density in the laboratory environment relative to LEO. The parameter ω_{ce}/ν_e most closely represents LEO when a 6 G magnetic field is generated in Test Campaign 3.

Table 4.4: Comparison of Ionospheric Plasma Environment with the Laboratory Environment in Test Campaign 1, 2, and 3. Ionospheric Parameters are from Hastings and Garret (1996) [62].

Parameter	Typical Ionosphere	Test Campaign 1	Test Campaign 2	Test Campaign 3
Plasma density, n_e (cm^{-3})	10^4–10^6	8×10^7	1.6×10^8	1.1×10^8
Electron temperature, kT_e/q (eV)	0.1–0.2	1.5	0.7	0.6
Ion mass, m_i (g)	2.7×10^{-23}	21.8×10^{-23}	21.8×10^{-23}	21.8×10^{-23}
Magnetic field, B (G)	0.35	0.45	0.45	0.2–6
Representative bias voltage, V_{pmax} (V)	70	70	70	70
Anode radius, r_p (cm)	1–5	0.5	0.5	0.5
	Calculated Parameters			
Debye length, λ_D (cm)	0.2–3.3	0.1	0.05	0.06
Electron gyroradius, r_L (cm)	2–3	6.5	4.4	0.3–8.4
Electron gyrofrequency, ω_{ce} (s^{-1})	9.8×10^5	1.3×10^6	1.3×10^6	6×10^4–2×10^7
Electron collision frequency, ν_e (s^{-1}) where $\nu_e = \nu_{ei} + \nu_{en}$	5–1.2×10^3	7×10^5	2×10^5	6×10^4
	Scaling Parameters			
r_p/λ_D	0.3–25	5	10	9
r_p/r_L	0.3–2.5	0.1	0.1	0.01–1.8
ω_{ce}/ν_e	8×10^2–1.7×10^5	1.8	7.4	9–290
qV_{pmax}/kT_e	250–500	46	100	140

4.2.3.4 Evaluating the Impact of Insulated Probe Electrical Leads on the Experiment

This section presents a basic, "back-of-the-envelope" analysis to evaluate the disturbance caused by electrical insulation near the probes. Consistent with the rest of this chapter, the focus here is the impact on current measured near and above the plasma potential. The electrical insulation is shown in Figures 4.5, 4.6, and 4.10. Figure 4.15 shows a simple illustration of a probe and the insulated electrical leads connected to the probe. The electrical leads were insulated to ensure that they did not draw current from the plasma. Although insulation does not collect net current, it reduces the plasma density in the vicinity of the insulator, which can reduce the current collected by the probe [194]. This effect has been studied by Waymouth (1962) and is explained in the following paragraphs [194].

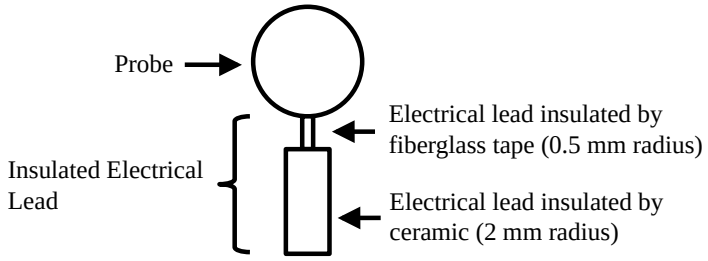

Figure 4.16: Illustration of the spherical probe and the supporting electrical leads.

An unbiased probe and electrical insulation will both collect thermal ion and electron flux on their surfaces when immersed in plasma. Equation 4.3 (section 4.2.1.1 of Chapter 4) gives the expression for electron thermal current and Equation 2.33 (section 2.3.2.3 of Chapter 2) gives the expression for ion thermal current. Electron thermal current is much higher than ion thermal currents because ions are more massive, so the electrode and the insulator surfaces rapidly accumulate negative charge and reaches a potential below the plasma potential of the quasi-neutral bulk plasma. The potential of the floating electrode (or “floating potential”) retards the flow of plasma electrons and ensures that the electron and ion fluxes are equal [175]. As charged particles in the plasma redistribute, a non-neutral ($n_e > n_i$) sheath region forms around the object that shields the undisturbed plasma from the potential disturbance. If the electrons are

Maxwellian and ion and electron current from the plasma are the only currents to the surface, the floating potential is given by [175]

$$V_f = V_p + \left({}^{kT_e}/_{q}\right) \ln\left(0.6\sqrt{\frac{2\pi m_e}{m_i}}\right), \quad \text{(Eq. 4.21)}$$

where V_p is the plasma potential and V_f–V_p is the potential difference across the sheath.

When the probe is biased positively or negatively with respect to the surrounding plasma, particles of the opposite charge are drawn to the electrode and particles of like charge are repelled from it. As a result, the sheath grows or shrinks and the net charge in the sheath shields out the potential disturbance. However, when a bias is applied to the electrical leads connected to the probe, the sheath at the insulator's surface *expands* in response to the potential disturbance and *collapses* to the floating potential sheath as electrical charge accumulates or builds up on the surface of the insulator [104]. This occurs on a time scale of the ion plasma period, τ_{pi} [195], [196]. The ion plasma period for singly charged ions is given by

$$\tau_{pi} = 2\pi\sqrt{\frac{\varepsilon_0 m_i}{q^2 n_i}}, \quad \text{(Eq. 4.22)}$$

where it is assumed that $n_i \approx n_e$ from quasi-neutrality in the bulk plasma. Approximating the $n_i \approx 10^8$ cm^{-3} in the laboratory test campaigns, the sheath formation timescale was about 5 μs. In contrast, each bias voltage in the current-voltage sweep was applied for ~10 ms, so it is reasonable to assume that the insulating surfaces were surrounded by a steady-state, floating potential sheath. The sheath that forms around the insulating surfaces reduces the plasma density in the vicinity of the insulator and, as a result, the insulated leads connected to the probe can decrease current collected by the probe.

In order to estimate the floating potential sheath size, first it was necessary to estimate the floating potential on the insulator. Using Equation 4.20 to calculate the floating potential and assuming $T_e \approx 0.7$ eV in the laboratory tests (laboratory test parameters are summarized in Table 4.4), the floating sheath potential was about 5.8 V. The sheath size can be estimated from the sheath potential. Bettinger and Walker (1965) developed an estimate for sheath thickness for a cylinder in stationary, non-magnetized,

isotropic Maxwellian plasmas [129]. The estimated sheath radius, r_{sh}, [129] around the insulated cylindrical supports of radius r_{ins} can be estimated by solving the expression

$$\left(\left(\frac{r_{sh}}{\lambda_D}\right)^2 + 2\frac{r_{sh}r_{ins}}{{\lambda_D}^2}\right)\ln\left(1+\frac{r_{sh}}{r_{ins}}\right) = \pi\psi_s\left(1+\frac{2}{3}\psi_s\right)^{1/2}, \qquad \text{(Eq. 4.23)}$$

where Ψ_s is the sheath potential normalized by the electron temperature.

Using Equation 4.21, the resulting sheath thickness in the test campaigns was roughly $4.5\lambda_D$, or ~4 mm. This is large, as a rule of thumb is to estimate that the sheath extends ~$2-3\lambda_D$, but this was assumed for the purpose of conducting a *worst-case assessment* on the impact of the sheath surrounding the insulation. The insulator's floating potential sheath (i.e., plasma depletion region) can then be modeled as a ~4-mm diameter cylinder originating at the probe's surface and extending along the length of the 0.5-mm insulated electrical lead and expanding at the 2-mm-radius ceramic insulator. In this "back of the envelope" analysis, the probe is assumed to collect current along the sheath edge and the insulating electrical lead removes a ~4 mm-radius circle from the probe's sheath, representing a proportional loss in collection current. As the probe sheath grows, the area represented by the floating potential sheath becomes a smaller fraction of the probe effective collection area, indicating that the impact on collection current decreases with probe voltage.

Equation 3.12 (section 3.4.4 of Chapter 3) was be used to estimate the size of the probe's sheath as a function of bias voltage. When the probes was biased to the plasma potential, the insulator reduces the spherical and planar probe's current by about 20% and the cubic probes area by about 10%. However, the probe's sheaths expand with bias voltage and the disturbed region in the vicinity of the insulated electrode makes up a smaller portion of the effective current collection area. At 15 V above plasma potential, the insulator's floating potential sheath is less than 5% of the spherical and planar probe's sheath. Recall that the probes were biased to about 70 V above the plasma potential, so the effect of the insulator on collection current was relatively small.

When the magnetic field was increased in Test Campaign 3, electrons traveled along magnetic flux tubes and probes were "shadowed" on one side by their insulated electrical leads. Sheath expansion in a strong, non-drifting plasma can be approximated using the Parker−Murphy model, which estimates that current is collected by along two

disks of radius r_0 that are normal to field lines and slowly expand with increasing bias voltage. Parker–Murphy provides the theoretical model for the effective collection radius radius r_0 for a large ($r_L << r_p$), positively biased sphere in a non-drifting, collisionless, magnetized plasma, which is given by [83]

$$r_{\mathrm{PM}} = r_0 \left(1 + \left(\frac{8q(V_{\mathrm{anode}} - V_p)}{m_e \omega_{\mathrm{ce}}^2 r_p^2} \right)^{\frac{1}{2}} \right)^{1/2}, \qquad \text{(Eq. 4.24)}$$

where r_0 is the radius of the sphere, the electron gyrofrequency, ω_{ce}, is equal to qB/m_e, and the effective current collection area is $2\pi r_0^2$, or the area of 2 disks of radius r_0. At the plasma potential, the effective collection area is simply the cross sectional area normal to field lines, so this estimate is, again, a worse-case estimate for the disturbance caused by the probes. The actual sheath can more likely be approximated as an ellipsoid elongated in the direction of the magnetic field [197]. Nevertheless, using this worst-case estimate, in Test Campaign 3 at the maximum magnetic field value of 6 G, the insulating support reduces the probe's areas by ~40% when the probe is biased at the plasma potential. However, the radius r_0 increases with voltage and by 10 V above the plasma potential the disturbance caused by the floating potential sheath reduces to just a few percent of the effective collection area. The ions were magnetized, so the impact on ion saturation current would be even smaller.

In summary, the probe insulation can disturb the plasma in the vicinity of the probe and cause a small reduction in effective collection area. This can cause error in the electron density measurement, making it too small. The reduction is small, except in the case of the magnetic field, where the probe supports can cause some degree of "shadowing" along field lines. However, as the probe sheath expands, the impact of the probe supports becomes small.

4.2.3.5 Identifying Potential Sources of Measurement Error

A brief experimental error analysis is presented here prior to experimental results. The primary source of experimental error was the plasma potential measurement. The electron density and temperature were calculated from the EEDF, which requires an

accurate plasma potential measurement. If the electron density had instead been calculated from the electron saturation current rather than using the EEDF, the plasma potential would still be necessary to determine the electron saturation current.

The plasma potential was determined at the inflection point of the *I*−*V* characteristics. Small variations on the order of 0.1−0.3 V were occasionally observed between consecutive sweeps and some displayed what appeared to be multiple inflection points within a 0.1−0.3 V range. These effects may have been indicative of the plasma potential changing between or even during *I*−*V* sweeps. It was also observed that the cathode potential oscillated with a peak-to-peak amplitude of ~0.5 V and a frequency of ~10 KHz, and these oscillations may have generated fluctuations in the plasma potential. This effect was observed in a hollow cathode plume by Goebel et al. (2007) [161].

An emissive probe using the separation point technique also made plasma potential measurements. In the separation point technique, the crossing point between hot and cold emissive probe *I*−*V* characteristics indicates the plasma potential. However, it was observed that there was not a single crossing "point" but rather an overlapping region between the hot and cold probe sweeps that was up to 0.5 V wide. Aside from this, the accuracy of the separation point method is on the order of kT_w or greater, where kT_w is the temperature of the emitting filament in eV and $kT_w/e \approx 0.2$ V for emission using tungsten [176].

Assuming that the plasma potential error was within ±0.5 V of the measured value, the resulting electron density and electron temperature were calculated at V_p±0.5 V to estimate peak error in density and temperature. The resulting variation in electron temperature and density was about ±50% of the values reported in Table 4.4.

4.2.4 Experimental Results

In this section, we present and compare the *I*−*V* characteristics of the spherical, cubic, and planar probes in Test Campaign 1, 2, and 3. Test Campaign 1 is the baseline condition where current collection is assessed to probes in a flowing plasma. In Test Campaign 2, the probes were re-oriented with respect to the plasma flow. In Test Campaign 3, the magnetic field strength was reduced below the ambient field and increased to a scaled value appropriate to approximate the LEO environment considered

in this study. The $I-V$ characteristics in each experimental test campaign are also presented in normalized form. The normalized current I_0 is I/I_{the} and the normalized voltage Φ_0 is $q(V-V_p)/kT_e$, where kT_e/q is the electron temperature in eV. Normalized $I-V$ characteristics allow the current collection per unit area to be evaluated for each probe geometry, giving a measure of "collection efficiency."

This section also compares the normalized $I-V$ characteristics of the probes to the WLP current collection model that was used to predict current collection earlier in the study (Chapter 3). In the following chapter, a revised collection model is developed from $I-V$ characteristics collected when the laboratory conditions captured several of the scaling parameters of LEO.

Langmuir probes measurements were taken before and after the cubic and planar probe $I-V$ characteristics. These measurements were used to determine the plasma potential, electron density, and electron temperature needed to normalize the $I-V$ characteristics. The extent of the normalized voltage for each $I-V$ characteristic is slightly different because the electron temperature that was measured varied between experimental test campaigns and slightly during tests. In this study, we are interested in collecting current in the electron saturation regime, so only voltages above the plasma potential are shown in the normalized $I-V$ characteristics (i.e., $\Phi_0 > 0$).

4.2.4.1 Analysis of Current Collection in a Flowing Plasma

In this section, the current collection behavior of the cubic and planar probes in Test Campaign 1 is described and compared with the current collection behavior of the spherical probe and the WLP model. The $I-V$ characteristics from Test Campaign 1 are shown in Figure 4.16. The planar probe's current collection behavior is similar to that of the spherical probe. The cubic probe collects more current than either the planar or spherical probe, but it has almost twice the surface area. The normalized $I-V$ characteristic reveals that the cubic probe collects less current per unit area than the spherical or planar probe.

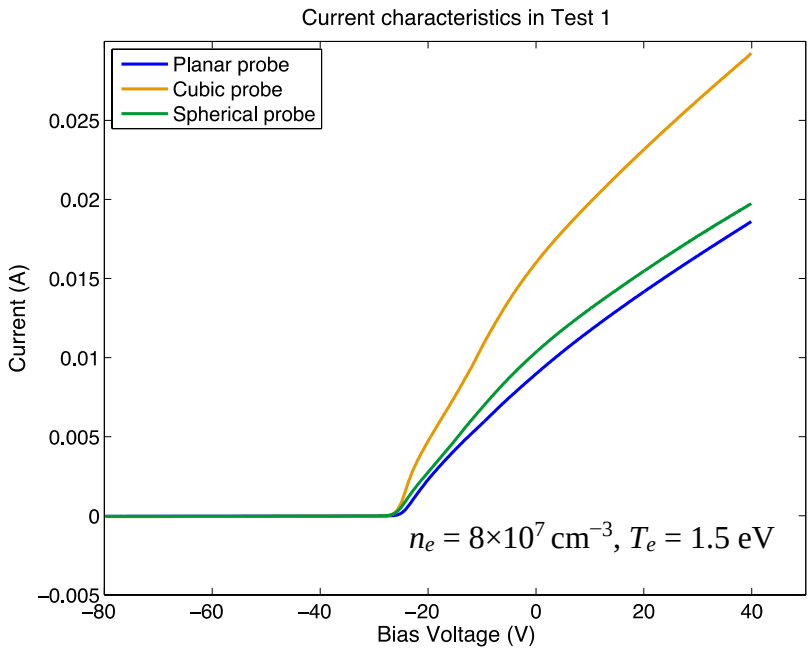

(a)

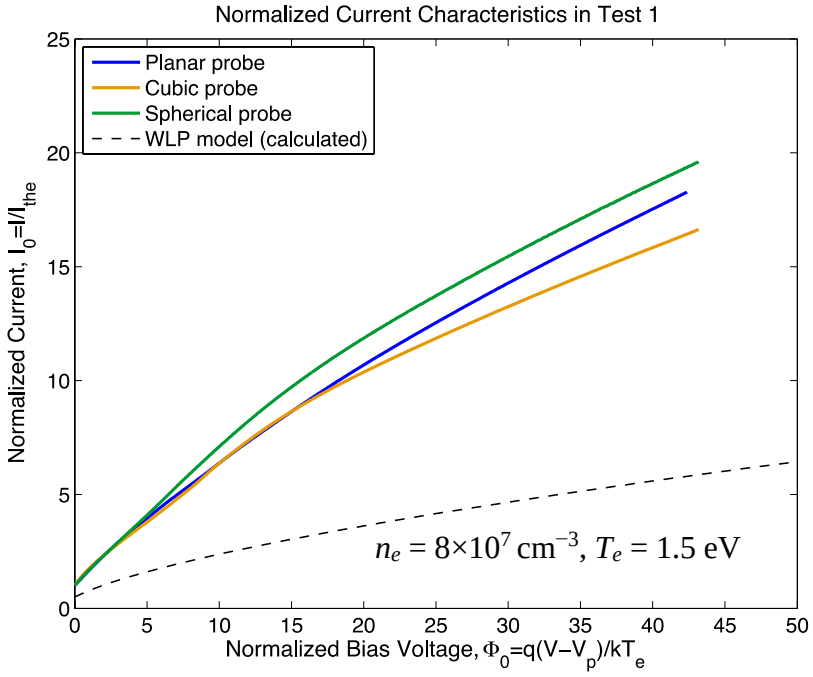

(b)

Figure 4.17: Current characteristics and normalize current characteristics in Test 1. The normalized *I–V* sweep is compared to the WLP model. In Test 1, $n_e = 8\times10^7$ cm^{-3} and $kT_e/q = 1.5$ eV. The resulting ratio r_p/λ_D was representative of the LEO environment considered here. The normalized voltage range in Test 1 is small. The peak normalized voltage $\Phi_0 = 46$ would roughly correspond to 4.5 V above the plasma potential in LEO, assuming $T_e \approx 0.1$ eV in LEO.

On a per-unit-area basis, the sphere was the most efficient collector, the cube was the least efficient collector, and the plate was between the sphere and the probe. The cubic probe's relatively low normalized current characteristic could be due to the inefficient collection on the probe's large, flat faces. It is also interesting to note that the planar probe collects nearly as much current as the sphere. This may be attributed to current collection at the probe's edges and corners. It should also be noted that if each probes' current were normalized by the minimum drag area, the planar probe would be the most efficient collector because it has the smallest cross-sectional area profile.

4.2.4.2 Analysis of Current Collection with Probes Re-oriented Relative to Plasma Flow

In Test Campaign 2, the probes were re-oriented with respect to the plasma flow. The current characteristics are shown in Figure 4.17. The electron density in Test Campaign 2 was roughly twice the electron density in Test Campaign 1 and the electron temperature in Test Campaign 2 was about half the electron temperature in Test Campaign 1. These conditions generated a smaller λ_D and a thinner sheath than in Test Campaign 1. Although the total current collected is higher for each probe, the normalized current collection characteristics in Test Campaign 2 grows less rapidly than the normalized current in Test Campaign 1, which suggests that the sheath is expanding less rapidly with increasing voltage when the parameter r_p/λ_D increases. Using maximum normalized voltage in Test Campaign 1 (Φ_0 = 45) for comparison, the normalized spherical probe current decreased by ~28% and the normalized cubic probe current decreased by ~37% in Test Campaign 2. This is a result worth noting that the growth the collection current with bias voltage is sensitive to r_p/λ_D. This also suggests that the current characteristic could change during an orbit as the surrounding ionospheric density and temperature change.

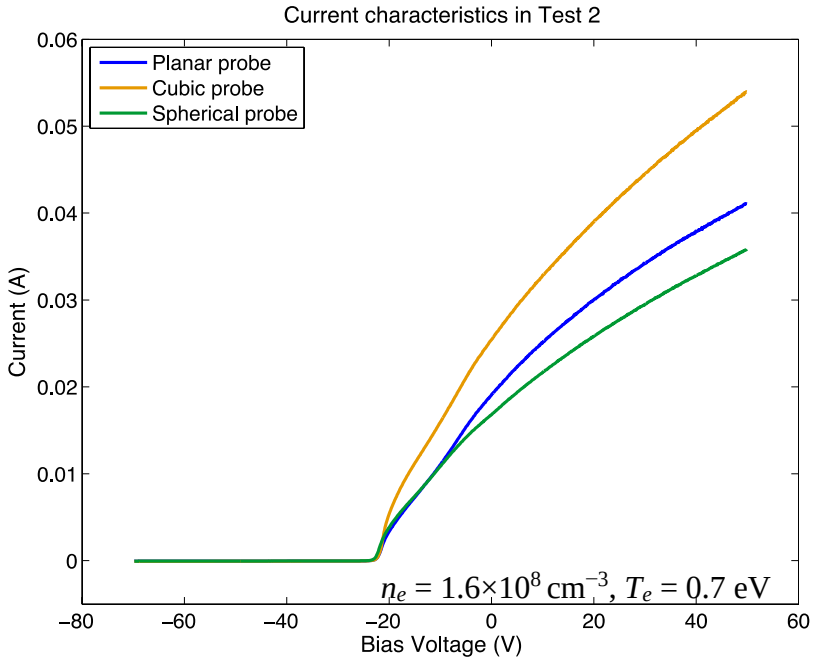

(a)

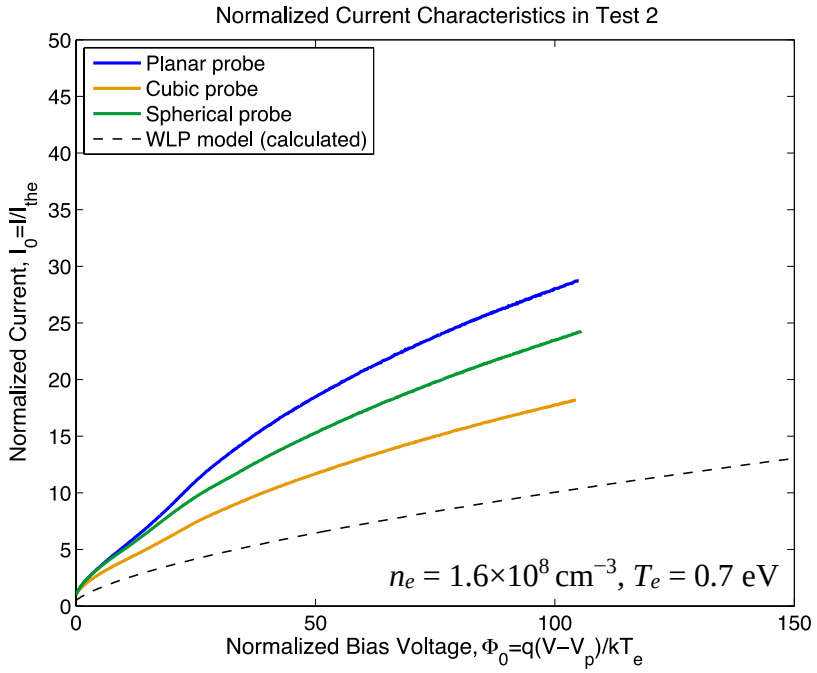

(b)

Figure 4.18: Current characteristics and normalize current characteristics in Test 1. The normalized *I–V* sweep is compared to the WLP model. In Test 2, n_e = 1.6×10^8 cm^{-3} and kT_e/q = 0.7 eV. The resulting ratio r_p/λ_D = 10 was representative of the LEO environment considered here. The planar probe is oriented with the maximum cross-sectional area perpendicular to the flow. The Debye length in Test 2 is also about half the Debye length in Test 1, changing the spherical and cubic probe current characteristics.

Additionally, the probes' current collection characteristics can be compared to the current predicted by the WLP model. In the voltage range tested, the WLP model falls well below the spherical, cubic, and planar probe currents. The spherical probe, the planar probe, and the cubic probe collect 3.5, 3, and 2.8 times as much current as the WLP model predicts. Thus, in the limited data set from Test Campaign 1, the WLP model provides a conservative estimate for current collection. Also, it should be mentioned that Test Campaign 1 represents a very small voltage range in LEO. The equivalent voltage range would only be about 4.6 V in LEO, assuming $T_e \approx 0.1$ eV.

In Test Campaign 2, the planar probe was oriented so the maximum cross-sectional drag area was facing the plasma flow. When $\Phi_0 < 10$, the planar probe current characteristic was about the same as the spherical probe characteristic. At about $\Phi_0 \approx 10$, the planar probe's current rose until about $\Phi_0 \approx 30$. In this orientation, the planar probe had the highest collection efficiency (i.e., the highest current collection per unit area), exceeding the spherical probe's collection efficiency by about 20%. In contrast, the planar probe's collection efficiency was 5% below the spherical probe's collection efficiency when it was oriented so the minimum cross-sectional area faced the plasma flow. Using the spherical probe as a reference, the increase in the planar probe's is then roughly 25% [155].

This increase in the planar probe's current suggests that current collection is impacted by the orientation of the collector with respect to the plasma flow, even in a plasma with a small fraction of drifting ions. It should also be noted that the 25% increase in collected current is not proportional to the increase in ram facing area. Between Test Campaign 1 and 2, the ram facing area increased 3.7 times. In a high-speed plasma, it is expected that the upstream face would experience significant current enhancement [89], [164], [198]. However, the effect would be different and less pronounced in presence of a large fraction of thermalized ions. This suggests that the experimental environment is not fully capturing the sheath anisotropy due to high-speed plasma flow.

Similar to Test Campaign 1, all of the probes in Test Campaign 2 collected more current than the WLP model calculated current. The cubic probe current characteristic also displays a small "knee" at the same normalized potential as the planar probe, but the current enhancement is relatively small.

4.2.4.3 Analysis of Current Collection in a Flowing Plasma with a Reduced and Enhanced Magnetic Field

In this section, experimental results are presented that evaluate the impact of the magnetic field on electron current collection. First, the effect of reducing the magnetic field below the ambient field strength is discussed. Afterwards, results are presented that show the impact of increasing the magnetic field to a mangitude scaled to approximate the LEO environment.

The spherical, cubic, and planar probe characteristics are shown in Figures 4.18 and 4.19, where the magntiude of the vertical component of the ambient magnetic field was reduced from 0.4 G to ~0.02 G. This reduced the total magnetic field magnitude to ~0.19 G. In the limited range of magnetic field strengths tested, no impact on current collection was observed when the field was reduced. The difference in the electron saturation current between the two magnetic field cases was less than 2% for all of the probes.

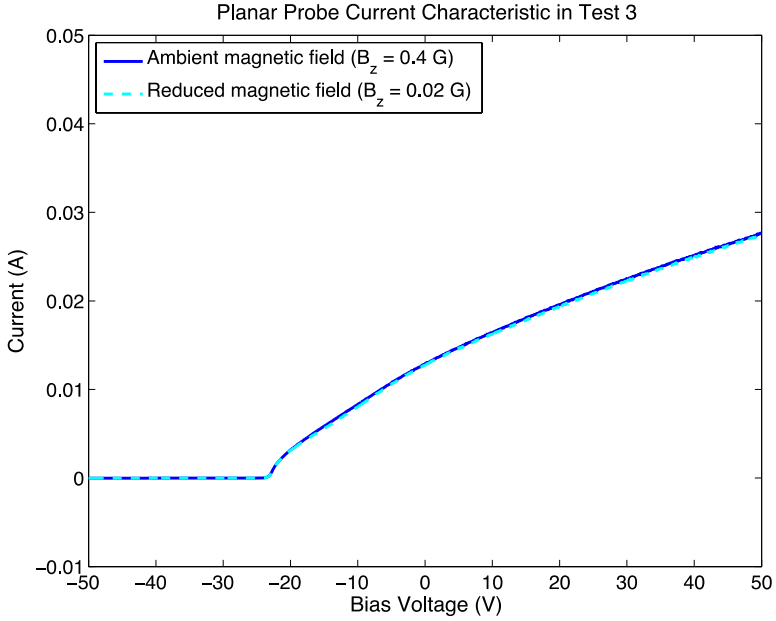

Figure 4.19: Current characteristics of the planar probe in the ambient magnetic field (0.4 G) and with the vertical component of the field reduced to ~0.02 G, which reduced the total magnetic field magnitude to 0.2 G.

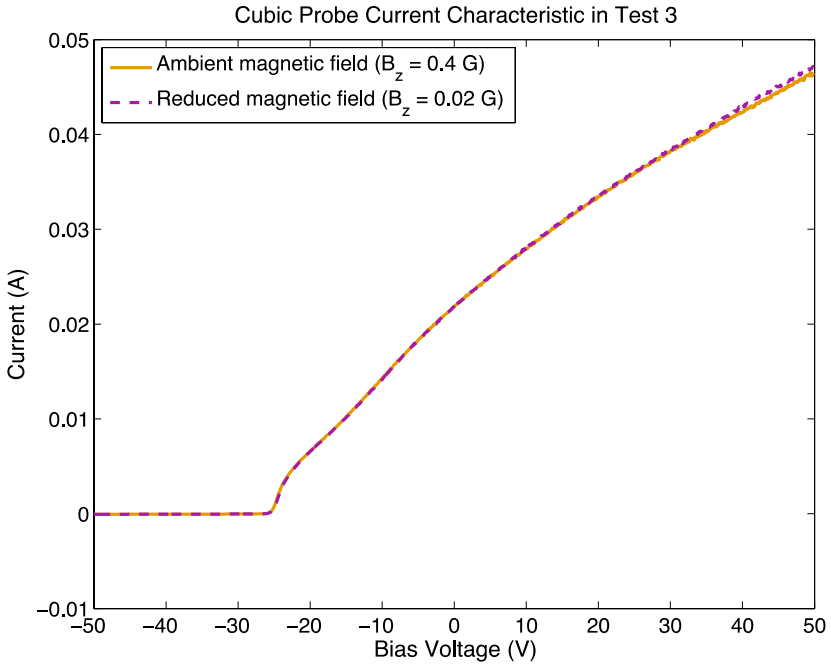

(a)

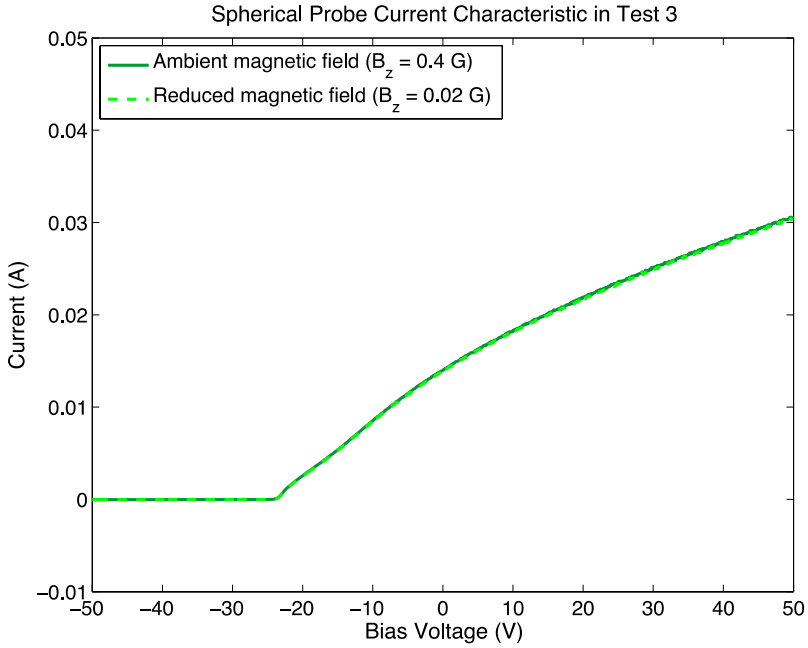

(b)

Figure 4.20: Current characteristics of the cubic and spherical probes in the ambient magnetic field (0.4 G) and with the vertical component of the field reduced to ~0.02 G, which reduced the total magnetic field magnitude to 0.2 G.

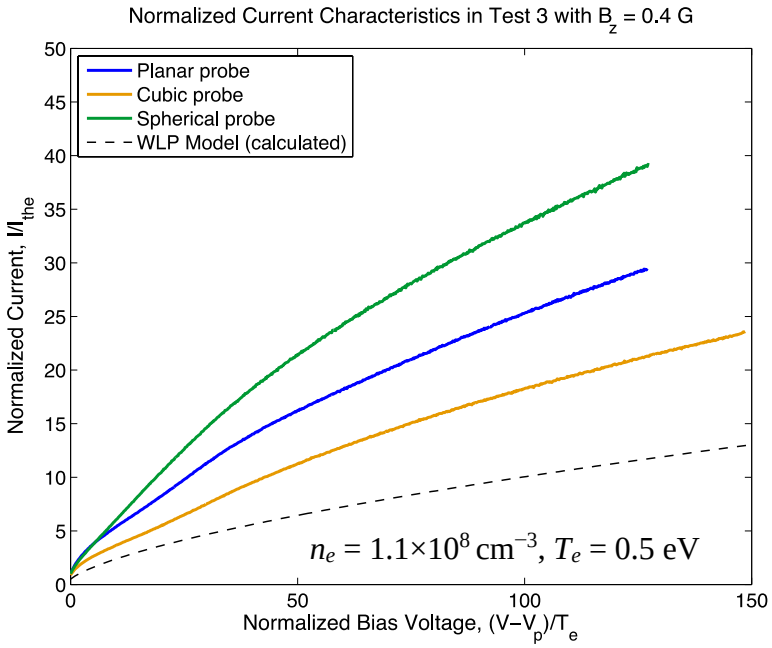

(a)

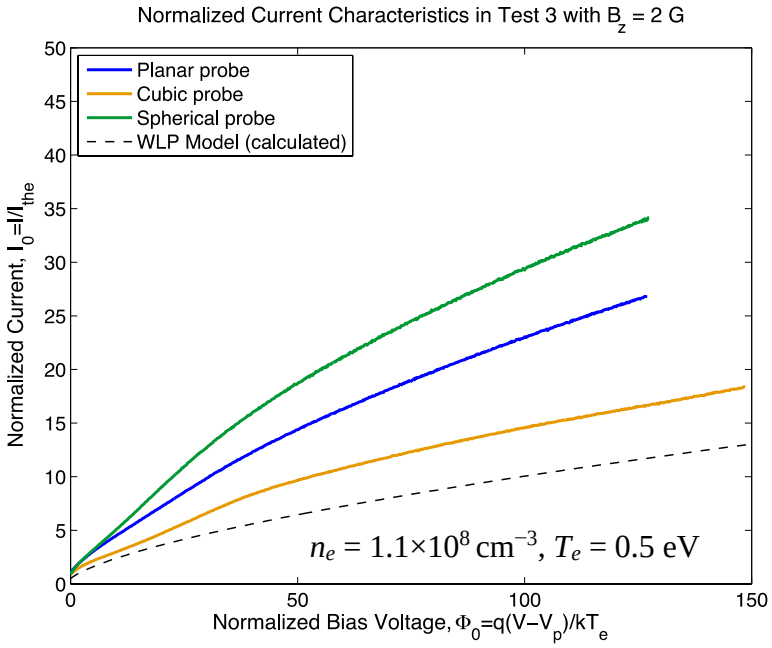

(b)

Figure 4.21: Normalized current characteristic for the cubic, planar and spherical probes in Test 3 with a vertical component of magnetic field of 0.4 G and 2 G. The normalized *I–V* sweeps are compared to the WLP model. In Test 3, $n_e = 1.1\times10^8$ cm^{-3} and $kT_e/q = 0.5$ eV. The resulting ratio $r_p/\lambda_D = 10$ was representative of the LEO environment considered here. The ratio r_p/r_L was 0.1 at 0.4 G and 0.6 at 2 G, which is approaching LEO conditions.

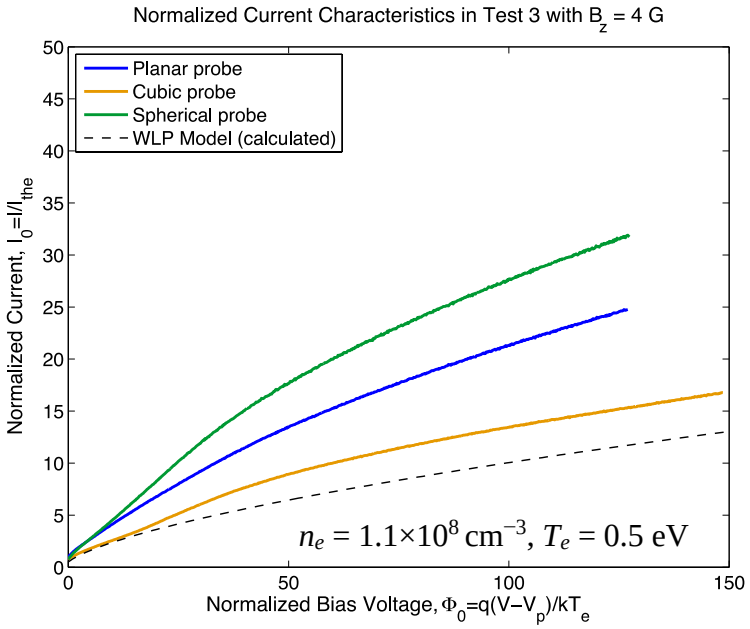

(a)

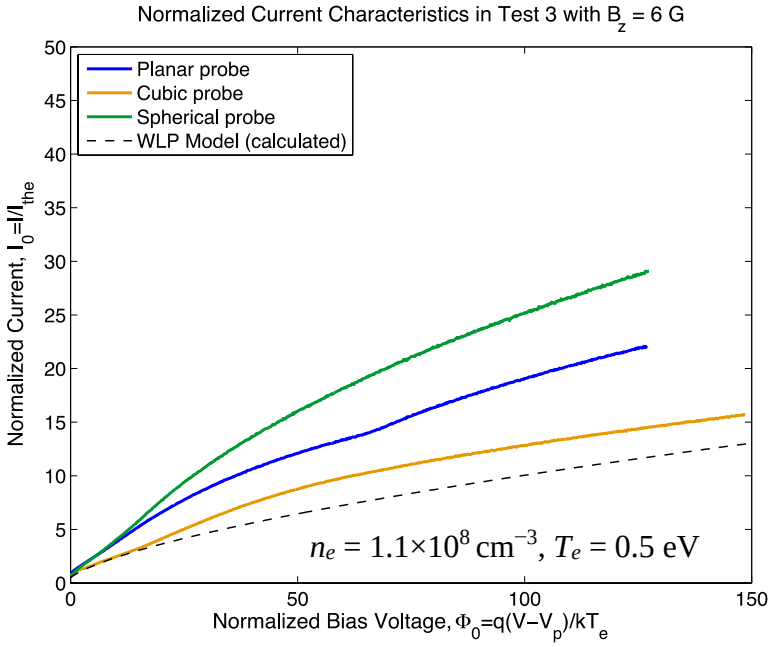

(b)

Figure 4.22: Normalized current characteristics in Test 3 with the vertical component of magnetic field equal to 4 G and 6 G. The normalized *I–V* sweeps are compared to the WLP model. In Test 3, n_e = 1.1×10^8 cm^{-3} and kT_e/q = 0.5 eV. The ratio r_p/λ_D = 10 was representative of the LEO environment considered in this study. At 4 G, r_p/r_L = 1.2. At 6 G, r_p/r_L = 1.8, which was representative of LEO conditions considered here.

The effect of enhancing the magnetic field is shown in Figures 4.21 and 4.22. Enhancing the magnetic field supresses the electron saturation current [150], which can be seen in Figures 4.20 and 4.21 as the slope of the *I–V* characteristics for all of the probes decreased with increasing magnetic field. When the magnetic field was 6 G, the ratio r_p/r_L was scaled to simulate the LEO environment and ω_{ce}/ν_e is about 1/3 of the LEO environment. In the 6 G field condition the WLP model was about 50% less at equal bias voltages than the planar probe current and 15% less than the cubic probe current.

In order to compare the effect of the magnetic field for each probe geometry, the ratio of electron to ion saturation current was determined for each probe. This ratio can be used to show the reduction in electron collection current at varying magnetic field levels [199], [200]. The plasma potential was determined for each probe and the electron saturation current was the current at V_p. The ion saturation current was calculated as [63]

$$I_{\mathrm{is}} = 0.6qn_i\sqrt{\frac{kT_e}{m_i}}A_{\mathrm{probe}}, \qquad \text{(Eq. 4.25)}$$

where A_{probe} is the probe area, $n_i \approx n_e$ in a quasi-neutral plasma, and the ion temperature is much less than the electron temperature, which is believed to be the case here. The electron density was determined from the current characteristic when B_z = 0.4 G (ambient magnetic field). This is a reasonable approach because the ion saturation current was about the same for each *I–V* sweep as the magnetic field strength was increased, varying by no more than 5%.

The ratio I_{es}/I_{is} is shown in Figure 4.22. I_{es}/I_{is} is not the same for each probe. As the magnetic field gets larger, I_{es}/I_{is} decreases. Interestingly, the change in I_{es}/I_{is} is also different for each probe, which suggests that the reduction in current collection due to magnetic field effects depends on probe geometry. This is shown more clearly in Figure 4.20, where I_{es}/I_{is} is normalized by the peak I_{es}/I_{is}. The magnetic field impacts the spherical probe's current collected most, decreasing the electron saturation current by ~40% at B_z = 6 G. The reduction in collection current for the cubic probe is similar to the spherical probe current.

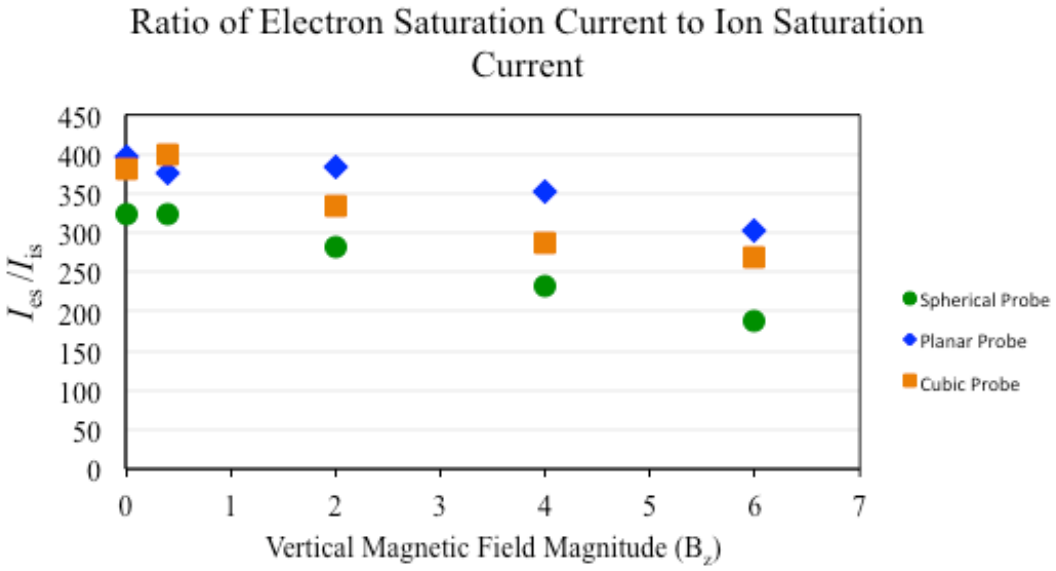

(a)

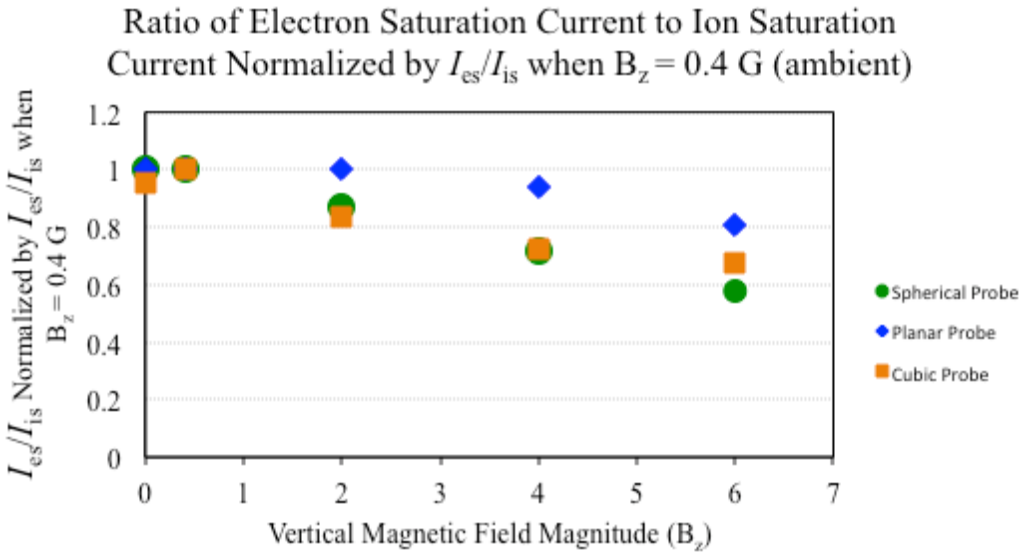

(b)

Figure 4.23: Ratio of the electron saturation current to the ion saturation current. The smallest magnetic field strength that appears to reduce the electron saturation current amplitude is $B_z = 2$ G. The ratio I_{es}/I_{is} is shown relative to the ambient magnetic field condition to show how the magnetic field decreases the electron current. The reduction in electron saturation current appears to be related to collector geometry.

The planar probe current reduction, however, is much less severe. The planar probe collection was roughly unchanged at 2 G where current from the other probe currents had reduced. At 6 G, the planar probe electron saturation current reduced less than 20%. The planar probe also appears to have a rise in its *I–V* characteristics at $\Phi_0 \approx 80$ that is not present at lower magnetic fields or in any other probe *I–V* characteristic. In the range of magnetic fields tested, the suppression of electron saturation current appears to be reduce linearly with the field strength with a slope determined, in part, by the shape and size of a probe relative to the gyroradius.

Here, a possible (qualitative) expanation for the change in probe currentis with magnetic field is offered. In Test Campaignt 3, the magetic field was directed vertically, perpendicular to the largest faces of the thin, planar probe. When the magnetic field was 6 G, the parameter r_p/r_L was similar to LEO ($r_p/r_L \sim 1.8$) and ω_{ce}/υ_e was about 300, sugesting that electrons were magnetized. Rubinstein and Laframboise (1982) reported that the electron current collected by a spherical electrode in a magnetized, stationary, collisionless plasma is the sum of the electron current traveling along a "magnetic bottle" that intersects the electrode and electron current traveling on flux tubes in "encircling orbits" that just touch the probe surface parellel to the field lines [201]. As the magnetic field strength increases, the electron gyroradii become smaller, the contribution from encircling orbits shrinks and the current collection area shifts to the area projected along magnetic field lines [201]. Although these probes are not in a completely stationary or collisionless plasma, the observed decrease in collected current in Test Campaign 3 could be the result of a reduction in the effective collection area with increasing magnetic field strength.

To explore this point further, the probe geometries must be consided. Of the probe geometries tested, the planar probe's current at $B_z = 6$ G decreases the least. Interestingly, the planar probe also has the largest fraction of its total area perpendicular to the magnetic field. The planar probe's total surface area is only slightly bigger than the area normal to the field. If the collection area were limited to the area normal to the field, the change would be relatively small. In constrast, the projected area of the cubic and spherical probe normal to the field is much less than the overall surface area. In this case, a change in the effective collection area could produce a significant reduction in

collection area. The planar probe and the cubic probe are compared in Figure 4.23. The top and bottom faces of the cubic and planar probes are normal to the magnetic field and have the same area. In Figure 4.23, it appears that the cubic probe current characteristic is roughly approaching the shape of the planar probe characteristic at B_z = 6 G, suggesting that the magnetic field is limiting collection to the area projected along the field lines. In addition, these results are consistent with Figures 12−14 of Dote et al. (1964) for spherical and planar probes in a magnetized plasma [202].

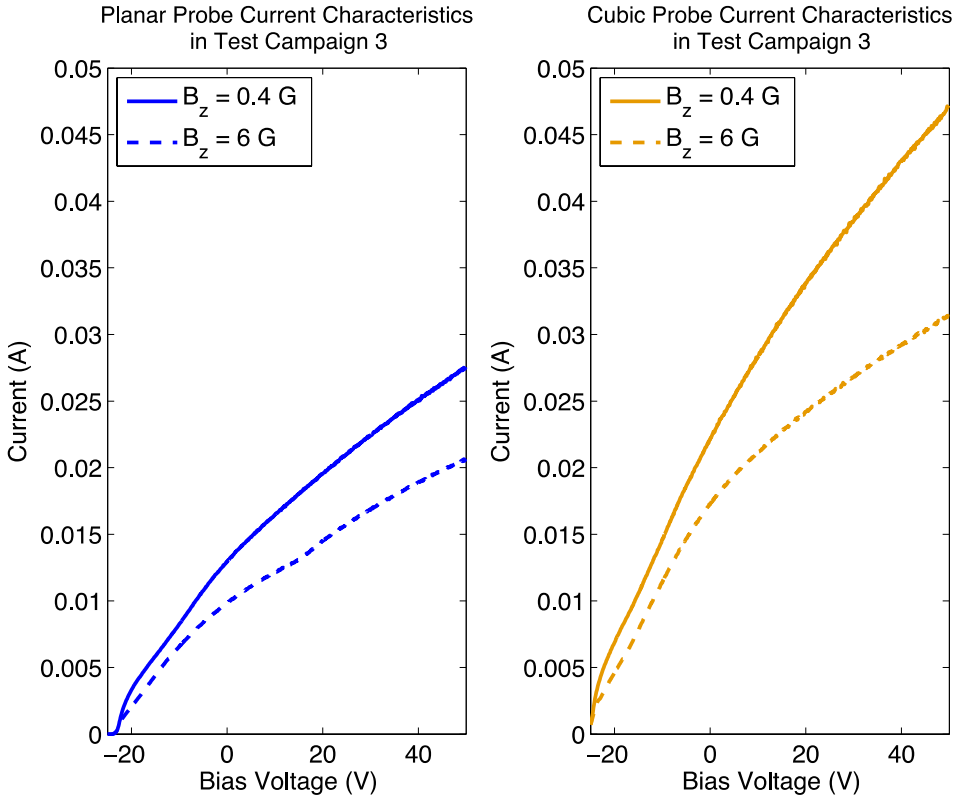

Figure 4.24: The current characteristics of the planar and cubic probes in ambient magnetic field and 6 G magnetic field.

To more completely analyze the anode, current collection should be investigated for different orientations between the probe and the magnetic field. From Test Campaign 2 and 3, the orientation of a probe with respect to the magnetic field *and* flow direction appear to be important. Future experiments will need to carefully investigate collection

on the ram facing side of the probe which, here, is also parallel to field lines. It is noted, however, that collisional effects in the laboratory plasma environment can cause current enhancement that is not representative of the collisionless LEO environment [151]. This motivates testing in an environment that better represents the mesothermal and collisionless conditions in LEO.

In summary, the effect of the magnetic field on current collection was observed and the current reduction related to magnetic field effects was least significant for the probe that had a majority of its area perpendicular to field lines. This suggess that a probe's current may change as the magnetic-field projected surface area changes during an orbit.

4.3 Present Status and Conclusions

The following conclusions were drawn from the experimental Test Campaigns:

- The spherical, cubic, and planar probe current characteristics exceeded estimates from the WLP model in each experimental test described. The WLP model was most similar to the collected currents at in the 6 G field condition of Test Campaign 3, where it was about 50% less at equal bias voltages than the planar and spherical probe current and 15% less than the cubic probe current.
- The probe size-to-Debye length ratio, r_p/λ_D, had a large effect on growth of the current-voltage characteristic. Generally, it was observed that increasing r_p/λ_D resulted in much less growth in collection current with bias voltage. This can be associated with a thinner sheath dimension. As λ_D decreased by a factor of 2 between Test Campaign 1 and Test Campaign 2, at an equal bias voltage the spherical probe collected ~28% current and the cubic probe collected ~37% current. This is significant because the plasma environment changes throughout an orbit in the ionosphere, and the shape of current characteristic may change as well.
- The planar probe's current was enhanced when it was oriented so the maximum cross-sectional area faced the plasma flow. In this orientation, the planar probe had the highest current collected per unit area, or

"collection efficiency," exceeding the spherical probe collection efficiency by about 20%. In contrast, the planar probe's collection efficiency was 5% below the spherical probe's collection efficiency when it was oriented so the minimum cross-sectional area faced the plasma flow. This suggests that the area facing the plasma flow is the dominant collection surface.

- The cubic probe has the lowest collection efficiency in all laboratory tests. This may be due to inefficient collection by its large (relative to λ_D), planar faces and because collection is dominated by the area facing the plasma flow and not as significant for the wake-facing area or sides parallel to the plasma flow. Future experiments could test collection for various orientations of the cubic probe to observe changes in collection due to attitude. It is thought that the plasma flow effects were likely degraded by the relatively high fraction of thermalized, charge exchange ions.
- Enhancing magnetic field strength from ambient to an appropriately scaled value to simulate the LEO environment decreased the electron saturation current as well as the growth in the current-collection characteristics. When B_z was increased to 6 G, the spherical and cubic probe electron saturation currents decreased by 40% and the planar probe electron saturation current decreased by almost 20%. This is attributed to the planar probe having a majority of its surface area normal to magnetic field lines. As magnetic field strength increased, it is expected that current is increasingly collected on magnetic flux tubes intersecting the probe. As a result, the cubic collector's collection current approached the planar probes collection current, suggesting the effective collection area was being limited by the magnetic field to the area projected in the direction of the field. Reducing the magnetic field strength below the ambient value had no noticeable impact on collection.
- The ratio ω_{ce}/ν_e in the experimental Test Campaigns was not representative of the LEO environment (approaching within a few times at the largest magnetic field value.). The electron collision frequency in the

experiment was much higher than the electron collision frequency in LEO. The higher collisions frequency may have produced higher rates of cross-field diffusion that enhanced collection current. Reducing the background neutral density could lower the electron collision frequency. Operating the experiment closer to the vacuum pump or performing the experiment in a vacuum facility with a higher xenon pumping speed could achieve this.

- The experiment also had a limited voltage range. Assuming $T_e \approx 0.1$ eV in the orbital environment, the equivalent voltage in LEO range was only a 10−15 V above the plasma potential. Experimental Test Campaigns that span a larger normalized voltage range could help determine the current characteristic over a larger voltage range.
- In future experiments, it will be important to characterize the ion velocity so the plasma flow can be more precisely characterized.

CHAPTER 5

Application of Experimental Results to the Miniaturized Electrodynamic Tether Study

This chapter evaluates the impact of the laboratory test results on the larger system concept study. In the laboratory experiment described in Chapter 4, current−voltage (I−V) measurements were taken in conditions approximating the low Earth orbit (LEO) environment. The results are discussed in this chapter and used to refine estimates of current collection and miniaturized electrodynamic tether (EDT) performance in LEO.

5.1 Summary of Experimental Results

A set of simplifying assumptions were made earlier in this study to facilitate estimating electron collection current. It was assumed that electron collection would take place on the external conducting surfaces of one of the tethered picosats or femtosats. Figure 3.2 in Chapter 3 provides an illustration of the picosats or femtosats considered in this study. The dimensions are listed in Table 3.1. The model used to estimate electron collection to the picosat and femtosat surfaces was based on an expression developed to interpret plasma parameters from the spherical wide sweeping Langmuir probe instrument (WLP) on the International Space Station (ISS) [145]. The model is described in section 4.1 in Chapter 4 and referred to as the "WLP model."

In order to evaluate previous estimates, ground-based plasma experiments were conducted to capture key characteristics of the satellite-LEO interaction. A cubic and a planar probe were used to approximate the small, “box-shaped” spacecraft considered in

this study. The laboratory tests investigated changes in electron current collection behavior due to (a) probe orientation relative to plasma flow and (b) magnetic field strength. The impact of varying the magnetic field strength was evaluated in the third laboratory test campaign, referred to as Test Campaign 3, which utilized a Helmholtz coil to generate an enhanced magnetic field that was scaled appropriately to simulate the magnetic field in LEO. The key observations and conclusions from the laboratory tests are as follows:

- Generally, the cubic probe's current was about 30−50% larger than the spherical probe's current at equal bias voltages. The planar probe's current was about 10−20% less than the spherical probe's current at equal bias voltages when the planar probe was oriented with the minimum cross sectional area projected in the direction of the plasma flow (in orbit, this would be the "minimum drag" orientation).
- The spherical, planar, and cubic probe current exceeded the current predicted by the WLP model in all tests. The WLP model was most similar to the measured current when the magnetic field in Test Campaign 3 was scaled appropriately to represent LEO. In this test, the WLP model predicted current that was about 50% less than the spherical probe current.
- Enhancing the magnetic field strength from ambient to an appropriately scaled value to simulate the LEO environment decreased the electron saturation current as well as the growth in the current-collection characteristics. As magnetic field strength increased, it appeared that the effective current collection area was being limited to the cross-sectional probe area normal to the field. The results appreared consistent with Figures 12−14 of Dote et al. (1964) for spherical and planar probes in a magnetized plasma [202].
- The ratio of electron gyrofrequency-to-collision frequency, ω_{ce}/ν_e, was not fully representative of the LEO environment. Instead, it was about ⅓ of the value in LEO at the maximum field strength used in the experiment. The reason the parameter ω_{ce}/ν_e was not fully representative of LEO was because the neutral density in the experiment was much higher than LEO, producing a higher electron collision frequency.

- The current collection behavior was sensitive to the probe radius-to-Debye length ratio, r_p/λ_D. It was observed that increasing r_p/λ_D resulted in less growth in the collection current with bias voltage.

These conclusions and observations are relevant to the following sections of the chapter as the experimental data is interpreted and compared to the LEO environment.

5.2 Development of a Current Collection Model from Experimental Results

In this section, the experimental data presented in Chapter 4 is analyzed and used to develop models for current collection in LEO. As a first step, analytical models are developed to estimate the current collection behavior of spherical, planar, and cubic probes in a magnetized plasma. These models are then compared to the experimental results and the WLP model in LEO. The laboratory environmental conditions that best approximated LEO are determined, and the model parameters from these environments are used to estimate current collection in LEO. This is *similar* to the approach taken by Siguier et al. (2013), Choinière et al. (2005), and Fuhrhop et al. (2009) to investigate current collection in the ionosphere by using ground-based laboratory measurements [89], [198], [203]. The current collection models are used in the following section to estimate EDT system performance.

5.2.1 Current Collection Models

In this section, a model is developed to estimate the electron saturation current collected by a spherical, planar, and cubic probe in the experiment and in LEO. Development of a model was necessary because the author was not able to identify an analytical model that could be readily applied to predict current collection in a mesothermal, magnetized plasma for the anode sizes and shapes considered in this study. The author attempted to fit the $I-V$ characteristics obtained in the laboratory experiments with analytical models from Mott-Smith and Langmuir (1926), Parker and Murphy (1967), Linson (1969), Rubinstein and Laframboise (1982), and Parker (1980) [83], [147, p. -], [201], [204], [205]. None of these models provided a good fit to the experimental data or the WLP data reported in Barjatya et al. (2009). In addition, they were all

developed for spherical electrodes or simple electrode geometries (infinite cylinders or infinite plates).

An OML-like expression of the form

$$I_{\text{fit}} = \alpha I_{\text{the}} \left(1 + \frac{q(V - V_p)}{kT_e}\right)^{\beta} \quad \text{(Eq. 5.1)}$$

was also used to fit the data, where the parameters α and β were varied to provide the best fit. I_{the} is the electron thermal current (Equation 4.2). However, α and β for each probe varied between laboratory tests and magnetic field conditions, making it difficult to use Equation 5.1 as a tool to predict current.

The purpose of the spherical, planar, and cubic probe models developed in this section is to fit the electron saturation characteristics measured in the laboratory experiments and, in the case of the spherical probe model, also fit the WLP data. Each model is developed following the same process:

1. Estimate the sheath size for each probe geometry as a function of sheath potential.
2. Estimate the current collected by the probe using the sheath size estimate.
3. Add a term to account for the reduction in electron saturation current due to magnetic field effects.
4. Add an additional term to more accurately fit the experimental data. This term is discussed further in the chapter.

The goal here is to develop expressions that can be used to calculate the electron saturation current collected on the conducting surfaces of picosats and femtosats, where the dimensions of the collecting body are roughly the same order of magnitude as the Debye length and the electron thermal gyroradius. It should be mentioned that the spherical, planar, and cubic probe electron saturation current models described in this section are developed in a manner similar to the ion saturation current collection model developed in Johnson and Holmes (1990) for small planar probes [206].

5.2.1.1 Spherical Probe Model

Current collection in the electron saturation regime increases as the sheath surrounding the body increases in size. The sheath essentially extends the effective area

for particle collection beyond the surface of the electrode. When an electrode is biased to the plasma potential, the collected current is simply the thermal current incident on the surface of the electrode. As the sheath expands with increasing bias voltage, the current collected by the electrode can be approximated as the thermal current incident on the sheath edge [206]. It should be noted that although the potential disturbance of the biased electrode is mostly screened out in the sheath, a small fraction of the total voltage (~T_e/2) falls in a second, extended region that connects the sheath to the plasma known as the pre-sheath. The sheath region is described in further detail in section 2.3.2.3 of Chapter 2 and section 4.2.3.4 of Chapter 4.

Figure 5 shows an illustration of the sheath surrounding a spherical collecting body in an isotropic plasma. When the sheath is very large with respect to the collecting body, the kinetic energy and angular momentum of the particles becomes important. In this regime, current collection is "orbit motion limited" and some particles that enter the sheath are not collected [147]. This is the thick-sheath OML regime, which is described in section 4.2.1.1 of Chapter 4. When the sheath is very small with respect to the collecting body dimensions, it can be treated as a narrow gap between the electrode and the plasma. In this regime, collection is “space charge limited.” Growth in a very thin sheath does not appreciably increase the effective collection area, and the resulting collection current is expressed as the random thermal current incident on the surface of the body.

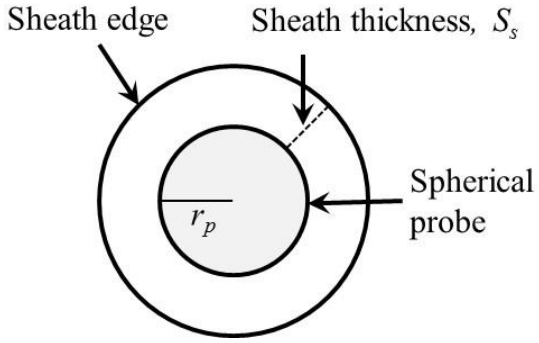

Figure 5.1: Sheath geometry for a spherical electrode in an isotropic plasma.

Walker (1965) developed an expression for the thickness of a sheath around a spherical electrode [207]. It is assumed here that the expression for sheath thickness can

be used to estimate collection current by multiplying the sheath area by the thermal current density [206]. The sheath thickness is given by [208]

$$S_s = 0.83 r_p^{\frac{1}{3}} \lambda_D^{\frac{2}{3}} \left(\frac{q(V-V_p)}{kT_e}\right)^{\frac{1}{2}}, \quad \text{(Eq. 5.2)}$$

where V is the bias voltage on the spherical body, V_p is the plasma potential, and when $V-V_p \geq 1$. Equation 5.2 assumes sheath expansion in an isotropic, Maxwellian, collisionless plasma.

The area of the sheath is therefore

$$A_s = 4\pi\left(r_p + S_s\right)^2, \quad \text{(Eq. 5.3)}$$

where r_p is the radius of the sphere. At $V=V_p$, the sheath area is simply the area of the sphere. The thermal current collected by the sheath is

$$I_s = J_{\text{the}} 4\pi\left(r_p + S_s\right)^2, \quad \text{(Eq. 5.4)}$$

where the thermal current density, J_{the}, is

$$J_{\text{the}} = \frac{1}{4} q n_e \sqrt{\frac{8kT_e}{\pi m_e}} \quad \text{(Eq. 5.5)}$$

and the thermal current, I_{the}, is the product of the thermal current density and the probe area, or $J_{\text{the}} A_{\text{probe}}$.

Assuming, as Johnson and Holmes (1990) [206], that the thermal current collected at the sheath edge is equal to the current collected by the probe, the electron saturation current can be expressed as

$$I_s = J_{\text{the}} 4\pi {r_p}^2 \left(1 + \frac{S_s}{r_p}\right)^2. \quad \text{(Eq. 5.6)}$$

Substituting in Equation 5.6 for S_s, one can obtain the expression

$$I_s = J_{\text{the}} 4\pi {r_p}^2 \left(1 + 0.83 \left(\frac{\lambda_D}{r_p}\right)^{\frac{2}{3}} \left(\frac{q(V-V_p)}{kT_e}\right)^{\frac{1}{2}}\right)^2, \quad \text{(Eq. 5.7)}$$

which gives the approximate collection current to a sphere in a collisionless, isotropic, Maxwellian plasma.

It was assumed here that the sheath has a well-defined "edge" to facilitate calculation of the electron collection current. In fact, it would be more accurate to approximate the sheath “edge” as a second region that gradually transitions to the undisturbed plasma over the width of the pre-sheath [64]. The assumption of the defined sheath edge may cause error in current collection estimates, although this error is not quantified here. It is also important to reiterate that Equation 5.7 is based on an assumption made for sheath thickness as a function of bias voltage (expressed in Equation 5.2). This assumption does not apply when the probe is much larger than the Debye length. In fact, Bettinger and Walker (1965) found that the error in the sheath size (Equation 5.2) increases with the probe size-to-Debye length ratio, and becomes large for spherical electrodes where $r_p/\lambda_D >> 1$ [208]. In other words, Equation 5.7 may not accurately estimate current collection in the thin sheath regime, suggesting a limit on the applicability of Equation 5.7.

Magnetic fields limit the diffusion of current across field lines and reduce the electron saturation current. Magnetic field effects on current collection were discussed in section 4.2.1.2 of Chapter 4. To capture the effect of the magnetic field on current collection, the electron saturation current can be expressed as [199]

$$I_{\mathrm{sB}} = \eta_s I_s. \qquad \text{(Eq. 5.8)}$$

where η_s represents a reduction in electron saturation current ($0 < \eta_s < 1$) and I_{sB} represents the current collected to a spherical electrode in the presence of a magnetic field. Dote et al. (1964) developed an expression for η_s, which can be approximated as [202]

$$\eta_s \approx \left(1 + \frac{\pi}{2}\left(1 + \left(\frac{\omega_{ce}}{\nu_e}\right)^2\right)^{\frac{1}{2}} \frac{r_p}{\lambda_e}\right)^{-1}, \qquad \text{(Eq. 5.9)}$$

where λ_e is the electron mean free path and $\omega_{\mathrm{ce}}/\nu_{\mathrm{e}}$ is the ratio of electron gyrofrequency-to-collision frequency. The electron mean free path is the ratio of the mean thermal speed and the collision frequency which, for a Maxwellian plasma, is given by

$$\lambda_e = \frac{1}{\nu_e}\sqrt{\frac{8kT_e}{\pi m_e}}. \qquad \text{(Eq. 5.10)}$$

In an unmagnetized plasma, η_s = 1. Equation 5.9 assumes ions are not magnetized (the ion gyroradius is much larger than the probe size), effects other than collisions that cause cross-field transport, like turbulence, are negligible, and the disturbance in the plasma caused by the probe is large with respect to the probe dimensions [202].

It should be noted that in case of cuboid or box-shaped collecting bodies, the coefficient representing the reduction in the electron saturation current is different for surfaces parallel and perpendicular to magnetic field lines [202], [209]. Diffusion of electrons along field lines is not reduced and thus the collection current for surfaces normal to field lines is not restricted as severely as current collection to surfaces parallel to field lines. As a result, one coefficient is used to represent the reduction in electron saturation current to surfaces parallel to field lines, $\eta_{\parallel}$, and a separate coefficient is used to represent the reduction in current to surfaces perpendicular to field lines, $\eta_{\perp}$. In the case of a sphere, however, a single value for η_s is used.

Finally, a coefficient, α_s, was included to more accurately fit the laboratory and LEO data. A similar fitting coefficient was also added to the planar and cubic probe models, although the amplitudes of the coefficients are different. It is not clear why the coefficient was necessary to fit the experimental data and the WLP model, but high-speed plasma flow presents one possible explanation to be investigated further. Plasma flow has been observed to cause current enhancement. The TSS-1 and TSS-1R missions are examples of this. Electron saturation current 4−6 times the Parker−Murphy current was measured in the TSS-1 mission [157]. In the TSS-1R mission, electron saturation current 2−3 times the Parker−Murphy current was measured [57]. The enhancement appeared when the anode was biased above the ram kinetic energy of the O^+ ions.

Including the fitting parameter α_s, the final expression for the collection current is

$$I_s = \alpha_s \eta_s J_{\text{the}} 4\pi {r_p}^2 \left(1 + 0.83 \left(\frac{\lambda_D}{r_p}\right)^{\frac{2}{3}} \left(\frac{q(V-V_p)}{kT_e}\right)^{\frac{1}{2}}\right)^2 \qquad \text{(Eq. 5.11)}$$

for a spherical electrode. It can be seen that in Equation 5.11 that the ratio of the Debye length to the probe size impacts the collection current. This ratio is essential for estimating collection current in a regime where the probe size is of the same order of

magnitude as the Debye length and current collection is neither in a thick or thin sheath regime.

5.2.1.2 Planar Probe Model

This section presents a model developed to estimate the electron saturation current to a planar probe. Figure 5.2 shows an image of a planar probe and the sheath. The current collection expression developed in this section for the planar probe is derived in a manner very similar to the spherical probe current collection expression. The first in developing the current collection expression is to estimate the sheath thickness around the probe edges and faces.

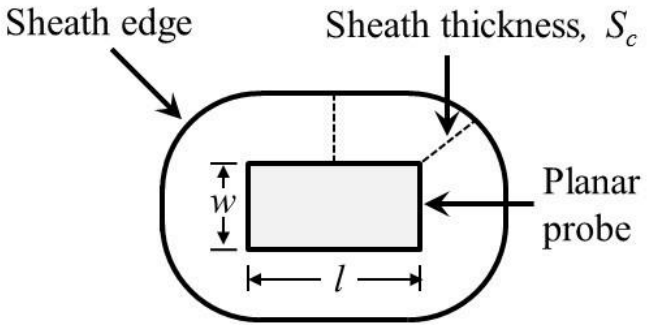

Figure 5.2: Sheath geometry for the planar probe in an isotropic plasma.

The current collected by the large, flat, planar face of an electrode in an isotropic, collisionless plasma can be estimated by approximating the sheath as a gap in a planar diode [206]. The current crossing the gap would be space-charge limited. The Child-Langmuir law for current across a gap is [210]

$$J_e = \frac{4\varepsilon_0}{9}\left(\frac{2q}{m_e}\right)^{\frac{1}{4}}\frac{(V-V_p)^{\frac{3}{2}}}{{S_c}^2}, \qquad \text{(Eq. 5.12)}$$

where S_c is the distance across the gap. The distance S_c can be expressed as [206]

$$S_c = \kappa_c \lambda_D, \qquad \text{(Eq. 5.13)}$$

which simply expresses the gap distance in terms of the Debye length. Substituting Equation 5.13 into Equation 5.12, the expression for current across the gap becomes

$$J_e = \frac{4}{9}\left(\frac{2}{m_e}\right)^{\frac{1}{2}}\left(\frac{n_e}{T_e}\right)\frac{\left(q(V-V_p)\right)^{\frac{3}{2}}}{{\kappa_c}^2}. \qquad \text{(Eq. 5.14)}$$

The electron thermal current density at the sheath edge is given by Equation 5.5. Assuming that thermal current incident on the sheath edge is equal to the current crossing the sheath, κ_c can be solved for as

$$\kappa_c = \left(\frac{8}{9}\right)^{\frac{1}{2}} \pi^{\frac{1}{4}} \left(\frac{q(V-V_p)}{kT_e}\right)^{\frac{3}{4}}. \quad \text{(Eq. 5.15)}$$

Thus, the growth in the sheath can be expressed as a function of the bias voltage.

In the planar electrode geometry considered here, the electrode has dimensions $w \times w \times l$. In other words, the planar electrode has two square faces of area w^2 and four rectangular faces of area wl. Although these dimensions are used to represent the planar probe, the 200-g planar picosat, and the 10-g ChipSat, all of which have 2 square and 4 rectangular faces, this model could easily be applied to an arbitrary box-shaped electrode with dimensions $w \times h \times l$, where $w \neq h \neq l$.

For infinite planar electrodes, the planar sheath area does not significantly "grow" or increase the effective collection area in contact with the plasma, allowing the sheath area to be approximated as the area of the face [147]. For finite planar electrodes, however, the sheath around the edges increases in size with bias voltage. As the "rounded" sheath around the edges grows, the collection current increases. In fact, it is this rounded sheath that has been identified as the cause of the increase in collection current with bias voltage for planar electrodes [206], [211]. Here, it is assumed that the sheath around each 90° edge can be approximated as one-quarter of a cylinder with radius $\kappa_c\lambda_D$ stretching the length of the edge [206]. Using this approximation, the sheath area around an edge of length l would be $\frac{1}{4}(2\pi\kappa_c\lambda_D l)$ and the sheath area around each edge of length w would be $\frac{1}{4}(2\pi\kappa_c\lambda_D w)$ [206].

To estimate the collection current in the presence of a magnetic field, it will be important later in this section to distinguish between faces perpendicular and parallel to magnetic field lines. Recall that the reduction in electron saturation current is different in each case. For this reason, the strategy taken here is to develop an expression for the current collected by a single face. This allows the total current to be calculated by adding up the contributions from all of the faces. In this way, it is possible to "build" a current collection model for a box-shaped electrode.

It should be noted that adjacent faces share an edge. For this simple model, the solution is to "split the sheath in two," adding ½ of the sheath area around each edge to the sheath area of the adjacent faces. A more sophisticated model would include current collection to corners as well, but that is beyond the scope of this dissertation.

The assumptions for this simple geometry model are summarized below:

- The sheath around each face has (a) a planar region that has an area equal to the area of the face and (b) a rounded region generated by the corners.
- The sheath around the corners is approximated as a quarter of a cylinder with radius $\kappa_c\lambda_D$. The sheath area around each edge of length l would be $\frac{1}{4}(2\pi\kappa_c\lambda_D l)$ and the sheath area around each edge of length w would be $\frac{1}{4}(2\pi\kappa_c\lambda_D w)$.
- Each edge is shared by two adjacent faces. It is assumed here that the sheath area around the edges can be split evenly between the faces in contact with the edge.
- Each face has 4 edges, so the sheath around each face will have a contribution from all 4 edges.

The resulting sheath area of a single face with dimensions $w \times l$ would be

$$A_{1\text{face}} = wl + \frac{1}{2}\frac{2\pi\kappa_c\lambda_D l}{4} + \frac{1}{2}\frac{2\pi\kappa_c\lambda_D l}{4} + \frac{1}{2}\frac{2\pi\kappa_c\lambda_D w}{4} + \frac{1}{2}\frac{2\pi\kappa_c\lambda_D w}{4}. \quad \text{(Eq. 5.16)}$$

The current collected at the sheath edge is

$$I_{1\text{face}} = J_{\text{the}}wl + \frac{1}{2}J_{\text{the}}\pi\kappa_c\lambda_D l + \frac{1}{2}J_{\text{the}}\pi\kappa_c\lambda_D w. \quad \text{(Eq. 5.17)}$$

This current can also be written as

$$I_{1\text{face}} = J_{\text{the}}wl\left(1 + \frac{\pi}{2}\kappa_c\lambda_D\frac{w+l}{wl}\right). \quad \text{(Eq. 5.18)}$$

Substituting in Equation 5.18 for κ_c, the current collected by the face is given by

$$I_{1\text{face}} = J_{\text{the}}wl\left(1 + \lambda_D\frac{w+l}{wl}\left(\frac{2}{9}\right)^{\frac{1}{2}}\pi^{\frac{5}{4}}\left(\frac{q(V-V_p)}{kT_e}\right)^{\frac{3}{4}}\right). \quad \text{(Eq. 5.19)}$$

Similarly, the current collected by a face of dimensions $w \times w$ would be

$$I_{1\text{face}} = J_{\text{the}} wl\left(1 + \frac{\lambda_D}{w}\left(\frac{8}{9}\right)^{\frac{1}{2}}\pi^{\frac{5}{4}}\left(\frac{q(V-V_p)}{kT_e}\right)^{\frac{3}{4}}\right). \quad \text{(Eq. 5.20)}$$

Equation 5.20 assumes the planar diode model for each face, which may not be accurate if ½w << λ_D or ½l << λ_D (this is analogous to r_p << λ_D).

The magnetic field reduces the electron saturation current. If the face has area w×l perpendicular to field lines, the current collected is

$$I_{1\text{face}\perp} = \eta_\perp J_{\text{the}} wl\left(1 + \lambda_D \frac{w+l}{wl}\left(\frac{2}{9}\right)^{\frac{1}{2}}\pi^{\frac{5}{4}}\left(\frac{q(V-V_p)}{kT_e}\right)^{\frac{3}{4}}\right), \quad \text{(Eq. 5.21)}$$

where

$$\eta_\perp = \alpha_B{}^{\frac{1}{2}} \frac{1+\frac{32}{3}\frac{\lambda_e}{\pi r_p}}{\left(1+\frac{32}{3}\frac{\lambda_e}{\pi r_p}\alpha^{\frac{1}{2}}\right)} \quad \text{(Eq. 5.22)}$$

and $\alpha_B = (1+(\omega_{ce}/\nu_e)^2)^{-1}$. If the face has cross-sectional area w×l parallel to magnetic field lines, the collection current is

$$I_{1\text{face}\parallel} = \eta_\parallel J_{\text{the}} wl\left(1 + \lambda_D \frac{w+l}{wl}\left(\frac{2}{9}\right)^{\frac{1}{2}}\pi^{\frac{5}{4}}\left(\frac{q(V-V_p)}{kT_e}\right)^{\frac{3}{4}}\right), \quad \text{(Eq. 5.23)}$$

where

$$\eta_\parallel = \frac{\pi\alpha^{\frac{1}{2}}}{2K(k)} \frac{1+\frac{32}{3}\frac{\lambda_e}{\pi r_p}}{\left(1+\frac{16}{3}\frac{\lambda_e\alpha^{\frac{1}{2}}}{K(k) r_p}\right)}. \quad \text{(Eq. 5.24)}$$

$K(k)$ is the elliptic integral of the first kind for $k = (1-\alpha_B)^{½}$. In the presence of a magnetic field, generally speaking, $\eta_\parallel < \eta_\perp$. It is assumed in Equations 5.22 and 5.24 that the ions are not magnetized, effects other than collisions that cause cross-field transport, like turbulence, can be neglected, and $r_p > \lambda_D$. Equations 5.21 and 5.23 can easily be re-written if the cross-sectional area w×w is normal to magnetic field lines.

The current collected by the probe is

$$I_{\text{p}} = 2I_{1\text{face}\perp} + 4I_{1\text{face}\parallel}, \quad \text{(Eq. 5.25)}$$

where the appropriate areas and dimensions are used for the parallel and perpendicular faces. Equation 5.25 was modified in the following manner to fit to the experimental data:

$$I_{\mathrm{p}} = \alpha_p(2I_{1\mathrm{face}\perp} + 4I_{1\mathrm{face}\parallel}). \qquad \text{(Eq. 5.26)}$$

Thus, the planar probe current has a fitting coefficient similar to the spherical probe.

There are limitations to the applicability of Equation 5.26. The planar diode model was used to approximate the sheath that forms on the flat faces of the box-shaped electrode. Approximating the sheath as a planar diode may not be appropriate for finite planar surfaces in the thick sheath regime, where $r_p/\lambda_D << 1$ [147], [211]. Additional testing would provide valuable insight into the model that is appropriate when the planar probe collects current in the thick sheath regime.

5.2.1.3 Cubic Probe Model

The cubic probe model is simply treated here as a special case of the planar probe model where $l = w$, making the dimensions $w \times w \times w$. An illustration of the cubic probe sheath is shown in Figure 5.3. It is assumed here that the expressions developed for sheath thickness for a planar probe, Equation 5.13 and Equation 5.15, also apply in the case of a cubic probe.

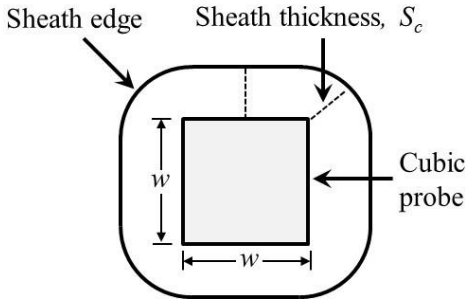

Figure 5.3: Sheath geometry for the cubic probe.

The same expressions, 5.21 and 5.23 can be used to estimate current collection. However, an additional fitting parameter was added to provide a better fit to the laboratory measurements. Equation 5.23 can be expressed as

$$I_{1\text{cubeface}\parallel} = \eta_{\parallel} J_{\text{the}} w^2 \left(\alpha_{c2} + \frac{\lambda_D}{w} \left(\frac{8}{9}\right)^{\frac{1}{2}} \pi^{\frac{5}{4}} \left(\frac{q(V-V_p)}{kT_e}\right)^{\frac{3}{4}} \right). \quad \text{(Eq. 5.27)}$$

It should be noted that Equation 5.27 has an additional fitting parameter α_{c2}. The reason for this additional term α_{c2} is not clear, but the need for this term to adequately fit the laboratory data may suggest that a better model is needed to estimate current collection to a cube. For a square face with dimensions $w \times w$ perpendicular to magnetic field lines, Equation 5.21 can be expressed as

$$I_{1\text{cubeface}\perp} = \eta_{\perp} J_{\text{the}} w^2 \left(1 + \frac{\lambda_D}{w} \left(\frac{8}{9}\right)^{\frac{1}{2}} \pi^{\frac{5}{4}} \left(\frac{q(V-V_p)}{kT_e}\right)^{\frac{3}{4}} \right). \quad \text{(Eq. 5.28)}$$

The cube's collection current is then

$$I_{\text{c}} = \alpha_{\text{c1}} (2I_{1\text{cubeface}\perp} + 4I_{1\text{cubeface}\parallel}). \quad \text{(Eq. 5.29)}$$

Thus the expression of cubic probe current is similar to the expression for planar probe current, although it was determined that an additional fitting parameter was needed to adequately fit the experimental data. The limitations of the cubic probe model, represented by Equation 5.29, are similar to the limitations of the planar probe model (i.e., not assumed to be applicable when $r_p/\lambda_D << 1$).

5.2.2 Comparison of the current collection models to experimental results

In this section, current calculated using the spherical, planar, and cubic probe model is compared to *I*−*V* characteristics obtained in the laboratory experiments for each probe. Figures 5.4−5.6 show the current calculated using the models and the *I*−*V* characteristics obtained in the experiments. The coefficients used for fitting are listed in Table 5.1. The plasma parameters for each experimental test campaign are listed in the previous chapter in Table 4.4.

It can be seen that the current collection models generally fit the laboratory data well at relatively high voltages of the *I*−*V* characteristics (>20 V) but not well at the relatively low voltages (<0 V). Fitting the entire electron saturation *I*−*V* characteristic using the models developed in the previous section was challenging because the shape of

the *I*−*V* characteristic changed with bias voltage. There appeared to be three distinct characteristics in the electron saturation current for all of the probes. The first, referred to here as the "low voltage characteristic," was apparent in the voltage range between the plasma potential and 5−10 V above the plasma potential. At higher voltages, a second *I*−*V* characteristic appeared and the current increased more rapidly with bias voltage than in the low voltage characteristic. Finally, about 20−30 V above the plasma potential, the *I*−*V* characteristics assumed a different, less steep slope. This last section is referred to here as the "high voltage characteristic." The characteristics are most apparent in the cubic probe's *I*−*V* characteristic, shown in Figure 5.6. However, this behavior was observed in the *I*−*V* characteristics of all of the probes in all of the laboratory experiments. It is important to point out that there is a smooth, gradual transition between each of the characteristics rather than a well-defined, "hard boundary."

The shape of the measured *I*−*V* characteristics in Figures 5.4−5.6 is consistent with other *I*−*V* characteristics measured in a high-speed flowing plasma. This topic was discussed in the previous chapter, in sections 4.2.3.2 and 4.2.4.2. The growth in current apparent between the low voltage and high voltage characteristics has been associated with the deflection of high-speed ions and, in a magnetized plasma, the onset of turbulence that may enhance current collection [57], [155]. Figure 1 in Skøelv et al. (1984) shows similar regions of the electron saturation characteristic for a planar Langmuir probe in a flowing plasma [155]. In addition, a somewhat similar increase in the *I*–*V* characteristic was observed during the Tethered Satellite System Reflight (TSS-1R) space mission when the anode was biased (above the plasma potential) to the potential equal to the kinetic ram energy of ionospheric O^+ ions (5.3 eV) [57].

However, the models developed here clearly do not account for different regions in the electron saturation current. Instead, the models developed here fit the small low voltage characteristic relatively well by using a fitting coefficient close to 1. When a fitting coefficient greater than one was used, the models fit the high voltage characteristic well. It will be important in future work to better understand the shape of the electron saturation current and develop a model that more adequately captures the current enhancement.

A decision was made here to fit the high voltage characteristics for each probe. It was assumed that the high voltage characteristics for each probe would be most representative of the current collection behavior at large bias voltages in LEO. Current collection at large bias voltages is considered particularly important here because the EDT anode will likely be biased well above the plasma potential to collect sufficient current for propulsion.

It should also be noted that the fitting parameters varied between 2 and 4 for the different shapes and varied between experiments. Recall that B_z is the vertical component of the magnetic field, and that B_z varied during Test Campaign 3. The fitting parameter changed very little as B_z was increased from 2 to 6 G, suggesting that the model adequately estimates the reduction in electron saturation current due to magnetic field effects.

It is not clear why the fitting coefficients changed between experimental test campaigns. The change in the fitting coefficient did not appear to correlate with any of the plasma parameters that were measured. It is possible that the fitting coefficient were impacted by measurement error. Additional testing is necessary to better understand these changes. Figure 5.6b shows that the cubic probe current collection model provided a relatively poor fit to the measured cubic probe's current, or a reasonable fit to a small range of bias voltages.

Table 5.1: Coefficients used to fit the laboratory data in Test Campaign 1, 2, and 3.

Fitting Parameter	Test Campaign 1	Test Campaign 2	Test Campaign 3			
			$B_z = -0.4$ G	$B_z = 2$ G	$B_z = 4$ G	$B_z = 6$ G
Spherical probe fitting coefficient, α_s	2.8	3.6	4	4	4	4
Planar probe fitting coefficient, α_p	2.2	3.4	3	2.5	2.7	2.6
Cubic probe fitting coefficient, α_{c1}	2.15	3.25	3.25	2.3	2.3	2.3
Cubic probe fitting coefficient, α_{c2}	1	1	1	4	4	4

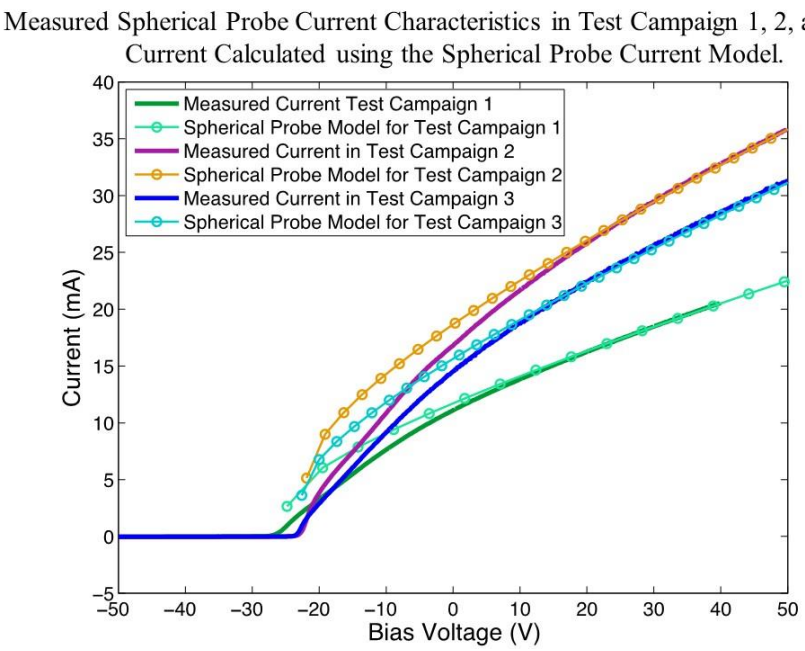

(a)

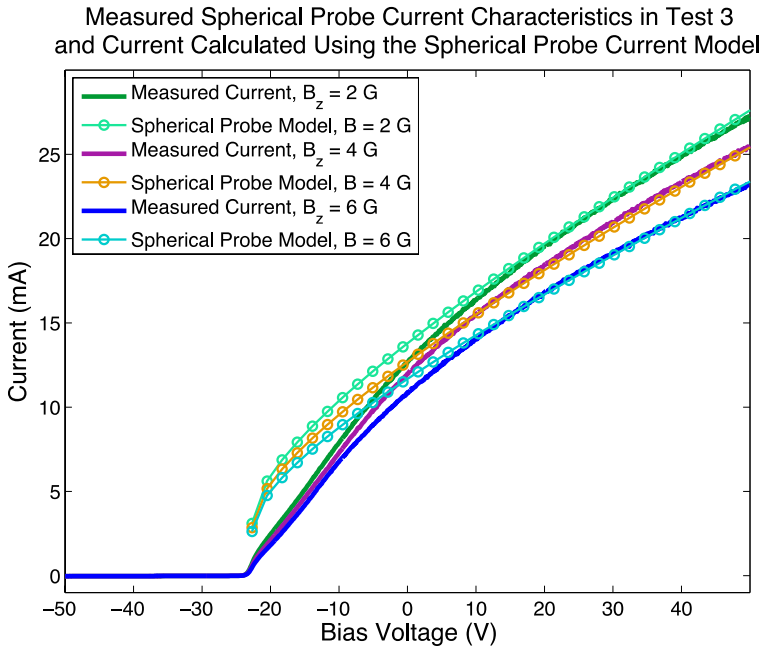

(b)

Figure 5.4: (a) The spherical probe characteristics from Test Campaign 1, 2 and 3 and lines fit to the characteristics. The plasma parameters varied between test campaigns and are listed in Table 4.4. The magnetic field strength was unchanged. (b) The spherical probe characteristics from Test Campaign 3 when B_z = 2 G, 4 G, and 6 G and lines fit to the characteristics. The spherical probe model uses Equation 5.11, plasma parameters provided in Table 4.4, and the fitting parameters provided in Table 5.1.

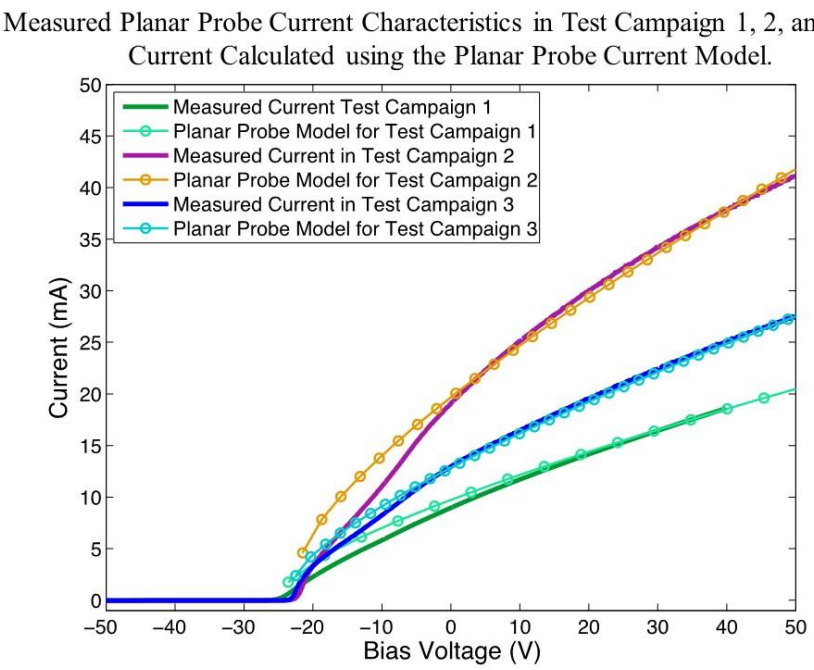

(a)

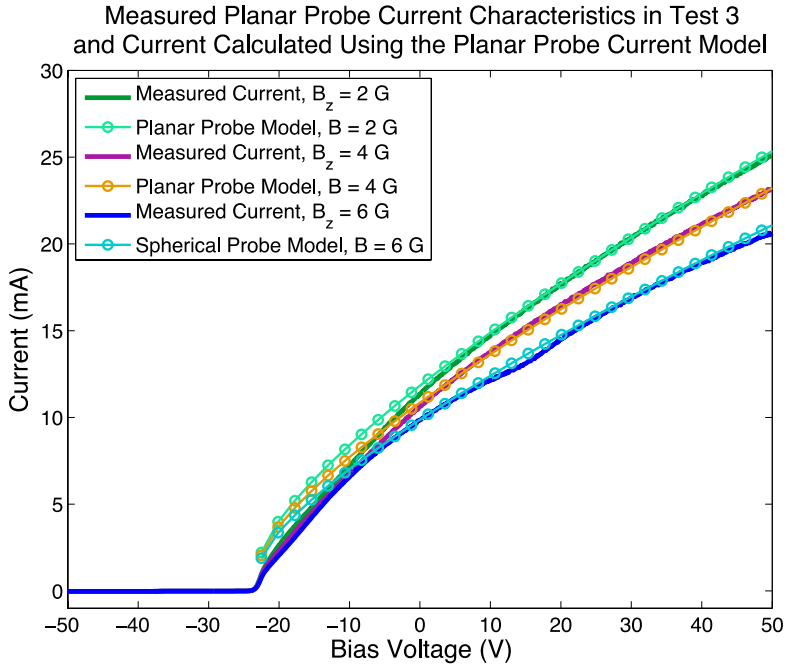

(b)

Figure 5.5: (a) The planar probe characteristics from Test Campaign 1, 2 and 3 and lines fit to the characteristics. The plasma parameters varied between test campaigns and are listed in Table 4.4. The magnetic field strength was unchanged. (b) The planar probe characteristics from Test Campaign 3 when B_z = 2 G, 4 G, and 6 G and lines fit to the characteristics. The planar probe model uses Equation 5.25, plasma parameters provided in Table 4.4, and the fitting parameters provided in Table 5.1.

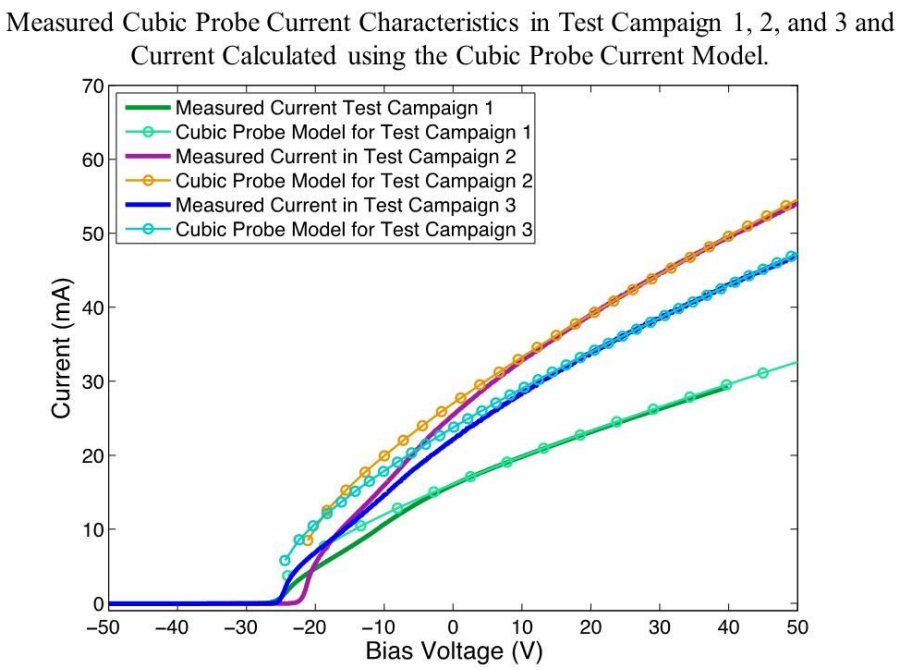

(a)

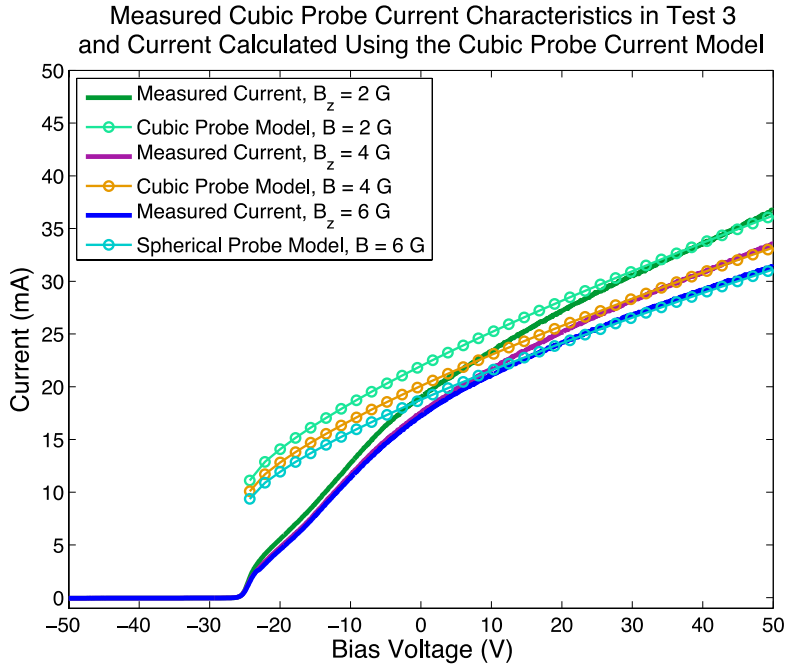

(b)

Figure 5.6: (a) The cubic probe characteristics from Test Campaign 1, 2 and 3 and lines fit to the characteristics. The plasma parameters varied between test campaigns and are listed in Table 4.4. The magnetic field strength was unchanged. (b) The cubic probe characteristics from Test Campaign 3 when B_z = 2 G, 4 G, and 6 G and lines fit to the characteristics. The cubic probe model uses Equation 5.29, plasma parameters provided in Table 4.4, and the fitting parameters provided in Table 5.1.

5.2.3 Representative Orbital Environment Simulated in the Laboratory Tests

In this section, the laboratory test that most adequately approximated the orbital environment is determined. The key parameters used for comparison are the scaling parameters r_p/λ_D, r_p/r_L, and ω_{ce}/ν_e. These parameters are described in detail in section 4.2.1 of Chapter 4. Here, a brief summary is provided to facilitate the comparison between the laboratory environment and LEO.

- The parameter r_p/λ_D plays an important role in current collection behavior. When $r_p/\lambda_D >> 1$, for example, the sheath is thin relative to the probe dimensions and the resulting collection current is the thermal current incident at the collector's surface [147]. Alternatively, when $r_p/\lambda_D \leq 1$, the growth in the sheath for increasing bias voltage produces an increase in probe current [147]. A goal of the experiment was to produce a ratio of r_p/λ_D in the laboratory environment that lies within a range of r_p/λ_D expected for our application in the LEO environment.
- The parameter r_p/r_L is an important parameter for evaluating the effect of the magnetic field on current collection. Magnetic field effects are often neglected when the electron thermal gyroradius, r_L, is very large relative to the probe radius but are considered an important factor affecting current collection when r_L is small relative to the probe radius [149]. Strong magnetic fields ($r_p/r_L >> 1$) generally reduce the electron collection current [150].
- The ratio of the electron gyrofrequency to the collision frequency, ω_{ce}/ν_e, can also be used to assess the effect of a magnetic field on current collection. Electrons gyrate around field lines in the presence of a magnetic field, traveling on magnetic flux tubes, and are collected when intersecting flux tubes intersect with the probe [151]. Collisions can scatter electrons off magnetic field lines [150]. Thus, this parameter helps determine if electrons are confined to travel along field lines. Fluctuations or "plasma turbulence" can allow electrons to diffuse across magnetic field lines as well [151],

although this effect was not explicitly measured in the laboratory tests described in Chapter 4.

In summary, parameters r_p/λ_D, r_p/r_L, and ω_{ce}/ν_e provided an indication for how closely the laboratory plasma captured characteristics of the orbital environment that directly impact electron current collection.

Before comparing the experimental plasma to LEO, it is necessary to briefly review assumptions made earlier in the system concept study regarding the orbital environment. The system concept study, discussed in detail in Chapter 3, assumed the EDT was in a circular, equatorial orbit at a 400-km, 500-km, and 600-km altitude. The electron density, electron temperature, and magnetic field strength are listed in Table 3.2 (section 3.2 of Chapter 3). The electron density and temperature were obtained from the International Reference Ionosphere (IRI) model [105]. Solar high was assumed because the elevated neutral-to-electron-density ratio during high solar activity represented the worst-case scenario for thrusting. Table 5.2 provides a more detailed and descriptive list of parameters representing the orbital environment. The 400-km altitude described by Table 5.2 serves as a specific example used for the analysis presented here. Performance at different altitudes and under different solar conditions and inclinations is assessed later in this chapter. The laboratory plasma parameters are presented in Table 5.3 for comparison.

Table 5.2: Orbital environment and scaling parameters for the WLP sphere and the 200-g planar picosat, the 150-g cubic picosat, and the 10-g ChipSat considered in this study (400 km).

Parameter	WLP Sphere	200-g Planar PicoSat	150-g Cubic PicoSat	10-g ChipSat
Plasma density, n_e (cm^{-3})	1×10^6	1×10^6	1×10^6	1×10^6
Electron temperature, kT_e/q (eV)	0.11	0.11	0.11	0.11
Magnetic field, B (G)	0.35	0.35	0.35	0.35
Anode radius, r_p (cm)	5	5	2.5	1.25
Neutral density, n (cm^{-3}) [62]	1.5×10^8	1.5×10^8	1.5×10^8	1.5×10^8
	Calculated Parameter			
Debye length, λ_D (cm)	0.2	0.2	0.2	0.2
Electron gyroradius, r_L (cm)	2.3	2.3	2.3	2.3
Electron gyrofrequency, ω_{ce} (s^{-1})	9.8×10^5	9.8×10^5	9.8×10^5	9.8×10^5
Electron collision frequency, ν_e (s^{-1}), where $\nu_e = \nu_{ei} + \nu_{en} \approx \nu_{ei}$	1×10^3	1×10^3	1×10^3	1×10^3
	Scaling Parameters			
r_p/λ_D	20	20	10	5
r_p/r_L	2.22	2.22	1.11	0.55
ω_{ce}/ν_e	930	930	930	930

Table 5.3: Laboratory environment and scaling parameters during Test Campaign 3 at three different magnetic field levels, B_z = 2 G, 4 G, and 6 G. The planar probe, the cubic probe, and the spherical probe all shared the same equivalent radius, where r_p = 0.5 cm.

Parameter	Test Campaign 3 6 G	Test Campaign 3 4 G	Test Campaign 3 2 G
Plasma density, n_e (cm^{-3})	1.1×10^{8}	1.1×10^{8}	1.1×10^{8}
Electron temperature, kT_e/q (eV)	0.5	0.5	0.5
Magnetic field, B (G)	6	4	2
Anode radius, r_p (cm)	0.5	0.5	0.5
Neutral density, n (cm^{-3})	6.1×10^{12}	6.1×10^{12}	6.1×10^{12}
	Calculated Parameter		
Debye length, λ_D (cm)	0.05	0.05	0.05
Electron gyroradius, r_L (cm)	0.3	0.4	0.8
Electron gyrofrequency, ω_{ce} (s^{-1})	1.70×10^{7}	1.1×10^{7}	1.70×10^{7}
Electron collision frequency, ν_e (s^{-1}) where $\nu_e = \nu_{ei} + \nu_{en}$	5.8×10^{4}	5.8×10^{4}	5.8×10^{4}
	Scaling Parameters		
r_p/λ_D	10	10	10
r_p/r_L	1.8	1.2	0.6
ω_{ce}/ν_e	292	194	97

The scaling parameters r_p/λ_D, r_p/r_L, and ω_{ce}/ν_e were calculated in the laboratory environment using the parameters listed in Table 4.4 (section 4.2.3.3 of Chapter 4). Test Campaign 3 is used for this comparison because it was the only set of tests where the magnetic field strength was scaled appropriately to generate conditions similar to LEO. It should be noted that the planar probe, the cubic probe, and the spherical probe in the laboratory plasma all shared the same equivalent radius, where r_p = 0.5 cm.

Using the scaling parameters as a basis for comparison, it is evident that the conditions in Test Campaign 3 were reasonably representative of the 400-km-altitude orbital environment. No test exactly replicated the scaling parameters seen in the orbital environment. However, the scaling parameter values in the laboratory setting were reasonably close to the orbital environment. Specifically, the parameters r_p/r_L and r_p/λ_D in the laboratory environment was within a factor of 2 of the orbital environment. It should be noted that the parameter ω_{ce}/ν_e was not fully scaled to represent LEO. The neutral density in the experiment was much higher than LEO, producing a much lower value for ω_{ce}/ν_e. The magnetic field strength in the experiment was also much higher than in LEO, producing a larger value for ω_{ce}. As a result, ω_{ce}/ν_e in the laboratory environment was less than the value in LEO by a factor of 3 for the highest magnetic field condition (6 G)

in Test Campaign 3. Collisions can knock electrons off of magnetic flux tubes, potentially causing current enhancement [151].

It should also be noted that the WLP data was obtained at an altitude of ~350 km during solar minimum conditions, rather than at an altitude of 400 km during solar maximum conditions [145]. Nevertheless, the orbital average neutral density and plasma density in Table 5.2 are approximately representative of the WLP environment.

The laboratory conditions and probes that provide the best match for LEO are listed below:

- The 6 G magnetic field condition provided an environment reasonably representative of the 200-g planar picosat in LEO. The planar probe in the experiment had the most similar shape to the 200-g planar picosat, so the planar probe's $I-V$ characteristic is used to estimate the spacecraft's current collection behavior in LEO.
- The 4 G magnetic field condition provided an environment reasonably representative of the 150-g cubic picosat in LEO. The cubic probe had the most similar shape to the 150-g cubic picosat, so the cubic probe's $I-V$ characteristic is used to estimate the spacecraft's current collection behavior in LEO.
- The 2 G magnetic field condition provided the most representative environment for the 10-g ChipSat in LEO. The planar probe had the most similar shape to the 10-g Chipsat, so the planar probe's $I-V$ characteristic is used to estimate the spacecraft's current collection behavior in LEO.
- The 6 G magnetic field condition provided an environment reasonably representative of the WLP in LEO. The spherical probe in the experiment had the same shape as the WLP, so the spherical probe's $I-V$ characteristic is used for direct comparison with the WLP model.

In Chapter 4, it was observed that increasing r_p/λ_D caused a reduction in the current collected per unit area, or "collection efficiency." For the 10-g ChipSat, the parameter r_p/λ_D was larger in the laboratory setting than in the 400-km-alitude orbital environment. This suggests that this spacecraft may collect *more* current per unit area in the orbital environment than predicted by the laboratory experimental results. On the other hand, the

parameter r_p/λ_D for the 200-g planar picosat was smaller in the laboratory environment then in the 400-km-alitude orbital environment. In this case, the spacecraft may collect *less* current per unit area in the orbital environment than predicted by the laboratory experimental results. A more exhaustive set of tests under a wider range plasma and magnetic field conditions could more precisely simulate current collection for each spacecraft shape and under ionospheric conditions.

5.2.4 Comparison of the WLP model to the spherical probe model using plasma parameters from the orbital environment

This section compares the WLP model to the spherical probe model developed earlier in this section. It is important to compare them because the spherical electrode used in the laboratory setting was approximately scaled to the size of the WLP relative to the Debye length and the electron thermal gyroradius. The WLP model is described in section 4.1 of Chapter 4. Recall that the WLP model can be expressed as

$$I_{\mathrm{WLP}} = \frac{I_{\mathrm{the}}}{2}\left(1 + \frac{q(V - V_p)}{kT_e}\right)^{\beta}, \qquad \text{(Eq. 5.30)}$$

where the parameter β was observed to vary between 0.5 and 1 in LEO, which is shown in Figure 9 of Barjatya et al. (2009) [145]. For our model, we chose $\beta = 0.65$ because this was the apparent value of β when the measured electron density was in the range of the electron densities considered in this study.

Figure 5.7 shows the *I–V* characteristic calculated using the WLP model and the spherical probe model. It should be noted that the precise values of β, n_e, and T_e were not reported in Barjatya (2009), so approximate values were determined from Figure 9 of Barjatya (2009) [145]. In addition, the magnetic field strength, ~0.35 G, was estimated by using magnetic field data and expressions in Hastings and Garret [62]. In order to adequately fit the orbital data with the spherical probe model, the fitting term $\alpha_s = 2.4$ was used. This is smaller than the value of α_s in the laboratory tests. Again, it is not clear which factors in the plasma environment influence the magnitude of α_s.

The current calculated using the spherical probe model and the WLP model are in excellent agreement, with error of only a few percent in a relatively large voltage range. This result suggests that the spherical probe model is capable of estimating the current collected by the WLP. However, no explanation is provided here for $\alpha_s = 2.4$ producing a good fit in the plasma conditions considered.

The fitting parameter $\alpha_s = 2.4$ is about 40% less than the value of α_s in the laboratory experiment that had the most LEO-like environment, Test Campaign 3. In order to estimate current collection in the orbital environment, it is assumed here that the fitting coefficients for the planar and cubic probes, α_p and α_{c1}, should also be reduced by 40%. This assumption is used in the following sections to estimate current and ultimately EDT thrust. Clearly, additional testing in a more LEO-like environment is needed to evaluate this assumption

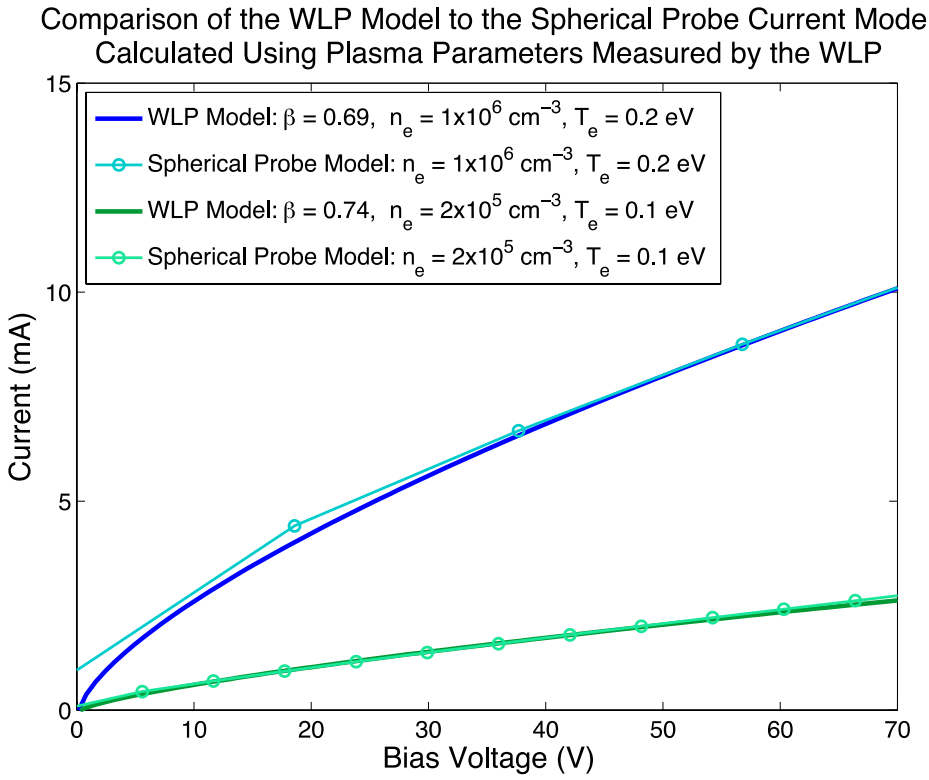

Figure 5.7: The WLP model compared to the spherical probe model. This shows that the spherical probe model and the WLP model are in good agreement for the plasma conditions shown. The parameters β, n_e, and T_e that were used to calculate the I–V characteristics shown here were reported in Barjatya (2009) [145]. It should be noted that the precise values of β, n_e, and T_e were not published in Barjatya (2009), so approximations were determined from Figure 9 of Barjatya (2009).

5.2.5 Application of the Revised Current Collection Model to Estimate Current in the Ionosphere

The collection current was estimated for each spacecraft using the appropriate plasma parameters from the orbital environment and orientation with respect to the magnetic field. To be clear, in this study the 200-g planar picosat and the 10-g ChipSat have two possible orientation: one orientation where the largest faces are normal to field lines and one where the smallest faces are normal to field lines. As a result, they have two $I-V$ characteristics. Table 5.4 lists the cross-sectional areas normal to magnetic field lines of each orientation. The current collection characteristics calculated in LEO using the laboratory data are shown in Figure 5.8.

Table 5.4: Spacecraft dimensions and effective areas for electron collection.

Spacecraft	Dimensions (cm)	Largest Effective Collection Area Normal to Field Lines (cm^2)	Smallest Effective Collection Area Normal to Field Lines (cm^2)
200-g Planar Picosat	10 × 10 × 2	200	40
150-g Cubic Picosat	5 × 5 × 5	50	50
10-g ChipSat	2.5 × 2.5 × 0.5	12.5	2.5

Several observations can be made about the refined current collection estimates derived from the laboratory data as compared to the current calculated using the WLP model:

- For the 200-g planar picosat, current estimates using the refined collection model were less than the current calculated using the WLP model by ~20% when the largest faces were normal to magnetic field lines. When the smallest faces were normal to field lines, the current was about 40% less than the current calculated using the WLP model. This first observation is consistent with laboratory measurements, where the planar probe collected roughly 20% less current than the spherical probe.

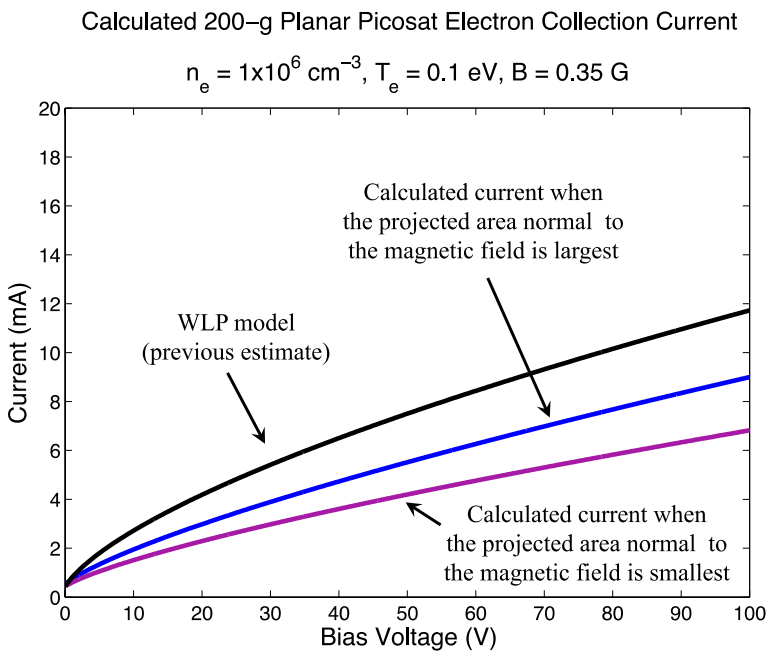

(a)

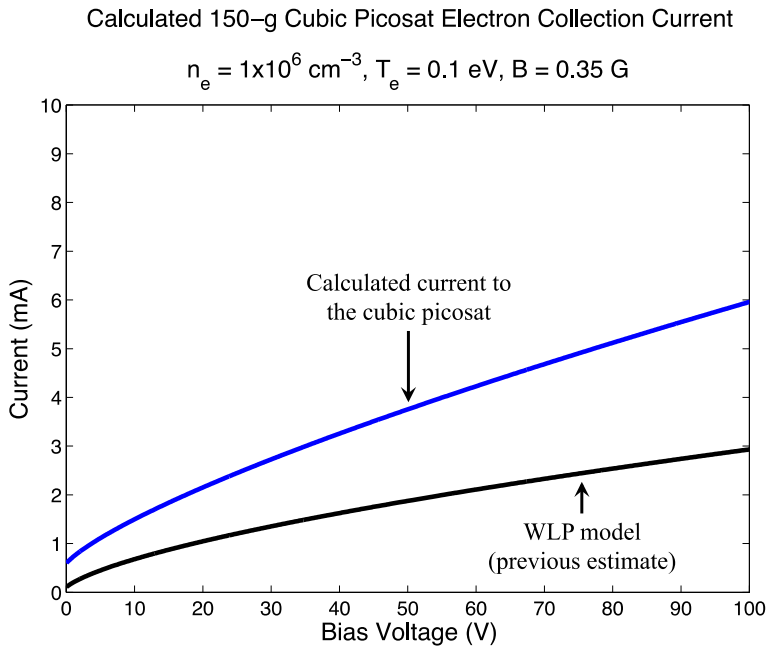

(b)

Figure 5.8: Current collection estimates for the 200-g planar and 150-g cubic picosats compared to the WLP model. Current estimates for 200-g planar and 150-g cubic picosats were calculated using the current collection models developed here. (a) The current collection estimate for the 200-g planar picosat and (b) the current collection estimate for the 150-g cubic picosats. The 200-g planar picosat has two potential current profiles, each determined by the surface area normal to magnetic field lines.

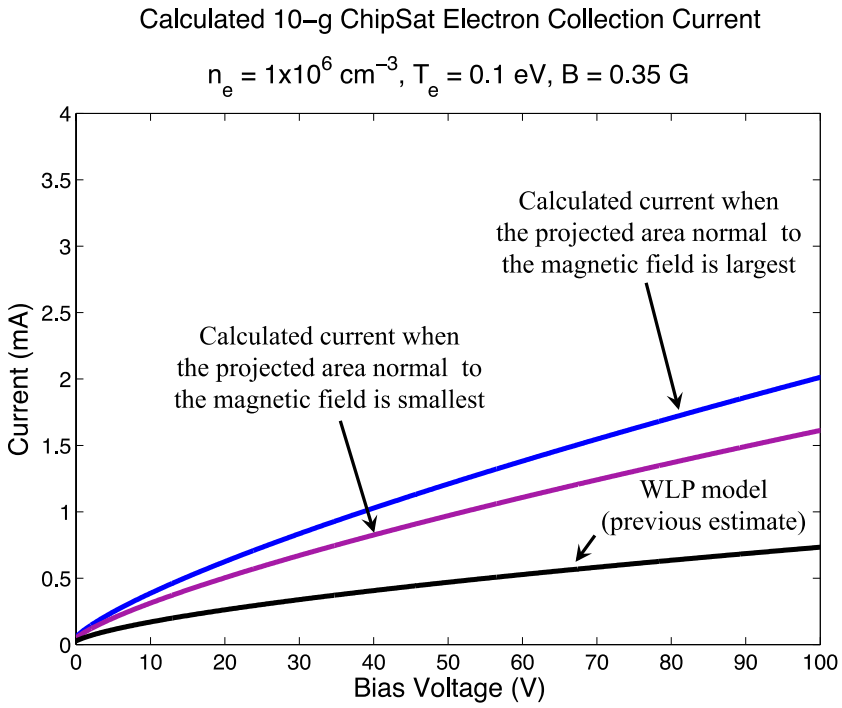

(c)

Figure 5.8 (Continued): The planar probe electron collection model compared to the WLP model. (c) The current collection estimate for the 10-g picosat in LEO.

- For the 150-g cubic picosat, current estimates using the refined collection model were about twice the WLP model.
- For the 10-g ChipSat, current estimates using the planar probe current collection model estimated 2.7 times the current calculated using the WLP model when the largest faces of the spacecraft were normal to magnetic field lines. When the smallest faces were normal to field lines, the current was about 2.3 times the WLP model. The high current relative to the WLP estimate is likely due to the small size of the probe.

5.3 Impact on the System Concept

The goal here is to consider how the experimentally refined anode current collection model impacts our previous estimate for tether system performance and

maneuverability. To do this, EDT thrust was calculated in a 400-km equatorial, circular orbit using the refined anode collection model. This orbit was selected to be consistent with the analysis performed earlier in the chapter. The impact of the revised electron collection model on the estimated thrust is shown in Table 5.5.

The change in the anode electron collection characteristic represents a change in the anode's impedance. In cases where the refined electron collection estimate exceeds the WLP model estimate, this signifies a reduction in the anode impedance. The reduction in anode impedance allows the EDT system to deliver more current to the tether at a given input power, producing higher peak thrust. Reduced anode impedance also implies that the same magnitude of thrust can be generated at lower input power levels or the propulsion system can tolerate additional inefficiencies. Conversely, when the refined anode current estimates predict less current than the WLP model, this corresponds to an *increase* in the anode impedance. The result is more electrical power is required to produce the same thrust level, or the thrust is less for the same input power.

Table 5.5: Estimated Parameters using Revised Anode Electron Current Collection Model. A 400-km-altitude equatorial orbit is assumed.

Parameter Calculated Using Revised Anode Model	Pair of 200-g Planar Picosats with 11-m EDT		Pair of 150-g Cubic Picosats with 12-m EDT	Pair of 10-g ChipSats with 4-m EDT	
Dimensions (cm)	10 × 10 × 2		5 × 5 × 5	2.5 × 2.5 × 0.5	
Cross-sectional area Normal to the Magnetic Field (cm^2)	200	40	50	12.5	2.5
Thrust Estimate (N)	1.8×10^{-6}	1.7×10^{-6}	1.3×10^{-6}	6.5×10^{-8}	6.1×10^{-8}
Thrust, Relative to Thrust Estimate using the WLP Model (% difference)	10% less than previous WLP estimate	15% less than previous WLP estimate	44% more than previous WLP estimate	35% more than previous WLP estimate	30% more than previous WLP estimate

It can also be concluded from Table 5.5 that the WLP model provided a reasonable, order-of-magnitude estimate or tether thrust. Additional experimental tests in more conditions that more precisely simulate the LEO environment could be used to refine the electron collection model further.

The results here may motivate some form of spacecraft attitude control so the effective collection area normal to the field lines is maximized. The optimal angle for a

given attitude is beyond the scope of this dissertation, although this is deserving of further study.

5.4 Assessing Performance in Other Conditions

The purpose of this section is to extend the analysis to estimate EDT performance in a broader range of orbital conditions. In previous sections of the chapter, the analysis assumed a 400-km-altitude equatorial orbit in solar maximum conditions. The purpose of this section is to consider the change in thrust as the altitude, solar activity, and orbital inclination changes. To be clear, the goal here is to observe trends in thrust and not necessarily the precise magnitude of thrust.

To do this, EDT thrust was determined under a range of environmental conditions. The analysis was performed for a pair of 200-g planar picosats in the orbital environment. It was assumed that the spacecraft could be oriented so its two largest faces (i.e., 200 cm^2) were normal to magnetic field lines. It was also assumed that the tether would be vertically aligned. The software tool TeMPEST was used to simulate the EDT system in orbit. TeMPEST is described in section 3.7 of Chapter 3. Thrust values were obtained for a single orbit and averaged to produce the orbital average thrust.

First, the orbital average thrust at 300-km, 400-km, 500-km, 600-km, and 700-km altitudes was determined using TeMPEST for an equatorial orbit during both solar maximum and solar minimum. Figure 5.9 shows the average thrust magnitude at these altitudes. Solar maximum and minimum are described in Section 3.2. January 1, 2000 was the date used for solar maximum orbital simulations and January 1, 2009 was the date used for solar minimum orbital simulations. (January 1, 2000 was the maximum of solar cycle 23 and January 1 was the minimum of solar cycle 24 [106], [212].) In both solar maximum and minimum conditions, the thrust magnitude varies with altitude. Thrust at 400 km is almost 4 times higher than thrust at 700 km. The thrust varies because of variations in electron density, which determines the electron collection current and tether current. The electron density profile in the ionosphere is shown in Figure 3.2 (section 3.2 of Chapter 3) as a function of altitude and solar activity. The peak thrust is obtained when the electron density is highest. At higher altitudes, the electron density decreases and the magnitude of thrust decreases. It can also be seen that the thrust

magnitude decreases with solar activity. This again mirrors the change in electron density due to decreased solar activity.

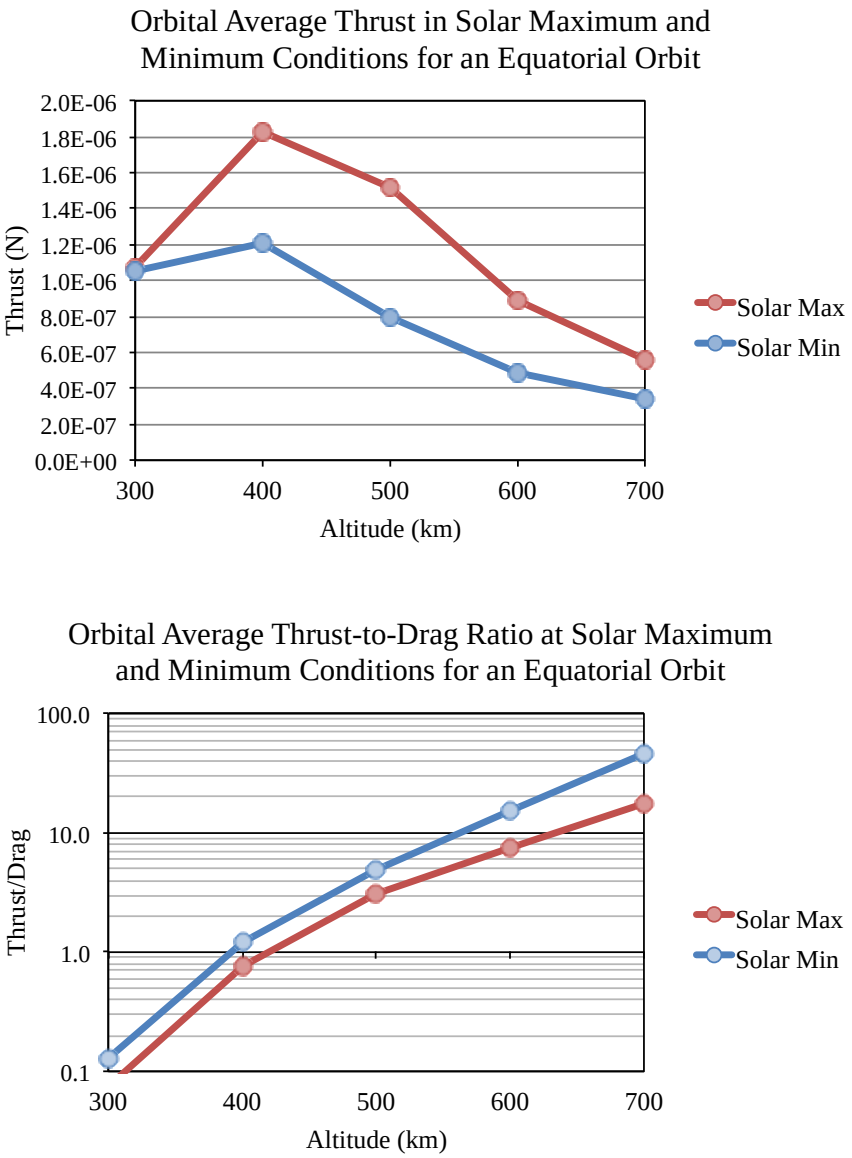

Figure 5.9: (a) Orbital average thrust for an equatorial orbit at 300-km, 400-km, 500-km, 600-km, and 700-km altitude. The thrust is being generated by a pair of 200-g planar picosats connected by an 11-m long EDT. The tether is assumed to be vertically aligned. The date for solar maximum was January 1, 2000. The date for solar minimum was January 1, 2009. Thrust values were obtained using TeMPEST. (b) Thrust-to-drag ratio in different altitudes.

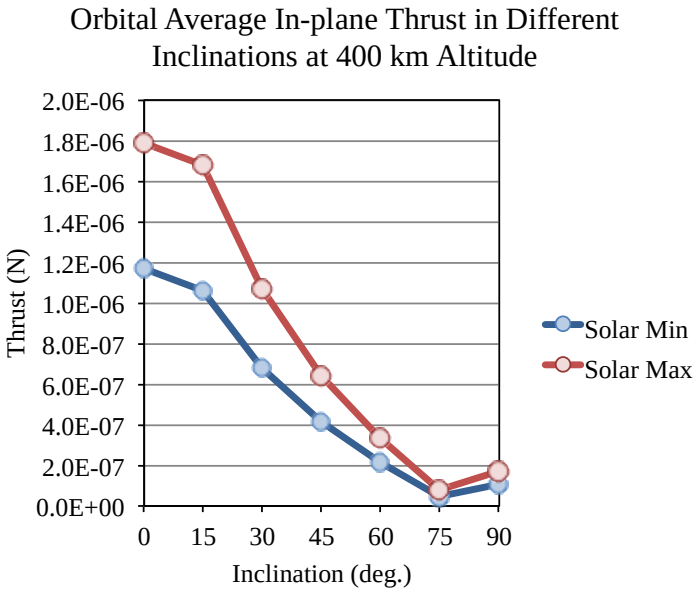

(a)

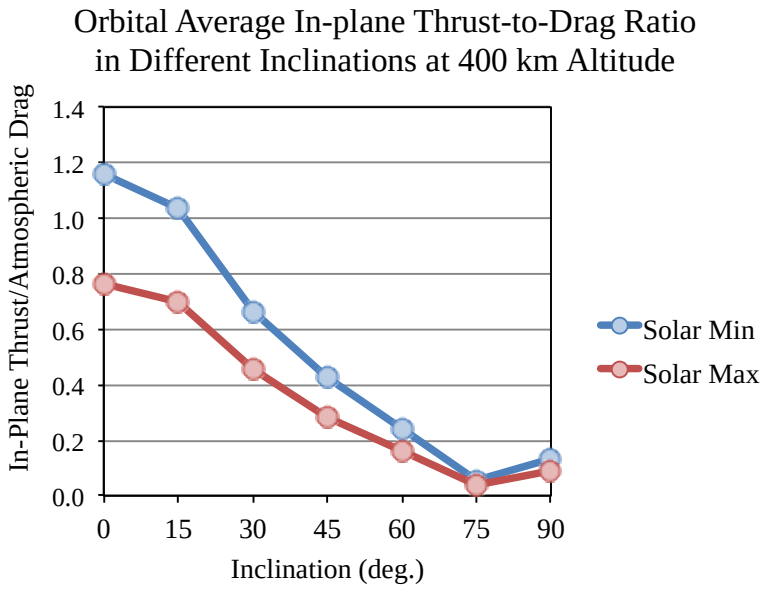

(b)

Figure 5.10: (a) Orbital average thrust at 0°,15°,30°,45°,60°,75°,and 90° inclination in solar maximum and minimum conditions. Here, the thrust is being generated by a pair of 200-g planar picosats connected by an 11-m long EDT. The tether is assumed to be vertically aligned. The date for solar maximum was January 1, 2000. The date for solar minimum was January 1, 2009. Thrust values were obtained using TeMPEST. (b) In-plane thrust-to-drag ratio in different inclinations in solar maximum and minimum.

The thrust also changes with inclination. The average thrust for different orbital inclinations is shown in Figure 5.10. Inclination is explained in Section 2.1.1 of Chapter 2. As inclination increases from 0°, the EDT approaches to the Earth's magnetic poles. The geomagnetic field can be modeled approximately as a dipole tilted about 11° from rotation axis of the Earth and shifted towards the Atlantic Ocean [62]. A spacecraft in a high inclination orbit passes near or over the geomagnetic poles, where the dominant component of the magnetic field is along the local vertical [62]. As a result, the thrust force, $\mathbf{F} = I_{\text{tether}}\mathbf{L}\times\mathbf{B}$, decreases at higher inclinations because the tether is aligned with the dominant component of the magnetic field [55].

In addition, the portion of thrust that is directed out-of-plane increases for higher inclination orbits. This is also due to the relative orientation of the tether with respect to the magnetic field. Out-of-plane thrust can be used to change inclination. Thrust contributing to boosting or de-boosting maneuvers, known as in-plane thrust because it is within the plane of the velocity vector, is maximized for low inclination orbits.

5.5 Sensitivity Analysis

The laboratory test campaigns used to estimate current collection in LEO represented a limited range of ambient conditions in LEO. The electron density, for example, undergoes large variation in the orbital environment. From Figure 3.3 in Chapter 3, it can be seen that the electron density can vary by more than 3 orders of magnitude in LEO and by 1−2 orders of magnitude in a given altitude. In the laboratory setting, however, the electron density and temperature varied by a factor of 2. Thus, the laboratory tests were conducted in a range of plasma densities, electron temperatures, and Debye lengths that was more limited than LEO. While the current collection models developed in this chapter can generally be used when the dimensions of the collecting body are roughly the same order of magnitude as the Debye length and the electron thermal gyroradius, it is difficult to predict how the fitting parameters would change with large variations in electron density, temperature, or Debye length.

The “validation” of the spherical probe model (section 5.2.4) was also conducted over a limited range of plasma parameters. The accuracy of the spherical probe current

collection model was evaluated by comparing current calculated using the spherical probe model to current calculated using the WLP model. The comparison is shown in Figure 5.7, revealing that the spherical probe model and the WLP model are in good agreement. However, in order to calculate current using the WLP model, a value for the exponent β is needed (see Equation 5.30). Published β values for the WLP model and corresponding plasma parameters are currently limited to the range $n_e \approx 10^5$–10^6 cm^{-3} and $T_e \approx 0.1$−0.2 eV [145]. Thus, the agreement between the WLP model and the spherical electrode model builds confidence in the spherical probe model in this relatively narrow range of electron densities and temperatures. It has not yet been determined how accurate the spherical probe model is outside of this regime.

The range of ν_e and ω_{ce}/ν_e in LEO is also large. The highest value of ω_{ce}/ν_e obtained in the laboratory environment, however, was less than ω_{ce}/ν_e in the altitude range considered here. Thus, the values of ν_e and ω_{ce}/ν_e generated in the laboratory experiment were not fully representative of LEO. Computational plasma simulations, additional laboratory experiments, and tests performed in the actual LEO environment would provide much needed insight to estimate current collection in LEO.

5.6 Alternative Current Collection Approaches Influenced by the Laboratory Results

In this thesis, it has been assumed that electron current will be collected on the conducting surfaces of picosats or femtosats. In this section, alternatives approaches are considered to enhance current collection while limiting mass and atmospheric drag effects as well as volume during launch. Figure 5.11 shows illustrations of the approaches considered.

The simplest approach would be to increase the effective current collection area by attaching thin (i.e., OML, thick-sheath regime), conducting wires or filaments to the external surfaces of the spacecraft. The current collection per unit area is highest in this regime. The effective collection area for each filament is the sheath edge, so an array of positively biased filaments connected to the spacecraft could increase the effective electron collection area without significantly increasing the drag area, mass or storage volume.

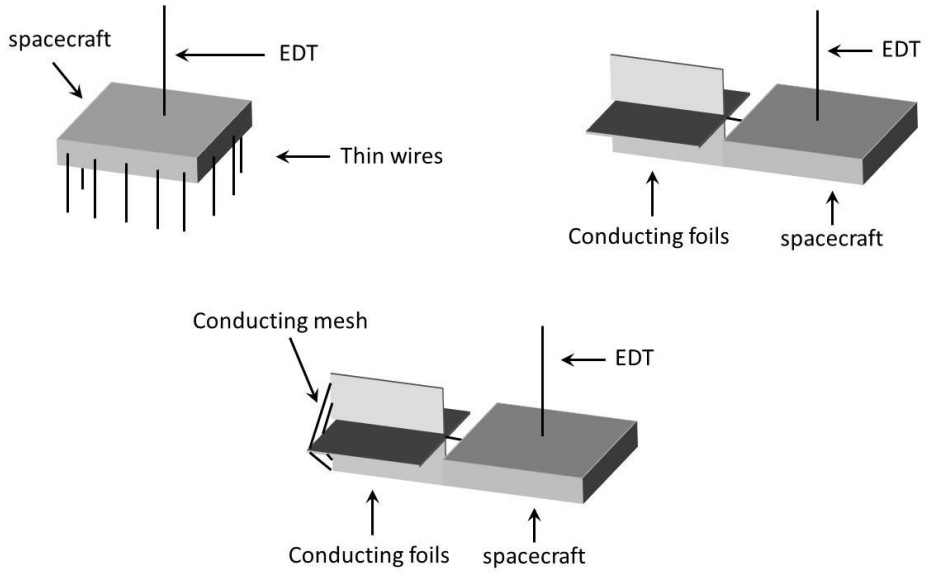

Figure 5.11: Illustrations of alternative approaches to enhance current collection

Another approach would be to use a pair of thin foils to enhance current collection. If these foils were located behind the spacecraft, they would ensure that the center of pressure was located behind the center of mass and provide some degree of attitude stabilization and atmospheric drag minimization. The benefit of the foils for current collection, however, would be that the area normal to geomagnetic field lines would be roughly the same in two axes. This concept could be enhanced further with a "net" or mesh made of thin wires, with wire spacing <10 Debye lengths (see Chapter 4 estimates for sheath size). A sufficiently fine mesh may have the potential to collect currently like a solid conducting structure [213]. This mesh could increase the electron collection surface area, especially if the magnetic field lines were normal to the mesh. Solar cells could also be placed on the orthogonal fins to enhance solar energy collection.

CHAPTER 6

Conclusions and Future Work

This thesis explores the potential of a miniaturized electrodynamic tether (EDT) to enhance the capabilities of picosatellites and femtosatellites. It has been shown that a tether only a few meters in length shows potential to provide a propellantless drag make-up force as well as boost and de-boost small spacecraft. This suggests the concept has the potential to provide picosats and femtosats with orbital maneuverability. Detailed experimental tests were performed to refine electron current collection estimates. These tests provided additional validation to initial tether thrust estimates, although they suggest that parameters like spacecraft attitude can also have a significant impact on tether current and, consequently, thrust.

This is the first investigation exploring the EDT concept for spacecraft at this scale. Although this study addresses the central questions related to miniaturized EDT propulsion, there are several aspects of the concept that warrant future study. In this chapter, conclusions from the study are presented and followed by suggestions of future work. Generally speaking, conclusions were presented within or at the end of each chapter, but they have been consolidated and summarized here. At the end of the chapter, suggestions for future work are proposed and potential applications of the concept are considered.

6.1 Summary and Conclusions of Research

6.1.1 System Concept Study

A detailed study was conducted to evaluate the capability of picosats and femtosats in the orbital environment. The results from the system concept study are summarized here. Based on a set of power generation estimates, the 200-g planar picosat,

the 150-g cubic picosat, and the 10-g ChipSat showed potential to generate a drag make-up force at 500 km and 600 km altitudes with an EDT a few meters in length. Only the 200-g planar picosat showed potential to generate a thrust force exceeding atmospheric drag at 400 km.

A propulsion power generation analysis was performed to estimate the ability of the small spacecraft to generate sufficient electrical power for drag make-up. It was estimated that a pair of 200-g planar picosats, 150-g cubic picosats, and 10-g ChipSats could generate 530 mW, 320 mW, and 30 mW, respectively. A simple expression was developed so power generation estimates could be re-calculated if power generation capability or power distribution efficiency differs from current estimates

The peak electrical current and EDT thrusting capability were evaluated for each spacecraft by solving Kirchoff's voltage law using models for tether resistance, motional emf, electron emission, and electron collection. The thrust force was compared to atmospheric drag and the gravity-gradient force at 400-km, 500-km, and 600-km altitudes in equatorial orbit during solar high. A range of tether lengths were identified that could produce thrust that exceeded atmospheric drag. The tether lengths selected were 11 m, 12 m, and 4 m for the 200-g planar picosats, 150-g cubic picosats, and 10-g ChipSats, respectively.

The peak tether current and thrust estimates are summarized in Table 3.5 (section 3.6.1 of Chapter 3). All of the spacecraft were able to generate a thrust force that exceeded drag at 500 km and 600 km. Only the 200-g planar picosat was able to generate thrust that exceeded drag at 400 km. The ability of the 200-g planar picosat to generate thrust results from its relatively low drag profile (i.e., high ballistic coefficient) and large area for collecting solar energy.

The thrust efficiency, defined here as the ratio of thrust to total power, was calculated for the 400-km, 500-km, and 600-km equatorial orbits previously analyzed for thrusting estimates. The thrust efficiency was low for the miniaturized EDT system, estimated to be less than 10% for each of the spacecraft at the altitudes considered. Thrust efficiency increases with tether length, so it is smaller for shorter tethers. For tether lengths below 100 meters, a majority of the available power is dissipated in collecting current from the ionosphere and only a small percentage increases the energy of the orbit

over time. However, the solar power available provided what is needed and the EDT is propellantless, so it is believed that the EDT can still provide a viable approach for propulsion.

The software tool TeMPEST was used to simulate the EDT system in orbit. A tethered pair of 200-g planar picosats was able to increase altitude by about 100 km in roughly 150 days from 400 km, 500 km, and 600 km starting altitudes using a 11-m EDT. A tethered pair of 150-g cubic picosats was able to increase altitude by about 100 km in roughly 175 days from 500 km and 600 km starting altitudes using a 12-m EDT. A tethered pair of 10-g ChipSats was able to increase altitude by about 50 km in roughly 200 days from 500 km and 600 km starting altitudes using an 4-m EDT. The 150-g cubic picosat and the 10-g planar Chipsat de-orbited at a 400-km starting altitude.

The de-boosting using an EDT was also investigated. The 200-g planar picosat and 150-g cubic picosat were able to de-boost from a 600-km starting altitude in about 150 days. De-boost periods were even shorter at lower starting altitudes. The 10-g ChipSat was able to de-boost from a 600-km starting altitude in about 200 days using an EDT.

In addition, the EDT was evaluated as an enhanced antenna aperture for small spacecraft. Picosat and femtosats have inherently small antenna apertures and low transmission power, but a conductive coating (e.g., gold, copper, silver, etc.) of adequate thickness compared to the skin depth on the semi-rigid tether core would provide the potential for a high performing, long, directional “traveling wave” antenna.

6.1.2 Experimental Results

An experimental test platform was developed to simulate characteristics of the low Earth environment in a ground-based laboratory facility. Three test campaigns were performed to investigate current collection in a flowing plasma and observe changes in collection due to (a) probe orientation relative to plasma flow and (b) magnetic field strength. The first experiment was the baseline experiment designed to study current collection in a flowing plasma. In the second experiment, the probes were re-oriented relative to the plasma flow to observe the impact of changing the cross-sectional area facing into the flow. In the third experiment, the impact of scaling the magnetic field to

simulate the LEO environment was assessed. Key parameters that impact electron collection, like the probe radius-to-Debye length ratio, r_p/λ_D, and the probe radius-to-electron thermal gyroradius ratio, were similar to the orbital environment. It was assumed earlier in the system concept study that current would be collected on the surface area of one of the tethered spacecraft. For this reason, it was important to capture the approximate shape of the spacecraft considered in this study.

The experiment provided a degree of validation useful for refining EDT anode electron collection estimates made earlier in the system concept study. Initially, the anode electron collection model was based on an expression developed to interpret plasma parameters from the wide sweeping Langmuir probe instrument (WLP) on the International Space Station (ISS). The experimental data was compared to the WLP model and interpreted to refine current collection estimates. The results were as follows:

- The spherical, cubic, and planar probe current characteristics exceeded estimates from the WLP model in each experimental test. The WLP model was most similar to the collected currents when a magnetic field of 2 G, 4 G, and 6 G was introduced. At 6 G, the WLP model current estimate was about 50% less at equal bias voltages than the planar and spherical probe current and 15% less than the cubic probe current.
- The probe size-to-Debye length ratio, r_p/λ_D, had a large effect on growth of the current-voltage characteristic. Generally, it was observed that increasing r_p/λ_D resulted in much less growth in collection current with bias voltage. This can be associated with a thinner sheath dimension. As λ_D decreased by a factor of 2 between Test Campaign 1 and Test Campaign 2, at an equal bias voltage the spherical probe collected ~28% less normalized current and the cubic probe collected ~37% less normalized current. This is significant because the plasma environment changes throughout an orbit in the ionosphere, so the shape of current characteristic may change as well.
- The planar probe's current was enhanced when it was oriented so the maximum cross-sectional area faced the plasma flow. In this orientation, the planar probe had the highest current collected per unit area, or "collection efficiency," exceeding the spherical probe collection efficiency by about 20%.

In contrast, the planar probe's collection efficiency was 5% below the spherical probe's collection efficiency when it was oriented so the minimum cross-sectional area faced the plasma flow. This suggests that the surface facing the plasma flow is the dominant collection surface.

- The cubic probe had the lowest collection efficiency in all laboratory tests. This may be due to inefficient collection by its large (relative to λ_D), planar faces and because collection is dominated by the area facing the plasma flow and not as significant for the wake-facing area or sides parallel to the plasma flow. Future experiments could test collection for various orientations of the cubic probe to observe changes in collection due to attitude.
- From rough estimates of the fraction of the hollow cathode plasma plume ions that had undergone charge exchange collisions downstream from the cathode orifice, is was concluded that the plasma flow effects were likely degraded significantly by a relatively high fraction of thermalized, charge exchange ions. This was not representative of the LEO environment.
- Enhancing magnetic field strength from ambient to an appropriately scaled magnitude to simulate the LEO environment decreased the electron saturation current as well as the growth in the current-collection characteristics. When the strength of the superimposed magnetic field in the experiment was increased to 6 G, the spherical and cubic probe electron saturation currents decreased by 40% and the planar probe electron saturation current decreased by almost 20%. This is difference is attributed to the planar probe having a majority of its surface area normal to magnetic field lines. As magnetic field strength increased, it is expected that current will be increasingly collected on magnetic flux tubes intersecting the probe. As the magnetic field strength increased, the cubic collector's current characteristic started to resemble the planar probe's current characteristic, suggesting that the effective collection area was being limited by the magnetic field to the area projected in the direction of the field. In future experiments, it will be imperative to test this hypothesis by observing the change in collection current as the orientation

between the probes and magnetic is varied. Reducing the magnetic field strength below the ambient value had no noticeable impact on collection.

- The ratio ω_{ce}/ν_e was not representative of the LEO environment. The electron collision frequency in the experiment was much higher than the electron collision frequency in LEO. The higher collisions frequency may have produced higher rates of cross-field diffusion that enhanced collection current. Reducing the background neutral density could lower the electron collision frequency. Operating the experiment closer to the vacuum pump or performing the experiment in a vacuum facility with a higher xenon pumping speed could achieve this.
- The experiment also had a limited voltage range. Assuming $T_e \approx 0.1$ eV in the orbital environment, the equivalent peak voltages from the laboratory experiment were only 10−15 V in LEO. Experimental test campaigns that span a larger normalized voltage range could help predict the current collection behavior over a larger voltage range.

The WLP equation form was used to fit the laboratory data. To predict the current collection behavior of the 200-g planar picosat, the 150-g cubic picosat, and the 10-g ChipSat, lines were fit to the normalized current characteristics of the probes that most closely represented them.

To estimate current collection in LEO, planar and cubic probe models were developed in Chapter 5. Additional experiments are needed to determine how accurate they are and under what conditions they are useful. The refined estimates were then used to estimate current collection in LEO. The observations from the refined current estimates were as follows:

- For the 200-g planar picosat, current estimates using the refined collection model were less than the current calculated using the WLP model by 20% when the largest faces on the spacecraft were perpendicular to magnetic field lines. When the smallest faces were perpendicular to magnetic field lines, the current was about 25% less than the current calculated using the WLP model.
- For the 150-g cubic picosat, current estimates using the refined collection model were twice the WLP model.

- For the 10-g ChipSat, current estimates using the refined collection model was about 2.7 times the current calculated using the WLP model when the largest faces on the spacecraft were perpendicular to magnetic field lines. When the smallest faces were perpendicular to magnetic field lines, the current was about 2.3 times the current calculated using the WLP model.

Finally, the refined electron collection model was applied to estimate thrust in the orbital environment. In cases where the refined electron collection estimate exceeded the WLP model estimate, this signified a reduction in the anode impedance. A reduction in anode impedance allows the EDT system to deliver more current to the tether at a given input power, producing higher peak thrust. Using the refined electron collection model, assuming a 400-km equatorial orbit and the largest faces were normal to magnetic field lines, thrust for the 200-g planar picosat was ~10% less than the thrust estimated by the WLP model, the 150-g cubic picosat thrust was 44% more than thrust estimated using the WLP model, and 10-g planar picosat thrust was 35% more than the thrust estimated using the WLP model. As solar activity decreases, the electron density decreases, reducing the anode current and the magnitude of the tether thrust. At 400-km, 500-km, and 600-km, the tether thrust is about 30% less in solar minimum than solar maximum. The thrust-to-drag ratio is higher, however.

6.2 Recommendations for Future Work

6.2.1 Future Work for the System Concept Study

The study conducted here could be expanded in a variety of ways to more precisely predict the performance of short tethers and understand their behavior on orbit. For example, the power generation capability of these uniquely small spacecraft should be evaluated more precisely. As more picosats and femtosats are built and flown, it should be possible to better estimate power generation capability.

Additional studies should also consider the changing attitude of the tether. The orbital simulation and thrust estimates were all completed assuming a vertically aligned tether. Future simulations should incorporate the pendulum-like tether libration and other dynamic effects that more adequately capture the tether in the orbital environment.

Further, the complex dynamics of deployment and issues related to long-term storage, like creep, should be assessed. Thermal bending of the tether as it passes in and out of sunlight should also be considered.

The shape of the tether also requires further investigation. The tether radius was selected to provide some degree of bending stiffness and reduce bowing on orbit. This is important because a tether that bends or bows crosses fewer magnetic field lines [55]. However, the analysis presented here assumed that the gravity-gradient tension was negligible and the drag force on both tethered spacecraft was identical. When the drag force on one spacecraft exceeds the drag force of the other, the differential drag can cause the spacecraft experiencing higher drag to trail the opposite spacecraft [55]. This can cause significant deflection and produce a torque on the system. At the same time, however, the gravity-gradient force produces a stabilizing torque that re-aligns the system along the local vertical. The resulting tether shape and attitude are impacted by a complex interplay between various forces in orbit. A future study should consider the complex dynamic interaction between forces experienced in orbit as well as their impact on deforming the tether.

The tether's capability to function as an antenna should also be evaluated further. This would make the tether a true multifunctional structure capable of propulsion and enhancing communication. Experimentation is needed to demonstrate the use of the tether as an antenna. There are challenges testing the tether as an antenna in the conventional laboratory setting. The far-field region of interest is [214]

$$R = \frac{2d^2}{\lambda}, \qquad \text{(Eq. 6.1)}$$

where d is the longest linear dimension of the radiating aperture and λ is the wavelength. The antenna far field distance can be large (>100 m) for a tether several meters in length and operating at frequencies of several hundred megahertz or higher, as discussed in Chapter 3 (section 3.8). This motivates tests of the tether as an antenna from high-altitude balloons or in the orbital environment.

The orbital environment would offer the best opportunity to validate the miniaturized EDT concept. Currently, the Miniaturized Tether Electrodynamics Experiment (MiTEE) is being planned at the University of Michigan. MiTEE will

evaluate the basic tether dynamics and plasma electrodynamics fundamental to a miniaturized EDTs operation in orbit as well as the tether's functionality as an antenna [215], [216].

6.2.2 Future Work Related to Validation of the Electron Collection Model

Future effort should be devoted to further validation of the electron collection model. The experimental tests covered a relatively limited voltage range and represented a relatively limited set of ionospheric conditions. The maximum equivalent bias voltage, for example, corresponded to only about 15 V in LEO, assuming $T_e \approx 0.1$ eV. The estimated anode bias voltages in the trade study exceeded this value, ranging from 10 V to more than 50 V. Future experiments should be conducted with a larger range of normalized bias voltages. This could be accomplished by sweeping a larger range of bias voltages and/or conducting experiments in an environment with a lower plasma temperature.

Future tests should also be conducted in an environment representative of a broader range of ionospheric environments, and covering a broader set of scaling parameters r_p/λ_D, r_p/r_L, and ω_{ce}/ν_e representative of the LEO environment. In particularly, replicating the parameter ω_{ce}/ν_e was challenging because the neutral density in the experiment was much higher than LEO. As a result, the electron collision frequency was more than 100 times higher and the experiment failed to fully simulate the orbital environment. Future experiments should be conducted in an environment where both r_p/r_L, and ω_{ce}/ν_e are represented, requiring an appropriately scaled magnetic field as well as a sufficiently low background neutral density. A lower neutral density could be obtained, for example, by operating in a facility with a higher pumping speed or making measurements closer to the vacuum pump. A lower neutral background density would also reduce the fraction of charge exchange ions in the plasma and more accurately simulate high-speed plasma flow. Future tests should also consider the orientation of the magnetic field with respect to the spacecraft flow. This presents a variety of possible tests as the probe orientation and the magnetic field are both adjusted relative to the plasma flow

6.3 Considerations for Future System Concepts

The concept presented in this thesis has the potential to enable dynamic, propellantless controllability and lifetime enhancement for small spacecraft. In turn, controlled fleets of small spacecraft can potentially be used in missions requiring distributed, multi-point sensing capability or rapid re-measurement of a single location [42]. The short, semi-rigid EDT has potential beyond providing orbital maneuvering capability. More generally, this study has shown that a short tether can be used to generate a useful force. This implies that a tether could also be used for attitude control, potentially even for larger spacecraft. Further, multiple EDTs extended along different axes may provide even more versatile thrust capability or attitude controllability, even as the strength and orientation of the magnetic field vector relative to the local vertical changes in orbit [141].

Additionally, spacecraft can be distributed along the length of an EDT to form a tethered constellation [55]. A string of tethered spacecraft, for example, could be used to make simultaneous, distributed, vertically-aligned measurements in the space environment, like measurements in the ionosphere of the vertical component of the electric field [217]. Thus, the miniaturized EDT concept has significant potential and may enable a range of capabilities. This thesis simply presents the early exploration of this truly novel system concept.

BIBLIOGRAPHY

[1] S. S. Iyengar and R. R. Brooks, *Distributed Sensor Networks, Second Edition: Image and Sensor Signal Processing*. CRC Press, 2012.

[2] D. J. Barnhart, T. Vladimirova, A. M. Baker, and M. N. Sweeting, "A low-cost femtosatellite to enable distributed space missions," *Acta Astronaut.*, vol. 64, no. 11–12, pp. 1123–1143, Jun. 2009.

[3] J. Keller, "Startup to Develop Satellite-On-A-Chip," *Mil. Aerosp. Electron.*, vol. 5, no. 2, p. 1, 1994.

[4] A. Huang, W. W. Hansen, S. W. Janson, and H. Helvajian, "Development of a 100-gm-class inspector satellite using photostructurable glass/ceramic materials," 2002, vol. 4637, pp. 297–304.

[5] S. W. Janson, H. Helvajian, and K. Breuer, "MEMS, microengineering and aerospace systems," *AIAA Pap.*, vol. 3802, 1999.

[6] D. J. Barnhart, T. Vladimirova, and M. N. Sweeting, "Very-Small-Satellite Design for Distributed Space Missions," *J. Spacecr. Rockets*, vol. 44, no. 6, pp. 1294–1306, 2007.

[7] J. R. Wertz, D. F. Everett, and J. J. Puschell, *Space mission engineering: the new SMAD*. Hawthorne, CA: Microcosm Press : Sold and distributed worldwide by Microcosm Astronautics Books, 2011.

[8] Mission Design Division Staff, "Small Spacecraft Technology State of the Art," NASA Ames Research Center, Moffett Field, California, Technical Publication NASA/TP–2014–216648/REV1, Jan. 2014.

[9] C. Zingale, V. Ahlstrom, and B. Kudrick, "Human factors guidance for the use of handheld, portable, and wearable computing devices," 2005.

[10] M. Garcia, "NASA - Hurricane Isabel." [Online]. Available: http://www.nasa.gov/mission_pages/station/main/iss007e14883_feature.html. [Accessed: 25-May-2015].

[11] H. Helvajian and S. W. Janson, *Small satellites: past, present, and future*. El Segundo, Calif.; Reston, Va.: Aerospace Press ; American Institute of Aeronautics and Astronautics, 2008.

[12] B. R. Bowman, W. N. Barker, and W. G. Schick, "Orbit perturbation analysis of West Ford needles clusters," *Am. Inst. Aerona Astronaut. Worldw.*, 2000.

[13] C. Wiedemann, J. Bendisch, H. Krag, P. Wegener, and D. Rex, "Modeling of copper needle clusters from the West Ford Dipole experiments," in *Space Debris*, 2001, vol. 473, pp. 315–320.

[14] P. Waldron, D. C. MacLellan, and M. C. Crocker, "The West Ford payload," *Proc. IEEE*, vol. 52, no. 5, pp. 571–576, May 1964.

[15] J. Yick, B. Mukherjee, and D. Ghosal, "Wireless sensor network survey," *Comput. Netw.*, vol. 52, no. 12, pp. 2292–2330, Aug. 2008.

[16] R. Jones, “Small spacecraft activities at JPL,” 1991.
[17] J. Bouwmeester and J. Guo, “Survey of worldwide pico- and nanosatellite missions, distributions and subsystem technology,” *Acta Astronaut.*, vol. 67, no. 7–8, pp. 854–862, Oct. 2010.
[18] W. A. Shiroma, L. K. Martin, J. M. Akagi, J. T. Akagi, B. L. Wolfe, B. A. Fewell, and A. T. Ohta, “CubeSats: A bright future for nanosatellites,” *Cent. Eur. J. Eng.*, vol. 1, no. 1, pp. 9–15, Mar. 2011.
[19] R. A. Deepak and R. J. Twiggs, “Thinking out of the box: Space science beyond the CubeSat,” *J. Small Satell.*, vol. 1, no. 1, pp. 3–7, 2012.
[20] K. Zack, J. G. Jernigan, and L. Cominsky, “The Development of a 3P PocketQube,” *Bull. Am. Phys. Soc.*, vol. 58, 2013.
[21] J. A. Atchison and M. A. Peck, “Length Scaling in Spacecraft Dynamics,” *J. Guid. Control Dyn.*, vol. 34, no. 1, pp. 231–246, 2011.
[22] Z. Manchester, M. Peck, and A. Filo, “KickSat: A Crowd-Funded Mission to Demonstrate the World’s Smallest Spacecraft,” *AIAAUSU Conf. Small Satell.*, Aug. 2013.
[23] J. Tristancho and J. Gutierrez-Cabello, “A probe of concept for femto-satellites based on commercial-of-the-shelf,” in *Digital Avionics Systems Conference (DASC), 2011 IEEE/AIAA 30th*, 2011, pp. 8A2–1.
[24] V. Kravchenko and others, “Design and Implementation of a femto-satellite technology demonstrator,” 2011.
[25] J. Tristancho Martínez and others, “Implementation of a femto-satellite and a mini-launcher for the N Prize,” 2010.
[26] L. Navarro Morales and others, “A multi-agent payload management approach for femtosatellite applications,” 2011.
[27] C. Colombo, C. Lücking, and C. R. McInnes, “Orbit evolution, maintenance and disposal of SpaceChip swarms through electro-chromic control,” *Acta Astronaut.*, vol. 82, no. 1, pp. 25–37, 2013.
[28] K. Zack, H. Khaleel, A. Isaac, and A. Bihnam, “Compact spiral antenna for space based applications,” in *2014 IEEE Antennas and Propagation Society International Symposium (APSURSI)*, 2014, pp. 1708–1709.
[29] S. Izquierdo Jimenez, “Implementation of a long range radio-link system for femto-satellites in very Low Earth Orbit,” Nov. 2013.
[30] D. J. Barnhart, T. Vladimirova, and M. N. Sweeting, “Design of self-powered wireless system-on-a-chip sensor nodes for hostile environments,” in *Circuits and Systems, 2008. ISCAS 2008. IEEE International Symposium on*, 2008, pp. 824–827.
[31] S. Janson and R. Welle, “The NASA Optical Communication and Sensor Demonstration Program,” *AIAAUSU Conf. Small Satell.*, Aug. 2013.
[32] G. E. Moore and others, “Progress in digital integrated electronics,” *IEDM Tech Dig.*, vol. 11, 1975.
[33] P. A. Iles, “Evolution of space solar cells,” *Sol. Energy Mater. Sol. Cells*, vol. 68, no. 1, pp. 1–13, 2001.
[34] G. Halpert, H. Frank, and S. Surampudi, “Batteries and fuel cells in space,” *Interface-Electrochem. Soc.*, vol. 8, no. 3, pp. 25–31, 1999.

[35] L. H. Krause, C. L. Enloe, R. K. Haaland, and P. Golando, “Microsatellite missions to conduct midlatitude studies of equatorial ionospheric plasma bubbles,” *Adv. Space Res.*, vol. 36, no. 12, pp. 2474–2479, 2005.
[36] C. L. Enloe, L. H. Krause, R. K. Haaland, T. T. Patterson, C. E. Richardson, C. C. Lazidis, and R. G. Whiting, “Miniaturized electrostatic analyzer manufactured using photolithographic etching,” *Rev. Sci. Instrum.*, vol. 74, no. 3, pp. 1192–1195, 2003.
[37] D. M. Wesolek, J. L. Champion, F. A. Herrero, R. Osiander, R. L. Champion, and A. M. Darrin, “A micromachined flat plasma spectrometer (FlaPS),” in *Micromachining and Microfabrication*, 2004, pp. 89–97.
[38] A. C. Lewis, J. F. Hamilton, C. N. Rhodes, J. Halliday, K. D. Bartle, P. Homewood, R. J. Grenfell, B. Goody, A. M. Harling, P. Brewer, and others, “Microfabricated planar glass gas chromatography with photoionization detection,” *J. Chromatogr. A*, vol. 1217, no. 5, pp. 768–774, 2010.
[39] L. Izquierdo and J. Tristancho, “Next generation of sensors for femto-satellites based on commercial-of-the-shelf,” in *Digital Avionics Systems Conference (DASC), 2011 IEEE/AIAA 30th*, 2011, pp. 8A4–1.
[40] “05B03 TCM8230MD ProdBrief - 05B03_TCM8230MD.pdf.” .
[41] Y. Tsuda, O. Mori, R. Funase, H. Sawada, T. Yamamoto, T. Saiki, T. Endo, and J. Kawaguchi, “Flight status of IKAROS deep space solar sail demonstrator,” *Acta Astronaut.*, vol. 69, no. 9, pp. 833–840, 2011.
[42] S. Janson and D. Barnhart, “The Next Little Thing: Femtosatellites,” *AIAAUSU Conf. Small Satell.*, Aug. 2013.
[43] C. S. Ruf, S. Gleason, Z. Jelenak, S. Katzberg, A. Ridley, R. Rose, J. Scherrer, and V. Zavorotny, “The CYGNSS nanosatellite constellation hurricane mission,” in *Geoscience and Remote Sensing Symposium (IGARSS), 2012 IEEE International*, 2012, pp. 214–216.
[44] D. Rose, M. Vincent, R. Rose, and C. Ruf, “The CYGNSS ground segment; innovative mission operations concepts to support a micro-satellite constellation,” in *Aerospace Conference, 2013 IEEE*, 2013, pp. 1–9.
[45] I. Bell, “Electrodynamic Tethers for ChipSats and Nanospacecrafts,” in *11th Spacecraft Charging Technology Conference*, Albuquerque, NM, 2010.
[46] W. P. Wright and P. Ferrer, “Electric micropropulsion systems,” *Prog. Aerosp. Sci.*, vol. 74, pp. 48–61, Apr. 2015.
[47] C. Rossi, “Micropropulsion for Space — A Survey of MEMS-based Micro Thrusters and their Solid Propellant Technology,” *Sens. Update*, vol. 10, no. 1, pp. 257–292, Jan. 2002.
[48] G. J. Hansel, “Power conversion and scaling for vanishingly small satellites with electric propulsion,” Massachusetts Institute of Technology, 2014.
[49] J. A. Atchison and M. A. Peck, “A passive, sun-pointing, millimeter-scale solar sail,” *Acta Astronaut.*, vol. 67, no. 1–2, pp. 108–121, Jul. 2010.
[50] C. Lücking, C. Colombo, and C. R. McInnes, “Electrochromic orbit control for smart-dust devices,” *J. Guid. Control Dyn.*, vol. 35, no. 5, pp. 1548–1558, 2012.
[51] M. A. Peck, B. Streetman, C. M. Saaj, and V. Lappas, “Spacecraft Formation Flying using Lorentz Forces,” *J. Br. Interplanet. Soc.*, vol. 60, pp. 263–267, 2007.
[52] J. J. Sellers, *Understanding space: an introduction to astronautics*. New York: McGraw-Hill, 2000.

[53] M. W. B. R. M. and Makemson, *An Introduction to Astrodynamics*. Academic Press, 1962.
[54] R. G. Jahn, *Physics of electric propulsion*. Courier Corporation, 2012.
[55] M. L. Cosmo, E. C. Lorenzini, and others, *Tethers in space handbook*, vol. 4. National Aeronautics and Space Administration, 1997.
[56] M. van Pelt, *Space Tethers and Space Elevators*. New York, NY: Springer New York, 2009.
[57] D. C. Thompson, C. Bonifazi, B. E. Gilchrist, S. D. Williams, W. J. Raitt, J.-P. Lebreton, W. J. Burke, N. H. Stone, and K. H. Wright, "The current-voltage characteristics of a large probe in low Earth orbit: TSS-1R results," *Geophys. Res. Lett.*, vol. 25, no. 4, pp. 413–416, Feb. 1998.
[58] S. G. Bilen, J. K. McTernan, B. E. Gilchrist, I. C. Bell, D. Liaw, N. R. Voronka, and R. P. Hoyt, "Energy Harvesting on Spacecraft Using Electrodynamic Tethers," 2012.
[59] P. M. Banks, "Review of electrodynamic tethers for space plasma science," *J. Spacecr. Rockets*, vol. 26, no. 4, pp. 234–239, Jul. 1989.
[60] S. D. Williams, B. E. Gilchrist, V. M. Agüero, R. S. Indiresan, D. C. Thompson, and W. J. Raitt, "TSS-1R vertical electric fields: Long baseline measurements using an electrodynamic tether as a double probe," *Geophys. Res. Lett.*, vol. 25, no. 4, pp. 445–448, Feb. 1998.
[61] M. C. Kelley, *The Earth's Ionosphere: Plasma Physics & Electrodynamics*, vol. 96. Academic press, 2009.
[62] D. Hastings and H. Garrett, *Spacecraft-Environment Interactions*. Cambridge: Cambridge University Press, 2004.
[63] R. L. Merlino, "Understanding Langmuir probe current-voltage characteristics," *Am. J. Phys.*, vol. 75, no. 12, pp. 1078–1085, 2007.
[64] N. Hershkowitz, "Sheaths: More complicated than you thinka)," *Phys. Plasmas 1994-Present*, vol. 12, no. 5, p. 055502, 2005.
[65] B. E. Gilchrist, L. Johnson, and E. Lorenzini, "Electrodynamic Tethers as Propulsion Systems: System Considerations and Future Plans," *6th Spacecr. Charg. Technol. Nov 1998*, pp. 147–151, 1998.
[66] I. Bell, B. Gilchrist, D. Liaw, V. Singh, K. Hagen, C. Lu, J. Cutler, S. Bilén, and J. McTernan, "Investigating the Feasibility and Mission Enabling Potential of Miniaturized Electrodynamic Tethers for Femtosatellites and Other Ultra-small Satellites," *AIAAUSU Conf. Small Satell.*, Aug. 2013.
[67] J. R. SANMARTIN, M. MARTINEZ-SANCHEZ, and E. AHEDO, "Bare wire anodes for electrodynamic tethers," *J. Propuls. Power*, vol. 9, no. 3, pp. 353–360, 1993.
[68] H. Kawano, T. Takahashi, Y. Tagashira, H. Mine, and M. Moriyama, "Work function of refractory metals and its dependence upon working conditions," *Appl. Surf. Sci.*, vol. 146, no. 1, pp. 105–108, 1999.
[69] D. M. Goebel and I. Katz, "Hollow Cathodes," in *Fundamentals of Electric Propulsion*, John Wiley & Sons, Inc., 2008, pp. 243–323.
[70] L. P. Rand, R. M. Waggoner, and J. D. Williams, "Hollow Cathode With Low Work Function Electride Insert," pp. 317–323, Jan. 2011.
[71] K. R. Fuhrhop, "Theory and experimental evaluation of electrodynamic tether systems and related technologies," The University of Michigan, 2007.

[72] C. M. Marrese, “A review of field emission cathode technologies for electric propulsion systems and instruments,” in *2000 IEEE Aerospace Conference Proceedings*, 2000, vol. 4, pp. 85–98 vol.4.
[73] David Howell, “Lecture 2: Electron Emission and Cathode Emittance.” .
[74] V. M. Anguero and R. C. Adamo, “Space applications of spindt cathode field emission arrays,” in *6th Spacecraft Charging Technology*, 1998, vol. 1, pp. 347–352.
[75] Y. Okawa, S. Kitamura, S. Kawamoto, Y. Iseki, K. Hashimoto, and E. Noda, “An experimental study on carbon nanotube cathodes for electrodynamic tether propulsion,” *Acta Astronaut.*, vol. 61, no. 11–12, pp. 989–994, Dec. 2007.
[76] G. N. Fursey, *Field Emission in Vacuum Microelectronics*. Springer Science & Business Media, 2007.
[77] J. Conklin, K. Balakrishnan, S. Buchman, R. Byer, G. Cutler, D. DeBra, E. Hultgren, J. Lipa, S. Saraf, S. Shimizu, and others, “The Drag-free CubeSat,” 2012.
[78] I. Katz, J. R. Lilley, A. Greb, J. E. McCoy, J. Galofaro, and D. C. Ferguson, “Plasma turbulence enhanced current collection: Results from the plasma motor generator electrodynamic tether flight,” *J. Geophys. Res. Space Phys.*, vol. 100, no. A2, pp. 1687–1690, Feb. 1995.
[79] M. J. GERVER, D. E. HASTINGS, and M. R. OBERHARDT, “Theory of plasma contactors in ground-based experiments and low earth orbit,” *J. Spacecr. Rockets*, vol. 27, no. 4, pp. 391–402, 1990.
[80] L. H. Krause, J. I. Minow, V. N. Coffey, B. E. Gilchrist, and W. R. Hoegy, “The Situational Awareness Sensor Suite for the ISS (SASSI): A Mission Concept to Investigate ISS Charging and Wake Effects,” presented at the Spacecraft Charging Technology Conference, 23-27 Jun. 2014, United States, 2014.
[81] J. G. Laframboise and L. W. Parker, “Probe design for orbit-limited current collection,” *Phys. Fluids*, vol. 16, no. 5, p. 629, May 1973.
[82] I. Langmuir and K. B. Blodgett, “Currents Limited by Space Charge between Concentric Spheres,” *Phys. Rev.*, vol. 24, no. 1, pp. 49–59, Jul. 1924.
[83] L. W. Parker and B. L. Murphy, “Potential buildup on an electron-emitting ionospheric satellite,” *J. Geophys. Res.*, vol. 72, no. 5, pp. 1631–1636, 1967.
[84] D. C. Thompson, C. Bonifazi, B. E. Gilchrist, S. D. Williams, W. J. Raitt, J.-P. Lebreton, W. J. Burke, N. H. Stone, and K. H. Wright, “The current-voltage characteristics of a large probe in low Earth orbit: TSS-1R results,” *Geophys. Res. Lett.*, vol. 25, no. 4, pp. 413–416, 1998.
[85] W. J. Raitt, N. B. Myers, D. C. Thompson, P. M. Banks, B. E. Gilchrist, T. Neubert, P. R. Williamson, and S. Sasaki, “Recent experimental measurements of space platform charging at LEO altitudes,” *Adv. Space Res.*, vol. 12, no. 12, pp. 49–52, 1992.
[86] E. Choiniere and B. E. Gilchrist, “Self-Consistent 2-D Kinetic Simulations of High-Voltage Plasma Sheaths Surrounding Ion-Attracting Conductive Cylinders in Flowing Plasmas,” *IEEE Trans. Plasma Sci.*, vol. 35, no. 1, pp. 7–22, 2007.
[87] N. H. Stone, W. J. Raitt, and K. H. Wright Jr., “The TSS-1R electrodynamic tether experiment: Scientific and technological results,” *Adv. Space Res.*, vol. 24, no. 8, pp. 1037–1045, 1999.
[88] D. L. Cooke and I. Katz, “TSS-1R electron currents: Magnetic limited collection from a heated presheath,” *Geophys. Res. Lett.*, vol. 25, no. 5, pp. 753–756, 1998.

[89] É. Choinière, S. G. Bilén, B. E. Gilchrist, K. R. Fuhrhop, and A. D. Gallimore, "Experimental investigation of electron collection to solid and slotted tape probes in a high-speed flowing plasma," *Plasma Sci. IEEE Trans. On*, vol. 33, no. 4, pp. 1310–1323, 2005.
[90] T. L. Wilson, D. Chlouber, and R. J. Jost, "Electrodynamic tether currents in the day/night ionosphere: Correlations during the Plasma Motor Generator mission," *J. Geophys. Res. Space Phys. 1978–2012*, vol. 101, no. A10, pp. 21657–21688, 1996.
[91] R. P. Hoyt and B. M. Minor, "Remediation of radiation belts using electrostatic tether structures," in *2005 IEEE Aerospace Conference*, 2005, pp. 583–594.
[92] P. M. Banks, P. R. Williamson, and K.-I. Oyama, "Electrical behavior of a shuttle electrodynamic tether system (SETS)," *Planet. Space Sci.*, vol. 29, no. 2, pp. 139–147, 1981.
[93] V. S. Aslanov and A. S. Ledkov, *Dynamics of Tethered Satellite Systems*. Elsevier, 2012.
[94] Y. Chen, R. Huang, X. Ren, L. He, and Y. He, "History of the Tether Concept and Tether Missions: A Review," 2013.
[95] J. D. Isaacs, A. C. Vine, H. Bradner, and G. E. Bachus, "Satellite elongation into a true' sky-hook,'" *Science*, vol. 151, no. 3711, pp. 682–683, 1966.
[96] G. Colombo, E. M. Gaposchkin, M. D. Grossi, and G. C. Weiffenbach, "The «Skyhook»: a Shuttle-borne tool for low-orbital-altitude research," *Meccanica*, vol. 10, no. 1, pp. 3–20, 1975.
[97] S. D. Drell, H. M. Foley, and M. A. Ruderman, "Drag and propulsion of large satellites in the ionosphere: An Alfvén propulsion engine in space," *J. Geophys. Res.*, vol. 70, no. 13, pp. 3131–3145, Jul. 1965.
[98] M. Dobrowolny, "Wave and Particle Phenomena Induced by an Electrodynamic Tether," *SAO Spec. Rep.*, vol. 388, 1979.
[99] N. Kawashima, S. Sasaki, K. I. Oyama, K. Hirao, T. Obayashi, W. J. Raitt, A. B. White, P. R. Williamson, P. M. Banks, and W. F. Sharp, "Results from a tethered rocket experiment (Charge-2)," *Adv. Space Res.*, vol. 8, no. 1, pp. 197–201, 1988.
[100] B. E. Gilchrist, C. Bonifazi, S. G. Bilén, W. J. Raitt, W. J. Burke, N. H. Stone, and J. P. Lebreton, "Enhanced electrodynamic tether currents due to electron emission from a neutral gas discharge: Results from the TSS-1R Mission," *Geophys. Res. Lett.*, vol. 25, no. 4, pp. 437–440, 1998.
[101] J. A. Atchison and M. Peck, "A passive microscale solar sail," in *AIAA SPACE 2008 Conference and Exposition, AIAA*, 2008.
[102] S. Macmillan and S. Maus, "International Geomagnetic Reference Field—the tenth generation," *Earth Planets Space*, vol. 57, no. 12, pp. 1135–1140, Jun. 2014.
[103] T. W. Hill, "Inertial limit on corotation," *J. Geophys. Res. Space Phys. 1978–2012*, vol. 84, no. A11, pp. 6554–6558, 1979.
[104] S. G. Bilén, "PULSE PROPAGATION ALONG CONDUCTORS IN LOW–DENSITY, COLD PLASMAS AS APPLIED TO ELECTRODYNAMIC TETHERS IN THE IONOSPHERE," The University of Michigan, 1998.
[105] D. Bilitza, L.-A. McKinnell, B. Reinisch, and T. Fuller-Rowell, "The international reference ionosphere today and in the future," *J. Geod.*, vol. 85, no. 12, pp. 909–920, 2011.

[106] D. H. Hathaway and S. T. Suess, “Solar cycle 23,” in *The Heliosphere through the Solar Activity Cycle*, Springer Berlin Heidelberg, 2008, pp. 21–39.
[107] A. E. Hedi, “Extension of the MSIS thermospheric model into the middle and lower atmosphere [J],” *J Geophys Res*, vol. 96, no. A2, pp. 1159–1172, 1991.
[108] R. P. Hoyt, “Stabilization of electrodynamic tethers,” in *AIP Conference Proceedings*, 2002, pp. 570–577.
[109] G. M. Scarpello and D. Ritelli, “Exact Solutions of Nonlinear Equation of Rod Deflections Involving the Lauricella Hypergeometric Functions,” *Int. J. Math. Math. Sci.*, vol. 2011, p. e838924, Sep. 2011.
[110] *Dynamics of Tethered Space Systems*. .
[111] J. M. Gere and S. P. Timoshenko, “Mechanics of materials Brooks,” *Cole Pac. Grove CA*, pp. 815–39, 2001.
[112] E. P. Popov, *Engineering mechanics of solids*. Prentice Hall, 1990.
[113] F. Beer, E. R. J. Jr, E. Eisenberg, and P. Cornwell, *Vector Mechanics for Engineers: Dynamics*, 9 edition. Boston: McGraw-Hill Science/Engineering/Math, 2009.
[114] I. Bell, B. Gilchrist, J. McTernan, S. Bilen, R. P. Hoyt, N. R. Voronka, and P. Mason, “The Potential of Miniature Electrodynamic Tethers to Enhance Capabilities of Femtosatellites,” presented at the 32nd International Electric Propulsion Conferenc, Wiesbaden, Germany, 2011.
[115] H. E. Boyer, *Atlas of stress-strain curves*. ASM International, 2002.
[116] “Monel alloy K-500.” SMC-062, Sep-2004.
[117] “PFA Coating; PFA Film | DuPont™ Teflon ® PFA.” [Online]. Available: http://www2.dupont.com/Teflon_Industrial/en_US/products/product_by_name/teflon_pfa/. [Accessed: 26-Apr-2015].
[118] “MISSE PEACE Polymers atomic oxygen erosion results.” [Online]. Available: http://www.academia.edu/2924456/MISSE_PEACE_Polymers_atomic_oxygen_erosion_results. [Accessed: 31-Mar-2015].
[119] K. R. Fuhrhop, “Theory and experimental evaluation of electrodynamic tether systems and related technologies,” The University of Michigan, 2007.
[120] D. Morris, B. Gilchrist, A. Gallimore, and K. Jensen, “Developing field emitter array cathode systems for electrodynamic tether propulsion,” *AIAA Pap. 00-3867*, 2000.
[121] L. T. Williams, V. S. Kumsomboone, W. J. Ready, and M. L. R. Walker, “Lifetime and Failure Mechanisms of an Arrayed Carbon Nanotube Field Emission Cathode,” *IEEE Trans. Electron Devices*, vol. 57, no. 11, pp. 3163–3168, Nov. 2010.
[122] C. M. Marrese, A. D. Gallimore, W. A. Mackie, and D. E. Evans, “The design of a cathode to operate in an oxygen-rich environment,” 1997.
[123] D. R. Whaley, R. Duggal, C. M. Armstrong, C. L. Bellew, C. E. Holland, and C. A. Spindt, “100 W Operation of a Cold Cathode TWT,” *IEEE Trans. Electron Devices*, vol. 56, no. 5, pp. 896–905, 2009.
[124] D. P. Morris, *Optimizing space-charge limits of electron emission into plasmas with application to in-space electric propulsion*. 2005.
[125] D. P. Morris, B. E. Gilchrist, and A. D. Gallimore, “Application of Dual Grids to Cold Cathode/Field Effect Electron Emission,” in *41 st AIAA/ASME/SAE/ASEE Joint Propulsion Conference & Exhibit*, 2005, pp. 1–8.

[126] J. K. McTernan and S. G. Bilen, “Electrodynamic Tether Systems on Small-Scale Spacecraft Using Dual-Purpose Materials for the Plasma-Spacecraft Interface,” 2013.
[127] E. C. Whipple, “Theory of the spherically symmetric photoelectron sheath: A thick sheath approximation and comparison with the ATS 6 observation of a potential barrier,” *J. Geophys. Res.*, vol. 81, no. 4, pp. 601–607, Feb. 1976.
[128] L. Conde, “An introduction to Langmuir probe diagnostics of plasmas,” 2011. [Online]. Available: http://plasmalab.aero.upm.es/~lcl/PlasmaProbes/Probes-2010-2.pdf. [Accessed: 30-Sep-2013].
[129] R. T. Bettinger and E. H. Walker, “Relationship for Plasma Sheaths about Langmuir Probes,” *Phys. Fluids*, vol. 8, no. 4, p. 748, Apr. 1965.
[130] A. Barjatya, C. M. Swenson, D. C. Thompson, and K. H. Wright, “Invited Article: Data analysis of the Floating Potential Measurement Unit aboard the International Space Station,” *Rev. Sci. Instrum.*, vol. 80, no. 4, p. 041301, Apr. 2009.
[131] R. D. Estes, “Alfven waves from an electrodynamic tethered satellite system,” *J. Geophys. Res. Space Phys. 1978–2012*, vol. 93, no. A2, pp. 945–956, 1988.
[132] D. E. Hastings and J. Wang, “The radiation impedance of an electrodynamic tether with end connectors,” *Geophys. Res. Lett.*, vol. 14, no. 5, pp. 519–522, 1987.
[133] S. C. Ekpo and D. George, “A system engineering analysis of highly adaptive small satellites,” *Syst. J. IEEE*, vol. 7, no. 4, pp. 642–648, 2013.
[134] J. K. McTernan, T. R. Brubaker, and S. G. Bilen, “Indium tin oxide coverings on solar panels for plasma-Spacecraft connection,” in *Photovoltaic Specialists Conference (PVSC), 2013 IEEE 39th*, 2013, pp. 2821–2826.
[135] D. J. Barnhart, “Very Small Satellite Design for Space Sensor Networks,” University of Surrey, Guildford, United Kingdom, 2008.
[136] “$50SAT | AMSAT-UK.” .
[137] S. G. Bilén, J. K. McTernan, B. E. Gilchrist, I. C. Bell, N. R. Voronka, and R. P. Hoyt, “Electrodynamic tethers for energy harvesting and propulsion on space platforms,” in *AIAA SPACE 2010 Conference & Exposition 30 August-2 September 2010, Anaheim, California AIAA*, 2010, pp. 1–11.
[138] I. Bell, B. Gilchrist, S. Bilén, and J. McTernan, “Investigating the Use of Miniaturized Electrodynamic Tethers to Enhance the Capabilities of Femtosatellites and other Ultra-small Satellites,” 2012.
[139] J. Corsi and L. Iess, “Stability and control of electrodynamic tethers for de-orbiting applications,” *Acta Astronaut.*, vol. 48, no. 5, pp. 491–501, 2001.
[140] N. R. Voronka, R. P. Hoyt, J. Slostad, B. E. Gilchrist, and K. Fuhrhop, “Modular Spacecraft with Integrated Structural Electrodynamic Propulsion,” NASA Institute for Advanced Concepts, NAS5-03110-07605-003-050, 2006.
[141] L. Weis and M. Peck, “Attitude Control for Chip Satellites using Multiple Electrodynamic Tethers,” in *AIAA/AAS Astrodynamics Specialist Conference*, Minneapolis, Minnesota, 2012.
[142] R. I. Samantha Roy, D. E. Hastings, and E. Ahedo, “Systems analysis of electrodynamic tethers,” *J. Spacecr. Rockets*, vol. 29, no. 3, pp. 415–424, 1992.
[143] C. K. Purvis, H. B. Garrett, A. C. Whittlesey, and N. J. Stevens, “Design guidelines for assessing and controlling spacecraft charging effects,” Sep. 1984.

[144] H. B. Garrett and A. C. Whittlesey, *Guide to mitigating spacecraft charging effects*, vol. 3. John Wiley & Sons, 2012.
[145] A. Barjatya, C. M. Swenson, D. C. Thompson, and K. H. W. Jr, "Invited Article: Data analysis of the Floating Potential Measurement Unit aboard the International Space Station," *Rev. Sci. Instrum.*, vol. 80, no. 4, p. 041301, Apr. 2009.
[146] K. H. Wright, C. M. Swenson, D. C. Thompson, A. Barjatya, S. L. Koontz, T. A. Schneider, J. A. Vaughn, J. I. Minow, P. D. Craven, V. N. Coffey, and others, "Charging of the International Space Station as observed by the floating potential measurement unit: Initial results," *Plasma Sci. IEEE Trans. On*, vol. 36, no. 5, pp. 2280–2293, 2008.
[147] H. M. Mott-Smith and I. Langmuir, "The theory of collectors in gaseous discharges," *Phys. Rev.*, vol. 28, no. 4, p. 727, 1926.
[148] D. E. Hastings, "A review of plasma interactions with spacecraft in low Earth orbit," *J. Geophys. Res. Space Phys. 1978–2012*, vol. 100, no. A8, pp. 14457–14483, 1995.
[149] J. D. Swift and M. J. R. Schwar, "Electrical Probes for Plasma Diagnostics.," 1970.
[150] N. Hershkowitz, "3 How Langmuir Probes Work," *Plasma Diagn. Disch. Parameters Chem.*, p. 113, 2013.
[151] J. G. Laframboise and L. J. Sonmor, "Current collection by probes and electrodes in space magnetoplasmas: A review," *J. Geophys. Res. Space Phys. 1978–2012*, vol. 98, no. A1, pp. 337–357, 1993.
[152] F. F. Chen and A. W. Trivelpiece, "Introduction to plasma physics," *Phys. Today*, vol. 29, p. 54, 1976.
[153] É. Coggiola and A. Soubeyran, "Mesothermal plasma flow around a negatively wake side biased cylinder," *J. Geophys. Res. Space Phys.*, vol. 96, no. A5, pp. 7613–7621, May 1991.
[154] W. J. Weber, R. J. Armstrong, and J. Trulsen, "Ion-beam diagnostics by means of an electron-saturated plane Langmuir probe," *J. Appl. Phys.*, vol. 50, no. 7, pp. 4545–4549, Jul. 1979.
[155] A. Skoelv, R. J. Armstrong, and J. Trulsen, "Ion beam diagnostics by means of plane Langmuir probes," *Phys FluidsUnited States*, vol. 27, no. 11, 1984.
[156] R. H. Varey, "Langmuir probes and ion flow," *J. Phys. Appl. Phys.*, vol. 3, no. 7, p. 1107, 1970.
[157] M. Dobrowolny, U. Guidoni, E. Melchioni, G. Vannaroni, and J. P. Lebreton, "Current-voltage characteristics of the TSS 1 satellite," *J. Geophys. Res. Space Phys. 1978–2012*, vol. 100, no. A12, pp. 23953–23957, 1995.
[158] J. G. Laframboise, "Current collection by a positively charged spacecraft: Effects of its magnetic presheath," *J. Geophys. Res. Space Phys. 1978–2012*, vol. 102, no. A2, pp. 2417–2432, 1997.
[159] N. Singh and W. C. Leung, "Numerical simulation of plasma processes occurring in the ram region of the tethered satellite," *Geophys. Res. Lett.*, vol. 25, no. 5, pp. 741–744, 1998.
[160] G. J. Williams Jr, T. B. Smith, M. T. Domonkos, A. D. Gallimore, and R. P. Drake, "Laser-induced fluorescence characterization of ions emitted from hollow cathodes," *Plasma Sci. IEEE Trans. On*, vol. 28, no. 5, pp. 1664–1675, 2000.

[161] D. M. Goebel, K. K. Jameson, I. Katz, and I. G. Mikellides, "Potential fluctuations and energetic ion production in hollow cathode discharges," *Phys. Plasmas 1994-Present*, vol. 14, no. 10, p. 103508, 2007.
[162] J. S. Miller, S. H. Pullins, D. J. Levandier, Y. Chiu, and R. A. Dressler, "Xenon charge exchange cross sections for electrostatic thruster models," *J. Appl. Phys.*, vol. 91, no. 3, pp. 984–991, 2002.
[163] D. M. Goebel and E. Chu, "High-Current Lanthanum Hexaboride Hollow Cathode for High-Power Hall Thrusters," *J. Propuls. Power*, vol. 30, no. 1, pp. 35–40, 2014.
[164] L. Oksuz and N. Hershkowitz, "Understanding Mach probes and Langmuir probes in a drifting, unmagnetized, non-uniform plasma," *Plasma Sources Sci. Technol.*, vol. 13, no. 2, p. 263, May 2004.
[165] X. Wang, C. T. Howes, M. Horányi, and S. Robertson, "Effect of filament supports on emissive probe measurements," *Rev. Sci. Instrum.*, vol. 84, no. 1, p. 013506, 2013.
[166] L. H. Brace, "Langmuir Probe Measurements in the Ionosphere," in *Measurement Techniques in Space Plasmas:Particles*, R. F. Pfaff, J. E. Borovsky, and D. T. Young, Eds. American Geophysical Union, 1998, pp. 23–35.
[167] G. Wehner and G. Medicus, "Reliability of Probe Measurements in Hot Cathode Gas Diodes," *J. Appl. Phys.*, vol. 23, no. 9, pp. 1035–1046, Sep. 1952.
[168] A. Barjatya, *Langmuir Probe Measurements in the Ionosphere*. ProQuest, 2007.
[169] I. K. Instruments, "2400 Series Source Meter User Manual," *Seventh Print. Clevel. Ohio USA*, 2002.
[170] R. J. D'Arcy, "Dielectric impurities and surface instability in Langmuir probe plasma measurements," *J. Phys. Appl. Phys.*, vol. 7, no. 10, p. 1391, Jul. 1974.
[171] E. Stamate and K. Ohe, "Influence of surface condition in Langmuir probe measurements," *J. Vac. Sci. Technol. A*, vol. 20, no. 3, pp. 661–666, May 2002.
[172] C. Winkler, D. Strele, S. Tscholl, and R. Schrittwieser, "On the contamination of Langmuir probe surfaces in a potassium plasma," *Plasma Phys. Control. Fusion*, vol. 42, no. 2, p. 217, Feb. 2000.
[173] E. L. Bronaugh, "Helmholtz coils for calibration of probes and sensors: limits of magnetic field accuracy and uniformity," in *, 1995 IEEE International Symposium on Electromagnetic Compatibility, 1995. Symposium Record*, 1995, pp. 72–76.
[174] D. J. DeTroye and R. J. Chase, "The Calculation and Measurement of Helmholtz Coil Fields, Army Research Laboratory," ARL-TN-35, 1994.
[175] F. F. Chen, "Langmuir probe diagnostics," in *Mini-Course on Plasma Diagnostics, IEEE-ICOPS Meeting, Jeju, Korea*, 2003.
[176] J. P. Sheehan and N. Hershkowitz, "Emissive probes," *Plasma Sources Sci. Technol.*, vol. 20, no. 6, p. 063001, 2011.
[177] R. Shastry, A. D. Gallimore, and R. R. Hofer, "Near-Wall Plasma Characterization of a 6-kW Hall Thruster," in *31st International Electric Propulsion Conference, IEPC-2009-133, Ann Arbor, MI*, 2009.
[178] V. A. Godyak and V. I. Demidov, "Probe measurements of electron-energy distributions in plasmas: what can we measure and how can we achieve reliable results?," *J. Phys. Appl. Phys.*, vol. 44, no. 23, p. 233001, Jun. 2011.

[179] S. Khrapak, “Floating potential of a small particle in a plasma: Difference between Maxwellian and Druyvesteyn electron velocity distributions,” *Phys. Plasmas 1994-Present*, vol. 17, no. 10, p. 104502, Oct. 2010.
[180] M. J. Patterson, “LOW CURRENT HOLLOW CATHODE. EVALUATION,” *Ann Arbor*, vol. 1001, p. 48109, 1999.
[181] G. Vannaroni, M. Dobrowolny, E. Melchioni, F. D. Venuto, and R. Giovi, “Characterization of the interaction between a hollow cathode source and an ambient plasma,” *J. Appl. Phys.*, vol. 71, no. 10, pp. 4709–4717, May 1992.
[182] É. Choinière, “Theory and experimental evaluation of a consistent steady-state kinetic model for 2-D conductive structures in ionospheric plasmas with application to bare electrodynamic tethers in space,” Citeseer, 2004.
[183] K.-S. Chung, “Mach probes,” *Plasma Sources Sci. Technol.*, vol. 21, no. 6, p. 063001, Dec. 2012.
[184] I. H. Hutchinson, “The invalidity of a Mach probe model,” *Phys. Plasmas 1994-Present*, vol. 9, no. 5, pp. 1832–1833, 2002.
[185] E. Ko and N. Hershkowitz, “Asymmetry reversal of ion collection by mach probes in flowing unmagnetized plasmas,” *Plasma Phys. Control. Fusion*, vol. 48, no. 5, p. 621, 2006.
[186] C. C. Farnell, J. D. Williams, and C. C. Farnell, “Comparison of hollow cathode discharge plasma configurations,” *Plasma Sources Sci. Technol.*, vol. 20, no. 2, p. 025006, Apr. 2011.
[187] J. E. Foster and M. J. Patterson, “Downstream ion energy distributions in a hollow cathode ring cusp discharge,” *J. Propuls. Power*, vol. 21, no. 1, pp. 144–151, 2005.
[188] S. B. Gabriel, J. E. Mccoy, and M. R. Carruth Jr, “Plasma flow measurements in a simulated low earth orbit plasma,” *AIAA PapUnited States*, vol. 82, no. CONF-820604-, 1982.
[189] B. Rubin, C. Farnell, J. Williams, J. Vaughn, T. Schneider, and D. Ferguson, “Magnetic filter type plasma source for ground-based simulation of low earth orbit environment,” *Plasma Sources Sci. Technol.*, vol. 18, no. 2, p. 025015, 2009.
[190] D. M. Goebel and I. Katz, *Fundamentals of Electric Propulsion: Ion and Hall Thrusters*, 1 edition. Hoboken, N.J: Wiley, 2008.
[191] A. J. Kelly, “Atom—Atom Ionization Cross Sections of the Noble Gases—Argon, Krypton, and Xenon,” *J. Chem. Phys.*, vol. 45, no. 5, pp. 1723–1732, 2004.
[192] B. Morris, “Charge-exchange collision dynamics and ion engine grid geometry optimization,” California Institute of Technology, 2007.
[193] J. D. Huba, “NRL: Plasma formulary,” DTIC Document, 2004.
[194] J. F. WAYMOUTH, “PERTURBATION OF A PLASMA BY A PROBE,” Dec. 1962.
[195] R. L. Stenzel, J. Gruenwald, C. Ionita, and R. Schrittwieser, “Electron-rich sheath dynamics. II. Sheath ionization and relaxation instabilities,” *Phys. Plasmas 1994-Present*, vol. 18, no. 6, p. 062113, 2011.
[196] T. Panagopoulos and D. J. Economou, “Plasma sheath model and ion energy distribution for all radio frequencies,” *J. Appl. Phys.*, vol. 85, no. 7, pp. 3435–3443, 1999.

[197] F. F. Chen, J. D. Evans, W. Zawalski, F. F. Chen, J. D. Evans, and W. Zawalski, "Electric Probes," in *In Plasma Diagnostic Techniques, edited by Huddlestone, R.H. and Leornard, S.L*, 1965.
[198] K. Fuhrhop, E. Choiniere, and B. Gilchrist, "A Comparison of Laboratory Experimental and Theoretical Results for Electrodynamic Tether Electron Collection Performance for Some Bare Tether Geometries," in *AIAA SPACE 2009 Conference & Exposition*, American Institute of Aeronautics and Astronautics.
[199] G. J. H. Brussaard, M. van der Steen, M. Carrère, M. C. M. van de Sanden, and D. C. Schram, "Langmuir probe measurements in an expanding magnetized plasma," *Phys. Rev. E*, vol. 54, no. 2, pp. 1906–1911, Aug. 1996.
[200] G. J. H. Brussaard, M. van der Steen, M. Carrère, M. C. M. van de Sanden, and D. C. Schram, "Langmuir probe measurements in expanding magnetized argon, nitrogen and hydrogen plasmas," *Surf. Coat. Technol.*, vol. 98, no. 1–3, pp. 1416–1419, Jan. 1998.
[201] J. Rubinstein and J. G. Laframboise, "Theory of a spherical probe in a collisionless magnetoplasma," *Phys. Fluids 1958-1988*, vol. 25, no. 7, pp. 1174–1182, 1982.
[202] T. Dote, H. Amemiya, and T. Ichimiya, "Effect of a Magnetic Field upon the Saturation Electron Current of an Electrostatic Probe," *Jpn. J. Appl. Phys.*, vol. 3, no. 12, p. 789, Dec. 1964.
[203] J.-M. Siguier, P. Sarrailh, J.-F. Roussel, V. Inguimbert, G. Murat, and J. SanMartin, "Drifting plasma collection by a positive biased tether wire in LEO-like plasma conditions: current measurement and plasma diagnostic," *Plasma Sci. IEEE Trans. On*, vol. 41, no. 12, pp. 3380–3386, 2013.
[204] L. M. Linson, "Current-voltage characteristics of an electron-emitting, satellite in the ionosphere," *J. Geophys. Res.*, vol. 74, no. 9, pp. 2368–2375, 1969.
[205] L. W. Parker, "Plasmasheath-photosheath theory for large high-voltage space structures," in *Space Systems and Their Interactions with Earth's Space Environment*, AIAA Press New York, 1980, p. 477.
[206] J. D. Johnson and A. J. T. Holmes, "Edge effect correction for small planar Langmuir probes," *Rev. Sci. Instrum.*, vol. 61, no. 10, pp. 2628–2631, 1990.
[207] E. H. Walker, "Plasma sheath and screening around a stationary charged sphere and a rapidly moving charged body." 01-Jan-1965.
[208] R. T. Bettinger and E. H. Walker, "Relationship for plasma sheaths about Langmuir probes," *Phys. Fluids 1958-1988*, vol. 8, no. 4, pp. 748–751, 1965.
[209] M. Sugawara, "Electron probe current in a magnetized plasma," *Phys. Fluids 1958-1988*, vol. 9, no. 4, pp. 797–800, 1966.
[210] Y. Y. Lau, "Simple theory for the two-dimensional Child-Langmuir law," *Phys. Rev. Lett.*, vol. 87, no. 27, p. 278301, 2001.
[211] T. E. Sheridan, "How big is a small Langmuir probe?," *Phys. Plasmas 1994-Present*, vol. 7, no. 7, pp. 3084–3088, 2000.
[212] R. C. Altrock, "Forecasting the Maxima of Solar Cycle 24 with Coronal Fe xiv Emission," *Sol. Phys.*, vol. 289, no. 2, pp. 623–629, Jan. 2013.
[213] É. Choinière, S. G. Bilén, B. E. Gilchrist, K. R. Fuhrhop, and A. D. Gallimore, "Experimental investigation of electron collection to solid and slotted tape probes in

a high-speed flowing plasma," *Plasma Sci. IEEE Trans. On*, vol. 33, no. 4, pp. 1310–1323, 2005.

[214] F. T. Ulaby, E. Michielssen, U. Ravaioli, W. H. Hayt, and J. A. Buck, "Fundamentals of Applied Electromagnetics, ISBN: 978-0-13-213931-1," *Instructor*, vol. 201409, 2014.

[215] N. Shastri, A. Western, A. Cauligi, R. Radhakrishnan, B. Bronner, R. Karnik, S. Varughese, B. E. Gilchrist, J. McTernan, and S. Bilén, "Exploring the Potential of Miniature Electrodynamic Tethers and Developments in the Miniature Tether Electrodynamics Experiment," 2014.

[216] I. C. Bell, K. A. Hagen, V. Singh, S. L. McCarty, J. W. Cutler, B. E. Gilchrist, J. K. McTernan, and S. G. Bilen, "Investigating Miniature Electrodynamic Tethers and Interaction with the Low Earth Orbit Plasma," presented at the 27th Annual AIAA/USU Conference on Small Satellites, Logan, Utah, 2013.

[217] R. S. Indiresan, B. E. Gilchrist, S. Basu, J.-P. Lebreton, and E. P. Szuszczewicz, "Simultaneous, dual-point, in situ measurements of ionospheric structures using space tethers: TSS-1R observations," *Geophys. Res. Lett.*, vol. 25, no. 19, pp. 3725–3728, Oct. 1998.